

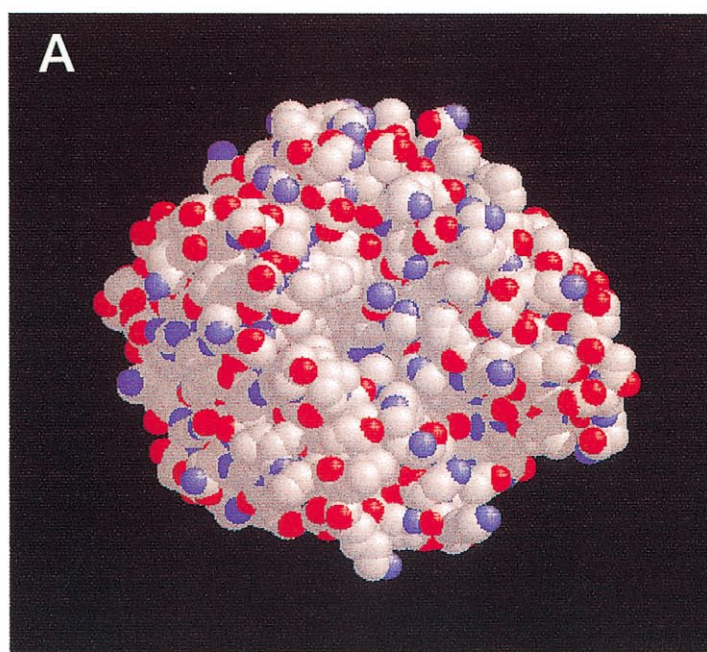
粉

**KONA**

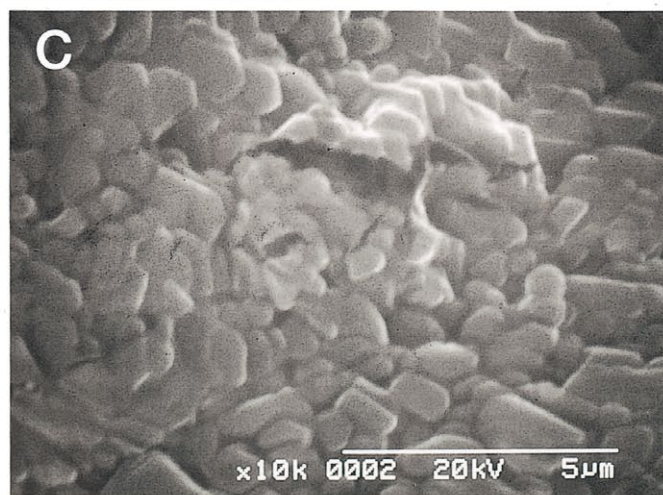
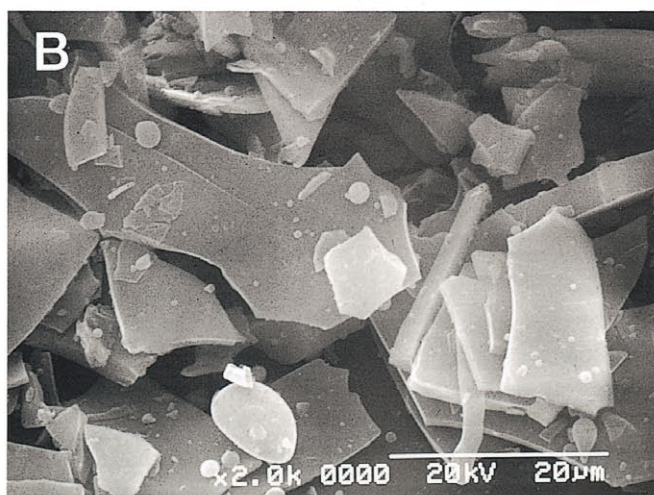
**POWDER AND PARTICLE**

**No. 14(1996)**

Published by Hosokawa Powder Technology Foundation



Electron micrograph of  
a protein (See page 4)



# KONA

## POWDER AND PARTICLE

KONA, issued annually since 1983 by Hosokawa Powder Technology Foundation, Japan, is a refereed journal publishing the articles on powder sciences and technology, and is distributed to the interested persons and institutions throughout the world.

### About the Cover of Journal "KONA"

The chinese character "粉" is pronounced as "KONA" in Japanese, and means "Powder". The hand written "粉" is after the late Mr. Eiichi Hosokawa, the founder of Hosokawa Micron Corporation.



Hosokawa Micron Corporation and its R&D Center

### Editorial Board

**K. Miyanami**

Editor in Chief  
(Univ. of Osaka Prefecture, JAPAN)

#### Asian Block

**Y. Kousaka**

Block Vice Chairman  
(Univ. of Osaka Prefecture, JAPAN)  
(Professor Emeritus of Kyoto Univ., JAPAN)  
(Chubu Powtech Plaza Lab., JAPAN)  
(Former Kyoto Institute of Tech., JAPAN)  
(Professor Emeritus of Himeji Institute of Tech., JAPAN)

**Y. Morikawa**

(Professor Emeritus of Osaka Univ., JAPAN)

**H. Masuda**

(Kyoto Univ., JAPAN)

**Y. Tsuji**

(Osaka Univ., JAPAN)

**H. Emi**

(Kanazawa Univ., JAPAN)

**Y. Kuwahara**

(National Industrial Research  
Institute of Nagoya, JAPAN)

**K. Higashitani**

(Kyoto Univ., JAPAN)

**P. Arnold**

(Univ. of Wollongong, AUSTRALIA)

**S. H. Kang**

(Yeungnam Univ., KOREA)

**W. Tanthapanichakoon**

(Chulalongkorn Univ., THAILAND)

**T. Yokoyama**

(Hosokawa Micron Corp., JAPAN)

**Secretariat**

**F. Nakagawa**

(Hosokawa Micron Corp., JAPAN)

#### European Block

**J. Schwedes**

Block Chairman  
(Univ. Braunschweig, GERMANY)

**B. Scarlett**

Block Vice Chairman  
(Delft Univ. of Technology,  
THE NETHERLANDS)

**K. Schöner**

(Technische Univ. Clausthal, GERMANY)

**H. Schubert**

(Bergakademie Freiberg, GERMANY)

**E. Forssberg**

(Univ. Lulea, SWEDEN)

**S. R. de Silva**

(Postec-Research A/S, NORWAY)

**J. F. Davidson**

(Univ. of Cambridge, UNITED KINGDOM)

**G. F. Ferrara**

(Univ. di Trieste, ITALY)

**J. F. Large**

(Univ. de Tech. de Compiègne, FRANCE)

**Secretariat**

**W. Peukert**

(Hosokawa MikroPul GmbH, GERMANY)

#### Americas Block

**T. P. Meloy**

Block Vice Chairman  
(West Virginia Univ., U.S.A.)

**R. K. Rajamani**

(Univ. of Utah, U.S.A.)

**B. H. Kaye**

(Laurentian Univ., CANADA)

**P. S. Santos**

(Univ. of São Paulo, BRAZIL)

**D. W. Fuerstenau**

(Univ. of California, U.S.A.)

**Secretariat**

**I. Pikus**

(Hosokawa Bepex Corp. U.S.A.)

**D. A. Scott**

(Hosokawa Micron Inter., U.S.A.)

### Publication Office

Hosokawa Powder Technology Foundation (Japan)  
in **Hosokawa Micron Corporation**

No. 9, 1-chome, Shoudai Tajika, Hirakata-shi, Osaka 573 Japan

### Notes

- Hosokawa Powder Technology Foundation has entrusted the editorial duty to the editorial board organized by the Council of Powder Technology, Japan.

(Complimentary Copy)

Printed in Japan

## The Letter from the Editor

Malcolm G. McLaren July 22, 1928-April 13, 1996

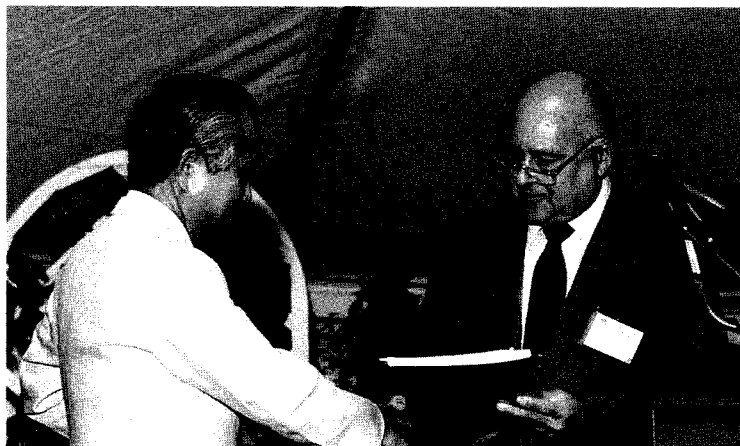


Photo. Dr. McLaren with Mr. M. Hosokawa, Chairman of the Hosokawa Micron Group at the opening ceremony of the Technical centre of Hosokawa Micron Int. in Summit, N.J.

It is with our deep regrets that we inform the KONA readers of the death of our KONA Americas Block chairman, Dr. Malcolm G. McLaren, professor of ceramics and director of the Institute for Engineered Materials at Rutgers University. He passed away on Sunday, April 13, 1996. We have been very surprised and so sorry to hear his sudden death.

On behalf of the KONA Editorial Committee, we all lament his death and extend our condolences heartily. We are also greatly thankful to him for his enormous contributions to the publication of the KONA journal since 1990. His dedication to the KONA Board is evident by his tireless efforts and service to the Board until his death in 1996. His own latest contribution to the KONA journal has appeared in KONA No.12, p.5-6 (1994), entitled as "The Necessity for Establishment of International Standards for Powders", followed by his short biography.

More importantly, we have lost a friend and respected colleague who has left each of us with many fond memories.

It is with great sadness that we report the death of Malcolm G. McLaren, Chairman of the Americas' Block KONA Editorial Committee. Dr. McLaren, professor of ceramics and director of the Institute for Engineered Materials at Rutgers University, was an active researcher and leader in ceramic science and technology. Internationally recognized for his work in ceramics, he authored or coauthored more than 100 publications, lectured in the United States, Europe, Brazil, Australia and China.

A longtime friend of the Hosokawa Micron Group, Dr. McLaren served the KONA Board as the Americas' Block Chairman since 1990. His dedication to the KONA Board was evident by his tireless efforts and service to the Board until his death in 1996.

The Americas' Block  
KONA Editorial Committee



Kei Miyanami,  
Editor-in-Chief

# KONA

## GENERAL INFORMATION

### HISTORY OF THE JOURNAL

KONA journal has been published by the Council of Powder Technology, Japan (CPT), from No.1 to no.12 issues, under the sponsorships of Hosokawa Micron Corporation (No.1 to No.9) and Hosokawa Powder Technology Foundation (No.10 to No.12).

The CPT has been established in 1969 as a non-profit organization to enhance the activities of research and development on powder sciences and technology in Japan under the sponsorship of Hosokawa Micron Corporation. In 1983, the CPT has decided to issue an international journal named "KONA", which publishes the excellent articles appeared in Japanese journals concerning with powder sciences and technology, after translated into English, throughout the world. After the seventh volume issued in 1989, the CPT has changed its policy to internationalize the "KONA" from the 8th issue (1990) and on by incorporating the monographs originally written in English from the authors throughout the world. Immediately, the present editorial board including Asian, Americas' and European Blocks has been organized.

From the 13th issue and on, the Hosokawa Powder Technology Foundation has taken over the role of KONA publisher from the CPT and the Foundation has entrusted the editorial duty to the present KONA editorial board organized by the CPT without requesting any shift in our present editorial policies. This switching of publisher has been simply and only to make the aim and scope of the Foundation definite. Essentially no change has been observed in continuously editing and publishing this journal except in the designation on a part of the journal cover.

### AIMS AND SCOPE OF THE JOURNAL

KONA Journal is to publish the papers in a broad field of powder sciences and technology, ranging from fundamental principles to practical applications. The papers discussing technological experiences and critical reviews of existing knowledge in specialized areas will be welcome.

These papers will be published only when they are judged, by the Editor, to be suitable for the progress of powder sciences and technology, and are approved by each Block Editorial Committee. The paper submitted to the Editorial Secretariat should not have been previously published except the translated papers which would be selected by the Block Editorial Committees.

### CATEGORY OF PAPERS

- Invited papers  
Original research and review papers invited by the Block KONA Editorial committees.
- Contributed papers  
Original research and review papers submitted to the Block KONA Editorial Committees, and refereed by the Editors.
- Translated papers  
Papers translated into English, previously published in other languages, selected by the Block KONA Editorial Committees with the permission of the authors and/or the copyright holder.

### SUBMISSION OF PAPERS

Papers should be sent to each Block KONA Editorial Secretariat.

- Asian Block Editorial Secretariat  
F. Nakagawa  
Hosokawa Micron Corporation Micromeritics Laboratory  
1-9, Shoudai Tajika, Hirakata, 573 JAPAN
- European Block Editorial Secretariat  
Dr. W. Peukert  
Hosokawa Mikropul GmbH  
Welserstr. 9-11, 51149 Köln  
Postfach 900749, 51117 Köln  
GERMANY

- American Block Editorial Secretariat  
Hosokawa Micron International Inc.  
Dr. I. Pikus or D.A. Scott  
10 Chatham Road, Summit, NJ 07901 USA

### FREQUENCY

KONA will be issued once each calendar year.

### SUBSCRIPTION

KONA is distributed free of charge to senior researchers at universities and laboratories as well as to institutions and libraries in the field throughout the world. The publisher is always glad to consider the addition of names of those who wish to obtain this journal regularly to the mailing list. Distribution of KONA is made by each Block Secretariat.

### INSTRUCTIONS TO AUTHORS

- (1) Manuscript format
  - Two copies should be submitted to the Editorial Secretariat, in double-spaces typing on pages of uniform size.
  - Authorship is to give author's names, and the mailing address where the work has been carried out on the title page.
  - Abstract of 100-180 words should be given at the beginning of the paper.
  - Nomenclature should appear at the end of each paper. Symbols and units are listed in alphabetical order with their definitions and dimensions in SI units.
  - Literature references should be numbered and listed together at the end of paper, not in footnotes. Alphabetical order is accepted. Please give information as in the following examples:  
1) Carslaw, H.C. and J.C. Jaeger: "Conduction of Heat in Solids", 2nd ed., Clarendon Press, Oxford, England (1960).  
2) Howell, P.A.: US Patent, 3,334,603 (1963).  
3) Rushton, J.H., S. Nagata and D.L. Engle: AIChE J., 10, 298 (1964).  
4) Seborg, D.E.: Ph. D. Dissertation, Princeton Univ., N.J., U.S.A (1969).
  - Original figures with each single copy should be submitted, on separate sheets. Authors' names and figure numbers are marked in the corner.
  - Figure numbers and captions are listed on a separate sheet.
  - Place of figure insertion is to be indicated in the margin of the manuscript.
  - Tables should be typed on separated sheets.
  - Submit an IBM-readable floppy disk (3 1/2) with your unformatted text file in ASCII code. If you use either WORD or WORD PERFECT – as word processing system, please add the formatted text file.
- (2) Reprints
  - The authors shall receive 50 free reprints. Additional reprints will be furnished when ordered with return of galley proofs.
- (3) Publication policy
  - All papers submitted for publication become immediately the property of the CPT and remain so unless withdrawn by the author prior to acceptance for publication or unless released by the Editor. Papers are not to be reproduced or published in any form without the written permission of the CPT.

# KONA Powder and Particle No. 14 (1996)

## Contents

### <Review>

• A Model of Attrition in the Jetting Region of Fluidised Beds	<i>M. Ghadiri and R. Boerefijn</i> .....	5
• Powder Characterization by Particle Shape Assessment	<i>P. Singh and P. Ramakrishnan</i> .....	16
• Segregation of Particulate Materials – Mechanisms and Testers –	<i>J. Mosby, S.R. de Silva and G.G. Enstad</i> .....	31
• A Review of Ceramic Powder Compaction	<i>D.E. Niesz</i> .....	44
• Classification of Particles in the Submicron Range in an Impeller Wheel Air Classifier	<i>K. Leschonski</i> .....	52
• Electrostatic Manipulation of Bioparticles	<i>M. Washizu</i> .....	61
• Mixing of Particulate Solids	<i>K. Sommer</i> .....	73
• Particles Heat Treating in a Pulsating Gas Stream	<i>A. Parnas</i> .....	79
• Adsorption of Microorganisms to Sand and Diatomaceous Earth Particles Coated with Metallic Hydroxides	<i>J. Lukasik, S.R. Farrah, S. Truesdail and D.O. Shah</i> .....	87
• Relevance of Sol-Gel Methods for Synthesis of Fine Particles	<i>H.K. Schmidt</i> .....	92
• The Brazilian Method for the Determination of Airborne Inorganic Fibres Concentration (Including Asbestos Fibres) – Membrane Filter Method –	<i>R. S. I. Zamataro and W. J. Meirelles</i> .....	104

### <Original Research Paper>

• Particle Identification by Image Processing	<i>G. Bonifazi and P. Massacci</i> .....	109
• Rapid Shape Analysis of Crushed Stone Using Image Analysis	<i>D.A. Broyles, H.W. Rimmer and G.T. Adel</i> .....	130
• Studies on the Effect of Moisture Content and Coarse and Fine Particle Concentration on Segregation in Bins	<i>D.F. Bagster</i> .....	138
• Dust Explosions	<i>P. Wolanski</i> .....	144

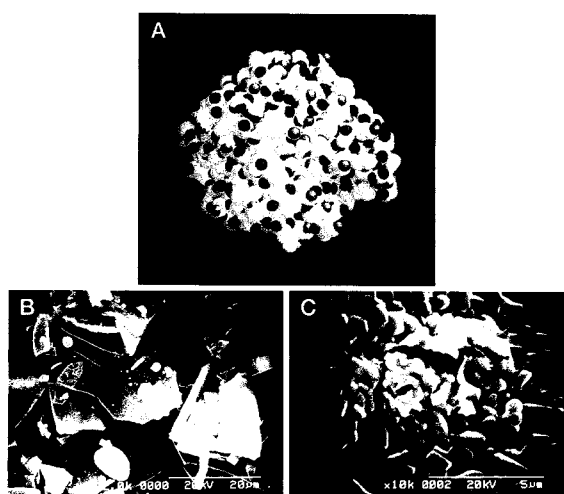
### <Translated Research Paper>

• Preparation of Microcapsule Toner and Their Properties	<i>M. Tanaka, I. Kimura, N. Saitou and H. Tominaga</i> .....	153
• Control of Dispersion of Agglomerated Particles in Water by Electrostatic Repulsion Force	<i>Y. Kousaka, Y. Endo, T. Horiuti and Y. Sasaki</i> .....	162
• Preparation of a Oxide Superconductive Composite using Aerosol Process Technology	<i>Y. Takao M. Awano, Y. Kuwahara and Y. Murase</i> .....	168

• Motion of Grinding Media in Axial Direction and its Effect on Comminution in an Agitation Bead Mill	<i>Y. Hashi and M. Senna</i> .....	176
• Influence of Particle Size of Titanium Dioxide on UV-ray Shielding Property	<i>M. Sakamoto, H. Okuda, H. Futamata, A. Sakai and M. Iida</i> .....	182
• Information Article .....		191

### Explanation of the Cover Photograph

**Electron micrographs of a protein (carbonic anhydrase from bovine; CAB) crystallized at its native condition or precipitated at stressed condition.**



(a) Native structure of CAB visualized by the molecular visualizing software (RasWin Molecular Graphics Ver. 2.6, R. style, Glaxo Wellcome Research and Development Stevenage, Hertfordshire, U.K.) on the basis of the protein data (from Protein Data Bank (PDB), Brookhaven National Laboratory, U.S.A.; PDB Entry ID, 2CAB; Author, K.K. Kannan, M. Ramanadham, T.A. Jones). (b) SEM of the crystals of native CAB (X2000) without heat stress and (c) the inactive aggregates of stressed CAB (X10000), which were precipitated after CAB was exposed to the heat stress (65°C, 10min in 50mM Tris buffer, pH 8.0).

By courtesy of Mrs. H. Umakoshi, H. Ota, K. Yamahara and Prof. R. Kuboi, Dept. of Chem. Sci. and Eng., Faculty of Eng. Sci., Osaka University.

# A Model of Attrition in the Jetting Region of Fluidised Beds<sup>†</sup>

M. Ghadiri and R. Boerefijn

Department of Chemical and Process Engineering  
University of Surrey\*

## Abstract

*Attrition causes material loss and environmental hazards in powder processing. In fluidised beds, the jetting region is the main contributor to attrition. The present paper reviews the recent investigations of the effects of the interaction between single particle properties and jet hydrodynamics. A model of attrition in the jetting region of fluidised beds is presented, based on the impact attrition propensity of single particles and on modelling of the particle flow patterns in the jetting region. The experimental work, carried out for the purpose of evaluation of the model, focused especially on the effects of orifice gas velocity and diameter. The experiments involve measurements of impact attrition of single particles and measurements of particle velocities and solids concentrations in fluidised bed jets. The test materials are fluid cracking catalyst and common salt, both representatives of widely used classes of composite and crystalline materials, respectively. Significant effects of orifice gas velocity and diameter were predicted, which corroborated the experimental data. Hence, the model successfully establishes a link between single particle properties and bulk behaviour in a fluidised jet.*

## 1. Introduction

Attrition, the unintentional breakage of particulate solids during processing, handling and storage, causes material loss and environmental hazards. Fluidised bed operations have become increasingly popular in industrial particle processing, for the ease of solids handling, mixing and high rates of heat and mass transfer. These features are desirable for a number of processes, such as drying and reactor systems, e.g. fluid catalytic cracking and combustion. Unfortunately, the intensive particle motion in fluidised beds causes attrition at the same time. For example, material loss in fluidised catalytic cracking units can amount to several tonnes per day! Zenz and Kelleher [1] have identified the distributor region and the cyclone as important sites for attrition due to the presence of high local velocity gradients. The distributor region provides by far the largest contribution to attrition in fluidised beds, when compared to the bubbling bed and the freeboard above it. Several studies have been undertaken in the past to characterise the attrition propensity of particles in fluidised beds [2], but few take account of the material

properties of particles, or attempt to decouple the interacting hydrodynamic parameters. The dependence of the attrition rate in the jet region on the design and operating parameters, such as the distributor orifice size and gas velocity, and particle size and properties has so far not been established satisfactorily.

A number of empirical correlations for the rate of attrition in fluidised beds,  $R_a$ , have been reported in the literature. These are summarised in **Table 1**. Focusing on two main design and operation parameters, the orifice size,  $d_{or}$ , and the gas velocity,  $u$ , the correlations are generally written in the form of a power law:

$$R_a \propto u^n d_{or}^h \quad (1)$$

where  $u$  can be the orifice gas velocity ( $u_o$ ), or the superficial ( $u_s$ ) or excess gas velocity ( $u_s - u_{mf}$ ), with values of  $n$  ranging from 0.66 to 5.8 and of  $h$  from 0 to 1.11, as reported by different authors. The exponential correlation of Lin *et al.* [6] appears to be an exception to this general form, but replotting their data shows that there is no need for an exponential correlation, and that a good fit is also achieved with a linear regression. Notwithstanding this basic similarity, each of these correlations has been obtained for different materials, experimental set-up and ope-

\* Guildford – GU2 5XH (UK)

† Received: 3 June 1996

**Table 1. Overview of studies of fluidised bed attrition**

Authors	Modelling Equation	Dim. of Attrition Rate	Material	Time of Operation (hr)	Range of ( $u_s - u_{mf}$ ) (m s <sup>-1</sup> )	Range of $u_o$ (m s <sup>-1</sup> )	Grid Type	Background Fluidisation	Attrition Debris Criterion
Blinichev <i>et al.</i> [3]	$R_a = \frac{90 \varphi_s u_s^{5.8} \rho_f^{2.6} 10^{0.21 d_{or} d_p^{-1.8 f}}}{d_p^{1.9} \sigma_{br}^{1.3} \rho_p^{1.3}} \tau^{0.6}$	s <sup>-1</sup>	3-5 mm NaCl, 3-5 mm nitrofosk, 3-5 mm silica gel	1	0-11	20-240	1-8mm holes in perforated plate	None	Elutriate
Merrick and Highley [4]	$R_a = C M_b (u_s - u_{mf})$	kg s <sup>-1</sup>	3 types of coal 1.59 and 3.18 mm diameter	100	0.67-2.67	not indicated	not indicated	0.67-2.67 m s <sup>-1</sup>	Elutriate (smaller than 63 µm)
Chen <i>et al.</i> [5]	$R_a = C \frac{\rho_f Q (\beta u_o)^2}{W d_p \rho_p} f(d_p, \varphi_{so})$ with $f(d_p, \varphi_{so}) = \frac{(1 - \varphi_{so}) [1 - (1 - d_p/d_p^o)^k]}{\varphi_{so} + (1 - \varphi_{so}) (1 - d_p/d_p^o)^k}$	s <sup>-1</sup>	115-274 µm siderite iron ore and 210 µm lignite char	up to 24	0.2-0.5	up to 300	1.47-3.18 mm single jet in porous plate	Variable	Elutriate (smaller than 75 µm)
Lin <i>et al.</i> [6]	$R_a = C \exp(0.162 (u_s - u_{mf}))$	s <sup>-1</sup>	mixtures of 133-354 µm Silica sand and 10-113 µm char	5	0.1-0.32	up to 53.5	492 holes 0.24 cm wide in triangular pitch	None	Elutriate
Zenz and Kelleher [1]	$R_a = C (u_o \sqrt{\rho_f})^{2.5} z \frac{\pi d_{or}^2}{4}$	kg s <sup>-1</sup>	200 µm FCC	12-80	not indicated	33-303	Downward pipe holes 0.8-19 mm wide	Variable	Elutriate
Donsi <i>et al.</i> [7]	$R_a = C (u_s - u_{mf}) \frac{W_c}{d_p}$	kg s <sup>-1</sup>	0.4-3.0 mm coal in 0.2-1.0 mm sand	not indicated	0.55-1.3	82-135	76 upward pipe holes, 1.5 mm wide	None	Elutriate and bed inventory
Kono [8]	$R_a = C \rho_f u_o^3 d_{or}^{0.55} \text{ for } u_o \leq 3.6 \text{ m s}^{-1}$ $R_a = C \rho_f u_o^2 d_{or}^{0.55} \text{ for } u_o > 3.6 \text{ m s}^{-1}$	s <sup>-1</sup>	0.97-4.00 mm Mullite Alumina-Silicates	8-12	0.45-8.0	0.5-30	3.6-15.5 cm single tapered jet	None	Elutriate (smaller than 88 µm)
Sishtla <i>et al.</i> [9]	$R_{bed} = 1.6 \cdot 10^{-3} (u_s - u_{mf})^{0.66} (HGI)^{-0.05}$ $R_a = 2.8 \cdot 10^{-12} (\rho_f^{1.56} u_o^{3.12}) (HGI)^{2.15}$	s <sup>-1</sup>	500-841 µm char	14	0.3-0.6	67-134	6 bubble caps with 3 orifices, 0.24 cm wide, 30° downward	None	Elutriate and bed inventory (smaller than 500 µm)
Seville <i>et al.</i> [10]	$R_a = C (u_s - u_{mf})$	kg s <sup>-1</sup>	1.18-2.80 mm sand agglomerates	up to 0.25	0.15-1.15	74-111	139 holes, 1.5 mm wide on 12 mm triangular pitch	None	Elutriate
Werther and Xi [11]	$R_a = C \rho_f d_{or}^2 u_o^3$	kg s <sup>-1</sup>	106 µm spent FCC, 125 µm fresh FCC	up to 260	0.2	25-100	0.5-2.0 mm single jet in porous plate	Variable	Elutriate (smaller than 23-35 µm)
Ghadiri <i>et al.</i> [12-15]	$R_a = C u_o^n d_{or}^h$ with $n = \begin{cases} 5.1 & \text{for NaCl} \\ 3.31 & \text{for FCC} \end{cases}$ and $h = \begin{cases} 0.44 - 1.11 & \text{for NaCl} \\ 0.6 - 0.76 & \text{for FCC} \end{cases}$	hr <sup>-1</sup>	425-600 µm NaCl, 90-106 µm FCC	10-22	0-0.85	25-125	73, 110 and 175 1.0 mm holes in triangular pitch	None	NaCl: all smaller than 355 µm FCC: all smaller than 75 µm

rating conditions, making it difficult to compare them.

In this work, the attrition of common salt and fluid cracking catalyst (FCC) is considered, focusing in particular on the link between single particle properties and bulk attrition behaviour. These two material types, in addition to their own significance, may be considered as representatives of large classes of widely used materials, i.e. crystalline and composite structures. In this paper, the modelling approach will first be described. The experimental work supporting the development of the model is then presented.

## 2. Modelling Approach

In the present modelling approach, the impact breakage of single particles is coupled with a hydrodynamic model to predict the rate of attrition. The structure of the approach is represented schematically in **Figure 1**.

For impact attrition, Zhang and Ghadiri [16] have proposed the following correlation for the extent of attrition upon impact,  $R_i$ , based on the fracture mechanics of lateral crack formation:

$$R_i = \alpha \frac{\rho_p u_i^2 H d}{K_c^2} \quad (2)$$

where  $\rho_p$  is the particle density,  $u_i$  the impact velocity,  $H$  the hardness,  $K_c$  the fracture toughness,  $d$  a linear dimension of the particle, and  $\alpha$  is a proportionality constant to be determined experimentally. In practice, the value of the power index of  $u_i$  may differ slightly from 2, depending on the complexity of the particle structure. It is therefore more general to consider:

$$R_i \propto u_i^m \quad (3)$$

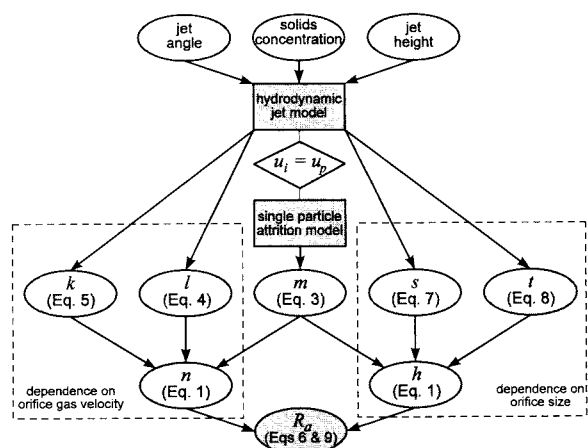


Fig. 1 Schematic representation of the modelling approach.

where the power index  $m$  may be obtained from particle impact tests.

In a fluidised bed with a jetting distributor region, the contribution of the bubbling zone to the attrition rate is usually very small compared to that of the jetting region [13]. The attrition mechanism in a fluidised bed jet involves the entrainment of particles into a dilute jet core, followed by the acceleration of the particles, whereafter they impact on the dense phase on top of the jet. Intense interparticle collisions are considered to cause attrition, at a rate that can be estimated from impacts of single particles on a rigid target, at an impact velocity,  $u_i$ , corresponding to the particle velocity,  $u_p$ , in the jet.

The number of particles engaged in the attrition process scales with the rate at which solids become entrained from the bulk into the dilute jet core. A hydrodynamic model may be used to obtain the dependence of  $W_s$ , and  $u_p$  on the orifice gas velocity. This can be done by power-law correlations [12]:

$$u_p \propto u_o^l \quad (4)$$

$$W_s \propto u_o^k \quad (5)$$

Ghadiri *et al.* [12] proposed that the attrition rate in the jetting region is linearly related to the single particle impact attrition and the solids entrainment rate. Thus, substituting Eq. (4) into Eq. (3), and multiplying by the solids entrainment rate,  $W_s$ , the attrition rate in a single jet may be given as:

$$R_a \propto W_s R_i \propto u_o^k u_p^m \propto u_o^{k+l+m} \quad (6)$$

In this way, a descriptive and predictive model is established, which incorporates the single particle attrition characteristics. The results of this approach will be presented in section 4.

The dependence of the attrition rate  $R_a$  on the orifice size, as reported in the literature, is inconsistent. The power index  $h$  in Eq. 1 given by Kono [8] and Ghadiri *et al.* [15] is of order unity, between 0.44 and 1.11. For comparison with other correlations that are expressed in different dimensions, e.g. those of Werther and Xi [11], and Zenz and Kelleher [1], it is necessary to normalise the correlations, e.g. by dividing the rate of attrition by the mass flow rate of fluidising gas. Following this approach, the correlations of Werther and Xi [11] and Zenz and Kelleher [1] indicate that the attrition rate does not depend on the orifice size.

For the analysis of the effect of the orifice size

on the attrition rate  $R_a$ , Ghadiri *et al.* [15] have employed a similar approach as described above for the effect of orifice gas velocity. Normalising the solids entrainment rate with respect to the gas flow rate,  $W_g$ , its dependence on the orifice diameter,  $d_{or}$ , can be expressed in a power law [15]:

$$W_s / W_g \propto d_{or}^s \quad (7)$$

and similarly for the dependence of the particle velocity:

$$u_p \propto d_{or}^l \quad (8)$$

Following the same approach as for the effect of velocity (Eq. 6), the attrition rate in the jet can be expressed as:

$$R_a \propto (W_s / W_g) R_i \propto d_{or}^s u_p^m \propto d_{or}^{s + tm} \quad (9)$$

Thus, the dependence of the attrition rate on the orifice size can be established by quantifying the power indices. This is described in section 4.

Independent studies of the hydrodynamics of fluidised bed jets by Massimilla and co-workers, firstly introduced by De Michele *et al.* [17], have provided comprehensive models of particle flow patterns in the jetting region [18]. With these hydrodynamic models, particle velocities and solids entrainment rates can be readily obtained for different orifice velocities and sizes. However, the application of these models requires knowledge of the relevant input parameters, describing the jet geometry, such as the jet penetration length, the jet divergent angle, and the solids concentration in the jet. These have to be obtained from separate experiments, which are described in sections 3.2 and 3.3.

### 3. Experimental

Several tests have been employed in the evaluation of the jet attrition model. The experiments involve firstly single particle impact tests for the determination of the impact attrition of single particles as a function of the impact velocity, as shown in Eq. 2. This is described in section 3.1. Secondly, the attrition rate in a fluidised bed with several gas distributors has been measured in order to compare these results with predictions from the attrition model. This is described in section 3.2. In order to quantify the power indices given in equations (6) and (9), it is first necessary to specify a number of hydrodynamic parameters, such as the jet angle.

This is described in section 3.3.

#### 3.1 Single particle impact test

Single particle impact tests have been carried out in an impact test rig developed previously [19] and shown in **Figure 2**. It consists of a funnel-shaped inlet section guiding the particles into an eductor tube, which ends in a collection chamber, where particles impact on a rigid horizontal target plate made of sapphire. The particle velocity before impact is measured with dual light diodes or with a laser Doppler velocimeter.

The impact product is analysed gravimetrically. As a criterion for attrition, the mass of debris passing through a sieve, with a size of two BS410 sieve sizes below the lower limit of the original size, is chosen. In the low range of impact velocities, where mainly surface damage (chipping) occurs, the fines produced will be far smaller than the original mother particles. Cleaver *et al.* [20] have shown that the attrition results are in this case insensitive to the specific criterion applied, as long as the sieve size, used for the separation of debris from the mother particles, lies in between the particle size distributions of the **Fine Product** and **Coarse Product**, as shown schematically in **Figure 3**. The attrition rate is then simply defined as the ratio of the mass of fine product to the initial sample mass of mother particles:

$$R_i = \frac{M_{\text{fine product}}}{M_{\text{mother particles}}} \quad (10)$$

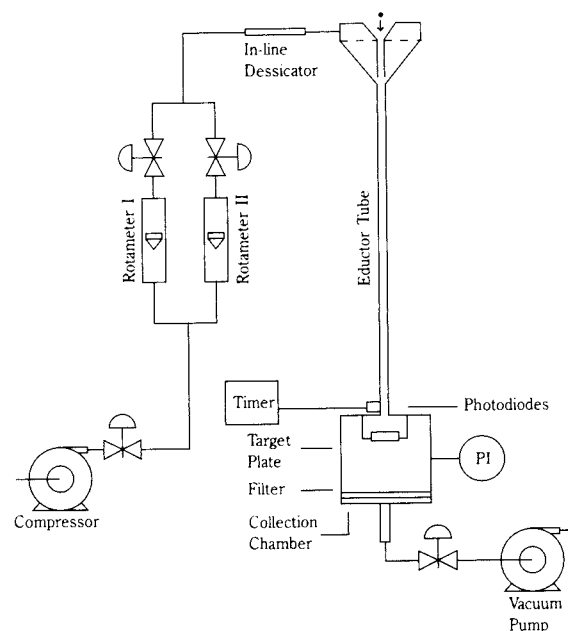


**Fig. 2** Air eductor single particle impact rig.

### 3.2 Fluidised bed attrition test

Fluidised bed attrition tests have been carried out for the determination of the variation of attrition with orifice gas velocity and size.

Two materials have been investigated, Pure Dried Vacuum (PDV) NaCl salt, produced by ICI plc, mean particle size  $d_p = 418 \mu\text{m}$ , with a density of  $2180 \text{ kg m}^{-3}$ , and FCC,  $d_p = 106 \mu\text{m}$ , with a density of  $1500 \text{ kg m}^{-3}$ . For FCC, the data of Werther and Xi [11] were used. The experimental set-up used for fluidised bed attrition tests of salt is shown in **Figure 4**. A detailed description can be found elsewhere [13]. Three different perforated plate distributors were used, with 73, 110, and 175 holes of 1 mm diameter, *i.e.* each with a different free area. This enabled the decoupling of the effect of superficial and orifice gas velocity on the attrition rate, since the bed could be operated at the same superficial velocity for three different orifice gas velocities. According to the correlation of Fakhimi and Harrison

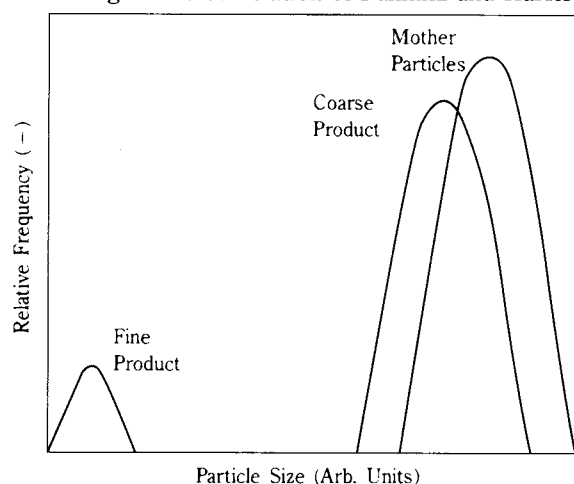


**Fig. 3** Particle size distribution for chipping attrition.

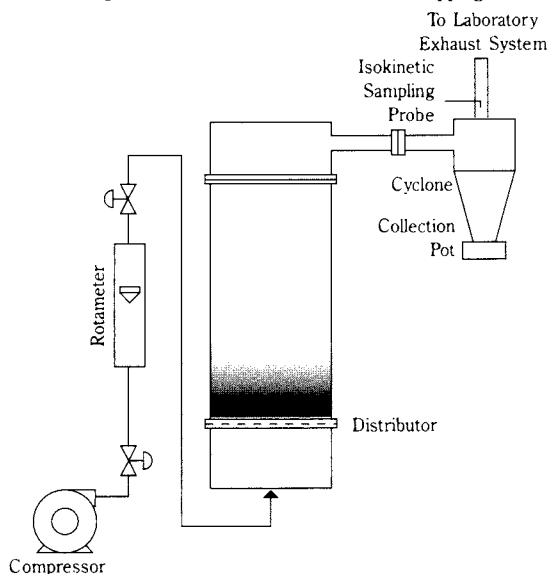


**Fig. 4** Fluidised bed used for attrition tests.

[21], all grid holes were active in all conditions, so that good distribution of air across the distributor was ensured.

The contributions of the jetting region and of the bubbling part of the bed to the attrition rate have been decoupled by operating the bed at different loading, yielding different bed heights. By plotting the attrition rate against bed height and extrapolating to a height equal to the jet height, the contribution of the jetting region to attrition has been quantified.

The effect of distributor orifice diameter on the attrition rate has been investigated by Ghadiri *et al.* [15] using salt as the test material in a 58 mm diameter cylindrical Perspex bed of 0.9 m height, otherwise similar to the set-up shown in **Figure 4**. The results are presented in section 4.

### 3.3 Measurement of jet parameters

In the hydrodynamic jet model of De Michele *et al.* [17], which is employed here, the particle flow patterns in the jet are calculated on the basis of Schlichting similarity profiles, following the turbulent jet theory of Abramovich [22]. These profiles scale with the actual geometry of the jet, as it extends axially and expands radially into the bulk of the bed. To establish these profiles for a given orifice size and velocity, several parameters, such as the jet angle and height, and the initial solids concentration at the jet exit need to be specified. All these parameters are difficult to measure, especially in a three-dimensional bed. A number of measurements have been carried out in two-dimensional and three-dimensional (cylindrical) fluidised beds, using various measurement techniques [12-15, 23-25]. The measurements with two-dimensional beds are only used for input in the two-dimensional version of the hydrodynamic model. However, comparison of the model predictions with the experimental data from two-dimensional configurations can be used to check the validity of the current approach.

Measurements of jet angles in the cylindrical fluidised bed, described in section 3.2, have been carried out using an X-ray facility using salt,  $d_p = 418 \mu\text{m}$ , and alumina particles,  $d_p = 107 \mu\text{m}$  [25].

Digital analysis of video images taken from a two-dimensional fluidised bed, shown in **Figure 5**, has been used for measurements of jet half angles with FCC catalyst,  $d_p = 90 \mu\text{m}$ . In this apparatus, the gas jet is produced by slots, sandwiched between two porous plates for background fluidisation [23].

In this two-dimensional set-up, a strong dependence of the jet angle on orifice gas velocity has

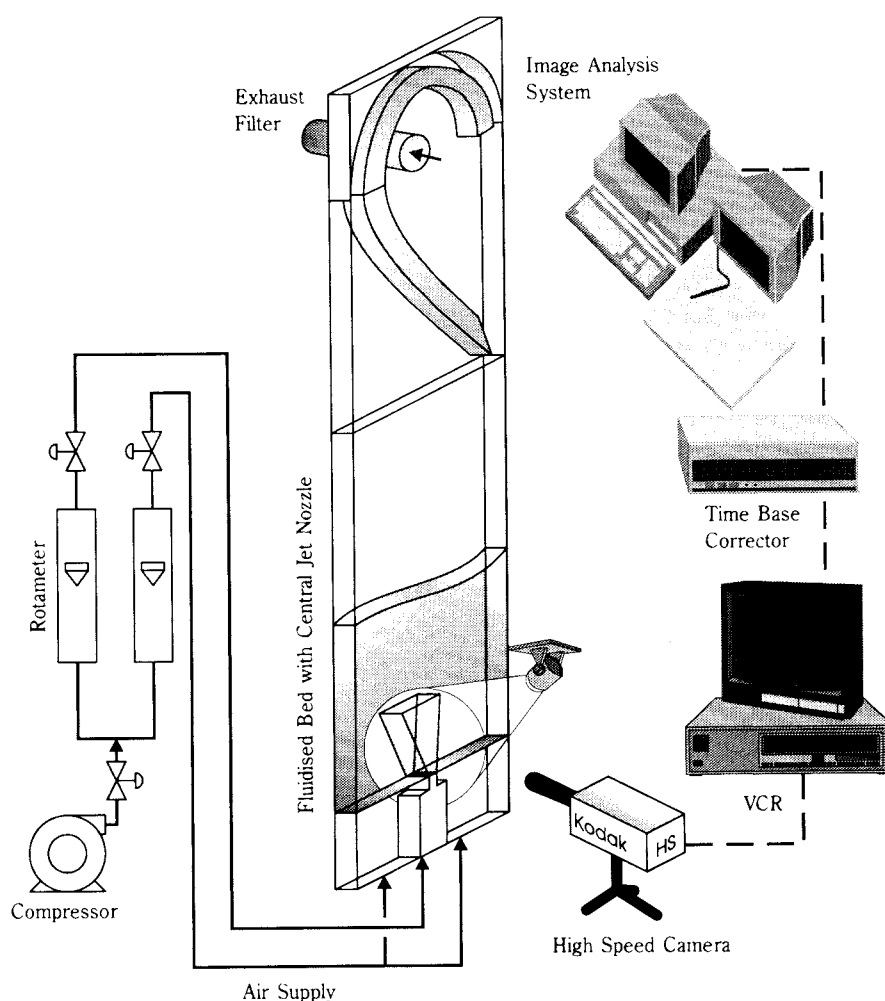


Fig. 5 Two-dimensional fluidised bed for high-speed video imaging of jets.

been found, even with a narrow orifice of 0.5 mm, where the jet half angle decreases in a linear fashion from  $11.5^\circ$  ( $u_o = 9.4 \text{ ms}^{-1}$ ) to  $7^\circ$  ( $u_o = 54 \text{ ms}^{-1}$ ). The trends for different orifices behave like tangents to a single hyperbolic curve, as shown in **Figure 6**. There is, however, a certain overlap in the gas velocity range, where the trendlines for neighbouring jet sizes cross over each other, indicating a distinct effect of the orifice size, rather than just a velocity effect. Similar effects, but to a different extent, were observed in the three-dimensional set-up [25].

Measurements of the initial solids concentration in the jet have been made using the two-dimensional fluidised bed, shown in **Figure 5**, which was equipped with optical glass walls for the specific purpose of video recordings with a high resolution camera [23]. Results of these measurements are shown in **Figure 7**. The solids concentration at the nozzle exit appears to increase with decreasing orifice size. This is supported by our visual observations [24] that with wide orifices, the jet core is clear of solids,

whereas with narrow orifices the jet core is occupied by a significant amount of solids, even at high  $u_o$ .

In order to compare the hydrodynamic model predictions with the actual solids flow patterns, measurements of particle velocities have been carried out in the two-dimensional bed equipped with optical glass walls, for the FCC and the NaCl salt. The results are shown in **Figure 8** and **9** [23, 24]. These measurements have been obtained, using digital image analysis of video images of the particle flow, recorded with a Kodak high speed video camera at frame rates up to 40500 frames per second.

For FCC (**Figure 9**), a good agreement is shown between experimental data and predictions from the hydrodynamic model. For NaCl (**Figure 8**), the agreement is fair, but the data are more closely matched for large orifice diameters. Considering the observation that NaCl particles do not accelerate significantly along the jet height for narrow orifices, because of the increased solids concentration, this feature suggests that there is a distinct effect of the ratio of

particle-to-orifice diameter on the flow pattern, which is currently not accounted for in the model.

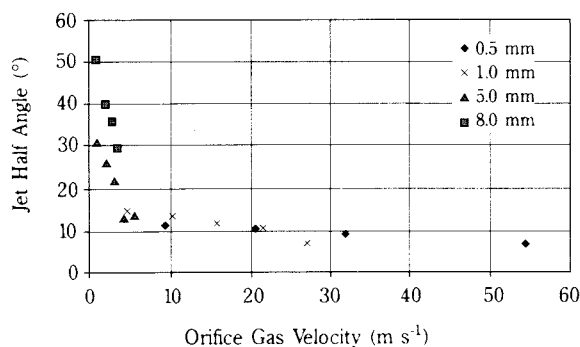


Fig. 6 Jet angles in a fluidised bed jet of FCC ( $d_p = 90 \mu\text{m}$ ) as a function of  $u_o$  for different orifices.

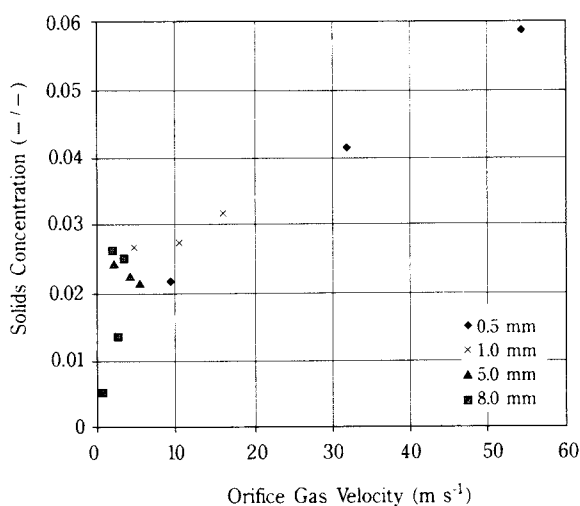


Fig. 7 Solids concentration in a fluidised bed of FCC ( $d_p = 90 \mu\text{m}$ ) at the orifice exit as a function of  $u_o$  for different orifices.

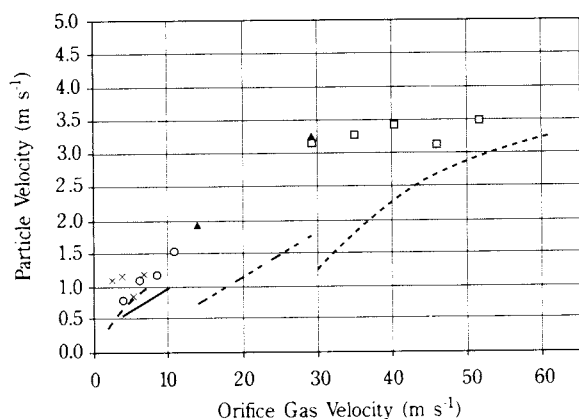


Fig. 8 Comparison of numerical predictions (lines) and experimental measurements (markers) of particle velocities of NaCl particles in jets from different nozzles.  
 $\times$ , --- :  $d_{or} = 8.0 \text{ mm}$ ;  $\circ$ , — :  $d_{or} = 5.0 \text{ mm}$ ;  
 $\blacktriangle$ , - · - :  $d_{or} = 0.5 \text{ mm}$ ;  $\square$ , ··· :  $d_{or} = 0.2 \text{ mm}$ .

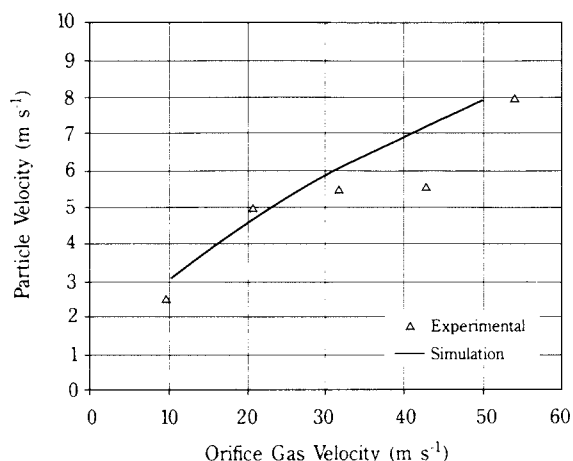


Fig. 9 FCC particle velocity in the jet from a 0.5 mm jet nozzle.

## 4. Attrition model application and evaluation

### 4.1 Effect of velocity on single particle impact attrition

The first step in the application of the attrition model is the establishment of the power index  $m$  in Eq. (3). The single particle impact tests show a slight variation from the theoretical value of 2 for some materials. Table 2 shows measured values of  $m$  for melt-grown and solution grown NaCl crystals, and for FCC. The solution grown NaCl crystals contain polycrystals and crevasses, which contribute to the deviation of  $m$  from 2. The index  $m$  is sensitive to internal and surface defects and structure, the presence of polycrystals, work-hardening and fatigue [13, 14, 16, 26].

Table 2. Impact attrition power indices

Material	$m$
NaCl melt-grown	2.0
NaCl solution-grown	2.6
FCC	2.34

### 4.2 Effect of distributor orifice size and velocity on fluidised jet attrition

The measurement of the fluidised bed jet attrition as a function of orifice velocity and size involved decoupling of a number of concurrent processes, such as the attrition in the jetting region and in the bubbling part of the bed. As described in section 3.2, experiments with different bed heights have been carried

out to enable the establishment of a correlation between the bed height and the attrition rate, from which the attrition in the jetting region may be inferred. The result of this operation is shown in **Figure 10**, where the data points are accompanied by a trendline of a best fit with a power index yielding a value of  $n$  in Eq. (6), as reported in **Table 3**.

The entrainment rate and particle velocity in the jet, as predicted by the hydrodynamic jet model, are shown in **Figures 11** and **12** for NaCl for a 1.0 mm orifice diameter. From the curve fits, values of the power indices  $k$  and  $l$ , for the particle velocity and the solids entrainment rate, respectively, as given in Eqs (4) and (5), may be obtained. These are given in **Table 3**, together with the value of  $m$ , from Eq. (3), for the NaCl particles. The overall attrition index  $n$  (Eq. 6) is then calculated and is given in **Table 3**.

The predicted results compare favourably with experimental data for NaCl and FCC, also shown in **Table 3**. The experimental value of  $n$  for FCC is that given by Werther and Xi [11]. Zenz and Kelleher [1] report a slightly lower value of 2.5 for larger FCC particles. Values of  $k$  and  $l$  for FCC have been obtained using the experimental parameters given

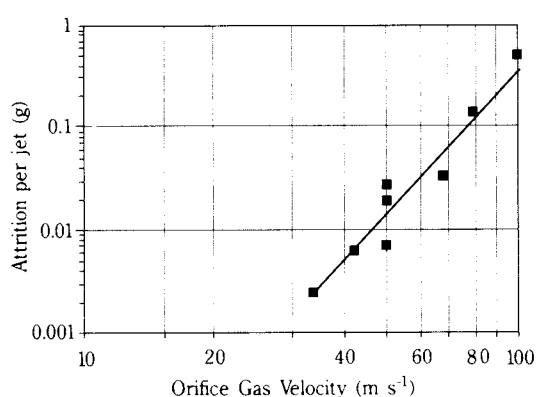


**Fig. 10** Variation of the attrition per jet with jet velocity for the jetting region of a fluidised bed containing PDV salt, calculated at a jet height estimated from the Yang and Kearns [31] correlation.

**Table 3.** Fluidised bed hydrodynamic and attrition power indices

Parameter	NaCl	FCC
$k$	1.9	1.3
$l$	0.9	0.9
$m$	2.6	2.3
$n$	4.3	3.3
$n$ (exp.)	4.6	3.0 [11]

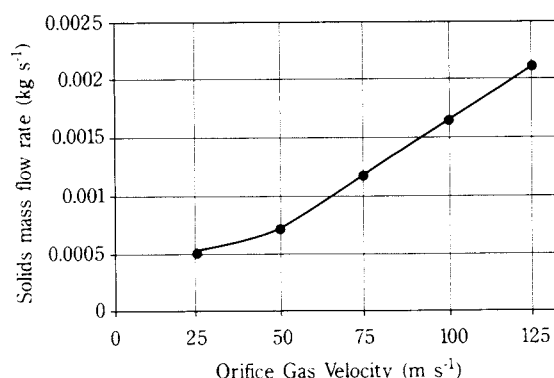


**Fig. 11** Predicted variation of the solids entrainment rate  $W_s$  in a fluidised bed of NaCl with the orifice gas velocity from a 1.0 mm orifice.

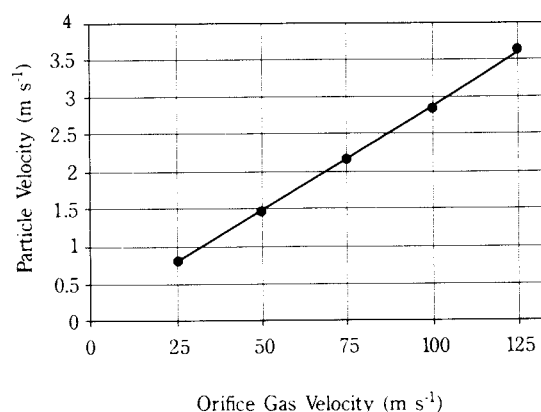


**Fig. 12** Prediction of particle velocity as a function of orifice velocity from a 1.0 mm orifice in a fluidised bed of NaCl.

by Werther and Xi [11] and  $m$  has been obtained by single particle impact testing [1] using the same material as used by Werther and Xi [11].

The predicted dependence of the attrition rate on the orifice diameter is shown in **Table 4**, where the values of  $s$ ,  $t$  and  $h$  have been given (see Eqs (7)-(9)). The values of  $h$  compare reasonably well with the experimental values of Kono [8] and Ghadiri *et al.* [15], but contradict with the absence of any effect of the orifice size, as indicated by Werther and Xi [11] and Zenz and Kelleher [1]. Variations in the level of background fluidisation may be responsible for this difference (see **Table 1**).

**Table 4.** Hydrodynamic and attrition parameters for the effect of the orifice diameter

$u_o$	FCC			NaCl		
	$s$	$t$	$h = \frac{h}{s+t \cdot m}$	$s$	$t$	$h = \frac{h}{s+t \cdot m}$
25	-0.006	0.41	0.95	-0.004	0.44	1.11
75	0.06	0.3	0.76	0.11	0.28	0.84
125	0.17	0.182	0.6	0.18	0.1	0.44

## 5. Discussion

The model of jet attrition combines a model of particle breakage with a hydrodynamic model of particle flow in a jet in order to predict the rate of attrition. The experimental observations of particle velocity and concentration profiles suggest that there is an influence of the orifice-to-particle size ratio, and this is currently not taken into account in the hydrodynamic model.

For orifices much larger than the particle size, the core of the jet is almost entirely clear of particles, whereas for orifices of size comparable to or smaller than the particle size the solids concentration in the jet was observed to be high. This strongly influences the particle-particle interactions. For the latter, at high orifice velocities, the particles will shear against each other, causing abrasion, whereas for the former, particles may accelerate freely, causing more integral damage, thus increasing the probability of fragmentation. Further refinement of the model is necessary to incorporate the effect of the ratio of orifice diameter to particle size.

There are several simplifying assumptions in the attrition model, whose validity may have to be assessed for particles of interest. These are as follows.

i) It is assumed that the dependence of interparticle impact damage on impact velocity follows the same trend as the impact of a particle on a rigid target. The latter may provide a more extensive damage as the target is rigid. However, the effect of impact velocity is not expected to be different from interparticle collisions.

Generally, the collision frequency in a fluidised bed is very high. The high speed video recordings of NaCl particles showed that particles in fact accelerate along the jet axis, which is almost clear of particles, and subsequently impact on the dense phase on top of the jet. The particles often scour the jet boundary as if they had been launched into a pin ball machine. However, most of the momentum is dissipated during the first impact, and the subsequent collisions take place at a velocity similar to the recirculation velocity of particles in the bulk. Therefore, the actual process of attrition will be contained in the first particle-bulk collision, and the similarity between the single impact and the jet impact is preserved.

ii) The influence of time is shown in **Figure 13** for NaCl particles. This effect has not been considered in several investigations, where tests have been performed for one hour only [3, 27], or even shorter periods [10]. Cairati *et al.* [28] have shown that

molybdate catalyst particles do not reach steady state equilibrium within one hour in the Forsythe-and-Hertwig test [27], and the present NaCl particles reach steady state only after five hours.

iii) Impact breakage studies have shown that repeated impacts at the same velocity may progressively either weaken or strengthen the particles, causing the attrition rate to vary with the number of impacts [29]. Plastic deformation of semi-brittle particles may cause work-hardening, which eventually leads to an increase in the attrition rate. On the other hand, the first few impacts may cause weaker particles to break, whence the remainder would appear to be more resistant to attrition.

iv) In the analysis of attrition, Ghadiri *et al.* [12-15] have carried out a complete analysis of the bed inventory, accounting for the debris in the bed. In a number of previous investigations, the attrition rate is quantified by the amount of fines elutriated from the bed. This process ignores the quantity of the debris [30] which is in dynamic equilibrium in the bed [31]. This may be a source for discrepancies in the trends reported in the literature.

The power index  $m$  for single particle impact damage does not vary widely from its theoretical value of 2 for FCC and different types of NaCl. However, the overall attrition index varies from 3 to about 5! It is interesting to note that the present approach is capable of identifying the relevant hydrodynamic parameters to predict the actual power index for attrition in the processing environment.

## 6. Conclusions

The model of attrition in fluidised bed jets provides a realistic prediction of the effect of a number of important design and operating parameters such as orifice size and gas velocity. The model takes account of the particle properties and hydrodynamic conditions of the jet. The procedure established to estimate the attrition rate in the jetting region of fluidised beds is to obtain a measure of the attrition propensity of single particles by impact testing and to couple this process with the rate of solids entrainment into the jetting region by the use of hydrodynamic modelling. The model has been successfully applied to two very different types of material, FCC powder and NaCl crystals. Further testing with materials such as weakly-bonded agglomerates and resins would be useful to establish the range of the applicability of the model.

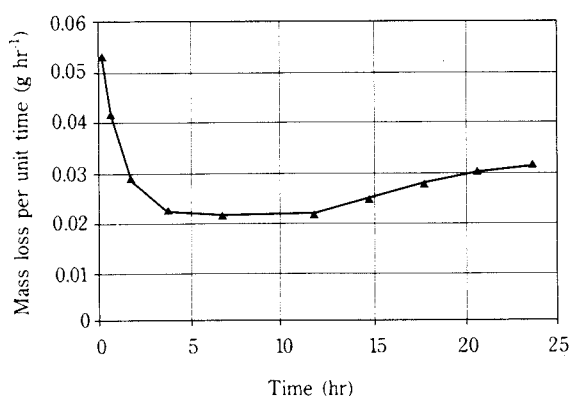


Fig. 13 Time dependent attrition rate of common PDV salt in a jetting fluidised bed [13].

## 7. Acknowledgement

Financial support from the University of Surrey and Shell Research B.V. is gratefully acknowledged. The authors are grateful to EPSRC and Mr Peter Goodyer for providing quick access to the high speed video and photography facilities from EPSRC's equipment pool. Dr W. Duo is thanked for his valuable comments on the manuscript.

## 8. Nomenclature

$C$	: Constant	(see Table 1)
$d$	: linear particle dimension	(m)
$d_{or}$	: distributor orifice size	(m)
$d_p$	: mean particle size	(m)
$d_{p,0}$	: initial mean particle size	(m)
$f$	: distributor free area	(-/-)
$h$	: power index (Eq. 1)	(-/-)
$H$	: hardness	(Pa)
$HGI$	: Hardgrove Grindability Index	(kg)
$k$	: power index (Eq. 5)	(-/-)
$K_c$	: fracture toughness	(N m <sup>-3/2</sup> )
$l$	: power index (Eq. 4)	(-/-)
$m$	: power index (Eq. 3)	(-/-)
$M$	: mass	(kg)
$M_b$	: total bed weight	(kg)
$n$	: power index (Eq. 1)	(-/-)
$Q$	: volumetric orifice gas flow rate	(m <sup>3</sup> s <sup>-1</sup> )
$R_a$	: fluidised bed jet attrition	(-/-)
$R_{bed}$	: fluidised bed bulk attrition	(-/-)
$R_i$	: single particle impact attrition	(-/-)
$s$	: power index (Eq. 7)	(-/-)
$t$	: power index (Eq. 8)	(-/-)
$u_i$	: particle impact velocity	(m s <sup>-1</sup> )
$u_{mf}$	: minimum fluidisation velocity	(m s <sup>-1</sup> )
$u_o$	: orifice gas velocity	(m s <sup>-1</sup> )
$u_p$	: particle velocity in the jet	(m s <sup>-1</sup> )

$u_s$	: superficial gas velocity	(m s <sup>-1</sup> )
$W$	: residue bed weight	(kg)
$W_c$	: carbon loading	(kg)
$W_s$	: solids entrainment rate	(kg s <sup>-1</sup> )
$W_g$	: gas mass flow rate	(kg s <sup>-1</sup> )
$z$	: number of grid jet holes	(-/-)
$\beta$	: correction factor	(-/-)
$P_f$	: fluid density	(kg m <sup>-3</sup> )
$P_p$	: solids density	(kg m <sup>-3</sup> )
$\sigma_{br}$	: crushing strength	(Pa)
$\tau$	: processing time	(s)
$\varphi_s$	: particle sphericity	(-/-)
$\varphi_{so}$	: initial particle sphericity	(-/-)

## 9. References

- 1) Zenz, F.A. and E.G. Kelleher: J. Powder & Bulk Solids Technol., 4 (2/3), 13 (1980)
- 2) Bemrose, C.R. and J. Bridgwater, Powder Technol., 49, 97 (1987)
- 3) Blinichev, V.N., V.V. Strel'tsov and E.S. Lebedeva: Intern. Chem. Engng, 8 (4), 615 (1968)
- 4) Merrick, D. and J. Highley: AIChE Symp. Series, 137 (70), 366 (1974)
- 5) Chen, T.P., C.I. Sishtla, D.V. Punwani and H. Arastoopour, "A Model for Attrition in Fluidized Beds", in *Fluidization*, J.R. Grace and J.M. Matsen eds, Engineering Foundation, New York, 445 (1980)
- 6) Lin, L., J.T. Sears and C.Y. Wen: Powder Technol., 27, 105 (1980)
- 7) Donsì, G., L. Massimilla and M. Miccio: Combustion and Flame, 41, 57 (1981)
- 8) Kono, H.: AIChE Symp. Series, 205 (77), 96 (1981)
- 9) Sishtla, C., J. Findlay, I. Chan and T.M. Knowlton: "The Effect of Temperature and Gas Velocity on Fines Generation in Non-Reactive Fluidized Beds of Coal Char", in *Fluidization VI*, J.R. Grace, L.W. Shemilt and M.A. Bergounou eds, Engineering Foundation, New York, 581 (1984)
- 10) Seville, J.P.K., M.A. Mullier, L. Hailu and M.J. Adams: "Attrition of Agglomerates in Fluidised Beds", *Proc. VII<sup>th</sup> Intern. Conf. on Fluidization*, Queensland, Engineering Foundation, New York, 587 (1992)
- 11) Werther, J. and W. Xi: Powder Technol., 76, 39 (1993)
- 12) Ghadiri, M., J.A.S. Cleaver and V.G. Tuponogov: "Modelling Attrition Rates in the Jetting Region of a Fluidised Bed", *Proc. Symposium of Attrition and Wear in Powder Technology*, Utrecht (NL), 79 (1992a)
- 13) Ghadiri, M., J.A.S. Cleaver and K.R. Yüregir: "Attrition of Sodium Chloride Crystals in a Fluidized Bed", *Proc. VII<sup>th</sup> Intern. Conf. on Fluidization*, Queensland, Engineering Foundation, New York, 603 (1992b)
- 14) Ghadiri, M., J.A.S. Cleaver, V.G. Tuponogov and J. Werther: Powder Technol., 80, 175 (1994)

- 15) Ghadiri, M., J.A.S. Cleaver and V.G. Tuponogov: "Influence of Distributor Orifice Size on Attrition in the Jetting Region of Fluidized Beds", *Preprints VIII<sup>th</sup> International Symposium on Fluidization*, Tours (F), Engineering Foundation, 799 (1995)
- 16) Zhang, Z. and M. Ghadiri: "Effect of Particle Size on Attrition", *Proc. First International Particle Technology Forum*, AIChE, Denver, Colorado, 247 (1994)
- 17) De Michele, G., A. Elia and L. Massimilla: *Ing. Chim. Ital.*, 12 (11-12) 155 (1976)
- 18) Massimilla, L.: "Gas Jets in Fluidized Beds", in *Fluidization*, 2<sup>nd</sup> ed., J.F. Davidson, R. Clift and D. Harrison eds, Academic Press, New York, 133 (1985)
- 19) Ghadiri, M., and K.R. Yüregir: "Impact Attrition of NaCl Particles", in *Tribology in Particulate Technology*, B.J. Briscoe and M.J. Adams eds, Adam Hilger, Bristol (1987)
- 20) Cleaver, J.A.S., M. Ghadiri and N. Rolfe: *Powder Technol.*, 76, 15 (1993)
- 21) Fakhimi, S. and D. Harrison: *Inst. Chem. Eng. Symp. Ser.*, 33, 29 (1971)
- 22) Abramovich, G.N.: "The Theory of Turbulent Jets", MIT Press, Cambridge Massachusetts (1963)
- 23) Boerefijn, R. and M. Ghadiri: "Attrition of Fluid Cracking Catalyst in Fluidised Beds", *Proc. 5<sup>th</sup> World Congress on Chem. Engng/2<sup>nd</sup> Intern. Particle Technol. Forum*, San Diego, 273 (1996a)
- 24) Boerefijn, R. and M. Ghadiri: "Motion Analysis of Fine Particles in Jets in Two-Dimensional Fluidised Beds", *Proc. IChemE Research Event/2<sup>nd</sup> European Conference for Young Researchers in Chemical Engineering*, Leeds/Bradford, 1048 (1996b)
- 25) Cleaver, J.A.S., M. Ghadiri, V.G. Tuponogov, J.G. Yates and D.J. Cheesman: *Powder Technol.*, 85, 221 (1995)
- 26) Papadopoulos, D.G. and M. Ghadiri: *Adv. Powder Technol.*, In Press (1996)
- 27) Forsythe Jr, W.L. and W.R. Hertwig: *Ind. & Engng Chem.*, 41 (6), 1200 (1949)
- 28) Cairati, L., L. Di Fiore, P. Forzatti, I. Pasquon and F. Trifirò: *Ind. Eng. Chem. Process Des. Dev.*, 19, 561 (1980)
- 29) Zhang, Z., PhD Thesis, Univ. of Surrey, 1994
- 30) Ayazi Shamlou, P., Z. Liu and J.G. Yates: *Chem. Engng Sci.*, 45 (4), 809 (1980)
- 31) Donsi, G., G. Ferrari, B. Formisani, and G. Longo: *Powder Technol.*, 61, 75 (1990)
- 32) Yang, W.-Y. and D.L. Kearns: *AIChE Symp. Series*, 205 (77), 28 (1981)

### Authors' short biography



#### Professor Mojtaba Ghadiri

Mojtaba Ghadiri graduated in Chemical Engineering from the University of Tehran, and subsequently obtained an MSc from Imperial College and a PhD from the University of Cambridge. He then worked for Unilever Research as a scientist for two years before joining the University of Surrey in 1983. Mojtaba Ghadiri holds the Chair of Particle Technology at the University of Surrey. His current research activities are on attrition and comminution of particulate solids, fluidisation, and electrical effects in bulk particulate systems. He has developed a specialised facility for mechanical testing of fine particulate solids and has worked extensively on linking the material properties with particle behaviour in attrition and comminution processes.



#### Ir Renee Boerefijn

Renee Boerefijn graduated in Mechanical Engineering from the University of Twente in 1994. For his Diploma Thesis, he spent a year at the University of Naples, where he worked on the hydrodynamics of fluidised beds and developed a special probe for measurement of voidage waves. His current research activities are focused on the interactions between the hydrodynamics of fluidised bed jets and attrition in fluidised beds, using state-of-the-art digital image processing and high-speed video techniques, as well as laser doppler anemometry, as part of his PhD dissertation. Additionally, his recent work includes the impact fracture behaviour of various types of particulate solids.

# Powder Characterization by Particle Shape Assessment <sup>†</sup>

**Paramanand Singh**

*Dept. of Metallurgical Engineering I.I.T., \**

**P. Ramakrishnan**

*Dept. of Metallurgical Engineering I.I.T., \*\**

## Abstract

*In addition to the process variables, the quality of the powder metallurgical products depends to a large extent on the materials, bulk properties and morphological characteristics of the powders. Material characteristics are relatively well established but the same is not the case with the other two variables because unequivocal definitions of some of the morphological characteristics like particle shape, size and texture on which the bulk properties are strongly depended are yet to be evolved. Among the morphological characteristics, particle shape, though one of the most investigated area remains the least understood. In spite of the complexity of the problem, the necessity for obtaining a better insight of concerned branches in which powders are extensively used have yielded many dimensional and dimensionless parameters for characterizing the powders based on particles shape. The present paper classifies the available literature on the particle shape into four main categories, briefly describes their salient features, critically assesses the merits and demerits of each class and thus makes the perspective more clear for proper and judicious application of one or more methods, of course, depending on the level of accuracy required for charactering the powders.*

## 1. Introduction

In powder metallurgy (P/M), characterization of the raw materials which are in the powdered state is a sine qua non prerequisite to ensure quality, reproductivity and low scatter of the properties of the sintered parts, but interestingly enough, one of the most important variables over which the P/M parts' manufacture has very little control is: the characteristics of the powder itself. Fundamentally, the characteristics of the powder are influenced by the material, method of powder production and the process variables in a particular method. These basic variables of powder production collectively give rise to plethora of characteristics, the knowledge of which becomes essential for powder characterization in course of its journey to the end product. Hausner<sup>1</sup>, in an attempt to demonstrate the intricacy of the problem of powder characterization, records as many as seventeen characteristics of a powder particles and twelve characteristics of mass of powder and mentions that several of the characteristics are hard to define and even more difficult to determine. Thus, visualizing the dire necessity of powder characteriza-

tion and at the same time the manifold problems involved therein, it becomes incumbent upon the researchers to dive deep and take up this challenging task. Considerable research has been going on in this direction. To maneuver the complex situation of powder characterization more pragmatically, characteristics of powder which influence its behaviour during handling and processing have been divided under two broad categories as shown in **Figure 1**.

Of these, material characteristics are well-understood and almost completely known since chemistry and physics of the material are highly developed areas, but the same is not the case with the morphological characteristics. It is an underdeveloped and underexplored area, and unequivocal and unambiguous definitions of some of the morphological parameters are yet to be evolved<sup>2</sup>. These ill-defined and even less-understood morphological features interact in a complex way, each one of them contributing varying degree of influence to the total behaviour of the powder mass.

Thus, in the light of the above prologue, the present work critically assesses the relevant knowledge pertaining mostly to the morphological features of the powder particles for the progress of better understanding in handling the powder with more confidence.

\* Madras 600 036, India

\*\* Bombay 400 076, India

<sup>†</sup> Received 27 April, 1996

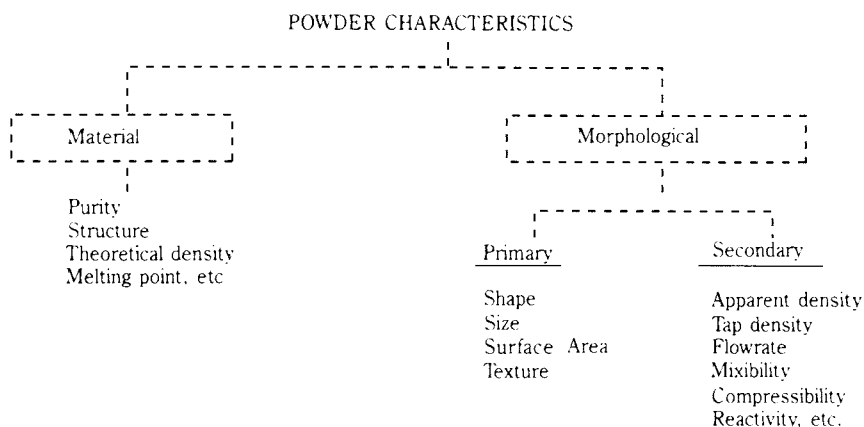


Fig. 1 A broad classification of powder characteristics.

## 2. Definition of shape and type of powder particle

Powder particle is a very complex entity. Its complexity depends upon the material as well as the process of production. It can be a smooth (even) and completely solid tiny mass or rough (jagged) and spongy in nature and hence, numerous categories are possible depending upon its external and internal details<sup>3</sup>.

Shape is the expression of only external morphology of the powder particle and it includes form (overall shape), roundness (smoothness) and surface texture<sup>4</sup>. **Figure 2** and **3** depict this definition of shape. Mathematically speaking, shape is the recognised pattern of relationships among all of the points which constitute the external surface<sup>2</sup>, i.e., complete description of shape requires the specification of a closed curve in space. Implementation of such a rigorous definition of shape for fine powder particles is difficult and complex and hence, in most of the situations a three dimensional particle is projected in a plane to obtain two dimensional closed curve and then this closed curve is taken to describe the particle shape. Based on the nature of the particle profile in two dimensional plane, particle can be put under two classes – Analytic or holomorphic particle and nonanalytic or nonhomomorphic particle<sup>2</sup>. Analytic or holomorphic particle is defined such that a vector from the centre of gravity of the particle to any point on the particle surface intersects the surface but once. This is pictorially represented in **Figure 4(a)** and **4(b)**. For example, gas atomized copper powder and to a large extent reduced copper powders belong to this category. Nonanalytic or nonholomorphic particle is defined such that at least one radius vector from the centre of gravity of the particle

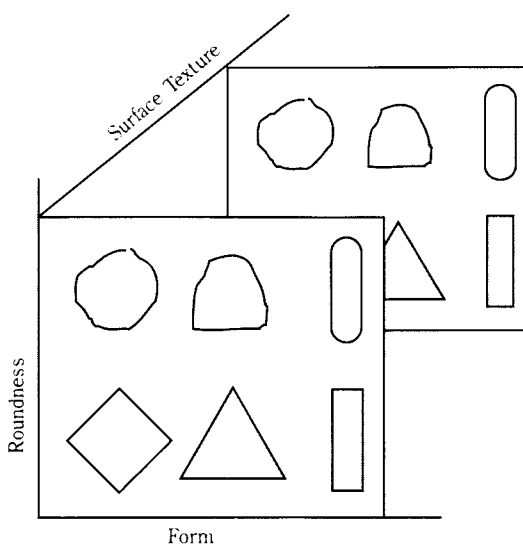


Fig. 2 Representation of form, roundness and surface texture by three linear dimensions to illustrate their independence.

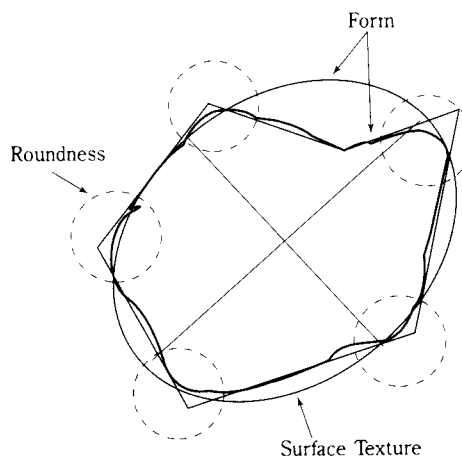
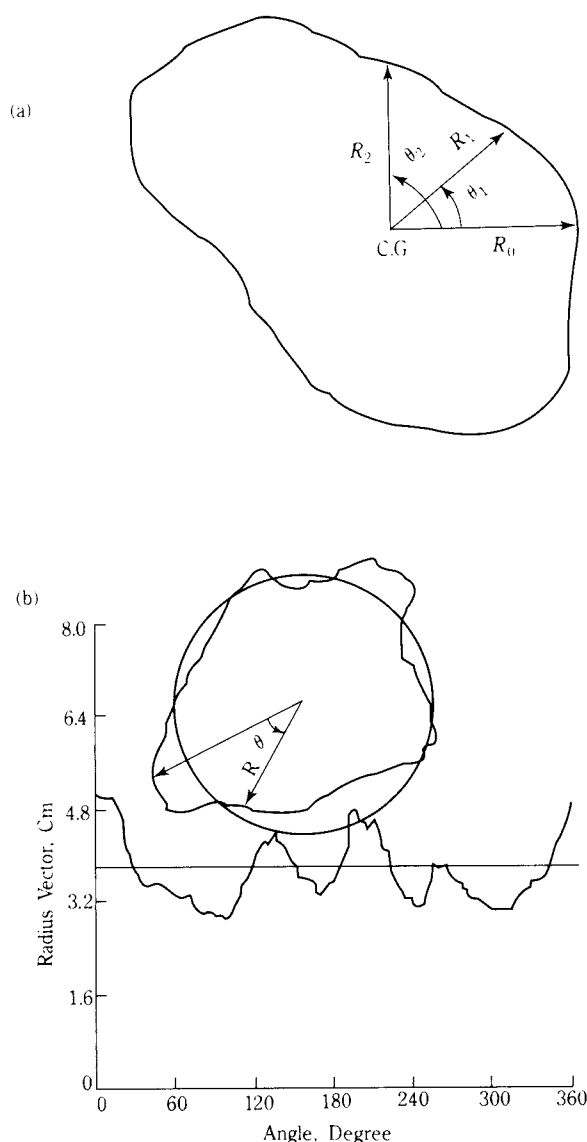


Fig. 3 A particle outline (heavy solid line) with its component elements dimensions to illustrate their independence.



**Fig. 4** (a) and (b) are two different ways of representing holomorphic or analytic particle profile.

intersects the surface of particle more than once. This is pictorially represented in **Figure 5(a)** and **5(b)**. Electrolytic copper powder and carbon black aggregates belong to this category.

The objective of the preceding definition of shape and classification of the particle types is to provide the basis for critically examining the merits and demerits and also of the level of accuracy of a particular approach for powder characterization reviewed under the subsequent subsections.

### 3. Panoramic view of powder characterization

Size and shape are fundamental characteristics of a powder particle and hence, of a given mass of powder. In fact, both size and shape are intimately

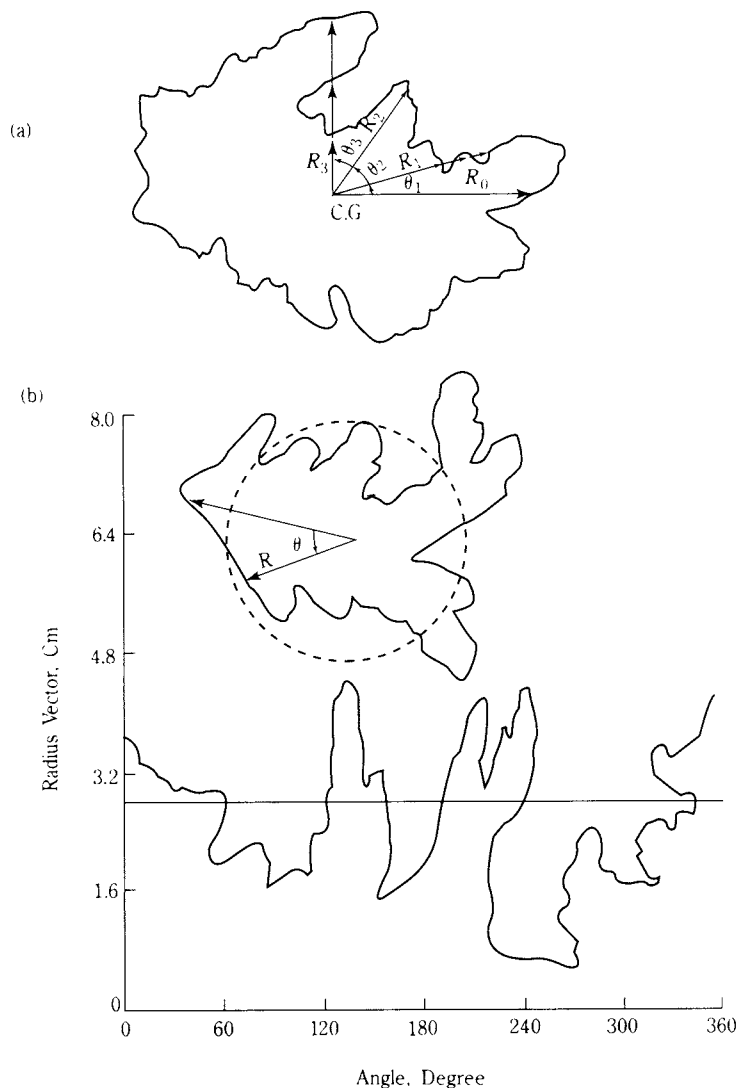


**Fig. 5** (a) and (b) are two different ways of representing nonholomorphic or nonanalytic particle profile.

related to and inseparable from each other. Most of the literature in the area of powder characterization is clustered around the measurement of these basic intrinsic properties and characteristics derived thereof in one form or another. Various methods available in the literature for this purpose can be divided into four general classes<sup>5</sup>: (i) the use of words to convey shape characteristics (verbalization of shape), (ii) the assessment of individual particle characteristics, (iii) shape generation by various methods and (iv) measurements of bulk properties of powders. Among these four classes, the (i) deals with the means of description, the (ii) and the (iv) deal with the means of observation and the (iii) deals with the transformation of particle profile into mathematical form. The succeeding sub-section describes the important methods lying under different general classes.

### 3.1 Verbalization of Shape

Words like discs, blades, rods and equidimensionals have been used, based on the breadth to length and thickness to breadth ratios of the powder particles, to classify the powders into different shape groups. In Heywood's system<sup>6</sup> of classification each particle is allocated to a different shape group which resembles one of the four geometrical forms – angular tetrahedral, angular prismoidal, subangular and rounded. The allocation of particles to a shape group is done based on the measurement of volume coefficient and surface coefficient. British standard<sup>7</sup> gives a glossary of descriptive terms like acicular, angular, fibrous, irregular, nodular, crystalline, dendritic, flaky, granular and spherical for characterising powder particles. These conventional terminologies refer to two distinct characteristics of a powder particle namely, the geometrical form and the relative proportion of length, breadth and thickness. Riley and Magnuson<sup>8</sup> characterized the refractory powder particles into four morphological classes – particles with hollows/porosity in them, dense particles, agglomerated particles and hollow particles equivalent to agglomerated pores. Beddow<sup>9</sup> has explored the possibility of using the concept of information theory to measure the information content of these linguistic variables (words or sentences) to characterize the powder particles. With the advent of fast character manipulating computers the concept can be used in pattern recognition technique to characterize powders.

### 3.2 Assessment of individual particle characteristics

Perhaps, the first attempt in quantitatively characterizing the powder particle would have been the measurements of its length, breadth and thickness. In a pioneer effort, Heywood<sup>6</sup> defined thickness, breadth and length as the three dimensions of an irregular particle resting on a plane in the position of its greatest stability. He defined thickness (T) as the distance between two planes parallel to the planes of greatest stability and tangent to the surface of the particle, breadth (B) as the minimum distance between two parallel planes which are perpendicular to the planes defining thickness and are tangential to the opposite surfaces of the particles and length (L) as the distance between two parallel planes which are perpendicular both to those planes defining thickness and breadth and which are also tangential to the opposite surfaces of the particle. **Figure 6** shows the classical measures of thickness, breadth and length of a particle. Based on these measurements

Heywood defined flatness ratio  $u$  and elongation ratio  $v$  as follows:

$$\text{Flatness Ratio, } u = B/T \quad (1)$$

$$\text{Elongation Ratio, } v = L/B \quad (2)$$

Heywood related these two ratios to the ratio  $d/w$  (diameter of the circle having the same area as the projection of the particle/sieve aperture) by the following formula:

$$\frac{d}{w} = 0.98 \left( \frac{2vu^2}{u^2 + 1} \right)^{1/2} \quad (3)$$

Tabulation of values for different  $u$ ,  $v$  and  $d/w$  ratios can help in characterizing the powder particles to a certain extent.

Davies<sup>10</sup> has measured length, breadth and thickness using Quantimet 720 Image Analyzer and utilized these information to construct triaxial contour diagrams of shape-sorted beach sands and silicon carbide powder. Hausnes<sup>11</sup> compared the characteristics of the complicated shapes with the rectangles of minimum area (length  $a$  and breadth  $b$ ) drawn around the projection of the particle in the most stable position, **Figure 7**. He defined three factors

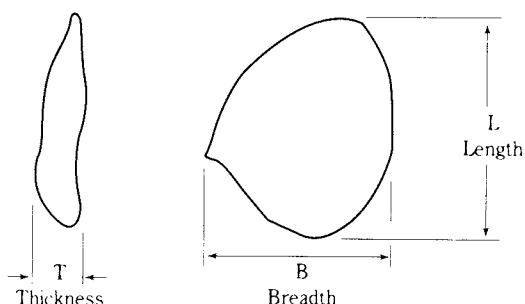


**Fig. 6** Classical measures of thickness, breadth and length.

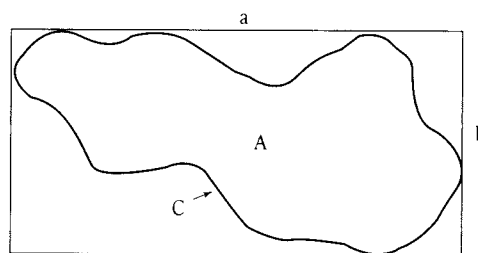


**Fig. 7** Rectangle of maximum area drawn around the particle projection.

as follows:

$$\text{Elongation Factor} = a/b \quad (4)$$

$$\text{Bulkiness Factor} = A/(a.b) \quad (5)$$

$$\text{Surface Factor} = C^2/(4\pi A) \quad (6)$$

$C$  is the circumference of the projected particle and  $A$  is the area of the projected particle.

Exner and Linck<sup>12</sup> used a simple shape index  $K$  which is defined as

$$K = \frac{4\pi A}{C^2} \quad (7)$$

for characterizing the shape distribution of lead powders. The value of  $K$  lies between 0 and 1.

Comparison of surface area and volume of the particle with that of the equivalent sphere gives surface coefficient  $f_s$  and volume coefficient  $f_v$  as follows<sup>13</sup>:

$$\text{Surface area of the particle} = f_s \cdot \bar{d}^2 \quad (8)$$

$$\text{Volume of the particle} = f_v \cdot \bar{d}^3 \quad (9)$$

$\bar{d}$  is the projected average diameter of the particle.

To give an idea of the overall shape of the particle Wadell<sup>14</sup> defined a term circularity as follows:

$$\text{Circularity} = \frac{\text{circumference of a circle of the same area as the particle}}{\text{circumference of the particle}} \quad (10)$$

Sphericity which also conveys the idea of the overall shape was defined by Wadell<sup>15</sup> as follows:

$$\text{Sphericity} = \frac{\text{surface area of a sphere of the same volume as the particle}}{\text{actual surface area of the particle}} \quad (11)$$

For two dimensional projection of particle,

$$\text{Sphericity} = \frac{\text{diameter of a circle with the same area as the particle projected on the two dimensional plane}}{\text{diameter of the smallest circle that circumscribes the particle projection}} \quad (12)$$

Circularity and sphericity are the measures of the degree to which the shape of a particle approaches

a circle and a sphere, respectively. To take into account of the fine details of the particle Wadell<sup>15</sup> defined roundness which is usually taken to be a measure of the sharpness of corners and edges of the particle, as follows:

$$\text{Roundness} = \frac{\sum_{i=1}^p r_i/p}{R} \quad (13)$$

$r_i$  are the radii of curvature of  $p$  corners of a projection or section of the particle and  $R$  is the maximum inscribed radius of the particle. Roundness value range from 0 to 1.

Lees<sup>16</sup> has shown that forms of identical roundness value can have visibly different actual roundness and hence, this led him to propose a measure of angularity of the particles in the following way, **Figure 8**.

$$\text{Angularity} = \sum_{i=1}^3 \sum_{j=1}^p (180 - \beta_{ij}) \frac{g_{ij}}{r_i} \quad (14)$$

$\beta_{ij}$  is the angle of each corner and  $g_{ij}$  is the distance of the corner from the centre of the maximum inscribed circle of radius  $r_i$  for each of the three sections through the long, intermediate and short axes of the profile. Defined this way, angularity increases by increase in acuteness of the corners, increase in number of corners and increase in relative distance of corners from the centre of the particle and varies from 0 to  $\infty$ .

Using the concept of mechanics to describe the distribution of mass in a fine particle profile, Medalia<sup>17</sup> and Medalia and Heckman<sup>18</sup> calculated the dimensions of an ellipse having the same radii of gyration about the central principal axes as those which the fine particle profile would have if it were a thin lamina fine particle. Three shape factors for carbon black

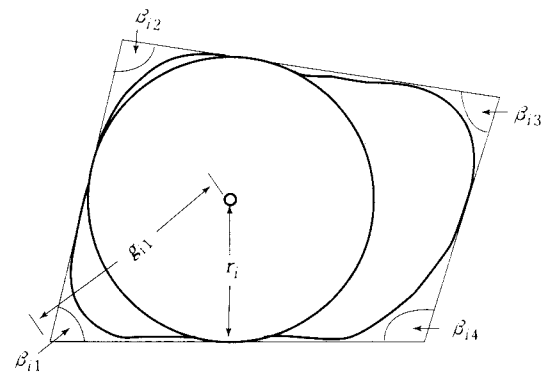


**Fig. 8** 2-D angularity of a particle.

aggregates were then defined as follows, **Figure 9**.

$$\text{Anisometry} = K_A/K_B \quad (15)$$

$$\text{Bulkiness} = \frac{\text{area of ellipse}}{\text{area of silhouette}} = \frac{4\pi K_A K_B}{A} \quad (16)$$

$$\text{Surface Factor} = (\text{Anisometry}) (\text{Bulkiness}) - 1 \quad (17)$$

$A$  is the area of silhouette of particle, and  $K_A$  and  $K_B$  are the larger and smaller radii of gyration about the central principal axes of the radius-equivalent ellipse.

Medalia<sup>19</sup> calculated three shape factors for both two and three dimensional bodies. Medalia's shape factors are based on the mechanics and therefore he referred to them as the dynamic shape factors. These shape factors are insensitive to highly reentrant and textured particles.

The shape factor, Shah, which is the ratio of the number of downward pointing projections on a small set of particles to the total particle population of the sample was developed by Staniforth and Rees<sup>20</sup> specifically to quantify the re-entrant particles. Shah is most useful in describing the mean particle shape of a sample of bulk powder but it can also be calculated for individual powder particle. The value of Shah for re-entrant particles increases to a maximum which is governed by the resolution at each magnification. Shah quantifies the degree of re-entrancy of

a particle but it is unable to characterize its geometric form. Staniforth and Rees<sup>21</sup> combined Shah and Heywood shape factor ( $f_v/f_s$ ) and formed a two dimensional matrix which is capable of describing re-entrant and non-re-entrant, simple and complex geometric forms.

Danielsson<sup>22</sup> proposed a shape factor  $G$  which is based on average distance between a picture element and its nearest border point  $\bar{g}$  and defined  $G$  by the following formula:

$$G = \frac{A}{9\pi(\bar{g})^2} \quad (18)$$

$A$  is the area of the particle profile. Fast computation of  $G$  requires that the particle be digitized into several pixels. Digitized version of the formula is given by

$$G = \frac{M^3}{9\pi \left( \sum_{i=1}^M g_i \right)^2} \quad (19)$$

$M$  is the total number of pixels in the profile and  $g_i$  is the distance of the  $i$ th pixel within the profile from its nearest border point. It is claimed by Danielsson that  $G$  captures the compactness of the profile.

Kaye<sup>23</sup> emphasizes that the quantitative gross shape descriptors of particle profiles should not tend to infinity as the scale of scrutiny is increased, and should be relatively easy to measure and for that he defined, external compactness as follows:

$$\begin{aligned} \text{External Compactness} &= \left( \frac{\text{diameter of a circle of equal area}}{\text{diameter of embracing circle}} \right)^2 \\ &= \left( \frac{D_A}{D_{Em}} \right)^2 \end{aligned} \quad (20)$$

Since it is possible to have the same external compactness but different general shapes of the profiles, Kaye uses another index chunkiness in conjunction with the former. He defines chunkiness as follows:

$$\text{Chunkiness} = B_m/L_m \quad (21)$$

$L_m$  is the maximum length of the profile and  $B_m$  is the maximum breadth of the projection of the profile on a direction at right angle to that in which  $L$  is measured. **Figure 10** shows the basic measurement

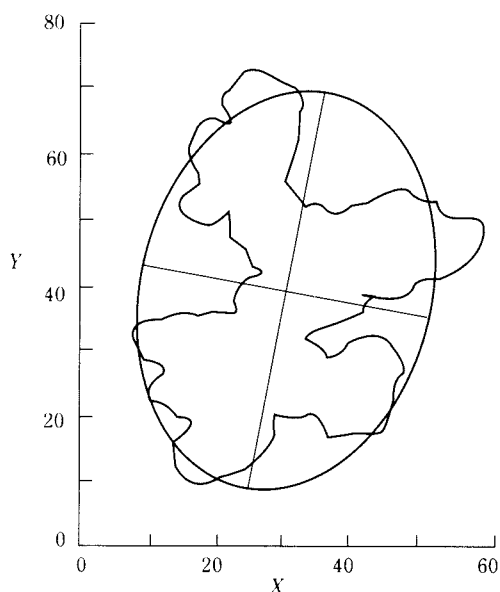


**Fig. 9** Silhouette of carbon black aggregate with central principal axes and radius-equivalent ellipse.

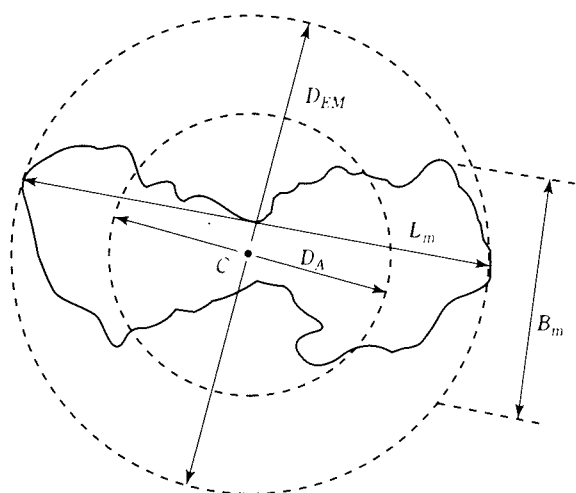


**Fig. 10** Chunkiness and external compactness of the particle profile.

used for calculation. By plotting the external compactness and chunkiness in two dimensional data space Kaye expresses the variability of shape exhibited by the atomized copper-lead powder and sponge iron powder. Since it is possible to completely separate the two powders in three dimensional data space, Kaye<sup>24</sup> expressed a measure of the ruggedness of the particle as follows:

$$-\delta = (D - 1) \quad (22)$$

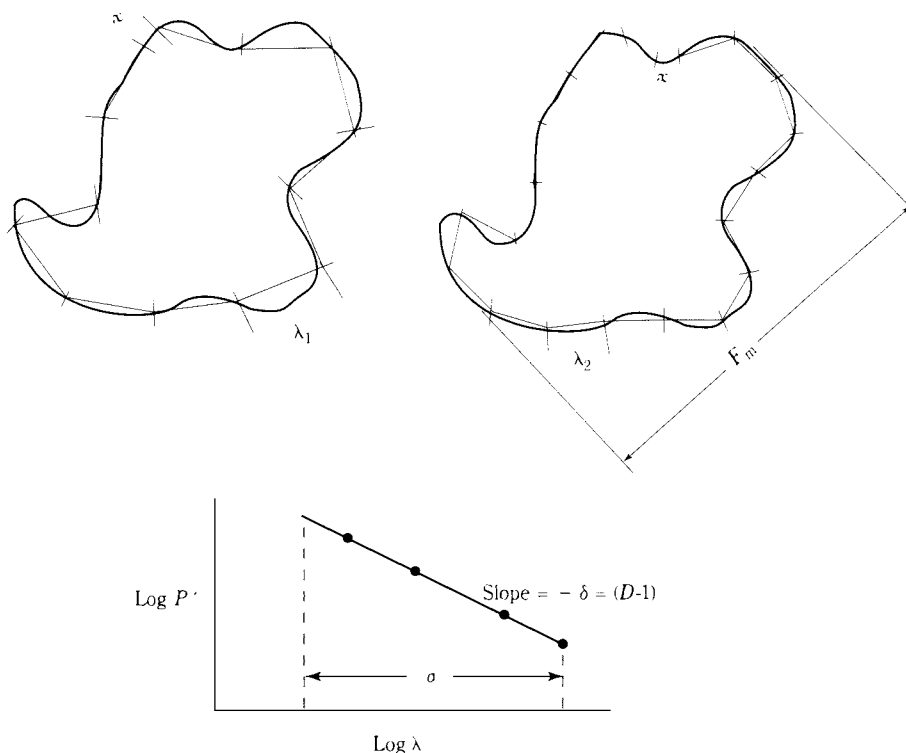


**Fig. 11** Perimeter-random walk stride graph.

$D$  is the ruggedness index or fractal dimension having the value between 1 and 2 and  $\delta$  is the slope of perimeter-random walk stride graph as shown in **Figure 11**.

To describe the structure of a two dimensional particle profile, concept of geometric signature waveform was developed by Schwarcz and Shane<sup>25</sup>. They used the magnitude of the vector  $R$  which rotates with constant angular velocity about the pivot point to generate the waveform by plotting  $R$  against  $\theta$ , **Figure 12**. The centre of the smallest circumscribing circle was used as the pivot point. The magnitude of the vector is normalized with respect to the largest value generated as the vector rotates about the pivot point touching the periphery of the profile. This waveform is vulnerable to variations in the location of the pivot point as shown in **Figure 13**. Reentrant particle profiles cannot be described by geometric signature waveform for the simple reason that rotating vector acquires multiple values as it crosses a re-entrant loop of the profile.

Kaye<sup>26</sup> generated Feret's diameter signature waveform (also called FERETS waveform) by plotting the magnitude of the Feret's diameter of the profile against the angle of orientation with respect to a fixed direction as the profile is rotated with uniform angular motion, **Figure 14**. Normalization of data can be done by dividing the measured projected

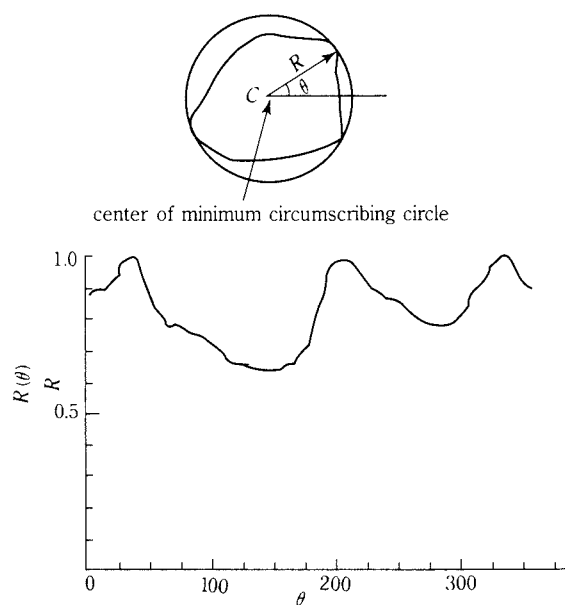


Fig. 12 Schwarz-Shane geometric waveform of the fine particle.

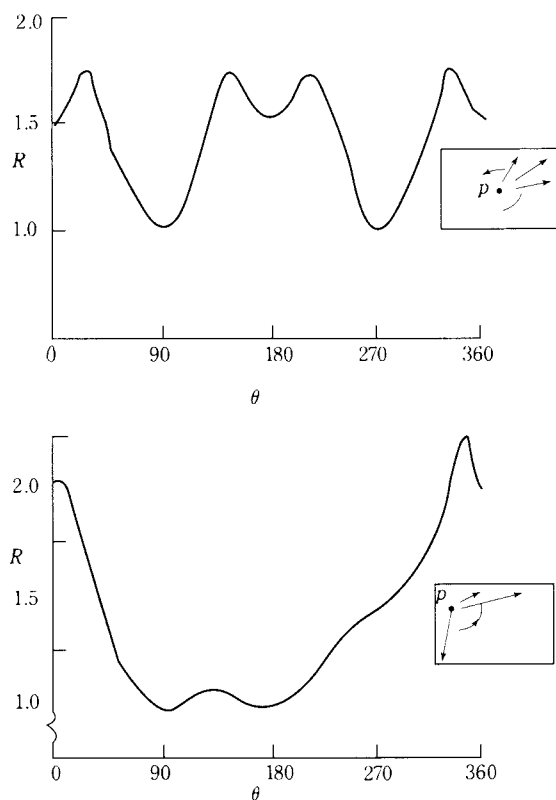


Fig. 13 Vulnerability to variations of Vector-pivot type geometric signature waveform-by the shift of the location of the pivot point.

diameter for a given profile by the maximum Feret's diameter for that profile. FERETS waveform is in

Fig. 14

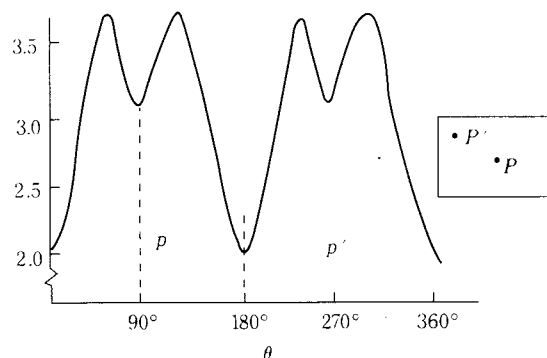


Fig. 14 Feret's diameter signature waveform showing the independence of the point of rotation.

dependent of the point about which the profile is rotated and is related to the perimeter of the profile.

Cauchy signature waveform<sup>27</sup> consists of the magnitude of the projected area plotted against the angular position rotated through 90° about the mounting axis and a further 90° perpendicular to the axis, **Figure 15**. Measurement of any concavities on the surface of the structure is not possible by this procedure.

Feret<sup>28</sup> suggested that the average value of the projected length of an array of particles with reference to a given direction can be used to characterize that array of the particles. Thus, originally it was used as a statistical diameter. However, the common usage has extended the term Feret's diameter to describe the projected dimension of an individual profile. Feret's diameter is the distance between the tangents which touch the two extremities of the particle profile in its position of rest at right angle to the direction of scan, **Figure 16**. Similarly, Martin's diameter is the distance which divides the particle profile into two equal halves in the direction of scan when the particle is in a position of rest, **Figure 17**. These direction vary depending on the orientation of the particle profile. Ratio of Martin's diameter to Feret's diameter of the particle population has been suggested as a useful shape factor, however, Church<sup>29</sup> has analyzed the major problem associated with this ratio as a shape factor. He has indicated that useful mathematical relationship can be set up between expected values of Martin's diameter and Feret's diameter and various shape factors for elliptical particles and also for particles of other shapes can be obtained.

Stereology which studies the three dimensional structure of materials from two dimensional sections or projections is being used for powder characteriza-

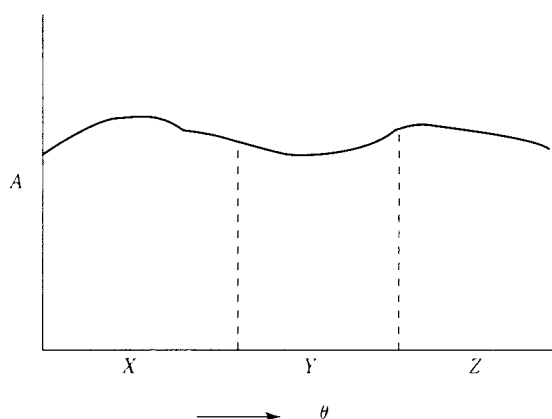


**Fig. 15** Cauchy signature waveform generated by plotting the area of the silhouette against the angle of rotation about x, y and z of the fine particle.

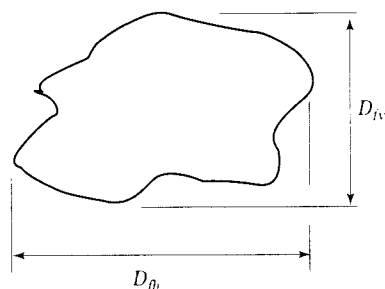


**Fig. 16** Horizontal and vertical Feret's diameter.

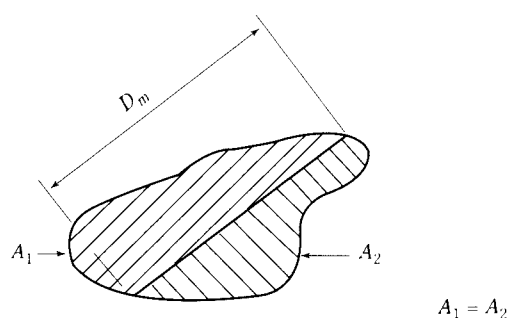


**Fig. 17** Martin's diameter.

tion. Underwood<sup>30</sup> has discussed the types of measurements obtained from sections and projections of the powder particle and the applicable formulae that serve to related particle characteristics or behaviour. Beddow et al.<sup>31</sup> selected few such measurements to define dimensionless features and subsequently applied for classifying four different types of powder by use of a pattern recognition technique. Underwood<sup>32</sup> has listed many shape indices which are evaluated by using stereological methods. Singh and

Ramakrishnan<sup>33-35</sup> used such stereological shape indices and established their correlation with the bulk properties of the powder and subsequently used it for characterizing copper powders of different origins.

There are host of parameters of similar nature<sup>36,37</sup>, but only few selected ones have been presented here to understand the general trend and utility of such parameters.

### 3.3 Shape generation and the recent developments

Presently available shape generation methods have been put under four categories<sup>5</sup>: Matrix mapping, polynomial fitting, syntactic methods and Fourier analysis technique. In matrix mapping, the silhouette of the particle is scanned by photoscanner or some such device which divides it into different grey levels. The particle silhouette is thus converted into digital map which becomes amenable for further computer processing. Polynomial generation of particle profile is simply a curve fitting task where different degree of polynomials are tried for representing the particle profile as closely as possible. There is a limit to attain the closeness of fit after which wide deviation starts when the degree of polynomial is increased. In syntactic method<sup>38</sup>, the specific pattern is developed from a given set of pattern primitives by the operation of rules of the grammar of the language. Beddow et al.<sup>39</sup> have used picture descriptive language (PDL) grammar to explain the construction of a pentagon.

In Fourier analysis technique of shape generation, the particle profile is analyzed to yield large number of Fourier coefficients. These coefficients capture all the details of the profile. By reversing the process, i.e., by using synthesis technique the profile can be regenerated to its near original shape. Schwarz and Shane<sup>25</sup> used Fourier analysis technique to measure the shape characteristics of sand grains. Ehrlich and Weinberg<sup>40</sup> used this technique to reproduce profiles of quartz grains very precisely and also to characterize grains from different sources. Several researches<sup>41-49</sup> have used this technique to characterize powder particles. Eppler and Meloy<sup>50</sup> have chronicled the development of this technique and have shown its potential applicability to a host of engineering and industrial problems. Fourier analysis technique has been explored extensively by Beddow and co-researchers<sup>50-60</sup> and this has led to identify three different methods of Fourier analysis depending on the nature of the particle profile and on the information required for characterization. These three different methods are  $(R, \theta)$  method,  $(\phi, \ell)$  method

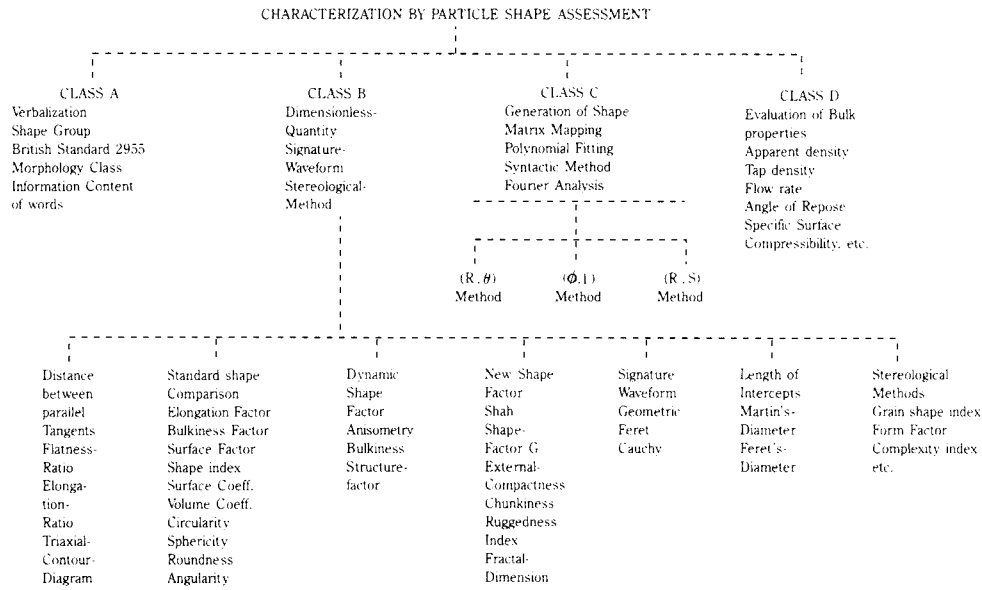


**Fig. 18** Classification of characterizing parameters based on particle shape assessment.

and  $(R, S)$  method.

In  $(R, \theta)$  method<sup>40,54,59</sup>, the particle profile is digitized and a set of  $(x', y')$  coordinates are obtained. This is then transformed to a set of  $(x, y)$  coordinates with reference to the centre of gravity. These  $(x, y)$  coordinates are then transformed to polar representation  $(r, \theta)$  and then  $R$  is represented as a function of  $\theta$  by truncated Fourier series:

$$R(\theta) = a_0 + \sum_{n=1}^N (a_n \cos n\theta + b_n \sin n\theta) \quad (23)$$

where,

$$a_0 = \frac{1}{2\pi} \int_0^{2\pi} R(\theta) d\theta \quad (24)$$

$$a_n = \frac{1}{\pi} \int_0^{2\pi} R(\theta) \cos n\theta d\theta \quad (25)$$

$$b_n = \frac{1}{\pi} \int_0^{2\pi} R(\theta) \sin n\theta d\theta \quad (26)$$

$$n = 1, 2, 3, \dots$$

$a_0$ ,  $a_n$  and  $b_n$  are zeroth order and  $n$ th order Fourier coefficients containing size and shape information. The Fourier coefficients  $\{a_n, b_n\}$  contain all the informations about the particle profile to reconstruct the particle profile analytically by equation (23). Since the Fourier coefficients and phase angle are not invariant to coordinate transformation, the particle shape representation is not unique.

The Fourier coefficients are transformed to the set of invariant features – size, shape, roughness, microroughness, partial rotational symmetry, partial mirror symmetry, partial inversion symmetry and moments of the radial distribution – according to the theory of morphology<sup>61,62</sup>. These features measure well-defined properties of the particle profile.

The  $(R, \theta)$  method in its classical form cannot handle multivalues of  $R$  at a given value of  $\theta$ . This is a significant drawback of the classical  $(R, \theta)$  method. However, using the variational method other boundary representations for reentrant profiles are possible by using a generalized concept of the angle and this gives to the generalized  $(R, \theta)$  method for the reentrant particle profile<sup>62</sup>.

In  $(\phi, \ell)$  method<sup>46,48,55,63</sup>, the particle profile is parameterized by a normalized arc length and a change of slope from its starting point. The normalized function can be written as

$$\phi^*(t) = \mu_0 + \sum_{n=1}^N (a_n \cos nt + b_n \sin nt) \quad (27)$$

where,

$$t = \frac{\ell}{L} 2\pi; t = (0, 2\pi) \text{ for } \ell = (0, L) \quad (28)$$

$$\ell_i = \sum_{i=1}^K \sqrt{\Delta x_i^2 + \Delta y_i^2} \quad (29)$$

$K$  = arc length from starting vertex to the  $K$ th vertex  
 $= 1, 2, 3 \dots 2N + 1$ , the number of coordinate points on profile

$$L = \sum_{i=1}^K \ell_i \quad (30)$$

The total arc length is  $L$  and the normalized parameter is  $t$ .  $a_n$  and  $b_n$  are the Fourier coefficients.

This method has the advantage that it can analyze both holomorphic and nonholomorphic particle profiles. This method does not yield analytical expression for the regenerated  $(x, y)$  coordinates. Regenerated coordinates must be calculated using numerical techniques and hence, important geometrical and physical quantities, such as area, moment of inertia, symmetry, etc. cannot be evaluated analytically.

In  $(R, S)$  method<sup>60,62</sup>,  $(x, y)$  coordinates on the particle profile are transformed to polar coordinate system  $(\gamma, \theta)$ . A normalized arc length  $s$  is calculated as in  $(\phi, \ell)$  method. Since  $\gamma$  as a function of  $s$  is a function of period  $2\pi$ , a Fourier series may be used to represent  $R(s)$ . In addition,  $\theta$  as well  $\theta'$  as functions of  $s$  are also functions of period  $2\pi$  and may also be represented by Fourier series. Thus,  $R(s)$  and  $\theta'(s)$  are represented as functions of normalized arc lengths, as follows:

$$R(s) = a_0 + \sum_{n=1}^N (a_n \cos ns + b_n \sin ns) \quad (31)$$

$$\theta'(s) = C_0 + \sum_{n=1}^N (C_n \cos ns + D_n \sin ns) \quad (32)$$

where,

$$s = \frac{\ell}{L} 2\pi \quad (33)$$

$$\ell_i = \sum_{i=1}^K \sqrt{\Delta x_i^2 + \Delta y_i^2} \quad (34)$$

$$L = \sum_{i=1}^K \ell_i \quad (35)$$

and

$$\theta'(s) = \frac{d}{ds} [\theta(s)] \quad (36)$$

Both reentrant and nonreentrant particle profiles can be analyzed by this method. It can also be used to differentiate between reentrant and nonreentrant profiles since profile containing reentrant points will have negative values of  $\theta'(s)$  at certain points of

reentrance, whereas profiles which do not contain reentrant points will have positive values of  $\theta(s)$  for all  $s$ . Analytical calculation of important geometrical and statistical quantities such as area, moment of inertia, symmetry, moments of radial distribution, etc. is possible by this method. A major disadvantage of this method is that it requires two Fourier expansions. This reduces the efficiency of this method as compared with  $(R, \theta)$  and  $(\phi, \ell)$  methods.

Since, even the minor differences in the shape of the particle is reflected in the Fourier coefficients, each particle can be uniquely distinguished from the other particles by simply comparing their harmonic amplitudes. However, a discriminatory ability which forces us to distinguish among all the particles encountered is not required. Such a level of differentiation would yield an almost infinite variety, which would be useless<sup>64</sup>. Therefore, if one wants to classify one powder lot from another, one must take into account the overall morphological features for each powder and make a comparison. Thus, to make use of the Fourier coefficients as characterizing tool, further treatment of the data becomes imperative for which many techniques have been developed and used by many researchers<sup>2,46,47,49,61,65-68</sup>.

Walsh Transform has been used by Lew et al.<sup>69</sup> for morphological classification of powders. It has been pointed out that a circular shift in starting point produces a different set of Walsh coefficients. This clearly indicates that Walsh transform is unsuitable for morphological analysis. Fast Fourier Transform (FFT) has been used to particle silhouettes to obtain morphological data<sup>70,71</sup>. Beddow<sup>72</sup> mentions the use of Ramtek device in particle image analysing system to analyze the color of particles as a morphic feature which assists in differentiation and classification processes. Use of color as a morphic feature extraction is one of the upcoming developments in the area of powder characterization.

### 3.4 Bulk properties evaluation

For a mass of powder, the bulk properties, such as apparent density, tap density, flow rate, angle of repose, specific surface, compressibility, etc. are dependent to a large extent on size, size distribution, shape and shape distribution of the powder particles and hence, these bulk properties have served as important parameters for characterizing powder. Many of these bulk properties can be determined by standard test procedures and the other can be evaluated by developing appropriate techniques.

Hausner<sup>11</sup> used the ratio of tap density to apparent

density as a qualitative measure of friction in the moving powder mass to distinguish three differently shaped copper powders of similar size distribution. This ratio, called friction index, was found to be high for flaky powder and low for spherical powder. Tap density to apparent density ratio has been applied as a shape parameter to classify electrolytic, reduced and atomized copper powders<sup>3,73</sup>. Kostelnik et al.<sup>74</sup> have shown the influence of this ratio on the compaction behaviour of copper and iron powders. Riley and Mann<sup>75</sup> using glass particles of four different shapes and Singh<sup>3</sup> using copper powders of different origins have shown that angle of repose increases with increasing departure from sphericity. Use of flow rate and specific surface as characterizing parameters are not hard to explore. Density-pressure relationship curves which can be obtained by compacting the powder successively at different pressures can be made use of in characterizing powders of different origins<sup>76</sup>. For successful characterization of powders by bulk properties evaluation it is essential that the measurements be carried out under identical conditions since these properties are sensitive to experimental conditions.

#### 4 Critical assessment

The parameters for characterizing the powders by particle shape evaluation are either of qualitative or quantitative nature. Words like acicular, angular, fibrous, etc. which are descriptive are qualitative parameters and different meanings can be ascribed to them by different persons. Thus, ambiguity creeps in while attempting to communicate the characteristics of powders using these parameters and therefore, such type of qualitative parameters are of little value in the scientific community. On the other hand, many of the quantitative parameters are based on the gross shape of the powder particles and therefore, finer details of particle shape are not taken into account by these parameters. Many of such parameters can have same values for differently shaped powders and therefore, misclassification can result when these parameters are used for powder characterization. The shape factor *Shah* by Staniforth<sup>20</sup> is a function of magnification and as the magnification increases, the value of *Shah* increases. This type of parameter cannot be unequivocally selected for characterizing the powder. Parameters like external compactness and chunkiness defined by Kaye<sup>23</sup> do not take into consideration the fine-scale perturbations of the particle profile. The use of signature waveforms is yet to be explored. Stereological methods can be applied both to indi-

vidual particle or systems of many particles. Since these methods are statistical in nature, large number of measurements has to be made to achieve high degree of accuracy and therefore, automatic image analysis systems have to be used to accomplish the task.

One of the major drawbacks of all such parameters is that in course of condensing the informations for characterizing the powders, one loses the sight of the actual particle profile and it becomes well-nigh impossible to reconstruct the original powder particle profile from these parameters. But, in the case of Fourier analysis technique it can be seen that it is very much possible to reconstruct the particle profile from Fourier coefficient to its near original shape and hence, this technique holds a great promise as a characterizing tool.  $(\phi, \ell)$  method and modified  $(R, \theta)$  method which take into account both holomorphic and nonholomorphic particle profile have been used extensively while  $(R, S)$  method which involves two Fourier series expansions has found limited application because of the difficulty arising in handling the huge quantity of data generated by this method.

Bulk properties are sensitive to particle morphology and also to experimental conditions. Hence, if the bulk properties are to be used for characterization of powders, experimental conditions have to be strictly controlled, otherwise, variation in bulk properties cannot totally be attributed to the change in particle characteristics.

Thus, it can be inferred that presently no single method exists which can characterize the powder completely and therefore, one has to use combination of different methods for characterizing the powder, but even then, the characterization remains short of mark as far as the finer aspects of particle characteristics are concerned; nevertheless, judicious combination of different methods can solve the problem to a great extent.

#### References

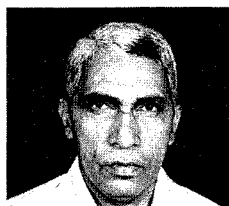
- 1) Hausner, H.H., Environmental effects on the behaviour of metal powder. *Int. J. Powder Met. Powder Tech.*, 14 (1978) 323.
- 2) Meloy, T.P., A hypothesis for morphological characterization of particle shape and physiochemical properties. *Powder Tech.*, 16 (1977) 233.
- 3) Singh, Paramanand., *Characterization of Powders* Ph.D. Thesis, IIT Bombay, India, 1983.
- 4) Barrett, P.J., The shape of rock particles, a critical review. *Sedimentology*, 27 (1980) 291.
- 5) Beddow, J.K., Sisson, K. and Vetler, A.F., Particle shape analysis, Part I. *Powder Met. Int.* 8 (1976) 69.

- 6) Heywood, H., The Scope of particle size analysis and standardization. In proceedings of Symposium on Particle size analysis, supplement to Trans. Inst. Chem. Engr., 25 (1947) 14.
- 7) Glossary of terms relating to powders. British Standard 2955 (1958).
- 8) Riley, R.E. and Magnuson, J.E., As cited in Ref. 4.
- 9) Beddow, J.K., Particle morphological analysis. In Advanced Particulate Morphology, eds. Beddow, J.K. and Meloy, T.P. CRC Press, Boca Raton, Florida, (1980) 1-84.
- 10) Davies, R., A simple feature-space representation of particle shape. Powder Tech., 12 (1975) 111.
- 11) Hausner, H.H., Latest development in the characterization of powders. In Powder Metallurgy and Material Strengthening, eds. Dhar, P.R., Sen, P.K., Basu, S. and Mukunda, P.G. Oxford and IBH Publishing Co., Calcutta, (1970) 9-18.
- 12) Exner, H.E. and Linck, E., Image analysis for characterization of size-and shape distribution of lead powders. Powder Met. Int. 9 (1977) 131.
- 13) Orr, C.J. and Dallavalle, J.M., Fine Particle Measurement, Macmillan Company, NY (1959) 25-26.
- 14) Wadell, H., Sphericity and roundness of rock particles. J. Geol., 41 (1933) 310.
- 15) Wadell, H., Volume, shape and roundness of quartz particles. J. Geol., 43 (1935) 250.
- 16) Lees, G., A new method for determining the angularity of particles. Sedimentology, 3 (1964) 2.
- 17) Medalia, A.I., Morphology of aggregates: Calculation of shape and bulkiness factor; Application to computer-simulated random flocks. J. Colloid Interf. Sci., 24 (1967) 393.
- 18) Medalia, A.I. and Heckman, F.A., Morphology of aggregates: 2. Size and shape factors of carbon black aggregates from electron microscopy, Carbon, 7 (1969) 567.
- 19) Medalia, A.I., Dynamic shape factors of particles. Powder Tech., 4 (1970/71) 117.
- 20) Staniforth, J.N. and Rees, J.E., Shape classification of re-entrant particles I: The Shape factor Shah. Powder Tech., 28 (1981) 3.
- 21) Staniforth, J.N. and Rees, J.E., Shape classification of re-entrant particles II: Description of re-entrant and non re-entrant particle shapes. Powder Tech., 28 (1981) 9.
- 22) Danielsson, Per-Erik., A new shape factor. Computer graphics and Image Processing, 7 (1978) 292.
- 23) Kaye, B.H., Fractal and shape index description of the shape and surface structure of metal powders. In Modern developments in Powder Metallurgy, eds. Hausner, H.H., vol.12, 1981, pp 67-82.
- 24) Kaye, B.H., Specification of the ruggedness and/or texture of a fine particle profile by its fractal dimension. Powder Tech., 21 (1978) 1.
- 25) Schwarcz, H.P. and Shane, K.C., Measurement of particle shape by Fourier analysis. Sedimentology, 13 (1969) 213.
- 26) Kaye, B.H., The use of Feret's diameter signature waveform as a shape characterization parameter. In Fine Particle Science. Proceeding of the symposium on the characterization of large colloidal particles at Anaheim, California, 1978.
- 27) Kaye, B.H., Sinha, S.N. and Lablanc, J.E., Signature waveforms for describing the three dimensional morphology of fine particles. Proceedings of Int. Symposium on Recent advances in particulate science and technology, IIT Madras, Preprints, Vol. 1, 1982, A-11.
- 28) Feret, R.L., as cited in Ref. 26.
- 29) Church, T., Problems associated with the use of the ratio of Martin's diameter to Feret's diameter as a profile shape factor. Powder Tech., 2 (1968/69) 27.
- 30) Underwood, E.E., Stereological analysis of particle characteristics. In Testing and Characterization of Powders and Fine Particles. eds. Beddow, J.K. and Meloy, T.P., Heyden & Sons Ltd., 1980, pp 77-96.
- 31) Beddow, J.K., Lew, G. and Vetter, A.F., On the classification of four different types of powder by a pattern recognition technique applied to particle shape characteristics. Report No. G178-77 001, Materials Engineering Division, The University of Iowa, Iowa City. 52242, USA.
- 32) Underwood, E.E., Quantitative Stereology, Addison-Wesley, Reading, Massachusetts, 1970, pp 227-232.
- 33) Singh, P.N. and Ramakrishnan, P., Correlation of shape indices with bulk properties of powders. Trans. of the PMAI, 7 (1980) 62-69.
- 34) Singh, P.N. and Ramakrishnan, P., Study of powder bulk properties in the light of stereologically evaluated particle characteristics. J. of Powder and bulk Solids Tech., 11 (1987) 13-17.
- 35) Balasubramaniam, V., Singh, P.N. and Ramakrishnan, P., Effects of some particle characteristics on the bulk properties of powders. Powder Met. Int., Vol. 16, 2 (1984) 56-59.
- 36) Pahl, M.H., Schadel, G. and Rumpf, R., Zusammensetzung von Teilchenformbeschreibungsmethoden. In Newsletter '76 in Stereology, ed. Ondracek, G., Gesellschaft fur Kernforschung mbH, Karlsruhe, 1976, pp 89-107.
- 37) Barrett, P.J., The shape of rock profiles, a critical review. Sedimentology, 27 (1980) 291.
- 38) Tou, J.T. and Gonzales, R.C., Pattern Recognition Principles, Reading, Addison Wesley, 1974.
- 39) Beddow, J.K., Philip, G.C. and Nasta, M.D., On the use of pattern recognition methods in particle shape analysis. Planseeber Pulvermetall., 24 (1976) 167.
- 40) Ehrlich, R. and Weinberg, B., An exact method for characterization of grain shape. J. Sed. Petrol., 40 (1970) 205.
- 41) Czarnecka, E.T., and Gillott, J.E., A modified Fourier method of shape and surface texture analysis of planar sections of particles. J. Testing and Evaluation, 5 (1977) 292.

- 42) Czarnecka, E.T., and Gillott, J.E., The effect of orientation on the analysis of shape and texture of concrete aggregates by modified Fourier method. *J. Testing and Evaluation*, 5 (1977) 299.
- 43) Czarnecka, E.T. and Gillott, J.E., Roughness of limestone and quartzite pebbles by the modified Fourier method. *J. Sed. Petrol.*, 50 (1980) 587.
- 44) Gotoh, K., Representation of the size and shape of a single particle. *Powder Tech.*, 12 (1975) 125.
- 45) Gotoh, K., Shape characterization of two dimensional forms. *Powder Tech.*, 23 (1979) 131.
- 46) Singh, Paramanand. and Ramakrishnan, P., Morphological classification by harmonic analysis. *Powder Met. Int.*, Vol. 20, 4 (1988) 12-15.
- 47) Singh, Paramanand, and Ramakrishnan, P., Morphological classification of copper powders of different origins by Fourier analysis. *Powder Met.*, Vol. 31, 4 (1988) 287-292.
- 48) Paramanand. and Ramakrishnan, P., Regeneration of form by Fourier technique and its application in powder characterization. *Part. Part. Syst. Charact.* 5 (1988) 179-185.
- 49) Singh, Paramanand. and Ramakrishnan. P., Application of few salient strategies for reduction of Fourier analysis data for powder characterization. In *Proceedings of international conference on Advances in Materials and Processes*, ed. Ramakrishnan, Oxford & IBH Publishing Co, 1993, pp 159-167.
- 50) Eppler, D.T. and Meloy, T.P., Applicability of sophisticated shape analysis technique to engineering and industrial problems-Fourier shape analysis. In *Fine Particle Processing*, ed. Somasundaram, P., Vol. 1, American Institute of Mining, Metallurgical and Petroleum Engineers, New York, 1980, pp 462-480.
- 51) Beddow, J.K. and Philip, G.C., On the use of a Fourier analysis technique for describing the shape of individual particles. *Planseeber Pulvermetall*, 23 (1975) 3.
- 52) Beddow, J.K. Philip, G.C. and Vetter, A.F., On relating some particle profile characteristics to the profile Fourier coefficients. *Powder Tech.*, 18 (1977) 19.
- 53) Beddow, J.K. and Vetter, A.F., A note on the use of classifiers in morphological analysis of particulates. *J. Powder and Bulk Solids Tech.*, 1 (1977) 42.
- 54) Beddow, J.K., Two different methods of morphological analysis of fine particles. Report No. G178 78 07, Materials Engineering Division, The University of Iowa, Iowa City, 52242, USA.
- 55) Fong, S-T., Beddow, J.K. and Vetter, A.F., A refined method of particle shape representation. *Powder Tech.*, 32 (1979) 17.
- 56) Beddow, J.K., Fong, S-T., and Vetter, A.F., Morphological analysis of metallic wear debris. *Wear*, 58 (1980) 201.
- 57) Lee, Y., Beddow, J.K. and Vetter, A.F., Morphological analysis of fine particle mixtures. *Powder Tech.*, 25 (1980) 137.
- 58) Beddow, J.K., Nasta, M.D. and Philip, G.C., Characteristics of particle signatures. Report No. NSF-76-006, Materials Engineering Division, The University of Iowa, Iowa City, 52242, U.S.A.
- 59) Luerkens, D.W., Beddow, J.K. and Vetter, A.F., Morphological Fourier descriptors. *Powder Tech.*, 31 (1982) 209.
- 60) Luerkens, D.W., Beddow, J.K. and Vetter, A.F., A generalized method of morphological analysis. *Powder Tech.*, 31 (1982) 217.
- 61) Beddow, J.K. and Luerkens, D.W., Effects of powder production and of material processing on powder particle morphology of adipic acid. *Powder Tech.*, 68 (1991) 163-173.
- 62) Luerkens, D.W., *Theory and Application of Morphological Analysis*, CRC Press, Boca raton, 1991, chapter 2, 6 and 7.
- 63) Singh, Paramanand. and Ramakrishnan, P., Particle shape quartization – a novel approach. *Trans. of PMAI*, 10 (1983) 19-26.
- 64) Beddow, J.K., *Particulate Science and Technology*, Chemical Publishing Co., New York, 1980, p 11.
- 65) Ehrlich, R., Brown, J., Yarus, J.M. and Eppler, D.T., Analysis of particle morphology data. In *Advanced Particulate Morphology*, eds. Beddow, J.K. and Meloy, T.P., CRC Press, Boca Raton, 1980, pp 101-119.
- 66) Beddow, J.K., Nasta, M.D., and Philip, G.C., Characteristics of particle signatures. In *Testing and Characterization of Powders and Fine Particles*, eds. Beddow, J.K. and Meloy, T.P., Heyden & Sons Ltd., Florida, 1980, pp 44-55.
- 67) Singh, Pramanand., and Ramakrishnan, P., Powder signature – a strategy for powder characterization by Fourier analysis. *Int. J. of Powder Met. and Powder Tech.*, Vol. 21, 2 (1985) 111-118.
- 68) Singh, P.N., Ramakrsihnan, P. and Beddow, J.K., Characterization of iron powders by Fourier analysis technique. In *Proceedings of International Symposium on Recent Advances in Particulate Science and Technology*, IIT Madras, 1982, pp 17-26.
- 69) Lew, G., Beddow, J.K. and Vetter, A.F., Morphological characterization of particle profiles derived from Walsh Coefficients. *Powder Met. Int.*, 11 (1979) 165.
- 70) Meloy, T.P., Fast Fourier transforms applied to shape analysis of particle silhouettes to obtain morphological data. *Powder Tech.*, 17 (1977) 27.
- 71) Okuda, Satoshi. and Takano, Hiroshi., Parameters for particle shape expression in Fast Fourier Transfer analysis. In *Powder Metallurgy and Related High Temperature Materials*. ed. P. Ramakrishnan, Oxford & IBH Publishing Co., 1985, pp 47-68.
- 72) Beddow, J.K., *Morphological analysis in particulate technology*. *Proceedings of International symposium on recent advances in Particulate Science and Technology*, ed. Ramanujam, M. IIT, Madras 1982.
- 73) Kostelnik, M.C. and Beddow, J.K., as cited in Ref. 5.

- 74) Kostelnik, M.C., Kludt, F.H. and Beddow, J.K., The initial stage of compaction of metal powders in a die. Int. J. Powder Met., 4 (1968) 19.
- 75) Riley, G.S. and Mann, G.R., Effects of particle shape on angles of repose and bulk densities of a granular solid. Mat. Res. Bull., 7 (1972) 163.
- 76) Paramanand. and Ramakrishnan, P. Effect of powder characteristics on compaction of parameters and ejection pressure of compacts. Powder Met., Vol. 27, 3 (1984) 163-168.

### Author's short biography



#### Paramanand Singh

Dr. Paramanand Singh graduated in Metallurgical Engineering in 1974, being awarded the gold medal for securing first rank. He received his M. Tech. in Nuclear Engineering and Technology from Indian Institute of Technology, Kanpur in 1976 and his Ph. D. in 1984 from Indian Institute of Technology, Bombay. After completing his Ph. D. he conducted research and taught at IIT Bombay until 1985 when he was invited as a visiting scientist to join the group of Professor F. Thummler and Dr. S. Nazare at Kernforschungszentrum, Karlsruhe, F. R. G. researching in the area of high temperature intermetallic compounds for structural applications. He is with the Department of Metallurgical Engineering, IIT Madras since 1988 and is actively engaged in teaching, research and development, industrial consultancy and sponsored projects in the fields of powder metallurgy, ceramics, composites and materials science in which he has published many papers in referred journals. He is on the editorial board of the Transactions of Powder Metallurgy Association of India.



#### P. Ramakrishnan

Dr. P. Ramakrishnan, Professor Department of Metallurgical Engineering and Materials Science, Chief Co-ordinator, Powder Metallurgy and High Temperature Material Centre, Indian Institute of Technology, Bombay is actively engaged in education, research and development, training and Industrial Consultancy in the field of Powder Metallurgy, Ceramic and Composite Materials. In these areas he has published over 350 technical papers in reputed journals and edited 12 books. A recipient of Binani Gold Medal of Indian Institute of Metals 1996, National Metallurgical Award of Government of India 1976, and the award of International Research Grant of National Science Foundation U.S.A. on different occasions. He was the chairman of International Hausner award committee of the International fine particle society, U.S.A. in 1980, and the past president of PMAI, and Chairman of ASM International Chapter. He is a member of Technical Advisory Board, Editorial Advisory Board, Editorial Board and International Liaison Committee of many professional bodies, journals and International Conferences.

# Segregation of Particulate Materials – Mechanisms and Testers†

Jostein Mosby and Sunil R. de Silva

Telemark College\*,

Gisle G. Enstad

Telemark Technological R & D Centre\*.

## Abstract

*The tendency of particulate materials to separate into various zones depending on their various physical characteristics is called segregation. The phenomenon is widely encountered in nearly all materials handling situations and leads, quite often, to significant variations in quality. This paper reviews the mechanisms which contribute to segregation and demonstrates, by means of laboratory scale tests, that the particular segregation pattern likely to be encountered in a given situation is a function of both material and process-related variables.*

## 1. Introduction

Segregation is the tendency of individual particles to move to different positions in a particle collective due to differences in properties. The properties that can give rise to segregation are size, density, shape, elasticity and surface texture. The earliest publications on segregation concerned coal [1–7], and, in 1925, Garve found that when filled into a silo, the larger coal particles were found near the walls, while the finer particles were found near the centre [8]. If, on discharge, the centre core was allowed to flow out first, then the fine and coarse fractions became nearly totally separated from one another. A flow pattern, later to be christened core or funnel flow by Jenike [9], which leads to this type of separation was already identified by Wittich [10] in 1915.

There has been some confusion regarding the classification of segregation. Thus one talks of ‘‘heap segregation’’ as though this was one particular mechanism of segregation. In practice, segregation that occurs in a heap is a result of several mechanisms, and which of these are mobilised in a given situation is very much dependent on the way in which the heap is formed. We will therefore review the MECHANISMS causing segregation, and explain the PROCESSES in which these will dominate, rather than dealing with individual manifestations of the phenomenon.

In the last part of this paper, we will describe segregation testers that can determine both the

type and extent of segregation that is likely to occur in the formation of a heap, and thereby show that the segregation patterns that occur are very much a function of the method used to form the heap, and of the geometry of the heap. For the sake of brevity, we will restrict most of our comments to heap segregation, but the mechanisms described can be encountered in any materials handling situation.

## 2. Segregation mechanisms

The main mechanisms of segregation are thought to be:

- Rolling
- Sieving
- Push-away effects
- Angle of repose effects
- Percolation
- Displacement
- Trajectory effects
- Air current effects
- Fluidization effects
- Impact effects

### 2.1 Rolling

Rolling effects were thought to be dominant in heap segregation [7, 8, 11]. These cause the result shown in **Figure 1**.

According to Brown [6], segregation in a heap is described as a surface phenomenon where the nature of the heap surface is approximately constant. This cannot be entirely true since the nature of the surface

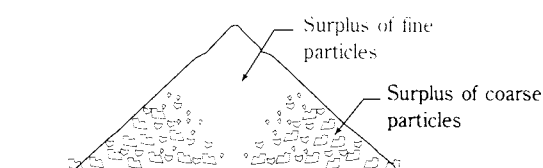


Fig. 1. Effect of rolling on heap structure.

\* Kjolnes Ring, N-3914 Porsgrunn, Norway

† Received: 13 June 1996

varies from the centre to the edge, and segregation occurs in layers that constantly flow from the centre to the edge.

Mattheè [12] showed that rolling is an important mechanism by demonstrating that the friction against rolling was greater for small particles than for larger ones. Miwa [13] pointed out that large particles can roll over protuberances on the surface with greater ease than small ones. He called the phenomenon a “stumbling” effect. There is little doubt that for particles with a high degree of sphericity and for low filling rates, rolling will be one of the dominant mechanisms in heap segregation, regardless of some recent attempts [14, 15] to assign this role to sieving.

## 2.2 Sieving

Holmes [3] included both rolling and sieving in his analysis of heap segregation. He pointed out that the larger particles rolling down the heap surface act as a non-blinding screen through which the smaller particles find their way. This situation continues until the supply of fines is exhausted, or until the larger particles come to rest. The situation is illustrated in **Figure 2**.

Lawrence and Beddow [16] studied central filling of two component mixtures of lead particles into cylindrical dies. These investigations showed that the centre core immediately beneath the filling point had an excess of fines. This was attributed to the sieving effect.

Shinohara and his co-workers have developed a mathematical model for this type of segregation [17–28]. Called the “Screening Layer Model”, it seeks to explain heap segregation solely on the basis of the sieving effect. Williams [29] also deals with sieving as a mechanism in heap segregation, and Williams and Khan [30] determined that the phenomenon can occur with binary mixtures with diameter ratios as

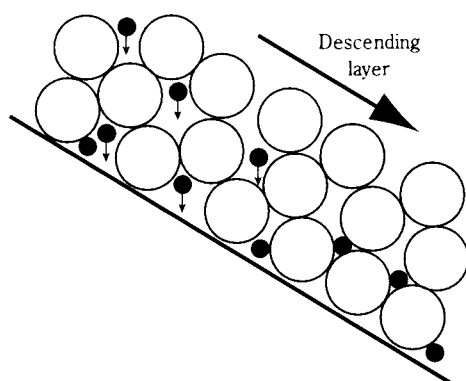


**Fig. 2** Sieving of smaller particles through spaces formed by larger particles.

low as 1.03:1. This ratio was established in a rotating drum in which a constant and moving inclined plane could be maintained.

Carson et al [14] and Johanson [15] conclude that sieving is the most important mechanism in heap segregation, especially when the content of fines is low. Sieving can, however, only be dominant when there is a sufficient amount of large particles to form a moving layer, and when the fines content is small enough for all of it to pass through this layer near the centre of the heap. It will be shown later that the extent to which sieving is responsible for heap segregation is dependent on how the heap is formed.

## 2.3 Push-away effects

The concept of push-away effects was introduced by Tanaka [31]. The effect is most likely to arise where components of different densities are involved. The effect is illustrated in **Figure 3**.

When the top sphere has a higher density than the two below, it will tend to push the latter aside. This results in heaps where heavier particles settle near the centre of the heap and lighter ones near the wall.

## 2.4 Angle-of-repose effects

Johanson [15] has given an illustration of what has been called the “angle-of-repose effect”. He used a mixture of 20% mung beans and 80% fine salt. Due to the high salt content, the sieving effect is inhibited, but there was still a preponderance of mung beans near the walls of the two dimensional silo in which the experiment was carried out. Johanson explains this on the basis of a higher angle of repose for salt than for mung beans, which leads to the mung beans rolling down surfaces formed by salt. One could pose the question whether this is more a rolling effect than an angle-of-repose effect, and the two effects are almost certainly related.

A better example of the angle-of-repose effect was observed by Mosby [32] during an investigation of

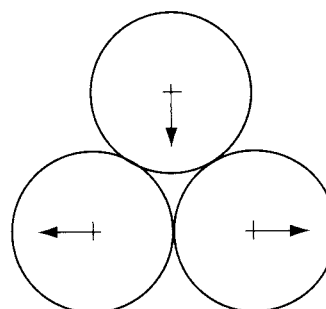


**Fig. 3** Heavy sphere of similar size to two lighter spheres pushing the latter aside.

the use of heaps for blending materials. In this operation, fine copper concentrate and coarser sand are filled in batches to form a blending heap. The sand had a greater dynamic angle of repose than the copper concentrate. When a batch of sand was added to the heap, it formed a cone with a high angle of repose on the top of the heap, allowing the next batch of copper concentrate to roll down to the edge of the heap. The next batch of concentrate with a low angle of repose did not allow the sand to flow down to the edge with a similar degree of ease, and the centre became richer in the coarser sand as a result. The situation is illustrated in **Figure 4**.

## 2.5 Percolation

Percolation of small particles was studied by Brown [6], who attributed it to vibrations causing fine particles to move downwards in a powder mass. Bridgwater and his co-workers [33–39] also studied the phenomenon. Bridgwater and Ingram [33] studied the migration of a single small sphere through a bed of larger particles, and determined that spontaneous percolation, due to gravity alone, will occur at diameter ratios of less than 0.1547 in a binary mixture.

Stephens and Bridgwater [34, 35] used an annular shear cell to investigate the effect of shear on percolation, and found that size ratios, shape and surface roughness all contributed to the percolation velocities. Finally, Scott and Bridgwater [36] used a rectangular shear box, whose principle is shown in **Figure 5**, to further study percolation under shear.

In these experiments, it was established that percolation depends on total strain, the ratio of sizes and the rate of strain. Percolation and sieving yield similar effects, but percolation does not require a moving layer of material to be present.

## 2.6 Displacement

Brown [6] had noticed that one single large particle, placed at the bottom of a bed of small particles, will

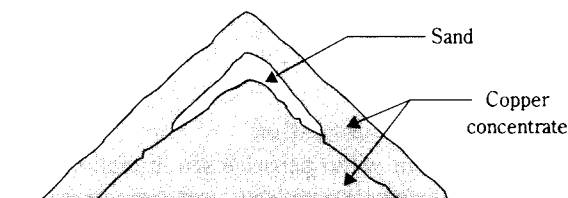


**Fig. 4** Concentration of a coarse sand in the centre of a heap due to angle-of-repose effects.

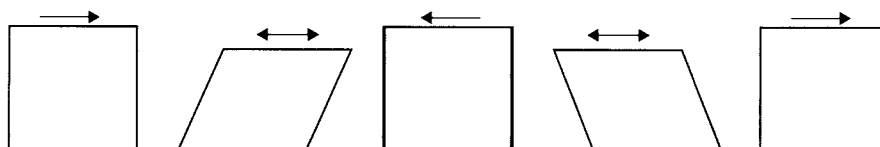


**Fig. 5** Principle of shear box used in the study of percolation under shear.

rise to the surface when the bed is vibrated. Brown explained the phenomenon on the basis of locally abnormal packing conditions around the large particle. Williams [40] examined the phenomenon in detail using a perspex box which was 100 mm wide, 3 mm deep and 150 mm high. The box was filled with glass beads of a diameter slightly less than its depth, and a brass disc was placed at the bottom. The box was then vibrated with increasing frequency. At first nothing happened. Then, at a critical frequency, the brass disc rose to just below the surface. Upon a further increase in frequency, the disc sank to a new position and found a new position of equilibrium.

Williams attributes the effect to a difference in pressure at various bed depths. When a large particle is placed in the middle of the bed, the pressure below this particle will be greater than the surrounding bed at the same depth. This locks smaller particles into place below the large particle and prevents its fall. The surrounding particles, however, are in motion and if this causes the large particle to move upwards, then fine material immediately flows underneath and becomes locked in position. At a certain depth, the pressure underneath the large particle will be insufficient to prevent the movement of small particles beneath it, and the large particle reaches an equilibrium position. This phenomenon is often observed in transport containers (IBCs, sacks or big bags) where a layer of coarse particles is found on the surface.

## 2.7 Trajectory effects

Taggart [11] indicates that larger particles which move along an inclined chute will discharge further away from the end of the chute than smaller ones, as illustrated in **Figure 6**.

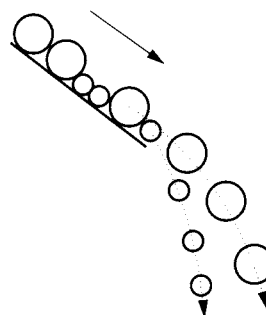


**Fig. 6** Trajectory segregation.

Holmes [3] investigated the segregation of anthracite and fluorspar particles filled onto a heap from a silo via a chute.

The conical heap was divided into six sections as shown in **Figure 7**, and each section analysed for fines content. There was a preponderance of fines in the side of the heap near the end of the chute, showing a high degree of trajectory segregation.

Bicking [41] studied the effects of filling heaps via vertical and inclined chutes and obtained similar results to those of Holmes with the inclined chute. Mitchell [1] showed similar effects when filling belt or bucket conveyors via transfer chutes. Stock [7] observed similar effects at the ends of belt conveyors and feeders. Williams [29] showed that trajectory segregation could have an effect in mixers in which particles are lifted up into the air and thrown with the intention of scattering them across a surface. Trajectory segregation is often compounded by other effects such as percolation [42, 43] or frictional effects [14].

## 2.8 Air current effects

Particles being filled centrally into a tall silo will induce a flow of air around the falling material stream, as shown in **Figure 8**.

If the material being filled into the silo contains a significant quantity of fine particles ( $< \text{ca. } 50 \mu\text{m}$ ), these will tend to be carried by the air flow towards the side of the silo, leaving the centre richer in

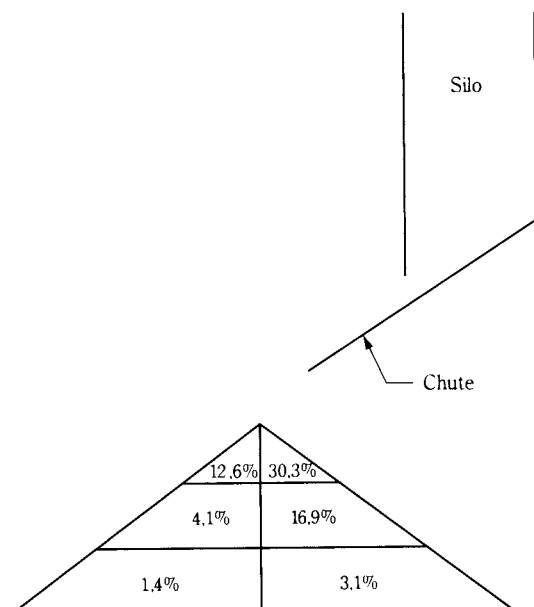


**Fig. 7** Segregation in a heap as a result of trajectory segregation. Content of fines is shown in different parts of the heap.

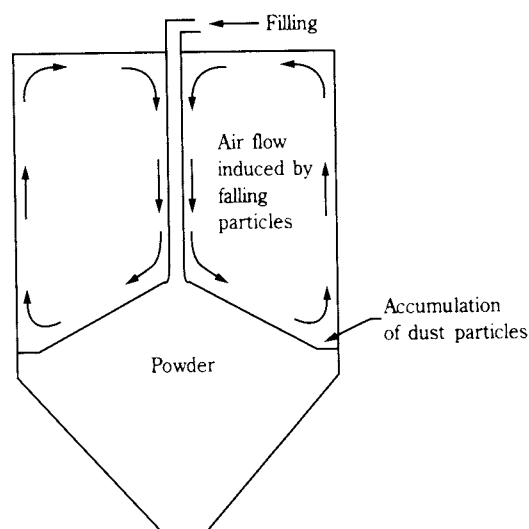


**Fig. 8** Air currents set up during the filling of a silo.

coarser material. The effect decreases with decreasing height of fall, and most of the fines become concentrated near the transition from the parallel to the converging section of the silo. The effect has been investigated and discussed by Carson, Royal and Goodwill [14], Johanson [44], De Silva and Enstad [45], Carruthers [46], Nilsen and Meland [47], Penne [48] and Medema [49].

## 2.9 Fluidization effects

The effect of fluidization on segregation has been little discussed in the literature. Johanson [40] was perhaps the first to do so in 1978. When a mixture of fine and coarse particles are filled into a silo, the fines may become aerated. The coarse particles fall through the aerated layer (jetsam), while the aerated layer of fines (flotsam) remains on the surface and moves upwards. Using small two-dimensional boxes, Johanson [15] went on to demonstrate that fluidization causes a high content of fines on the surface. The effect was also observed and reported on by Carson et al [14] and Medema [49].

## 2.10 Impact segregation

Impacts occur when particles are in motion. There are both inter-particle impacts, and impacts between particles and system boundaries. Brown [6] described the effect of collisions between small and large particles. Such collisions either bring the small particles to a stop, or give them an increased velocity. This leads to the smaller particles being spread over a larger area than the coarse particles.

Carson et al [14] also describe a situation in which impact effects (which they call dynamic effects) are shown to be due to differences in resilience, inertia and other dynamic characteristics. They refer to a situation in which finer plastic pellets were found near the walls of a silo, which is in contrast to what would normally be expected, and which could only be explained by a greater resilience being possessed by the fine particles. Another possible effect is the spreading effect described by Brown.

An investigation on the filling of smelters via chutes was undertaken by a group of students at Telemark College [50]. The materials used were quartz with a particle size of 16-20 mm (77%) and coke with a size of 2.5-5 mm (23%). The experimental set-up is illustrated in **Figure 9**.

When the rate of fill was slow, little segregation was observed. All the particles move freely, bounce against the walls and impact with each other, and the result is a reasonably homogeneous fill (heap).

As the rate of fill is increased, the collisions begin to influence the trajectories of the coke particles more than those of the quartz. The quartz particles bounce back from the front wall of the vertical channel, and are collected on the right-hand side of the heap, whereas most of the fine coke particles are prevented from hitting the wall by collisions with the quartz particles and with the other small coke particles, and therefore continue to the left-hand side of the heap.

At even higher rates of fill, the collisions were also significant for quartz, and segregation again decreased.

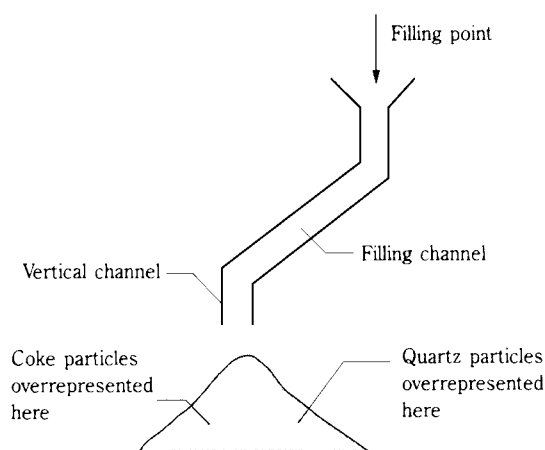


**Fig. 9** Filling of a smelter via a chute.

### 3. Segregation Testing

#### 3.1 Variables

It has been shown in the previous section that there are several mechanisms that can give rise to segregation. Which of these will dominate in any given situation is dependent on a large number of parameters. These parameters are dependent on both the nature of the particles and the process variables. Mosby [51] has listed the following parameters as being important:

Particle Properties	Process Variables
• Size and size distributions	• Fall height
• Density	• Rate of feed or fill
• Shape	• Effect of size of heap
• Modulus of elasticity	• Effect of moisture
• Friction coefficient	• Mixing ratio
• Surface texture	
• Cohesivity	
• Adhesion	

#### 3.2 Segregation testers

Many testers have been built with a view to determining the tendency of powders to segregate. Harris and Hildon [52] used the device shown in **Figure 10** to investigate mixtures of washing powders and bleaching agents.

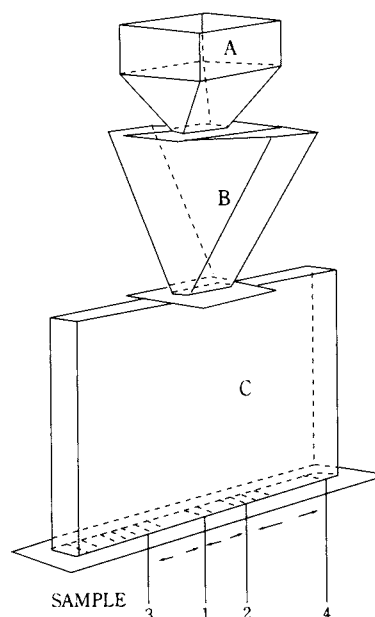


**Fig. 10** Segregation tester used by Harris and Hildon.

Shinohara [20] used the devices shown in **Figure 11** in the development of his screening layer theory.

Other versions were also developed by Drahn and Bridgwater [37] and Bagster [53].

Most of these testers had a shortcoming of some kind, and it was decided to build two completely new units at Telemark College. One was two-dimensional, and the other three-dimensional. The two-dimensional device is shown in **Figure 12**.

The tester consists of a rectangular box with a front wall in glass and a back wall of aluminium. The depth of the first version was 70 mm and the length of the surface of the heap formed was 630 mm. The tester is provided with 9 sample takers, and the angle of the tester to the horizontal is adjusted such that the sample takers are parallel to the surface of the heap. The design of the sample takers was given by Shinohara [54].

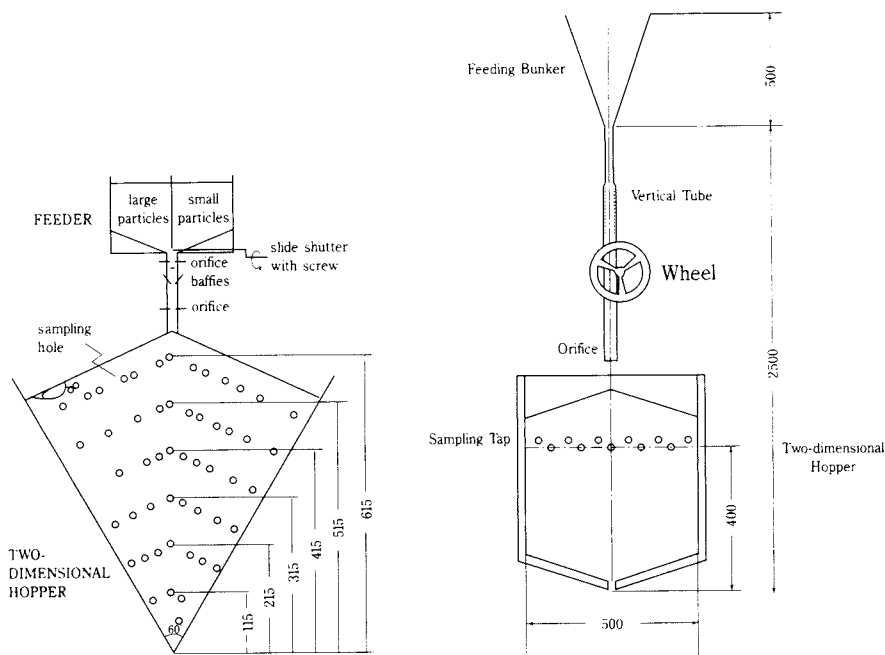


**Fig. 11** Two-dimensional testers developed by Shinohara.

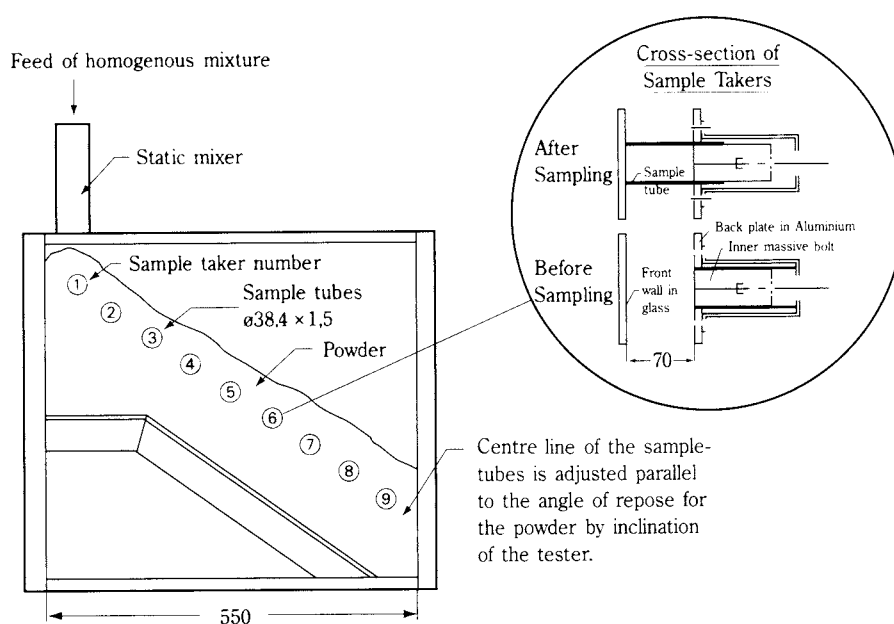


**Fig. 12** Two-dimensional segregation tester.

The materials to be tested are introduced at the upper left-hand corner of the tester. Where mixtures are used, they are introduced via a static mixer. The material then flows down the inclined bottom plate, and a heap is gradually built up. The special geometry chosen for the bottom was intended to reduce the quantity of powder necessary for a test.

After intensive testing with the 630 mm-heap-length unit had demonstrated that it produced extremely reproducible results, two further testers were built with heap lengths of 1100 mm and 2050 mm.

The three-dimensional tester had a similar form, but was cylindrical in shape. A special method was developed for taking representative samples from the tester [55]. The diameter of the tester was 1000 mm.

### 3.2 Results from the two-dimensional tester

A mixture of alumina and sand, with the particle size distributions shown in **Figure 13**, were used in the tests.

The physical characteristics of the two materials are given in **Table 1**.

**Figures 14-17** show the resulting segregation patterns for four different heap lengths, several mixing ratios ( $M_i$ ) and feed rates ( $Fr$ )

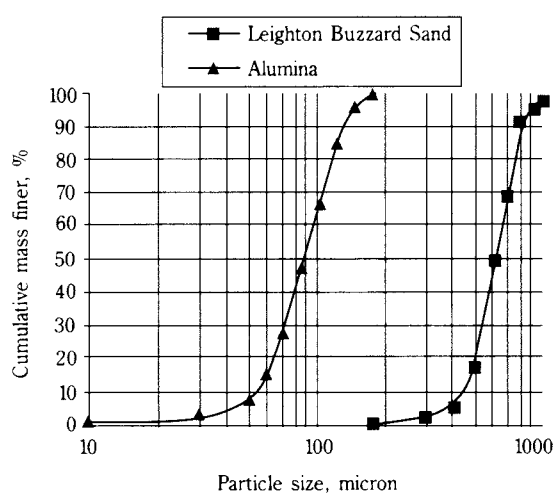


**Fig. 13** Particle size distributions of the alumina and sand used in the investigation of heap segregation.

**Table 1.** Characteristics of the alumina and Leighton Buzzard sand

	Alumina	Sand
Dynamic angle of repose	32°	36°
Static angle of repose	34°	37°
Poured density, g/cm <sup>3</sup>	1.00	1.51
Tapped density, g/cm <sup>3</sup>	1.12	1.66
Particle density, g/cm <sup>3</sup>	3.40	2.65

The figures demonstrate clearly that segregation patterns are dominated by the mechanisms that are mobilised under a given set of experimental conditions. The essential features of **Figures 14-17** are presented in **Figure 18**. In this figure, the length of the heap has been normalised on the x-axis in order to make the results comparable, and the five characteristic segregation patterns depicted will be further discussed below.

Curve A shows a special form of heap segregation which has seldom been described earlier. A similar effect was reported on by Lawrence and Beddow in their die filling experiments [16], when the fines content exceeded 60%. In the present case, this effect is felt to be caused by fluidization, with the alumina forming a very mobile fluidized layer and flowing to the edge of the heap. This effect was only observed when the alumina content was over 70%.

Curve B shows an even, almost linear, decrease of alumina from approximately 75% near the feed point to 55% in the sample taker nearest the end wall of the tester. Here, the rolling mechanism dominates. The high alumina content (64.5%) locks the sand into place near the centre of the heap and the excess simply rolls along the surface.

Curve C has a similar form to that of curve B up to about 75% of the heap length. At distances beyond this, the alumina content drops sharply. This is a manifestation of the sieving effect, although initially rolling will have played a role. Near the centre of the heap, there is sufficient alumina to fill the voids between the coarse sand particles and any excess rolls on the surface. After a certain distance the alumina is depleted to the point that it can no longer lock the sand particles, and sieving occurs—leading to a rapid reduction in alumina content.

Curve D shows a rapid drop in alumina content from the second sample point until it reaches 0% at 80% of the heap length. Here the sieving effect is dominant, and the screening layer model predicts the tendency quite well.

Curve E also shows the sieving effect.

### 3.3 Results from the three-dimensional tester

Similar results were also obtained with the three-dimensional tester, although the results were not directly comparable. In order to obtain comparable results, the feed rate to the three-dimensional tester must be much higher than that to the two-dimensional unit. Direct comparisons give qualitatively

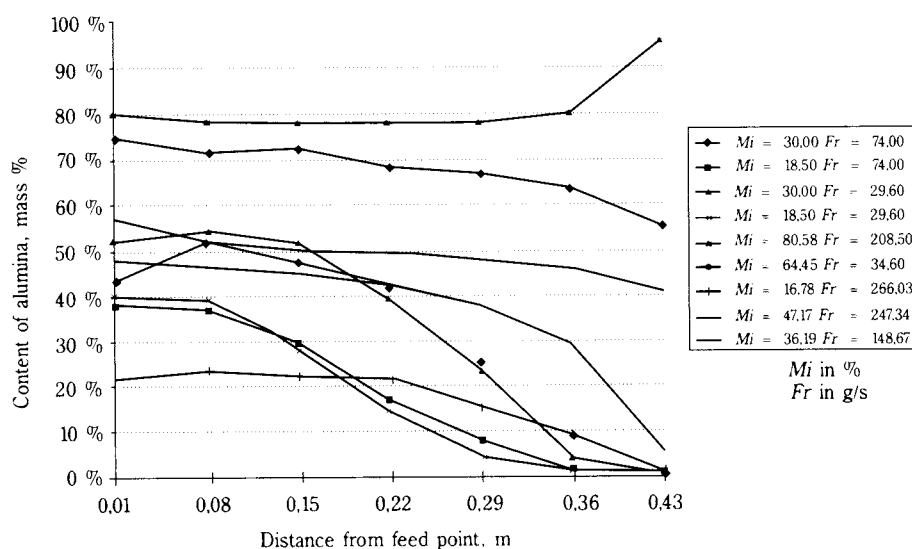


Fig. 14 Segregation pattern for the experiments with heap length 47 cm.

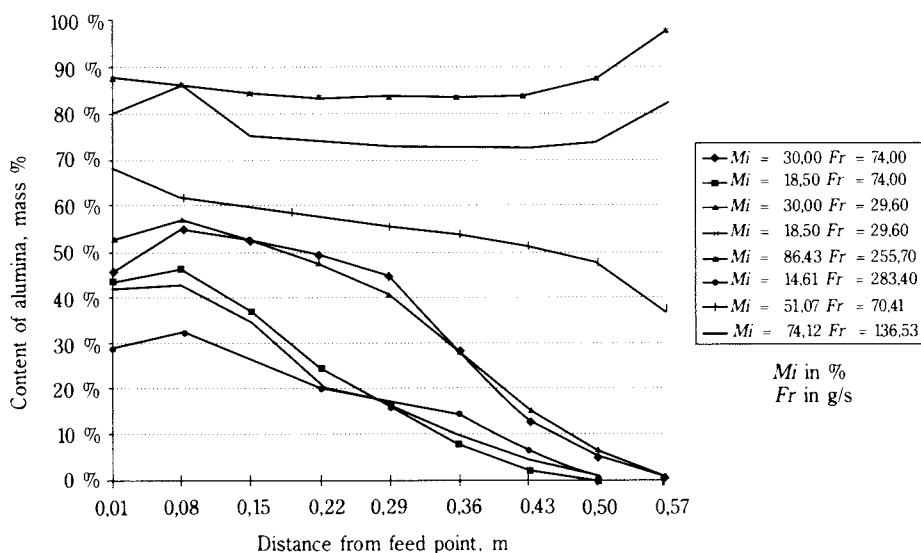


Fig. 15 Segregation pattern for the experiments with heap length 63 cm.

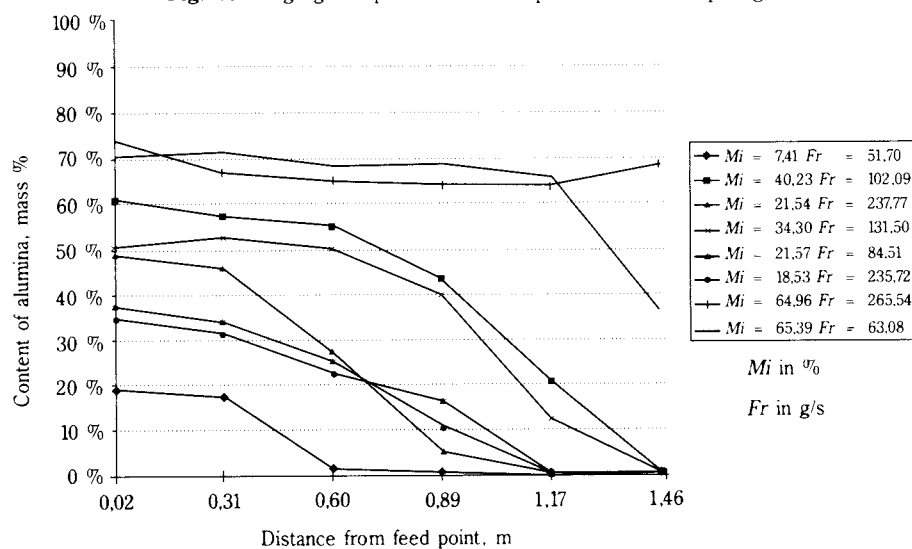


Fig. 16 Segregation pattern for the experiments with heap length 149 cm

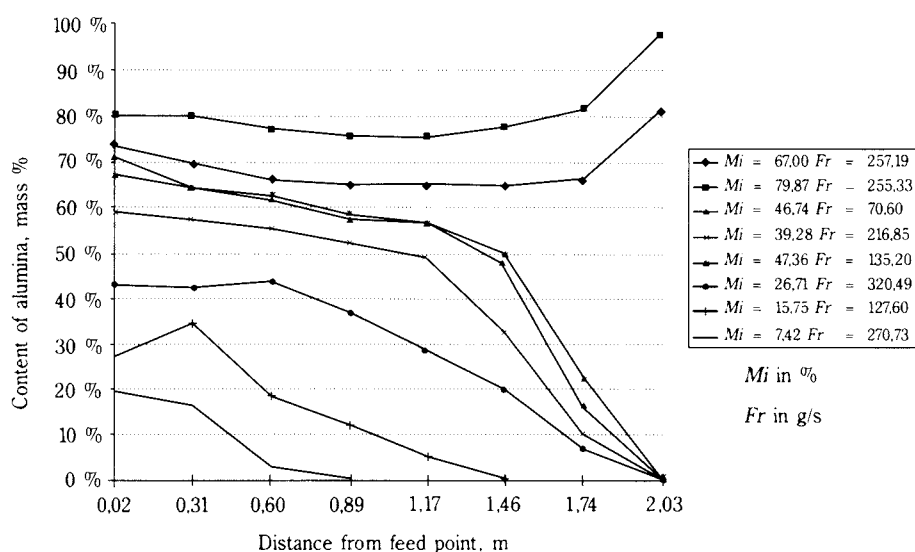


Fig. 17 Segregation pattern for the experiments with heap length 205 cm.

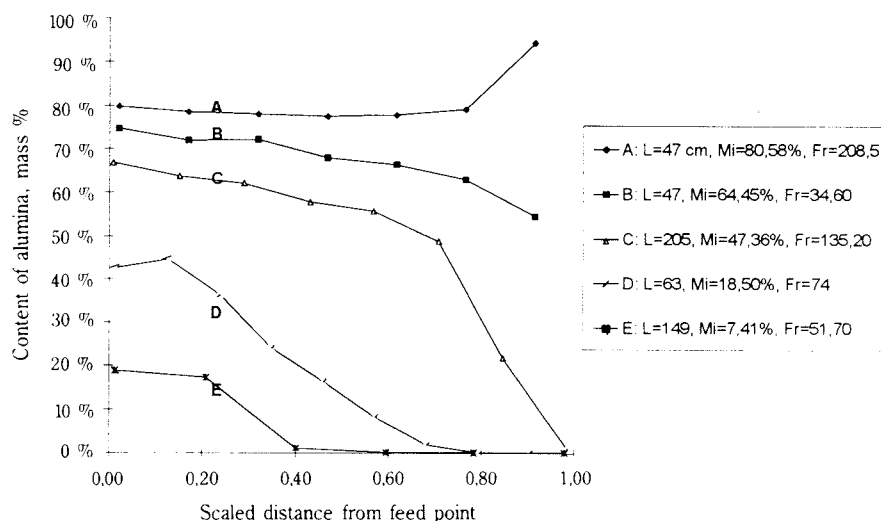


Fig. 18 Characteristic segregation patterns obtained with the two-dimensional segregation tester

similar results as shown in **Figure 19**, where the content of fines is relatively high.

When the content of fines is low, the differences are more significant as shown in **Figure 20**.

The higher levels of segregation in the three-dimensional tester are due to two major reasons. Firstly, the area covered by a layer of material increases with heap length, unlike in the two-dimensional unit where it stays constant. Secondly, the flow in a three-dimensional heap is not homogeneous, and layers flow in different zones and directions at different times. These factors make direct comparisons difficult, and a satisfactory method of obtaining quantitatively comparable results has yet to be developed.

In a first attempt to do so, both the mixing ratios and feed rates were scaled to allow for the increase

in area with distance from the centre. Unfortunately, no tests were available with a feed rate high enough on the three-dimensional unit to compare with a feed rate low enough on the two-dimensional unit. The comparison shown in **Figure 21** is therefore for feed rates of 74 g/s and 283 g/s on the two-dimensional unit (which correspond to 1661 g/s and 6351 g/s on the three-dimensional unit if the layer thickness is assumed constant), and 260 g/s on the three-dimensional unit.

The figure shows that the result of the three-dimensional tester lies between the results with the two-dimensional unit at a feed rate much lower than the equivalents used in the two-dimensional units. The reason for this discrepancy is thought to be the nature of the flow along the surface of a three-

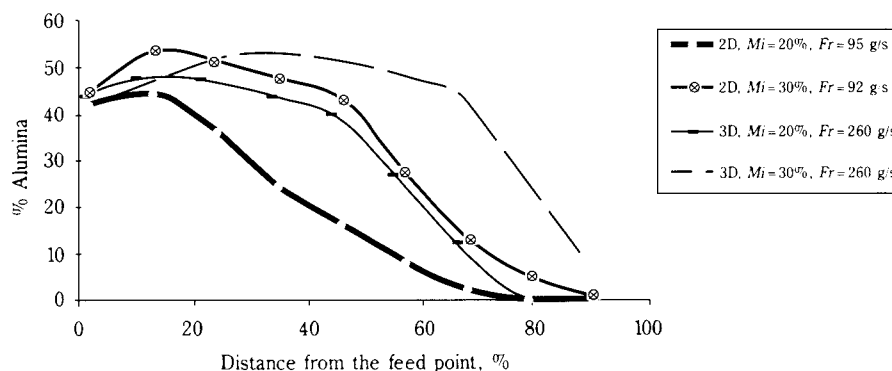


Fig. 19 Segregation patterns in the two and three-dimensional testers. Relatively high fines content.

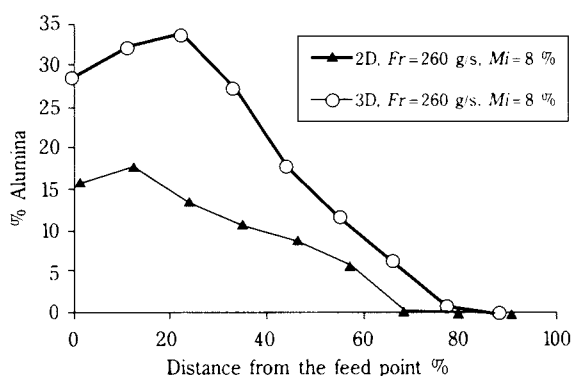


Fig. 20 Segregation patterns in the two and three-dimensional testers. Relatively low fines content.

dimensional heap, which is NOT evenly distributed, but highly concentrated in zones which keep changing location. Further work is necessary.

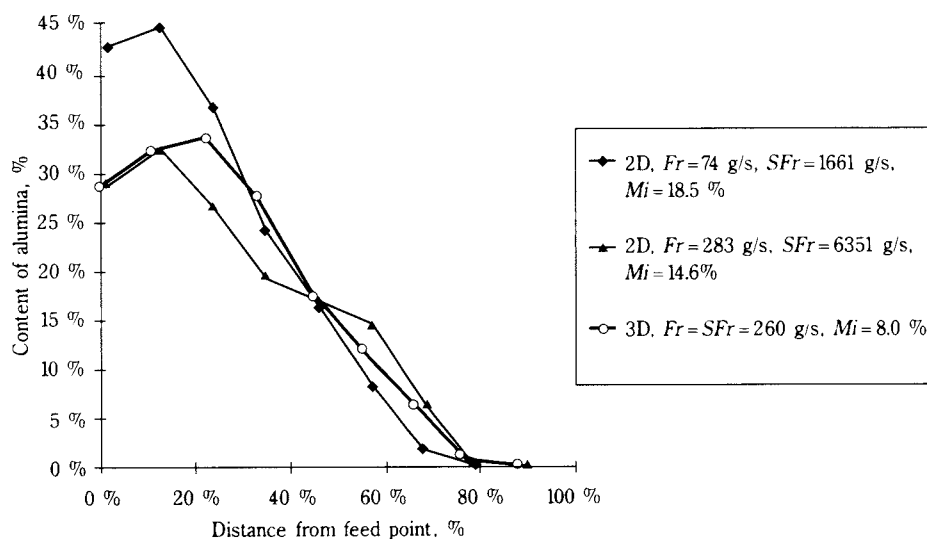


Fig. 21 Comparison of segregation patterns in two and three-dimensional testers with mixing ratios adjusted to be similar.

#### 4. Conclusions

It has been shown that the segregation patterns obtained in the filling of a heap are dependent on a number of variables, and that by changing these variables, quite different patterns can be obtained. Results from two-dimensional testers, although very reproducible, must be interpreted with care when they are used to interpret a three-dimensional situation, and further work is necessary before quantitative comparisons between two and three-dimensional testers can reliably be established.

#### Acknowledgements

The authors wish to thank the Norwegian Institute of Technology for a stipend to Jostein Mosby, and the Swedish Mineral Processing Research Foundation (*MinFo*) and members of our POSTEC programme for their financial support of this project.

## References

- 1) Mitchell, D.R.: Segregation in the Handling of Coal., American Institution of Mining, Metallurgical and Petroleum Engineers. Trans. 130 (1938).
- 2) Sherman, R.A., Kaiser, E.R.: Segregation of Coal in an Industrial Steam Plant Bunker. Combustion, December 1937, pp. 25-28.
- 3) Holmes: Colliery Engr. (1934) 11.
- 4) Castanoli: Amer. Min. Congress Yearbook (1935) 270.
- 5) Hebley: Appalachian Coals, Inc., Fuel Engineers Meeting, July 1936.
- 6) Brown, R.L.: The Fundamental Principles of Segregation, The Institute of Fuel, Journal Vol. 13 (1939).
- 7) Stock, A.J.: Coal Segregation in Boiler Plants, Mechanical Engineering 66 (1944).
- 8) Garve, T.W.: Jnl. Amer. Ceramic Soc. (1925) 8, p. 668.
- 9) Jenike A.W: Storage and Flow of Solids. University of Utah, Engineering Experiment Station, Bull 123, November 1964
- 10) Wittich: Tonindustrie Zeitung, July 1915.
- 11) Taggart, A.F.: Handbook of Ore Dressing, 1087, McGraw Hill Book Co., New York, 1927.
- 12) Matthée, H.: Segregation Phenomena Relating to Bunkering of Bulk Materials: Theoretical Considerations and Experimental Investigations. Powder Techn. Vol. 1, (1967/68), pp. 265-27
- 13) Miwa, S.: Funtai kogaku handbook, Asaka Publishing Co., Tokyo, 1965, p. 448.
- 14) Carson, J.W., Royal, T.A., Goodwill, D.A.: Understanding and Eliminating Particle Segregation Problems, Bulk Solids Handling Vol. 6, No. 1, February 1986, pp. 139-144
- 15) Johanson, J.R.: Solids Segregation – Causes and Solutions. Powder and Bulk Eng., August 1988, pp.13-19
- 16) Lawrence, L.R., Beddow, J.K.: Powder Segregation During Die Filling, Powder Technology, 2 (1968/69), pp. 253-259
- 17) Shinohara, K., Enstad, G.G.: Some Segregation Mechanisms and their Prevention. Reliable Flow of Particulate Solids II, August 1993, Oslo, Norway.
- 18) Shinohara, K., Idemitsu, Y., Gotoh, K., Tanaka, T.: Mechanism of Gravity Flow of Particles from a Hopper. Ind. Eng. Chem. Process Design and Development, Vol 9, No. 2, (July 1968)
- 19) Shinohara, K., Shoji, K., Tanaka, T.: Mechanism of Segregation and Blending of Particles Flowing out of Mass-Flow Hoppers. Ind. Eng. Chem. Process Design and Development, Vol 9, No. 2, (1970), pp. 369-376
- 20) Shinohara, K., Shoji, K., Tanaka, T.: Mechanism of Size Segregation in Filling a Hopper. Ind. Eng. Chem. Process Design and Development, Vol 11, No. 3, (1972), pp. 369-376
- 21) Shinohara, K.: Mechanism of Segregation of Differently Shaped Particles in Filling Containers. Ind. Eng. Chem. Process Design and Development, Vol. 18, No.2, (1979)
- 22) Shinohara, K., Miyata, S.: Mechanism of Density Segregation of Particles in Filling Vessels. Ind. Eng. Chem. Process Design and Development, Vol. 23, No.3, (1984), pp. 423-428.
- 23) Shinohara, K.: Some models on particle-segregation in filling hoppers. Aufbereitung-Technik, No. 3, 1985, pp. 116-122.
- 24) Shinohara, K.: General Mechanism of Particle Segregation during Filling of Hoppers. Proceedings of 9th CHISA Congress, section H: Particulate Solids, H.3.5, Prague, (1987).
- 25) Shinohara, K.: General Segregation Mechanism of Binary Solids Mixtures Filling Two-Dimensional Hoppers. Aufbereitungs-Technik, Vol. 31, No. 9, 1990, pp. 482-488.
- 26) Shinohara, K., Enstad, G.G.: Segregation Mechanism of Binary Solids in Filling Axis-Symmetric Hoppers. Proceedings of 2nd World Congress Particle Technology. September 1990, Kyoto, Japan.
- 27) Shinohara, K., Saitoh, J.: Segregation by Multi-Point Feeding of Binary Solids Mixture onto Two-dimensional Heap. Int. Conf. Bulk Mat. Handl and Transp.: Symposium on Freight Pipelines, Wollongong, Australia, July 1992.
- 28) Shinohara, K., Saitoh, J.: Mechanism of Solids Segregation over a Two-Dimensional Dead Man in Blast Furnace. The Iron and Steel Institute of Japan, Vol. 33 (1993), No.6, pp. 672-680.
- 29) Williams, J.C.: The Segregation of Particulate Materials. A Review. Powder Technology, 15 (1976), pp. 245-251.
- 30) Williams, J.C., Kahn, M.I.: The Mixing and Segregation of Particulate Solids of Different Particle Size. Chemical Engineering, 19, London, (1973), p. 169.
- 31) Tanaka, T.: Segregation Models of Solid Mixtures Composed of Different Densities and Particle Sizes. Ind. Eng. Chem. Process Design and Development, Vol 10, No. 3, (1971), pp. 332-340.
- 32) Mosby, J. Enstad, G.G.: Innledende studier av blanding og segregering av kobberkonsentrat og sand ved fylling i haug. Tel-Tek report no. 43003-2, 1994.
- 33) Bridgwater, J., Ingram, N.D.: Rate of Spontaneous Interparticle Percolation. Transactions of the Institution of Chemical Engineers, 49, (1971), pp. 163-169
- 34) Stephens, D.J., Bridgwater, J.: The Mixing and Percolation of Cohesionless Particulate Materials, Part I: Failure Zone Formation. Powder Technology, 21, (1978), pp.17-28.
- 35) Stephens, D.J., Bridgwater, J.: The Mixing and Percolation of Cohesionless Particulate Materials, Part II: Microscopic Mechanisms for Particles Differing in Size. Powder Technology, 21, (1978), pp.17-28.
- 36) Scott, A.M., Bridgwater, J.: Interparticle Percolation: A Fundamental Solids Mixing Mechanism. Ind. & Eng. Chemistry, 14, No. 1, (1975), pp. 22-27.
- 37) Drahn, J.A., Bridgwater, J.: The Mechanisms of

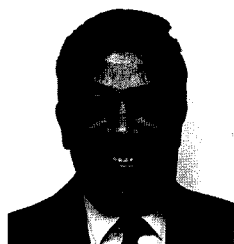
- Free Surface Segregation. Powder Technology, 36 (1983), pp. 39-53.
- 38) Foo, W.S., Bridgwater, J.: Particle Migration (short communication). Powder Technology, 36, (1983), pp. 217-273
  - 39) Bridgwater, J., Foo, W.S., Stephens, D.J.: Particle Mixing and Segregation in Failure Zones: Theory and Experiment. Powder Technology, 41, (1985), pp. 147-158.
  - 40) Williams, J.C.: The Segregation of Powders and Granular Materials. Fuel Society, Sheffield, Journal Vol. 14. (1963).
  - 41) Bicking, C.A.: The Sampling of Bulk Materials. Materials Research & Standards, March 1967.
  - 42) Johanson, J.R.: Particle Segregation, and What to do About it. Chemical Engineering, May 1978.
  - 43) Johanson, J.R.: Solids Segregation: Causes and Solutions. Powder & Bulk Solids, Conf. May 1991, Rosemont, Illinois.
  - 44) Johanson, J.R.: Solids Segregation – Case Histories and Solutions. Bulk Solids Handling Vol. 7, No. 2, April 1987, pp. 205-208.
  - 45) De Silva, S., Enstad, G.G.: Bulk Solids Handling in Scandinavia, A Case Study in the Aluminium Industry. Bulk Solids Handling, Vol. 11, Number 1, March 1991.
  - 46) Carruthers, A.N.: Segregation in Flat Bottomed Alumina Silos. Light Met, 1987, pp. 151-156.
  - 47) Nilsen, Ø., Meland, O.: Segregation in Fish Meal (in Norwegian) SSF Internal Report D-322 (1981).
  - 48) Penne, H.: Undersøkelse av problemet med finstøv i oksider. Når, hvordan og hvorfor. Elkem Aluminium, Lista, August 1991.
  - 49) Medema, J.G.: An Experimental Investigation of the Effect of Air Induced Segregation of Alumina During the Filling of Silos. POSTEC-Report 911301-1, 1991.
  - 50) Enggrav, S., Halvorsen, K., Holberg, J.K., Wendelborg, K.: Segregering av partikulære materialer ved strømning gjennom skråstilte rør og påfølgende fylling i haug. Student project at Telemark College, Institute of Technology, Report 2-PT-6, December 1989.
  - 51) Mosby, J.: Segregation of Particulate Solids: Processes, Mechanisms and Counteractions. Tel-Tek report no. 43003-2, 1994.
  - 52) Harris, J.F.G., Hildon, A.M.: Reducing Segregation in Binary Powder Mixtures with Particular Reference to Oxygenated Washing Powders. Ind. Eng. Chem. Process Des. Develop., Vol. 9, No. 3, (1970).
  - 53) Bagster, D.F.: The Influence of Cohesion on Segregation Patterns in Bins. Intern. Conf. Bulk Materials Storage and Handling and Transportation, Newcastle (1983), pp. 203-206.
  - 54) Shinohara, K.: Private communication.
  - 55) Bartolome, R.: Three-Dimensional Tester for Investigation of Heap Segregation. M. Sc. Dissertation Tel-Tek 1995.

## Author's short biography



### Jostein Mosby

Jostein Mosby obtained a diploma in Mechanical Engineering from Agder College of Engineering, Norway, and completed his Masters degree in Process Technology at Telemark College in 1991. He joined POSTEC Research A.S (now Telemark Technological R & D Centre's Dept. of Powder Science and Technology) immediately afterwards, and was later awarded a scholarship by the Norwegian Institute of Technology to undertake research for a Ph. D degree at Telemark College. This paper is based on the work carried out so far.



### Sunil R. de Silva

Sunil R. de Silva graduated in Chemical Engineering from the University of Technology, Loughborough, England, in 1967, which also awarded him a Ph. D in 1972 for a thesis entitled "The Transmission of Force through Particulate Systems with Restricted Geometry". After six years of research at the Universities of Karlsruhe and Clausthal, Germany, he served as Engineering Manager at Donaldson Europe in Belgium for another six years. In 1982 he joined the Powder Technology group at CMI in Bergen, Norway. In 1988 this facility was moved to Porsgrunn, Norway, and he became a visiting Professor at Telemark College and Managing Director of Powder Science and Technology Research A.S. When this company was integrated as a department of the Telemark Technological R & D Centre (Tel-Tek), de Silva became its Head. Since 1995, he has been a full professor at Telemark College. De Silva specialises in air classification, fluid energy grinding and pneumatic transport.



### Gisle G. Enstad

Gisle G. Enstad graduated in Fundamental Physics from the Norwegian Institute of Technology in 1971, and started his career as scientist at CMI, Bergen, in 1972, where he remained until the activities were moved to Porsgrunn. He was awarded a Dr.techn. degree by the Norwegian Institute of Technology for his thesis entitled "A Novel Theory on Arching and Doming in Mass Flow Silos" in 1981. In 1988 he was appointed Chief Scientist at Powder Science and Technology Research A.S., and continues to hold this post at Tel-Tek. Enstad specialises in powder mechanics, but has carried out, or supervised, projects in a variety of other areas such as electrostatic charging, mixing, tableting, segregation, and the design of silos. In 1992 he was appointed visiting professor in Powder Technology at Telemark College.

# A Review of Ceramic Powder Compaction<sup>†</sup>

D.E. Niesz

Center for Ceramic Research Rutgers,  
The State University of New Jersey\*

## Abstract

*The compaction behavior of ceramic powders is reviewed from the viewpoint of the factors involved and how these relate to green microstructure. The basis for the observed linear relationship between the logarithm of compaction pressure and relative density is discussed, and five generic types of compaction behavior are presented. The relation of granule properties to compaction behavior, green strength and green microstructure are discussed. Die friction, springback, die filling and green microstructure evolution are reviewed, and the needs for a better understanding of pressing are discussed.*

## 1. Introduction

Powder processing is the major technique for forming ceramic products, although vapor processes, chemical processes and melt processes are also important classes of ceramic fabrication technology. Of the numerous green forming techniques used in ceramic powder processing, pressing (die or isostatic) is the predominant technique used today because of its low cost, high speed and intermediate shape-forming capability. In recent years, however, little research has been conducted on pressing, while considerable research has been conducted on injection molding, colloidal processing and pressure casting. Currently, there has been a strong increase in the interest in pressing for two reasons. First, many large volume markets for structural ceramics such as automotive valves will only be realized if low cost parts can be manufactured, which probably will require pressing. The second factor is the demand for increased quality for products such as spark plugs that are formed by pressing and have been in production for many years. This will require a higher level of understanding of pressing science and technology.

The quality of the microstructure of a sintered powder compact depends strongly on the quality of the green compact, which in turn is determined by the behavior of powder during compaction. The compaction behavior of a powder is determined by the characteristics of the powder. Understanding the relationships among powder characteristics, compaction behavior, green microstructure, final microstructure and properties is critical to the manufacture of high

quality, low cost ceramic products to capitalize on potential markets.

This paper reviews ceramic powder compaction from the viewpoint of the factors involved and how these relate to green microstructure.

## 2. Basis for Pressure Density Relationship

In 1978 Whittemore<sup>(1)</sup> reviewed ceramic powder compaction. He cited work by Walker<sup>(2)</sup> in 1923 that noted a linear relationship between the logarithm of compaction pressure and the relative volume of the compact for several powders. He also cited Balshin's<sup>(3)</sup> work in 1938 which reported a similar compaction behavior and gave the following relation:

$$\ln P = AV + B \quad (1)$$

where  $P$  is the compaction pressure,  $V$  is the volume fraction of the powder in the die and  $A$  and  $B$  are empirical constants. He called  $A$  the pressing modulus and considered it analogous to Young's modulus. Several authors have noted the same relationship for loose<sup>(4)</sup>, precompacted<sup>(5)</sup> and spray dried<sup>(6)</sup> powders.

This relationship can be explained by the relationship between the compressive strength and porosity for brittle materials. In 1953, Ryshkewitch<sup>(7)</sup> showed that the relationship between compressive strength and porosity for alumina and zirconia was given by:

$$\ln S :: p \quad (2)$$

where  $S$  is the compressive strength and  $p$  is the volume fraction of porosity. Duckworth<sup>(8)</sup> noted that this relationship could be written as

$$S = S_0 e^{-bp} \quad (3)$$

\* Brett 4 Bowser Roads. P.O. Box 909, Piscataway,  
NJ 08855-0909 U.S.A

† Received 14 March, 1996

where  $S$  and  $S_o$  are the compressive strength and the calculated compressive strength of a nonporous body, respectively, and  $b$  is an empirical constant. Taking the logarithm of both sides gives

$$\ln S = \ln S_o - bp \quad (4)$$

Substituting  $(1-V)$  for  $p$ , gives

$$\ln S = b V + (\ln S_o - b) \quad (5)$$

If compaction pressure is substituted for compressive strength, this equation has the same form as Equation (1).

In 1959 Knudsen<sup>(9)</sup> showed that the logarithm of contact area of ideally packed spheres was proportional to the fractional theoretical density, as an assembly of spheres is densified by deformation at the contacts between spheres. Based on this result, he suggested that the relationship between the logarithm of compressive strength and porosity was a result of the semi-logarithmic relation of critical load bearing area (contact area between spheres) and porosity. If powder compaction is considered as a compressive test of an assembly of powder particles/granules, then it is reasonable to expect a semi-logarithmic relation between relative density and compaction pressure. More recently, Thompson<sup>(10)</sup> showed that applied pressure in powder compaction should be related to real contact area between particles in the compact, assuming no breakage of aggregates.

### 3. Types of Experimental Compaction Behavior

Experimental data show that powder compaction data for ceramic powders often show distinct pressure regimes, each of which shows a different linear relationship between the logarithm of compaction pressure and relative density. In these cases a different mechanism controls compaction in each region. Mort et al.<sup>(11)</sup> have reported an automated technique for generating compaction curves. Powders without aggregates that are not spray dried or granulated by other techniques show a linear compaction behavior on a plot of logarithm of pressure versus relative density from 0.1 MPa to 650 MPa<sup>(12)</sup> (**Figure 1, Curve 1**). In this case compaction is controlled by interparticle friction, which controls particle rearrangement. Powders containing aggregates that are weak enough to be fractured during compaction and are not granulated show a two-stage compaction curve on a similar plot. The first region is controlled by interparticle friction, and the second

region is controlled by the compressive strength of the aggregates (**Figure 1, Curve 2**)<sup>(4,12)</sup>. Aggregate fracture occurs at the contact points between aggregates where the local stress is very high and can exceed the compaction pressure by a factor of 100 or more. This is the type of compaction behavior exhibited by calcined ceramic powders that have not been reduced to their ultimate particle size, unless the aggregates are so strong that they do not show appreciable fracture during compaction. A typical metal powder also exhibits this type of compaction behavior, although the second region of the compaction curve is controlled by plastic yielding at the particle contacts<sup>(4)</sup> (**Figure 1, Curve 3**).

Spray dried ceramic powders typically show a three-stage compaction behavior<sup>(6)</sup> (**Figure 1, Curve 4**). Stages I, II, and III are each controlled by a different mechanism. The first stage is controlled by intergranule friction, which does not usually result in any significant compaction. The second stage begins when compaction begins to be controlled by plastic deformation and/or crushing at the granule contact points. This pressure is called the yield pressure<sup>(6)</sup>. During stage II, the compaction is primarily closing the intergranular pores. The slope of the compaction curve in stage II is the pressing modulus<sup>(13)</sup>. As compaction continues, the intergranular pores close, and the third stage of compaction begins. In this stage, compaction is controlled by interparticle friction within the granule relics as the intragranular porosity is removed. In this stage the compaction behavior is similar to that of the same powder-binder combination, if it had not been spray dried. A spray dried powder may show another stage which is controlled by fracture of powder aggregates, if the powder has not been reduced to its ultimate particle size and the aggregates are weak enough to show appreciable fracture during compaction (**Figure 1, Curve 5**). Further analyses of the above relationships are needed in order to improve product quality and manufacturing yields.

For spray dried powders, it is important to remove intergranular pores during pressing, since these pores are generally too large to be removed during sintering. Therefore, parts should be pressed in the stage III region. A transition region between stages II and III occurs because of imperfect packing of granules, a distribution in granule size, a hardness difference among granules or defects in granules such as hollow granules. As a result, intergranular pores close over a range of pressing pressures. As the number of remaining intergranular pores begins to

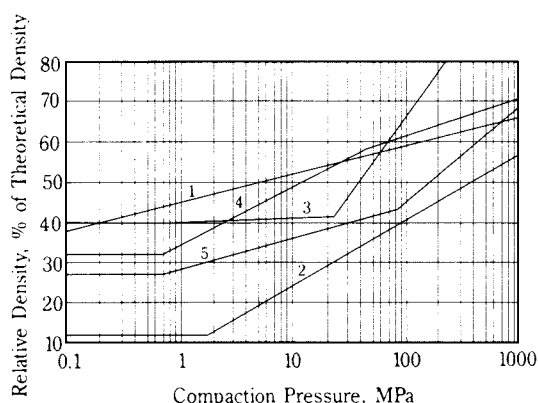


**Fig. 1** Generic shapes of compaction curves.  
*Curve 1*, powder without aggregates that has not been spray dried.  
*Curve 2*, powder containing aggregates which are weak enough to be broken during compaction and has not been spray dried.  
*Curve 3*, metal powder that exhibits plastic deformation at particle-particle contacts.  
*Curve 4*, spray dried powder without aggregates.  
*Curve 5*, spray dried powder that contains aggregates which can be broken during compaction.

decrease, the pressing curve begins to show a transition from stage II to stage III. Unfortunately, isolated intergranular pores can persist well into stage III. This presents a major challenge to the use of pressing as the green forming technique for structural ceramics such as silicon nitride automotive valves, where the cost advantage of pressing over other green forming techniques is critical to market penetration for this and similar components. Furthermore, the demand for increased quality presents similar challenges for products such as spark plugs, that are currently produced by pressing.

Commercial pressing is normally done in the early stage III region. Pressing further into stage III reduces the frequency of residual intergranular pores, but springback becomes more of a problem. Springback increases linearly with compaction pressure and density only increases with the logarithm of pressure. Two other reasons to press early in stage III are, first, that many pressing defects are caused by springback and, second, the capital cost and maintenance costs of presses and dies increase with compaction pressure.

#### 4. Selection of a Binder System

Selection of a binder system for a pressing powder depends on many factors<sup>(14)</sup>. Some of these are

- Granule plasticity and strength
- Green strength
- Green machinability
- Die friction
- Springback
- Spray drying behavior
- High speed pressing response
- Internal coefficient of friction
- Binder removal/residue

#### 5. Granule Properties

Ideally, spray dried granules should deform plastically to partially fill the intergranular pores and then fracture to assure knitting of particles across the granule-granule interfaces and to reduce the compaction pressure required to close the intergranular pores. Coupelle et al.<sup>(15)</sup>, Baklovti et al.<sup>(16)</sup> and Nebelung et al.<sup>(17)</sup> have studied the mechanical behavior of individual spray dried granules during compression between flat platens. Their results indicate that granules deform plastically until the binder system coatings on individual particles are extruded from between particle-particle contact points. The granules then fracture. If granules do not fracture, knitting at the interface generally does not occur. This compromises green strength and leaves low density planes in the green microstructure, especially if an external lubricant is used or if some binder migration occurs during spray drying. Fracture of granules also allows significant particle rearrangement which can reduce problems with residual intergranular pores. However, some amount of plastic deformation of granules is needed for high speed pressing to maintain the high permeability created by the large intergranular pores which allow rapid air removal in the early stages of pressing. Plastic deformation of granules also reduces density gradients caused by particle interlocking, such as that shown in radial compaction of solid or thick-wall cylinders.

The green strength required to allow parts to survive the manufacturing process up to firing is a major factor in binder selection. Some parts such as thin electronic substrates or capacitors require high green strength to avoid mechanical damage. Others such as spark plug blanks require little green strength, but must be compatible with green machining<sup>(18)</sup>. The percentage and type of binder, plasticizer and lubricant in the binder system must be tailored to these and other requirements. Where high green strength is required, a strong binder system is needed. This requires high pressing pressures to reach the stage III region and remove intergranular

pores. Where a low green strength is acceptable, a soft binder system can be used to achieve better compaction properties, since the stage III region can be reached at low pressing pressures. Spray drying slurries often contain a high percentage of solids to minimize the energy required for drying by minimizing the percentage of water to be removed. This can lead to granules with higher densities than what can be achieved in subsequent pressing. This guarantees residual intergranular pores<sup>(19,20)</sup>.

Several types of granulation other than spray drying have been used or are currently under development. These include drum pelletization, fluid bed granulation and freeze granulation. Pelletization produces granules that are hard due to their density, which makes intergranular pores difficult to eliminate. Mechanically agitated fluid beds are widely used in the pharmaceutical industry and are gaining wider acceptance in the ceramic industry. Nyberg et al.<sup>(21)</sup> reported that freeze granulation prevents binder migration to the outside of the granules which is often a problem in spray drying. This technique involves spraying a powder slurry into liquid nitrogen followed by freeze drying to remove the solvent. The authors claim that the cost of this process compares favorably with spray drying. This process is also reported to give higher quality, more uniform microstructure than can be achieved with spray dried powders. They conclude that the advantages result from the ability to design the density of granules, since the granule density is fixed by the percentage of solids in the starting slurry. Other advantages of this process are the ability to eliminate binder migration problems and the ease of preparing a granulated powder that is free from defects such as hollow granules, satellites and non-spherical granules, all of which are difficult to eliminate from spray dried powders. Thus, the granule properties can be designed to allow complete removal of intergranular pores during compaction.

## 6. Precompaction

One commonly used technique for increasing the fill density of a powder is to prepress and granulate the powder. This is a very effective technique for increasing the die fill density of the powder without spray drying. This reduces the compaction ratio (die fill density/pressed density), which helps reduce density gradients in green parts, allows for faster pressing speeds and allows thicker parts to be pressed in a die of a given size. Bruch<sup>(5)</sup> showed that

the final compaction pressure must exceed the prepressing pressure by a factor of about two to eliminate porous regions in the final sintered part. These porous regions are caused by residual pores between the granules of the prepressed and granulated powder. These are analogous to residual intergranular pores in compacts pressed from spray dried powders and are generally too large to be removed during sintering.

## 7. Die Friction

Die friction is a key problem in die pressing of ceramic powders and is the major cause of density gradients in die-pressed parts<sup>(13)</sup>. In combination with springback, it is also the cause of many of the common defects in die pressed parts<sup>(13)</sup>. Strijbos<sup>(22)</sup> studied die friction and concluded that slippage occurs within the powder (powder failure stress) rather than between the powder and the die wall (die wall failure stress), since the particle size of the powder is typically less than the asperities in the surface finish of the die. However, for carbide dies with a smooth surface finish and a powder containing a good binder-lubricant system, slippage probably occurs between the powder and the die wall, at least at low pressures. As the surface finish of the die deteriorates due to wear, slippage between the powder and the die wall becomes less likely.

Thompson<sup>(23)</sup> showed that end capping originates from the restraint of elastic springback when the punch pressure is released. He considered three terms: length/diameter ratio, powder fluidity index and the coefficient of friction at the die wall. The powder fluidity index is the ratio of the radial/axial stress at the die wall. For a fluid, this ratio is one. For ceramic powders, it depends on the internal coefficient of friction of the powder/binder system. Thompson concluded that addition of an internal lubricant to the powder may increase or decrease the die wall friction force. This results from the increase of the powder fluidity index as the internal coefficient of friction is decreased through the addition of a lubricant. Therefore, the increase in the radial force may more than offset the reduction in the friction coefficient. Another technique for reducing end capping and other defects caused by springback is to incorporate a hold-down pressure in the pressing cycle. This involves maintaining a large percentage of the pressing pressure on the part during ejection from the die. Modern presses are designed to provide a hold-down pressure.

External lubricants are often added to spray dried powders to reduce die friction. Internal lubricants are added to the slurry before spray drying and are distributed on the surfaces of the powder particles throughout the granules. However, external lubricants such as stearates are added to the powder after spray drying and coat only the external surfaces of the granules. Since the surface area of the granules is only a fraction of the surface area of the powder, a very small percentage of lubricant is needed to significantly reduce die wall friction. Only the lubricant on the granule surfaces that contact the die wall is effective. However, it has the same effect as lubricating the die wall between each pressing, which is not possible in high speed pressing. Often, if the internal binder system contains enough lubricant to produce the low die wall friction desired, the binder system requires such a high percentage of lubricant that pressing speed must be compromised due to die sticking problems.

## 8. Springback

Springback in dry pressing is a result of stored elastic energy in the part at the compaction pressure and may also result from trapped air. Differential springback within a part must also be considered, since it can result in pressing defects. The stored energy is usually the sum of several components. The contributing components can be separated into those caused by the organic components and those caused by the inorganic components. The organic components typically have both an elastic and a viscoplastic (time-dependent plastic) component. The contribution of the organics to total springback may be the dominant factor, since the elastic modulus of the organics is considerably less than that of the inorganic components<sup>(24)</sup>. However, the elastic strain stored in the organic components may not be fully recovered, since the recovery force may not be high enough to overcome the constraining force caused by interlocking of the inorganic particles and their adhesion from the binders or other forces. Since the binders may make a major contribution to springback, the binder system is designed to have a glass transition temperature below the pressing temperature<sup>(25-27)</sup>. This makes the binder behave as a liquid rather than a solid and substantially reduces springback caused by the organic components. However, springback still increases with the percentage of organics in the powder. For high speed pressing, it is important to recognize that the glass

transition temperature of a polymer is strain-rate dependent. If sufficient time is not allowed for stress relaxation by viscous flow at the pressing pressure, the binder will behave as an elastic solid rather than a viscous liquid and significantly increase springback.

The springback, due to elastic energy stored in the inorganic constituents, can be minimized by using spherical particles with a high elastic modulus. Sharp corners, non-equiaxed particles and porous aggregates all increase springback. Every particle can be viewed as a miniature spring. Contact points in the compact that involve sharp corners experience a higher stress and, therefore, a higher stored elastic strain than spherical contacts. Another reason powders with sharp corners exhibit high springback is that they increase particle interlocking, and interlocking particles can act like porous aggregates. Porous aggregates increase springback for two reasons. First, they act like particles with a significantly lower elastic modulus than dense particles, because the bridges at the particle-particle contacts in the aggregate may have a cross-sectional area that is only a fraction of that of the particles themselves. The second reason is that they store a significant strain in bending. This becomes much more significant as the shape deviates from equiaxed. Platy particles such as clay or talc, fibrous particles and non-equiaxed particles are also major contributors to springback, since these shapes can store a large amount of strain in bending.

As compaction begins, the powder contains considerable void space filled with air. The air must either escape from the die or be compressed, and this must be taken into account in designing the pressing cycle. Powder permeability, die clearance, green-body size, pressing speed/cycle and binder type/percentage all affect air removal that can cause defects during removal or on pressure release. Some dies are designed with vacuum ports to allow faster pressing without encountering defects due to trapped air. In designing the pressing cycle, it should be remembered that air removal is a function of volume reduction and not pressure. Therefore, air removal considerations are critical in the low pressure portion of the pressing cycle. Many pressing cycles are designed with one or two pressure relief cycles to enhance air removal.

## 9. Die Filling

Die filling is a critical part of a pressing cycle. Once the die is filled, the final compact microstructure

is relatively fixed. High speed pressing cycles usually include withdrawal of the bottom punch as the die is filling to speed filling and to avoid air pockets or air channels during the die fill. Since most cycles fill by volume rather than weight, it is critical to reproduce the fill density from part to part and from point to point throughout the die. This requires a reproducible granule density and granule size distribution in the spray dried powder. Even with a uniform spray dried powder, any size segregation in the powder during delivery to the press or in die filling will result in point-to-point or part-to-part variation in fill density and lead to density variation in the pressed part. Modern presses are designed to eliminate size segregation, since spray dried powders are very susceptible to this problem.

## 10. Green Microstructure Evolution

In order to understand how the microstructure of a powder compact develops during pressing, fracture and as-pressed surfaces can be examined using a scanning electron microscope after pressing at a sequence of pressures. These microstructures can be used along with the compaction curve, powder characteristics, the microstructure of the sintered sample and mechanical properties of the material to better understand how to fabricate a quality material. **Figures 2** and **3** show the pressed surfaces and fracture surfaces, respectively, for a high alumina porcelain composition which was spray dried by the manufacturer and pressed at several pressures. The pressed surfaces in **Figure 2** shown the progressive deformation and fracture of granules as the com-

paction pressure is increased. It also shows that isolated intergranular pores persist to very high pressures. Uematsu et al.<sup>(28)</sup> developed an excellent technique for direct observation of internal voids in green bodies. They infiltrated green bodies with a fluid that has a small mismatch in index of refraction with the powder. This makes the green body almost transparent, but voids throughout the body are visible. The intergranular pores are exaggerated in **Figure 2** by the fact that the boundary conditions are different adjacent to the die plunger than inside the compact. However, the wide variation of intergranular pore closure pressures is clearly shown. **Figure 3** shows fracture surfaces from compacts of the same powder. These clearly show the deformation and fracture of the granules. Although it is not possible to tell whether the granules fractured on pressing or on fracture, whole granules tend to pull out of the fracture surface if they did not fracture and knit across intergranular boundaries during compaction.

## 11. Conclusions

Much is known about ceramic powder compaction, but much more needs to be understood if it is to be used to produce the high quality, low cost ceramic products that are needed to develop markets for new products and provide the improved quality demanded for current products.

Many defects in the final microstructure can be traced to the green microstructure. Residual pores caused by hard or defective spray dried granules or by intergranular pores due to incomplete compaction in

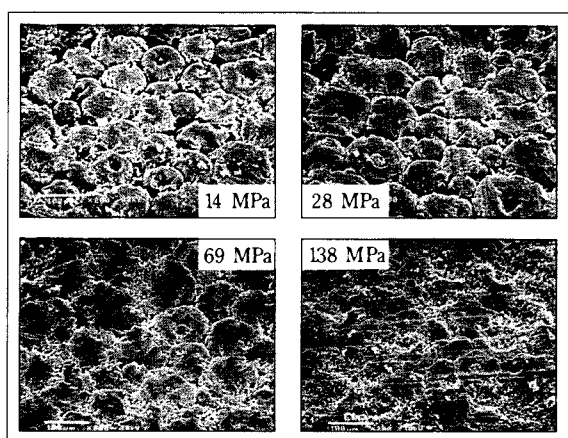


**Fig. 2** Scanning electron microscope views of the as-pressed surface after pressing at four pressures, of a 96% alumina porcelain which was commercially spray dried.

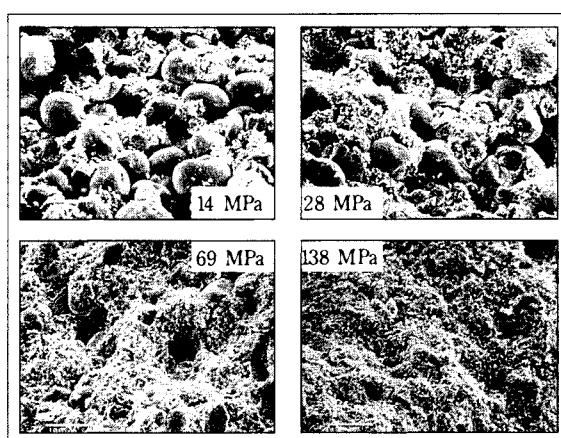


**Fig. 3** Scanning electron microscope views of the fracture surface, after pressing at four pressures, of a 96% alumina porcelain which was commercially spray dried.

isolated locations in the part are a problem. These pores are generally too large to be removed during sintering and cause defects in the final microstructure. More needs to be known about the origin of these pores and how to avoid them.

Another key problem is density variation within parts and among parts, since this affects both part quality and the ability to achieve tight dimensional tolerances. Die wall friction is a key reason for density variations, but the powder fluidity index is also important, since a low internal coefficient of friction helps reduce powder bridging that also causes density variation. Improved lubricants are needed to reduce the coefficient of friction both at the die wall and within the powder. A better quantitative understanding of the factors that affect differential shrinkage is also needed, since dimensional tolerances are also affected by differential shrinkage.

Springback is another area where a better understanding is needed. A quantitative understanding of the factors that affect springback is needed, since the combination of springback, die friction, green strength and the pressing cycle all interact to dictate defects in pressed parts. One factor that has not been given enough attention is the visco-plastic or time-dependent plastic properties of organic additives. The visco-plastic properties of an organic additive may cause the binder to behave very differently in high speed pressing where strain rates become very high and relaxation times very short compared to laboratory pressing trials.

Much can be learned by application of finite element analysis to powder compaction<sup>(29)</sup>. With the computing capability now available, finite element analysis integrated with a strong experimental compaction program should lead to the major advances in the quantitative understanding of powder compaction that are needed to improve the quality of ceramic components formed by powder compaction.

## Bibliography

### A Review of Ceramic Powder Compaction

- 1) Wittemore, O. J., Jr., "Particle Compaction," pp. 343-355 in *Ceramic Processing Before Firing*, Edited by G. Y. Onoda, Jr. and L. L. Hench, John Wiley and Sons, Inc., New York, NY, 1978.
- 2) Walker, E.E., "The Compressibility of Powder," *Trans. Faraday Soc.*, **19**, 73 (1923).
- 3) Balshin, M.Y., "The Theory of the Process of Pressing," *Vestnik Metalloprom*, **18** [2] 124-37 (1938).
- 4) Niesz, D.E., Bennett, R.B. and Snyder, M.J., "Strength Characterization of Powder Aggregates," *Am. Ceram. Soc. Bull.*, **51** [9] 677-80 (1972).
- 5) Bruch, C.A., "Problems in Die-Pressing Submicron Size Alumina Powder," *Ceram. Age*, **83** [10] 44-53 (1967).
- 6) Lukasiewicz, S. J. and Reed J. S., "Character and Compaction Response of Spray-Dried Agglomerates," *Ceram. Soc. Bull.*, **57** [9] 798-805 (1978).
- 7) Ryshkewitch, E., "Compression Strength of Porous Sintered Alumina and Zirconia - 9th Communication to Ceramography," *J. Am. Ceram. Soc.*, **36** [2] 65-68 (1953).
- 8) Duckworth, W., "Discussion of Ryshkewitch Paper," *J. Am. Ceram. Soc.*, **36** [2] 68 (1953).
- 9) Knudsen, F. P., "Dependence of Mechanical Strength of Brittle Polycrystalline Specimens on Porosity and Grain Size," *J. Am. Ceram. Soc.*, **42** [8] 376-87 (1959).
- 10) Thompson, R. A., "Mechanics of Powder Pressing: III, Model for the Green Strength of Pressed Powders," *Am. Ceram. Soc. Bull.*, **60** [2] 248-51 (1981).
- 11) Mort, P. R., Sabia, R., Niesz, D. E. and Riman, R.E., "Automated Generation and Analysis of Powder Compaction Diagrams," *Powder Technology*, **79** 111-19 (1994).
- 12) Niesz, D. E. and Bennett, R. B., "Agglomerate Structure and Properties," pp. 61-73 in *Ceramic Processing Before Firing*, Edited by G.Y. Onoda, Jr. and L. L. Hench, John Wiley and Sons, Inc., New York, NY, 1978.
- 13) Reed, J. S., *Principles of Ceramic Processing*, Second Edition, John Wiley & Sons, Inc., New York, NY, 1995.
- 14) Shanefield, D. J., *Organic Additives and Ceramic Processing*, KLUWER Academic Publishers, Boston, MA, 1995.
- 15) Coupelle, P., Destermes, J., Miglioretti, F., and Baumard, J. F., "Behavior of Spray-Dried Granules Under Compression Testing," pp. 453-58 in *Euroceramics II*, Vol. 1, Edited by G. Ziegler and H. Hausner, deutsche Keramische Gesellschaft, Köln, 1992.
- 16) Baklouti, S., Coupelle, P., Chartier, T., and Baumard, J.F., "Uniaxial Pressing of Spray-Dried Alumina Agglomerates," pp. 271-75 in *Ceramic Processing Science and Technology*, Edited by H. Hausner, G.L. Messing and S. Hirano, *Ceram. Trans.*, Vol. 51, The Am. Ceram. Soc., Westerville, OH, 1995.
- 17) Nebelung, M., Schubert, J. and Linder, T., "Complex Characterization of Ceramic Granules Processed by Spray Drying or Fluidized BED Granulation," Fraunhofer Establishment for Ceramic Technologies and Sintered Materials, Dresden, Germany, Paper C04-12 presented at the Third Conference of the European Ceramic Society, Madrid, Spain, 12-17 September, 1993.
- 18) Kennard, F. L., "Ceramic Component Fabrication," *Ceram. Eng. Sci. Proc.*, **7**, 1095-111 (1986).
- 19) Zheng, J. and Reed, J.S., "Particle and Granule Parameters Affecting Compaction Efficiency in Dry Pressing," *J. Am. Ceram. Soc.*, **71** C-456 - 458 [11] (1988).
- 20) Takahashi, H., Shinohara, N., Okumiya, M., Uematsu, K., Junichiro, T., Iwamoto, Y. and Kamiya H., "In-

- fluence of Slurry Flocculation on the Character and Compaction of Spray-Dried Silicon Nitride Granules," J. Am. Ceram. Soc., **78** [4] 903-08 (1995).
- 21) Nyberg, B., Carlström, E. and Carlsson, R., "Granulation of Ceramic Powders for Pressing by Spray-Freezing and Freeze-Drying," pp. 447-51 in Euro-Ceramics II, Vol 1, Basic Science and Processing of Ceramics, Edited by G. Ziegler and H. Hausner., Deutsche Keramische Gesellschaft, Köln, 1993.
  - 22) Strijbos, S., "Phenomena at the Powder-Wall Boundary During Die Compaction of a Fine Oxide Powder," Ceramurgia International, **6** [4] 119-22 (1980).
  - 23) Thompson, R.A., "Mechanics of Powder Pressing: II, Finite- Element Analysis of End-Capping in Pressed Green Powders," Am. Ceram. Soc. Bull., **60** [2] 244-47 (1981).
  - 24) Novak, S. and Spino, J., "The Influence of Processing Additives on the Compaction Behavior of Spray Dried  $\text{Al}_2\text{O}_3$ ," Seventh Cimtec World Ceramics Congress, Montecatini Terme, Italy, June 24-30, 1990.
  - 25) DeMilia, R.A. and Reed, J.S., "Dependence of Compaction on the Glass Transition Temperature of the Binder Phase," Am. Ceram. Soc. Bull., **62** [4] 484-88 (1983).
  - 26) Nies, C.W. and Messing, G.L., "Binder Hardness and Plasticity in Granule Compaction," *Advances in Ceramics*, **9** 58-66 (1984).
  - 27) Nies, C.W. and Messing, G.L., "Effect of Glass-Transition Temperature of Polyethylene Glycol-Plasticized Polyvinyl Alcohol on Granule Compaction," J. Am. Ceram. Soc., **67** [4] 301-04 (1984).
  - 28) Uematsu, K., Kim, J.Y., Miyashita, M., Uchida, N. and Saito, K., "Direct Observation of Internal Structure in Spray-Dried Alumina Granules," J. Am. Ceram. Soc., **73** [8] 2555-57 (1990).
  - 29) Mahoney, F.M. and Readey, M.J., "Applied Mechanics Modeling of Granulated Ceramic Powder Compaction," Submitted for publication in the Proceedings of the 27th International SAMPE Technical Conference, Albuquerque, NM, October 9-12, 1995.

### Author's short biography



#### Dale E. Niesz

Dale Niesz obtained a bachelor of science (cum laude), a master of science, and a doctor of philosophy degrees in Ceramic Engineering from The Ohio State University in 1962, 1963 and 1965, respectively. He spent 22 years in contract research at Battelle Columbus Laboratories, where he served as a research engineer, manager of ceramic research and manager of materials research. He joined Rutgers, The State University of New Jersey, in 1987 as a Professor in the Department of Ceramic Engineering. He currently serves as Director of the Center for Ceramic Research and Chair of the Department of Ceramic Engineering.

Professor Niesz is a Past President and Distinguished Life Member of the American Ceramic Society and Past President of the National Institute of Ceramic Engineers. He is a charter member of the Academy of Ceramics and Vice President of the International Ceramic Federation.

His principal research area is the relationships among powder characteristics, processing parameters, microstructural development and properties of technical ceramics. He has over 100 technical publications, presentations and major technical reports on a broad range of research topics.

# Classification of Particles in the Submicron Range in an Impeller Wheel Air Classifier

Kurt Leschonski  
Technical University Clausthal\*

## Abstract

*It is the aim of this paper to show that it is possible in principle to obtain submicron cut sizes with a counterflow centrifugal classifier, provided that a forced vortex is used in the classification chamber and the circumferential velocities are greater than 100 m/s. These findings can be generalized and are not limited to the geometrical dimensions of the classifier used in the experiments. With a new impeller or deflector wheel classifier, cut sizes as small as 0.3  $\mu\text{m}$  have been obtained with feed mass flow rates of 5 kg/h and higher.*

## 1 Introduction

The production of particle size distributions with top sizes of 1  $\mu\text{m}$  or even less is one of the most difficult tasks in the mechanical processing of powders. With comminution and classification in this size range, the separation of the particles from the flow and even the measurement of the size distributions produced demand principles and designs which have to be operated near or at their limits [1].

It appears that with minerals a natural size limit of approximately one micrometer seems to be stipulated by the physical laws which govern the above processes. Problems arising in the classification of fine particles are mainly due to the fact that gravity forces become negligible and stochastic particle movement caused by diffusion or Brownian motion and turbulence of the flow may become predominant. Fine particles follow the drag forces exerted by the flow more readily and it becomes more and more difficult to move the particles in directions which deviate from the direction of the flow. The choice of a size limit of approximately one micrometer is not arbitrary, although depending on the material, the size limit varies. The systematic movement of a particle in a flow, described by its trajectory, is governed by its stationary settling rate,  $w_g$ , in the gravity field. The most important forces controlling the systematic particle movement are, for example, drag force, gravity force, dynamic lift, inertia and electrical forces. The different classifier principles are defined by the main forces used and the principal movement of the coarse particles with respect to

the flow. If the removal of the coarse particles takes place against the flow, the classifier uses the counterflow principle. If the coarse particles travel perpendicular to the flow, the classifier is called a cross-flow classifier [2].

## 2 The Counterflow Principle

A gravity counterflow classifier [3] consists of a vertical tube of, for example, cylindrical cross-section. The air rises in the tube. On each individual flow line, a particle is taken to the top of the tube that is removed with the flow if its stationary settling rate,  $w_g$ , is smaller than the air velocity,  $v_a$ . It settles in the rising flow if its settling rate is greater. The so-called cut size is defined by:

$$v_a = w_{gc} = \frac{\rho_p g x_c^2}{18\eta} \quad (1)$$

The cut size, at least theoretically, does not leave the classification zone, because its exit velocity equals zero. In actual operation, cut size particles are distributed evenly to the fine and the coarse fraction, and are therefore sometimes called the equiprobable particles. Due to their small settling rates, gravity counterflow systems are unsuitable for small cut sizes. These demand a counterflow centrifugal system, the basic principle of which is shown in **Figure 1** [4]. It consists of a flat cylindrical classification zone of height  $H$ . Air is introduced at the periphery under a certain angle, thus inducing a free vortex sink flow passing through the classification zone on a spiral path (flow line). The feed particles enter the classification zone near the outer periphery. Fine particles follow the flow towards the centre while coarse particles remain

\* Institut für Mechanische Verfahrenstechnik, Leibnizstr. 19  
D - 38678 Clausthal-Zellerfeld, Germany

† Received: 4 July, 1996

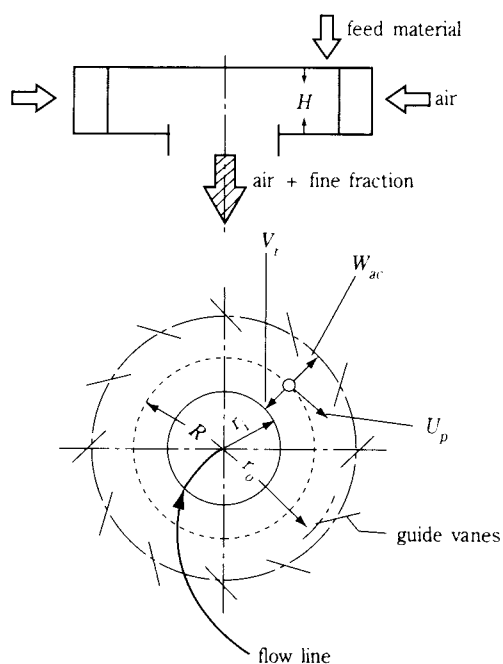


**Fig. 1** Principle of a counterflow centrifugal classifier or spiral classifier

near the outer periphery and must be withdrawn from there. The cut size, however, travels in the classification zone on a circular path. It remains, at least theoretically, in the classification zone. A radial force balance yields the basic equation for pre-calculation of the cut size,  $x_c$ , or its stationary settling rate,  $w_{gc}$ :

$$w_{ac} = v_r = w_{gc} \frac{a}{g} = w_{gc} \frac{r\omega^2}{g} = w_{gc} \frac{v_\varphi^2}{rg} \quad (2)$$

According to Eqn. 2, the radial velocity component of the air,  $v_r$ , equals the settling rate of the particles in the centrifugal field,  $w_{ac}$ . The latter exceeds the stationary gravity settling rate by the acceleration ratio,  $a/g$ . If the particle travels on a radius of  $r = 0.1$  m with a circumferential velocity of  $v_\varphi = 100$  m/s, the ratio of centrifugal acceleration,  $a$ , to gravity constant,  $g$ , becomes ten thousand, thus increasing the stationary settling rate considerably.

It is a well-known fact that counterflow centrifugal classifiers operated under the above or similar conditions have a lower cut size limit of approximately  $1 \mu\text{m}$  to  $2 \mu\text{m}$  for mineral particles. The production of even finer cut sizes demands:

- higher circumferential velocities,  $v_\varphi$ , of the air and of the particles, respectively, than those used up until today,
- a reduction of the volume flow rate of air, or the size of the classifier,
- operating the classifier at reduced air pressures using the so-called slip between the particles and the gas molecules.

## 2.1 Lower Cut Sizes Due to Increased Slip Between the Particles and the Gas Molecules

If the size of the particles settling in a gas becomes small in comparison to the scale of the molecular processes in the gas—for example, the mean free path of the gas molecules—the non-continuity of the gas becomes apparent and a slip of the gas adjacent to the particle surface may occur. This slip leads to the so-called Cunningham correction,  $Cu$ , which is equal to the ratio of the true terminal velocity to the terminal velocity in continuum flow.

The mean free path of the gas molecules can be calculated from:

$$\bar{\lambda} = \frac{kT}{\pi \sqrt{2} d_m^2 p} \quad (3)$$

With the Boltzman constant:  $k = 1.3804 \cdot 10^{-23}$  Nm/K, the temperature:  $T$ (K), the diameter of the molecules:  $d_m = 3.7 \cdot 10^{-10}$  m (air), and the gas pressure:  $p$ (Pa) one obtains:

$$\bar{\lambda} / \mu\text{m} = 22.7 \frac{T / \text{K}}{p / \text{Pa}} \quad (4)$$

The Cunningham correction may be calculated from Eqn. 5, first proposed by M. Knudsen and S. Weber [5] in 1911 and corrected by C.N. Davies [6] in 1945 with respect to their numerical constants:

$$Cu = 1 + \frac{2\bar{\lambda}}{x} \left\{ 1.257 + 0.4 \exp\left(-\frac{0.55x}{\bar{\lambda}}\right) \right\} \quad (5)$$

Introducing Eqn. 4 into Eqn. 5 yields Eqn. 6, where  $T$  has to be introduced in K,  $p$  in Pa and  $x$  in  $\mu\text{m}$ :

$$Cu = 1 + \frac{45.4T}{xp} \left\{ 1.257 + 0.4 \exp\left(-0.024229 \frac{xp}{T}\right) \right\} \quad (6)$$

It is convenient to plot  $Cu$  as a function of the product  $xp$  in  $\mu\text{mPa}$ , with the temperature,  $T$ , as the parameter. **Figure 2** shows that the Cunningham correction starts to rise as soon as the product  $xp$  becomes smaller than  $xp = 10^5 \mu\text{mPa}$ , or if the particle size drops to  $1 \mu\text{m}$  at 1 bar air pressure. If the product of particle size and pressure drops by a factor of 100, the Cunningham correction rises from  $Cu = 1.167$  at  $xp = 10^5 \mu\text{mPa}$  to  $Cu = 22.62$  at  $xp = 10^3 \mu\text{mPa}$ .

Y. Yamada, S. Doi and K. Iinoya [7] have described experiments performed with a counterflow centrifugal air classifier at a reduced pressure. The classifier was installed together with its ancillary equipment, for example, its feeder, etc. in a special tank and

operated at reduced pressure. The batch experiments were performed at a mass flow rate of 2.2 kg/h and a solids loading of  $\mu = 0.03$ . The experiments proved the expected shift in the cut size to finer particle sizes. In **Figure 3**, the cut size is plotted against pressure,  $p$ , in the classification chamber for two conditions:  $v_\varphi = 100$  and 50 m/s and  $v_r = 0.5$  m/s in both cases. One realizes that only a pressure reduction below approximately 0.2 bar leads to an effective reduction of cut size. The cut size drops from approximately 0.9  $\mu\text{m}$  or 1  $\mu\text{m}$  at 1 bar to approximately 0.35  $\mu\text{m}$  at 0.0921 bar.

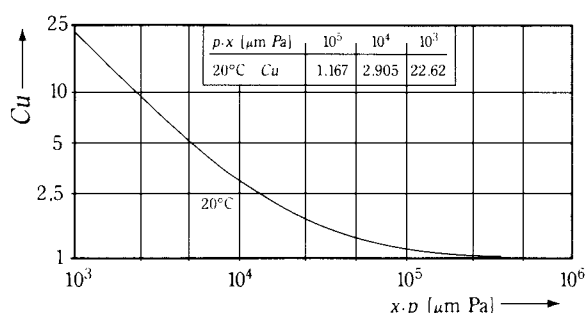


Fig. 2 Cunningham-correction :  $Cu = f(xp)$

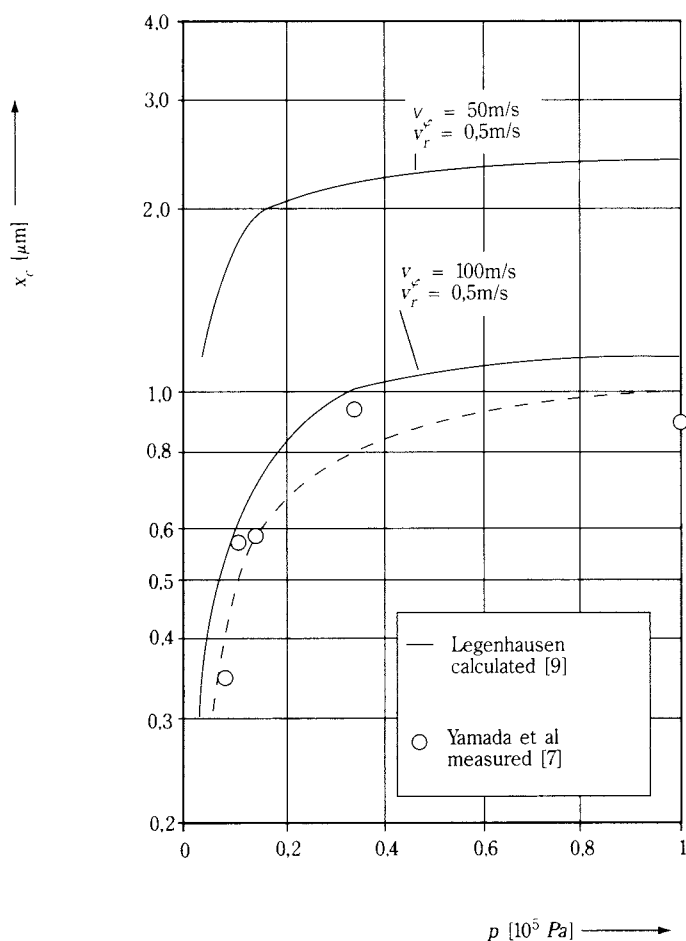


Fig. 3 Cut size =  $f$ (pressure)

Y. Yamada and his colleagues state [7] that the reduced pressure air classification still has many problems, the most important of which are the continuous operation, problems of dispersing the extremely fine feed materials and the low mass flow rate of solids.

## 2.2 Lower Cut Sizes at Higher Circumferential Air Velocities and in Smaller Classifiers

In a counterflow centrifugal classifier the cut size is defined by Eqn. 2. If one introduces the stationary settling rate of a spherical particle [7]:

$$\bar{w}_{gc} = \frac{\rho_p g x_c^2}{18\eta} \quad (7)$$

into this equation one obtains:

$$x_c v_\varphi = \sqrt{\frac{18\eta}{\rho_p}} \sqrt{v_r r} = \sqrt{\frac{18\eta}{\rho_p}} \sqrt{\frac{\dot{V}}{2\pi H}} \quad (8)$$

One realizes from Eqn. 8 that for a given flow rate of air and a given classifier size, the product of the cut size and circumferential speed,  $x_c v_\varphi$ , remains constant. With limestone particles of  $\rho_p = 2710 \text{ kg/m}^3$  and air of 20°C, the product  $x_c v_\varphi$  equals:

$$x_c v_\varphi = 3.4673 \cdot 10^{-4} \sqrt{v_r r} \quad (9)$$

**Figure 4** shows the dependence represented by Eqn. 9. The lower curve shows the range of cut sizes obtainable if the product  $v_r r = 0.1 \text{ m}^2/\text{s}$ , the second if  $v_r r = 0.01 \text{ m}^2/\text{s}$ .

Cut sizes below 1  $\mu\text{m}$  demand high circumferential velocities of the air and small products of  $v_r r$ , i.e. small classifiers and low radial velocities. With  $v_r r = 0.01 \text{ m}^2/\text{s}$ , a cut size of 1  $\mu\text{m}$  demands a circumferential air velocity of 110 m/s. Halving the cut size to 0.5  $\mu\text{m}$  doubles the circumferential air velocity. Therefore, depending on the conditions chosen, extremely high circumferential velocities may be necessary to obtain small cut sizes.

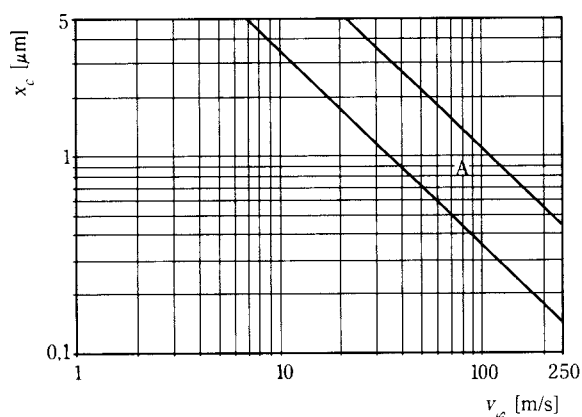


Fig. 4  $x_c = f(v_\varphi)$  and  $v_r r$

A further reduction of the cut size of a counterflow centrifugal classifier can only be obtained if the size of the classifier ( $r$ ) or the radial velocity component ( $v_r$ ) is reduced. However, due to the fact that the air can only carry a limited amount of particles, a certain mass throughput demands a certain flow rate of air. Therefore, if a certain volume flow rate of air and a certain radial velocity component have to be used because of:

$$\dot{V} = 2\pi r H v_r \quad (10)$$

the product  $r$  times  $H$  has to remain constant. If one intends to reduce the size or rather the radius,  $r$ , of the classifier, either the height,  $H$ , has to be increased or more than one classifier has to be used.

The above estimates also show that with small cut sizes, the ratio of radial to circumferential velocities,  $v_r/v_\varphi$ , i.e. the slope of the flow lines, becomes very small. The angle is of the order of 0.3 to 0.5 degrees, virtually impossible to obtain with a free vortex as used in ordinary spiral classifiers.

This problem can be overcome, however, by the introduction of a special impeller wheel into the centre of the classification zone. These impellers consist of a rotor with a series of radial blades at their outer periphery. **Figure 5** shows the set-up used in many cases of application.

At present, these deflector or impeller type wheel classifiers use maximum circumferential speeds of approximately 100 m/s to 120 m/s. They could be used, in principle, with higher speeds of rotation. However, the design of these rotors would then have to be changed for high-speed performance. This line of thinking has up until now not been pursued in actual practice, mainly because the power consumption of these high-speed systems may become high unless special design criteria have been fulfilled [9-11].

K. Legenhausen [9,10] showed in the investigation of flow patterns in a deflector wheel classifier that the flow pattern in the bladed area consists of a superposition of a forced vortex and a sink flow. In actual practice, however, this flow pattern can only be obtained if the flow approaching the outer periphery of the rotor has the same velocity as the tips of the rotor. Only then can vortices be avoided which form within the converging channels between the rotor blades. Under ideal conditions, the radial flow between the rotating blades runs parallel to the rotor blades, as shown in the centre of **Figure 6**. Due to small radial velocities and the dimensions of the channel, the flow is laminar.

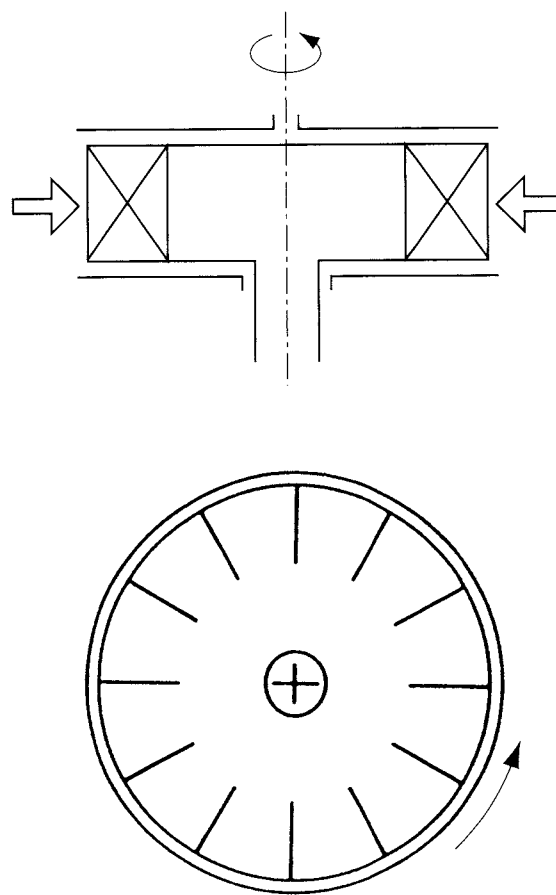


Fig. 5 Impeller classifier

In the investigation of the flow patterns in deflector wheel classifiers, K. Legenhausen [9,10] also found that the flow in the centre of the rotor, i.e. the bladeless zone, changes from a forced vortex into a free vortex flow or a flow with friction.

If one assumes the above flow fields, the course of the radial and the circumferential flow velocities with radius,  $r$ , in the outer zone and the inner zone of the impeller rotor can be introduced into Eqn. 8 in order to pre-calculate the course of the cut sizes with respect to the radius of the classification zone.

With:

$$v_r r = \text{constant} \quad (11)$$

and:

$$v_\varphi r^{-1} = \text{constant} \quad (\text{forced vortex}) \quad (12)$$

one obtains:

$$x_c = \sqrt{\frac{18\eta r_o^3 V_{ro}}{\rho_p v_{\varphi o}^2}} \frac{1}{r} \quad (13)$$

The cut size rises in a forced vortex spiral flow inversely proportionally to the rotor radius,  $r$ .

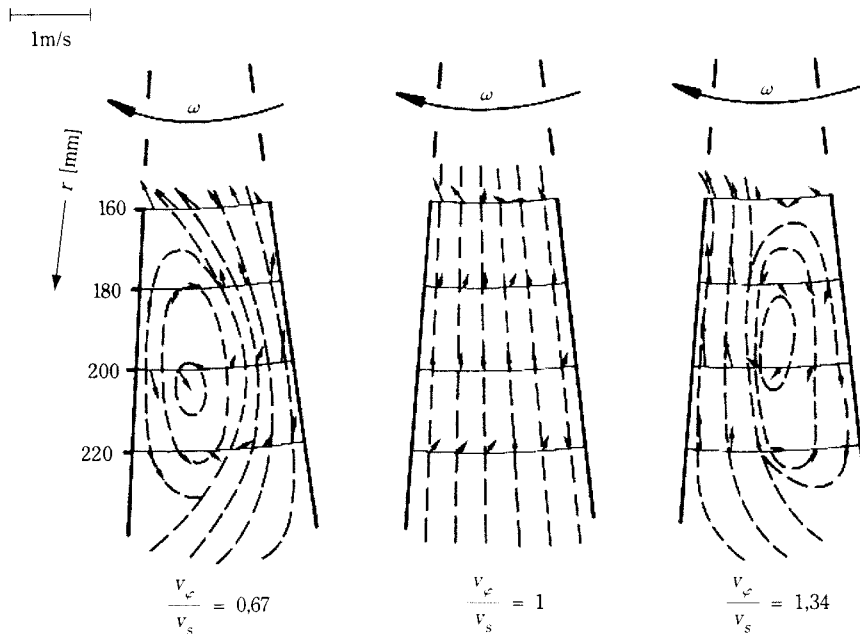


Fig. 6 Flow patterns with different  $v_\phi/\omega r$ -ratios

If, on the other hand, as observed in the inner bladeless zone of the rotor, the flow in circumferential direction follows a free vortex flow, one obtains Eqn. 15, because of:

$$v_\phi r = \text{constant} \quad (\text{free vortex}) \quad (14)$$

$$x_c = \sqrt{\frac{18\eta v_{ri}}{\rho v_{\phi i}^2 r_i}} r \quad (15)$$

In a free vortex spiral flow, the cut size rises linearly with radius,  $r$ .

One therefore obtains the situation as shown in **Figure 7**. The cut size rises from a given value at the outer periphery to a larger value at the inner blade radius. It then drops linearly to the centre of the rotor.

H. Rumpf and K. Leschonski [3] pointed out in 1967 in the investigation of a counterflow gravity classifier that a high sharpness of cut can only be obtained and a hold-up of small particles in the classification zone can only be avoided if the cut size in the direction of flow always increases.

If a deflector wheel is used with blades at the outer

periphery and a bladeless inner zone, this condition cannot be met, as can be seen from **Figure 7**. The cut size rises, as intended, within the zone with blades but drops again in the bladeless zone. Particles which passed the outer periphery of the rotor may therefore find a new equilibrium radius at smaller radii. These particles cannot, at least theoretically, be removed

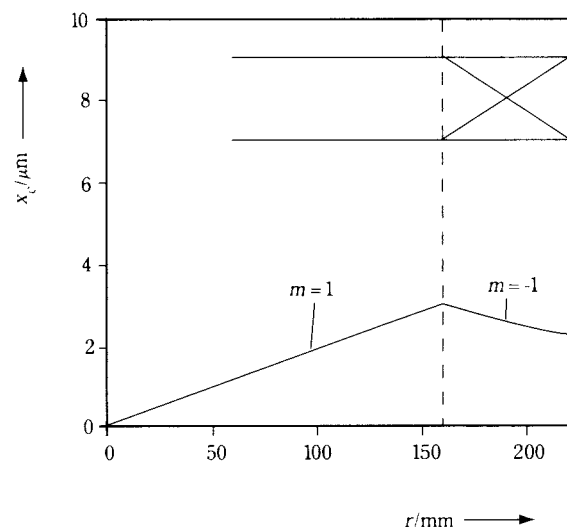


Fig. 7  $x_c = f(r)$  with  $v_\phi$  depending on  $r$  according to  $v_\phi r^m = \text{const.}$

from the classification zone. In order to avoid this situation, the removal of the fines together with the air should take place immediately behind or near the inner rotor blade edges [6]. This can either be achieved by using long rotor blades, extending to the center of the rotor, and a central fines outlet, or shorter blades and an annular withdrawal section at the inner blade radius. Avoiding the free vortex in the centre also results in an appreciable reduction of the pressure drop of the classifier.

### 3 Description of the Clausthal High-Speed Classifier

Based on the flow field measurements and earlier classification experiments, a high speed impeller wheel classifier was developed by the author and J. Galk and investigated in J. Galk's thesis [12]. **Figures 8 and 9** show sectional views of the classifier.

The high-speed rotor (**Figure 8**) consists of two circular discs, made from a special aluminium alloy. To lower the eigenstresses caused by high speeds of rotation, carbon-fibre-reinforced plastic rings are mounted at the outer periphery of the discs. The maximum speed of the rotor is 250 m/s [12].

The radial rotor blades are mounted in radial grooves cut into the plane surfaces of the discs. As shown in the cross-sectional view of **Figure 9**, only 16 long blades extend to the centre, i.e. the outer radius of the outlet. An additional 80 short blades, five of which are arranged between two long blades, guarantee the desired flow field, described in the centre of **Figure 6**.

The classifier air is fed into the classification zone at its outer periphery through three small rectangular channels, arranged tangentially. At least one of these channels is also used for the introduction of the feed particles with a special feeding and dispersion unit. Fine particles leave the central outlet together with the air. The coarse ones are collected at the inner periphery of the housing (**Figure 8**) and are removed from there through tangential outlets (**Figure 9**).

### 4 The Feeding and Dispersion Unit

In order to achieve cut sizes in air classifiers in the submicron range, a number of further prerequisites have to be fulfilled. Firstly, the feed material has to be dispersed in an air flow with the largest agglomerates presented to the classification zone being smaller than the desired cut size. Only then will the amount of particles smaller than the cut size

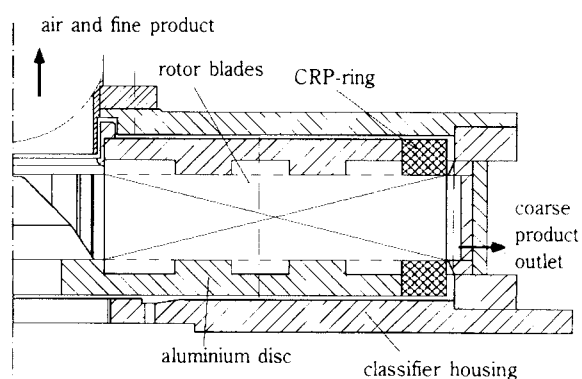


Fig. 8 Sectional view of the Clausthal Impeller Wheel Classifier

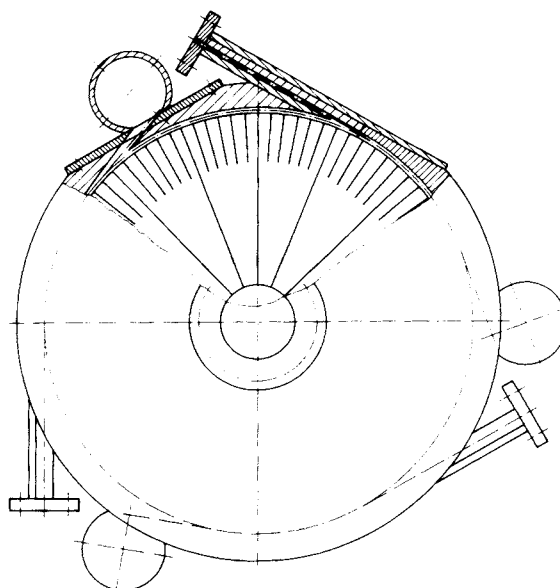


Fig. 9 Top view of the Clausthal Impeller Wheel Classifier

in the coarse fraction be small or even negligible and a high fine particle yield be obtained. Secondly, as the sharpness of cut and the cut size of an air classifier depend on the solids loading of the air, the mass flow rate of the feed material should vary as little as possible [14].

For the dispersion of the feed material in the air used for the classification process and the acceleration of both particles and air up to the circumferential speed of the rotor, a combination of a newly developed brush feeder and an injector is used [14,15]. The unit is shown in **Figure 10**. It consists of the feeding unit on the right and the dispersion unit on the left-hand side. Air is passing through both units from right to left. The rotating brush (1) receives the feed material from a small hopper (2). The feed material enters the voids between the bristles, is transported to the feeding point (3) and is then released into the incoming air travelling past the feeding point. The brush acts similarly to a rotary

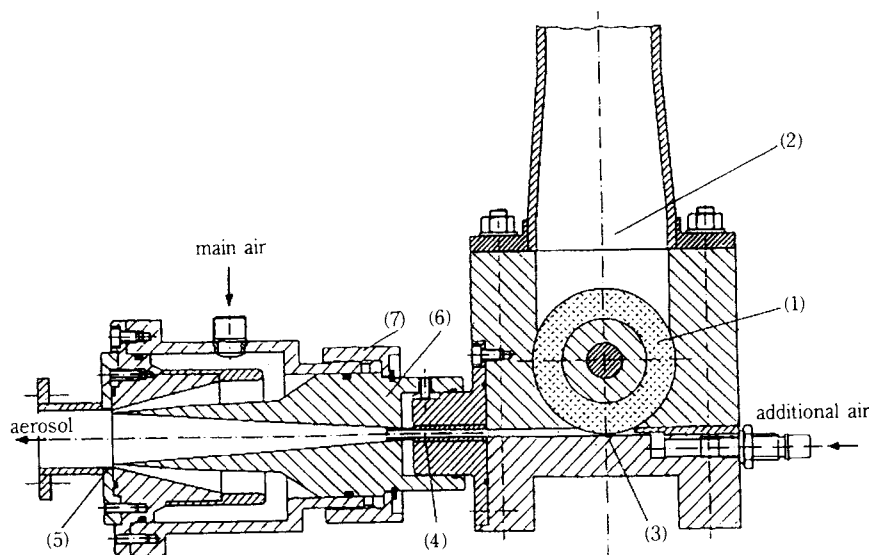


Fig. 10 The Clausthal feeding and dispersing unit

vane feeder, controlling the throughput of particles by means of its speed of rotation, while producing a constant mass flow rate with little fluctuation. The brush also acts, depending on its speed of rotation, as a pre-dispersing unit.

The pre-dispersed feed material then enters the dispersing and accelerating zone of a special injector. The dispersion of agglomerates in the turbulent high-speed zone (5) of an injector has been described by K. Leschonski, S. Röthele and U. Menzel in 1984 [13] and by K. Leschonski, B. Benker and U. Bauer in 1995 [14, 15]. It has been shown that the feeding and dispersion unit of **Figure 8** is suitable for dispersing feed materials with particles smaller than  $1 \mu\text{m}$ .

## 5 Experimental Data as Obtained with the Classifier

The development and the theoretical and experimental investigation of the Clausthal impeller or deflector wheel classifier has been performed mainly by J. Galk [12, 16] and at present by U. Bauer in their PhD theses. Some of the most recent grade efficiency curves obtained with the new classifier are shown in **Figure 11** and **12**.

The feed material was limestone with a median particle size of  $x_{50.3} = 1.2 \mu\text{m}$  and a maximum particle size of approximately  $4.2 \mu\text{m}$ . The grade efficiency curves given in **Figure 11** were obtained with a radial velocity of the air of  $v_{r0} = 1 \text{ m/s}$  and circumferential rotor velocity of  $v_{\phi 0} = 100, 150, 175$  and  $200 \text{ m/s}$ , respectively, at the outer rotor periphery. The cut size that is the median of the grade efficiency curve moves from  $1.3 \mu\text{m}$  to  $0.65 \mu\text{m}$ ,  $0.33 \mu\text{m}$  and  $0.28 \mu\text{m}$  at the highest circumferential

velocity. The grade efficiency curves were obtained at a feed mass flow rate of approximately  $5 \text{ kg/h}$ .

These experiments show that it is possible to obtain submicron cut sizes with a counterflow centrifugal

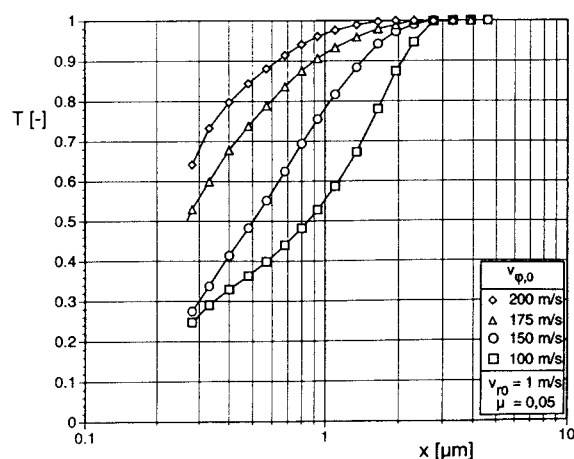


Fig. 11 Grade efficiency curves, variation of circumferential rotor velocity

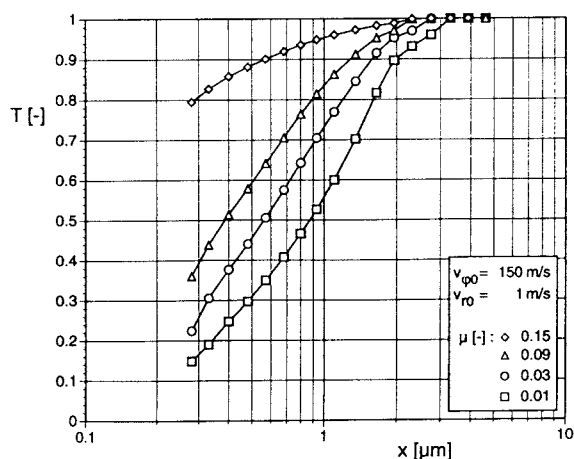


Fig. 12 Grade efficiency curves, variation of solids loading

classifier, provided that a forced vortex is used in the classification chamber and the circumferential velocities are greater than 100 m/s. These findings can be generalized and are not limited to the geometrical dimensions of the classifier used in the experiments.

The grade efficiency curves were calculated from laser diffraction measurements of all three products using the method proposed by H. Hermann and K. Leschonski [17] in 1979.

**Figure 12** shows the grade efficiency curves obtained with different solids loadings, i.e. different feed mass flow rates. With a radial velocity of  $v_{r0} = 1$  m/s and a circumferential rotor velocity of  $v_{\varphi 0} = 150$  m/s, the solids loading altered from  $\mu = 0.01$  to 0.03, 0.09 and 0.15. The grade efficiency curves shift to smaller cut sizes and the sharpness of cut decreases. It is the aim of the ongoing research to reduce the mass flow rate influence.

## 6. Acknowledgement

Thanks are due to the Deutsche Forschungsgemeinschaft (DFG), Bonn-Bad Godesberg, for sponsoring part of the published work.

## Symbols

$a$	acceleration, subscript: air	$\text{m/s}^2, -$
$c$	subscript: cut size	$-$
$Cu$	Cunningham correction	$-$
$d$	diameter	$\text{m}$
$g$	gravity constant, subscript: gravity	$\text{m/s}^2, -$
$H$	height of classification chamber	$\text{m}$
$k$	Boltzmann constant	$\text{Nm/K}$
$m$	subscript: molecular	$-$
$O$	subscript: outer periphery	$-$
$p$	pressure, subscript: particle	$\text{Pa}, -$
$r$	rotor radius	$\text{m}$
$r$	subscript: radial	$-$
$T$	absolute temperature, grade efficiency	$\text{K}, -$
$v$	velocity	$\text{m/s}$
$V$	volume flow rate	$\text{m}^3/\text{s}$
$w$	settling rate	$\text{m/s}$
$x$	particle size, equivalent diameter	$\text{m}$
$\eta$	viscosity	$\text{Pas}$
$\lambda$	mean free path	$\text{m}$
$\mu$	solids loading	$-$
$\varphi$	subscript: circumferential	$-$
$\rho$	density	$\text{kg/m}^3$
$\omega$	angular velocity	$1/\text{s}$

## References

- 1) Leschonski, K.: Air Classification, Recent Developments and Results, Proc. 2nd World Congress Particle Technology, Part III, Kyoto, Japan, September 19-22, 91-103 (1990)
- 2) Rumpf, H. and Leschonski, K.: Prinzipien und neuere Verfahren der Windsichtung, Chem.-Ing.-Techn. 39 (1967) 1231-1241
- 3) Leschonski, K. and Rumpf, H.: Principle and Construction of Two New Air Classifiers for Particle Size Analysis, Powder Technology 2 (1968/69) 175-185
- 4) Rumpf, H.: Über die bei der Bewegung von Pulvern in spiraligen Luftströmungen auftretende Sichtwirkung, Thesis, University Karlsruhe, 1939
- 5) Knudsen, M. and Weber, S.: Molekulare Wärmeleitung der Gase und der Akkomodationskoeffizient, Ann. Physik 36(1911) 981-994
- 6) Davies, C.N.: Definitive Equations for the Fluid Resistance of Spheres, Proc. Phys. Soc., London 57 (1945) 259-270
- 7) Yamada, Y. and Doi, S. and Inoya, K.: Powder and Bulk Solids (1987) 215-220
- 8) Leschonski, K.: The Classification of Particles in the Micron and Submicron Range, Proceedings Process and Product Requirements in Particle Technology, PARTEC 1992, Nürnberg, (1992) 11-38
- 9) Leschonski, K. and Legenhausen, K.: Flow Patterns in a Deflector Wheel Classifier, Proc. 2nd World Congress Particle Technology, Part III, Kyoto, Japan (1990) 198-205
- 10) Legenhausen, K.: Untersuchung der Strömungsverhältnisse in einem Abweiseradsichter, Thesis, Technical University Clausthal, 1991
- 11) Leschonski, K.: Verfahren und Vorrichtung zum Spiralwindsichten in Sichern mit beschauelten Rotoren, DP 4025458
- 12) Galk, J.: Feinsttrennung in Abweiseradsichtern, Thesis, Technical University Clausthal, 1995
- 13) Leschonski, K. and Röthele, S. and Menzel, U.: A Special Feeder for the Diffraction Pattern Analysis of Dry Powders, Part. Charact. 1 (1984) 161-166
- 14) Leschonski, K. and Benker, B. and Bauer, U.: Dry Mechanical Dispersion of Submicron Particles, Proc. PARTEC 95, 6th European Symp. Particle Charact. Nürnberg, (1995) 247-256
- 15) Leschonski, K. and Benker, B. and Bauer, U.: Dry Mechanical Dispersion of Submicron Particles, Part. Syst. Charact. 12(1995) 295-298
- 16) Galk, J. and Leschonski, K. and Legenhausen, K.: Air Classification with a Centrifugal Counterflow Classifier, Proc. 1st Int. Particle Technology Forum, Denver, USA, Part III (1994) 392-397
- 17) Herrmann, H., Leschonski, K.: Einfluß und Berücksichtigung von Fehlern der Partikelgrößenanalyse bei der Ermittlung von Trennkurven, Proc. 2nd Europ. Symp. Particle Characterization, Nürnberg (1979) 41-58

## Author's short biography



**Kurt Leschonski**

*Research:*

Particle characterisation; measurement techniques in twophase flow systems; impact grinding; classification (sieving, air classification); separation (wet scrubbers, inertia separators); sorting (recycling of waste materials). (150 publications).

*Education:*

Dipl. – Ing. (Mechanical Engineering), Technical University Braunschweig, 1957

Dr. – Ing. (Particle Technology), Technical University Karlsruhe, 1965

*Professional Experience:*

*Chief Engineer* at the Department of Particle Technology (Institut für Mechanische Verfahrenstechnik), Technical University Karlsruhe, (1957-1971)

*Visiting Reader*, Department of Chem. Engineering, Univ. of Technol., Loughborough, UK, (1968/69)

*Full Professor* and Head of Department of Particle Technology, (Institut für Mechanische Verfahrenstechnik) Technical University Clausthal (1971 –);

*Dean* of Faculty of Mechanical and Process Engineering (1978/81);

*Prorektor* and *Rektor* of the Technical University of Clausthal (1983/87);

*Managing Director* of the Clausthal Environmental Institute (CUTEC-Institute) (Ltd. Comp.) (1990 –).

# Electrostatic Manipulation of Bioparticles<sup>†</sup>

Masao Washizu

Kyoto University, Department of Mechanical Engineering\*

## Abstract

*In conventional biotechnology, bioparticles, such as cells or DNA are treated as uniform suspensions or solutions, and one can neither specify a particular particle, nor a particular position on the particle. On the other hand, recent advances in micromachining have enabled the fabrication of  $\mu\text{m}$ -scale structures, which, in combination with appropriate bioparticle manipulation method, is expected to introduce "spatial resolution" to the biotechnology, where individual bioparticles are handled in more efficient and automated manner. The author's group has been engaged in the development of electrostatic micromanipulation of bioparticles in micro-fabricated structures, using dielectrophoresis, electrostatic orientation, electrorotation, etc. as the actuation principle. This article summarizes our experimental results on cell and DNA manipulation/processing, together with the theoretical background.*

## 1. Introduction

The unit of life is biological cells, the size of which ranges from  $1\mu\text{m}$  of bacteria up to  $100\mu\text{m}$  of animal and plant cells. This small particle, enclosed by a cell membrane, contains a set of apparatus for metabolism and self-replication. The interior of the cell membrane, cytoplasm, is not a uniform solution; functional units supported by membranes and/or cytoskeltons form ordered structures for optimal performances. Molecular recognition and reactions are realized through contour-fitting of enzymes to respective substrates. The physical parameters, such as the position and the orientation of an enzyme and the substrate, and the molecular alignments for successive chain reactions, are the important factors for the efficiency and the yield of the reaction.

On the other hand, in conventional biotechnology, particles of interest, for instance cells, organelles, bio-molecules, bio-membranes, etc. (hereafter called "bioparticles"), have been treated as uniform suspensions or solutions. Here, one can neither specify a particular particle in the suspension, nor a particular position on the particle. In other words, the conventional methods lack "spatial resolution".

A typical example is seen in the DNA sequencing. The genetic information is recorded on a one-dimensional array as the sequence of four bases, A, T, C

and G, which are stacked between the sugar-phosphate backbones. The kind of the base as a function of molecular position is the entity of the information. However, we presently have only indirect and limited access to the "address" of a particular base in the total strand. For instance, the electrophoretic method, based upon the mobility analysis, determines the base-sequence of a DNA fragment with up to several hundred base-pairs (bps). But when the specimen is longer, as is usually the case, it must be cut into smaller fragments prior to the assay, at which instance the positional information is lost. We only have "relative address" in a strand of several hundred bps, not the "absolute address". As a result, the sequence of the longer fragment has to be inferred from those of the cut fragments making use of overlaps, but the process is time-consuming and becomes increasingly difficult as the number of fragments increases.

The recent advances in nanometer-scale technology, such as the scanning probe microscopes and the ultra-high sensitivity fluorescent imaging, have motivated explorations into dynamics of biological molecules in space- and time-domain, the field sometimes referred to as "nano-biology". Here again, the position of and in a molecule is one of the most important parameters in the biophysical description of the molecular interactions.

The development of bioparticle manipulation techniques will be a key in both investigations and applications of the next generation biotechnology. Handling

\* Sakyoku, Kyoto 606-01, Japan  
phone/fax: +81-75-753-4752, e-mail: washizu@mech.kyoto-u.ac.jp

<sup>†</sup> Received 16 July, 1996

of cells or biomolecules on one-by-one bases will enable unit-operations such as single cell surgery, dissection of individual chromosomes and DNA, in an efficient and automated manner.

Bioparticles size from  $\mu\text{m}$  down to nm, and they are usually soft and fragile. Most of them have to be maintained in water solution in order to maintain their biological activities. Observations are made under an optical microscopes, with the objective lens having only mm working distance, usually through a cover slip. Hence mechanical manipulators often have very limited access. An inverted microscope provides free water surface, but fluid motion hampers precise manipulations. Another problem with a mechanical manipulator is its limited force controllability for the handling of very fragile object, such as single DNA strand. Biomanipulation requires special devices with special methods of actuation.

Our approach to realize space-resolved manipulation of bioparticles uses electrostatic effects in microfabricated systems (**Figure 1**). The microfabrication techniques based on photolithography, originally developed for electronics circuit fabrications, provide methods to fabricate  $\mu\text{m}$ -scale structure of arbitrary 2-dimensional shape, which can be piled to form semi-3-dimensional structures. Transparent structures can be obtained not only by the use of originally transparent materials, e.g. glass or  $\text{SiO}_2$ , but also by the replication using plastics or silicon resin. Adsorption of biomaterials can be controlled by proper surface treatments.

The use of electrostatic force is known to be effective for controlling small particles. In addition, it is highly compatible with microfabricated systems. It basically requires no moving parts, and only conducting and insulating surfaces are to be fabricated. When flexibility in motion is required, laser-manipulations

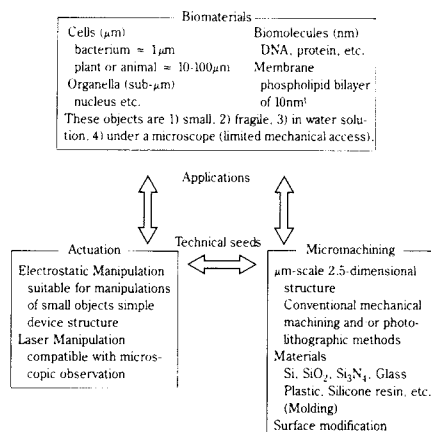


**Fig. 1** Technical seeds for bioparticle manipulations

may be used in addition to electrostatic effects.

This article reviews the principle of bioparticle manipulation together with our R&D efforts on its applications in the past 10 years.

## 2. The principle of the electrostatic biomani- pulation

Because the bioparticles are in aqueous solution, the electrophoretic effect is not suitable for their manipulations in microfabricated structures. The application of d.c. or low-frequency voltage causes electrochemical reactions on the electrodes, and the resultant bubbles, temperature rise, turbulent flow, and ionic species destroy particle motion, or the bioparticles themselves. The conventional electrophoresis chamber is equipped with buffering areas in which electrodes are immersed, so that chemical reactions occur in a distant area and does not affect the analyte. This kind of approach cannot be taken in microfabricated devices. Coating of the electrode with insulating material does not provide a solution, because it blocks the electrostatic field. The only way to avoid the chemical reaction is the use of high-frequency a.c. voltage, by which the capacitive voltage drop at electrode/water interface can be lower than theoretical dissociation voltages. This prohibits the use of electrophoretic effects, because the particles undergo oscillatory motion under a.c. field and does not result in net motion.

Several a.c. field effects which can be used for bioparticle manipulations are depicted in **Figure 2**. The pioneering work in this field is by H.A. Pohl, who named "dielectrophoresis" and showed its applications for characterization and separation of cells [1]. Dielectrophoresis (DEP, **Figure 2 a**) is a non-uniform field effect that induces translational motion of an electrically neutral particle along the field gradient. Under an electrostatic field, a particle

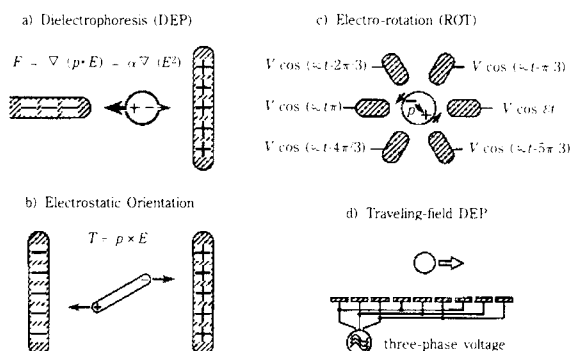


**Fig. 2** a.c. field effects for bioparticle manipulation

polarizes, and equal amount of positive and negative charge appears on the downstream and upstream side of the field lines. When the field is uniform, the force exerted on these positive and negative charges cancel each other. On the other hand, when the field is non-uniform, a net force appears as the difference of these two forces.

Mathematically, the force  $\mathbf{F}_d$  exerted on a dipole under an external field  $\mathbf{E}(r)$  is given by

$$\mathbf{F}_d = q \mathbf{E}(\mathbf{r} + \mathbf{d}) - q \mathbf{E}(\mathbf{r}) = (\mathbf{p} \cdot \nabla) \mathbf{E}(\mathbf{r}) \quad (1)$$

where  $q$ : charge,  $\mathbf{d}$ : separation between positive and negative charge,  $\mathbf{p}$ : the induced dipole moment  $\mathbf{p} = q \mathbf{d}$ . For the case where the dipole moment is induced by the external electrostatic field and is proportional to the field intensity, i.e.  $\mathbf{p} = \alpha \mathbf{E}$  where  $\alpha$  is polarizability of the particle, eq.(1) becomes

$$\mathbf{F}_d = \alpha/2 \nabla (E^2) \quad (2)$$

This equation states that the particle is driven to where the field is stronger or weaker, depending upon the polarity of  $\alpha$ .

For a particle in dielectric liquid, one has to be careful about the interpretation of  $q$  in eq.(1).  $q$  should be the “equivalent charge”, the virtual free (mobile) charge which would give rise to the same field distribution in fluid if the particle is replaced with the virtual charge [2]. For the case of a particle immersed in a homogeneous liquid,  $q$  is given by  $q = (\epsilon_m/\epsilon_0) q_{\text{total}}$ , where  $q_{\text{total}}$  is the total charge, the sum of the free and the polarization charge;  $q$  is different from the total charge itself.

When a spherical particle with radius “ $a$ ” is under the influence of the external sinusoidal field with the peak amplitude  $\mathbf{E}_0$ , the equivalent induced equivalent dipole moment can be calculated analytically, and becomes

$$\mathbf{p} = 4\pi a^3 \epsilon_m K(\omega) \mathbf{E}_0 \quad (3)$$

Hence the force on the dipole, i.e. the DEP force  $\mathbf{F}_{\text{dep}}$ , is given by

$$\mathbf{F}_{\text{dep}} = \pi a^3 \epsilon_m \text{Re}[K(\omega)] \nabla (E_0^2) \quad (4)$$

where

$$K(\omega) = \frac{\epsilon_p^* - \epsilon_m^*}{\epsilon_p^* + 2\epsilon_m^*}, \quad \epsilon_p^* = \epsilon_p - j \frac{\sigma_p}{\omega}, \quad \epsilon_m^* = \epsilon_m - j \frac{\sigma_m}{\omega} \quad (5)$$

and  $\epsilon_p, \sigma_p, \epsilon_m, \sigma_m$ : permittivities and conductivities of the particle and the medium,  $\omega$ : angular frequency of the applied field,  $j$ : the imaginary unit, and  $\text{Re}[\ ]$  denotes the real part. The quantity  $\epsilon^* = \epsilon - j \sigma/\omega$  is called the complex permittivity. Eq.(4) states that, if the particle is more polarizable than the medium and  $\text{Re}[K(\omega)] > 0$ , the DEP force acts toward where the field is stronger, and if the particle is less polarizable and  $\text{Re}[K(\omega)] < 0$ , the force is towards where the field is weaker. The former is termed positive DEP, and the latter negative DEP. For bioparticles, the positive DEP is more often observed experimentally than the negative.

**Figure 2 b)** shows the electrostatic orientation. This effect occurs for electrically non-symmetrical particles, such as non-spherical particles. The torque  $\mathbf{T}$  is given by the cross product of the dipole moment and the field

$$\mathbf{T} = \mathbf{p} \times \mathbf{E} \quad (6)$$

It is known that, with the careful choice of electrical parameters, one can align non-spherical particles with any of its three principal axis parallel to the field [2], however, the most often observed orientation of high aspect-ratio particles is with the longest axis parallel to the field. When the object is flexible string-like fiber, the electrostatic orientation occurs in every part of the fiber, so that the fiber is stretched straight along the field lines.

**Figure 2 c)** is the electrorotation [4]. Under a rotating field, the rotating dipole is induced on a particle. If the frequency of the field rotation is faster than the relaxation time of the system, the induced dipole delays, and the torque is exerted on the particle. The mathematical expression for the torque in a circularly polarized field of the amplitude  $E_0$ , where

$$E_x = E_0 e^{j\omega t}, \quad E_y = E_0 e^{j(\omega t - \pi/2)} \quad (7)$$

can be obtained from eqs.(3) and (6), and is

$$T_z = -4\pi a^3 \epsilon_m \text{Im}[K(\omega)] E_0^2 \quad (8)$$

where  $\text{Im}[\ ]$  denotes the imaginary part. The torque is proportional to the imaginary part of  $K(\omega)$ , because it is related to the phase delay of the induced dipole.

A traveling field, as depicted in **Figure 2 d)**, has the potential distribution in the form of

$$\phi = \phi_0 \exp(-k y) \cos(k x - \omega t) \quad (9)$$

and hence the electrostatic field

$$E_x = k \phi_0 \exp(-k y) \sin(k x - \omega t) \quad (10)$$

$$E_y = k \phi_0 \exp(-k y) \cos(k x - \omega t) \quad (11)$$

propagates towards positive  $x$  direction. This field is a non-uniform field with  $\nabla(E^2)$  in negative  $y$  direction, and at the same time, it is a rotating field when seen at a fixed point. Therefore, a particle in this field is subject to both the DEP and the electrorotational torque. The torque is given by eq.(8), however, the DEP force is not satisfactorily predicted by eq.(4). Eq.(4) accounts for the in-phase components of the polarization only, not for the out-phase component resulting from the phase delay. The full form of the DEP force and the torque for the traveling field is [5],

$$F_x = -4 \pi a^3 \varepsilon_m k \operatorname{Im}[K(\omega)] E_0^2 \quad (12)$$

$$F_y = -4 \pi a^3 \varepsilon_m k \operatorname{Re}[K(\omega)] E_0^2 \quad (13)$$

$$T_z = -4 \pi a^3 \varepsilon_m \operatorname{Im}[K(\omega)] E_0^2 \quad (14)$$

$$\text{where } E_0^2 = [k \phi_0 \exp(-k y)]^2 \quad (15)$$

$F_y$  is the conventional DEP force direction of which depends upon the polarity of  $\operatorname{Re}[K(\omega)]$ , while  $F_x$  is the conveyance force along the field propagation which is proportional to  $\operatorname{Im}[K(\omega)]$ . Therefore, a particle can be transported with the use of a traveling field [5].

The above theory is based on the assumption that the charge distribution induced on a spherical particle is approximated by a dipole moment. This is not always the case. For instance, when the particle is located at the center of a quadrupolar field (**Figure 3**), no dipole moment is induced because it has a  $180^\circ$  symmetry. Instead, the induced charge distribution is represented by a quadrupole. It has been shown that, in this case also, the force is proportional to  $\nabla(E^2)$  and the particle is driven either to where the field is stronger or to where it is weaker, depending upon the relative polarizability of the particle with respect to the medium. The force for arbitrary field distribution in fact is given by the superposition of the dipole, quadrupole, octupole, etc. terms, however, in reality, except for the case when the particle is at a field null as in **Figure 3**, or when the field has higher-order non-uniformity, the dipole term dominates the phenomenon. The explicit force and

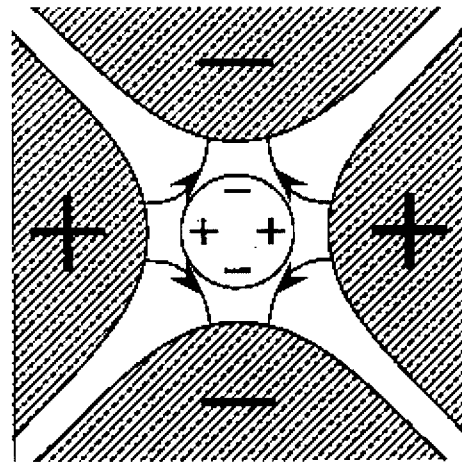


**Fig. 3** A particle in a quadrupole field

torque expression for arbitrary multipole moment is given in ref.[7].

Because the electrostatic potential  $\phi$  satisfies the Laplace equation,  $\phi$  takes a maximum or a minimum only on the boundaries, such as on the electrode surface. This means that, with Coulombic force a charged particle cannot be held in space without contact to the wall. On the other hand,  $E^2$  cannot take a maximum in space, but can take a minimum. The quadrupolar field of **Figure 3** is the typical example, where  $E^2 = \text{minimum} = 0$  at the center. Using the negative dielectrophoresis, a particle can be levitated here. The use of negative DEP also allows the suspension of particles against gravity in a traveling field, so that the particles can be transported smoothly along the field propagation.

All effects in **Figure 2** result from the interaction between the externally applied field and the dipole moment induced by the field. When the a.c. field alternates its direction, the induced moment also alternates, and the direction of the force or the torque remains unchanged. They are independent on the electrical charge the particle carries, and are equally effective in d.c. or a.c. field.

By using these effects under a high-frequency field, bioparticles in water can be attracted to or repelled from the electrode (DEP), aligned (electrostatic orientation), rotated (electrorotation), or transported (traveling field DEP), without being bothered by electrochemical reactions.

The factor that sets a limit to the smallest particle size that can be actuated by the field effect is the thermal randomization. Integrating eq.(4) and equating with  $kT$ , one can estimate the threshold field strength  $E_{th}$  to overcome the thermal randomization,

$$1/2 \propto E_{th}^2 = kT \quad (16)$$

**Figure 4** plots the threshold field strength for various particle size, for the case of  $Re[K(\omega)] = 1$  and 0.1. The electrostatic field of the order of  $10^3 - 10^4$  V/m, required for the DEP of biological cells having  $1 - 10 \mu\text{m}$  diameter is easily obtainable with the conventional mm-sized electrodes, say parallel wire electrodes. For typical biological macro-molecules with the diameter of several ten nm, such as protein, the required field strength is of the order of  $10^7$  V/m. Such a high field strength is not obtainable with mm-electrodes, because of 1) the impractical voltage requirement ( $10^4$  V to create  $10^7$  V/m field across 1 mm gap), and 2) the temperature rise due to Ohmic dissipation. On the other hand,  $\mu\text{m}$ -scaled microfabricated electrode system realizes the field strength with modest power supply, and because the high field region is  $\mu\text{m}$ -scale, it has large surface to volume ratio, and the generated Joule heat can easily be diffused, so that the temperature rise can be limited to practical level. Microfabrication is the prerequisite for molecular DEP. The microfabricated device in which bioparticles are manipulated using the electrostatic field effects is sometimes referred to as “Fluid Integrated Circuit (FIC)” [9].

### 3. Examples of the biomanipulation

#### 3.1 Cell manipulation

In **Figure 5** are shown some of the FIC cell manipulation devices. **Figure 5 a)** is the FIC cell fusion device [9], which is intended to produce one-to-one hybrid among two types of cells. One cell, say of type A, and another of type B, are fed by micro pumps (not shown in the fig.) to respective inlets. The inlets lead to fluid channels separated by an insulator wall, except at a small opening made at the center of the electrodes. When high-frequency voltage is applied between the electrodes, the field lines converges to this opening, and the field intensity becomes maximum here. Each cell sent from respective inlet is dielectrophoretically trapped into this opening to form a cell pair A-B. Then the fusion is initiated by applying a pulsed voltage. This procedure ensures that the fusant is exclusively one-to-one hybrid among cell A and B.

**Figure 5 b)** is the FIC device for cell storage, positioning, transport and delivery. The device is made up with a periodical structure of insulator walls and electrodes. First, a high frequency voltage is applied between the electrodes #2 and #4 in the

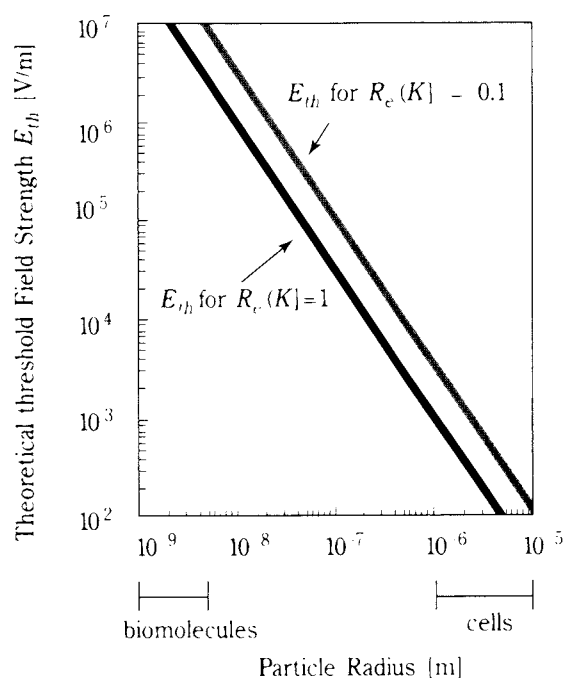


**Fig. 4** Theoretical field strength required for the DEP of bioparticles

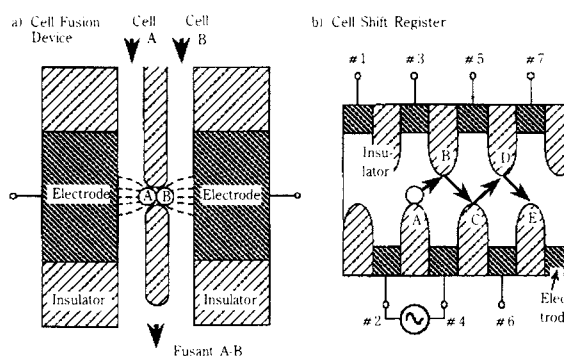


**Fig. 5** Fluid Integrated Circuit (FIC) cell manipulation devices

fig., which creates field maximum at the tip of A. The cell is dielectrophoretically attracted and trapped here. Then the voltage between #2 and #4 is removed, and applied between #3 and #5 instead. This moves the field maximum to the tip of B, and the cell is attracted towards here and trapped. Repeating the same procedure, the cell is transported step by step.

Electrorotation has found an application in the measurement of bacterial motor characteristics. Some bacterial species, such as *E. Coli* or *Salmonella*, are about  $2 \mu\text{m} \times 0.5 \mu\text{m}$  in size, and each bacterium possesses a number of spiral organ called flagella extruding from its body. The bacteria swim in water, rotating flagella like screws by flagellar motors

installed at the root of each flagellum. A flagellar motor is a molecular machinery which converts chemical energy to mechanical energy. An experimental difficulty in the investigation of the motor mechanism stems from its small size, only 50 nm in diameter. Electrorotation in microfabricated electrode system have successfully applied to the direct measurement of the torque-speed ( $T$ - $\omega$ ) characteristics [12].

When one of the flagella is attached to a substrate while the cell body is free, the counter torque of the motor rotates the bacterial body. Such a cell is called a "tethered cell". In a rotating electric field, the tethered cell is subject to electrorotation, and by changing the magnitude of the field, a controllable magnitude of the external torque can be applied to the cell (**Figure 6 a**). The direction of the external torque can be chosen to help the spontaneous rotation of the tethered cell, or to reverse, depending on the rotation direction of the applied rotating field. The frequency at which the cell rotates under the rotating field is optically measured for various external torque, by which the torque-speed curve of the motor is deduced.

**Figure 6 b**) plots the measured rotation speed against the externally applied electrical torque. On the right half plane is plotted the cases when external torque is in the direction to help the spontaneous rotation, while on the left half plane is plotted the case when the bacterial rotation is forced to reverse. The plot is made for one particular bacterium, both when the cell is alive (open square) and dead (solid square). The discrepancy between the two lines gives the torque generated by the bacterial motor, which appears to be constant in the measured range of rotation speed.

### 3.2 Molecular DEP

**Figure 4** predicts that DEP of protein molecules should occur under very high intensity field. Experimentally, the DEP of avidin (68kD in molecular weight) or other protein molecules are observed under a fluorescent microscope at c.a. 2MV/m, 1MHz [13]. This field strength is somewhat lower than the theoretically predicted value  $E_{th}$ . This may be attributed to the polarization mechanism of biological molecules, i.e. counter-ion polarization: ions loosely bound around charged groups (such as phosphates of DNA or  $\text{COO}^-$  of protein) migrate along the molecular contour by the electrostatic field, and the displacement of such counter-ion cloud causes the polarization. This means that the electrical equivalent radius of the molecule is the actual radius plus the thickness of counter-ion cloud. In fact, the polarizability of DNA, deduced from the field strength dependence of DNA orientation, is found to be orders of magnitude larger than the theoretical value for a conducting fiber having the same dimension as DNA, but it is well explained if the counter-ion cloud layer is taken into account [15]. Implications of this polarization mechanism are 1) it should be present in most biological molecules having charged groups on its exterior, and 2) to obtain negative DEP of biomolecules one has to use a frequency high enough that this counter-ion polarization can be neglected.

The molecular DEP can be used for the separation of biomolecules. **Figure 7 a**) shows the device which is used for the filtration of protein out of the solution. It consists of 3000 electrode array, each having wavy shape with the minimum gap of  $7\mu\text{m}$  to create high-field regions. Fluorescence-labeled avidin solution is fed from the inlet, and passed through the channel.

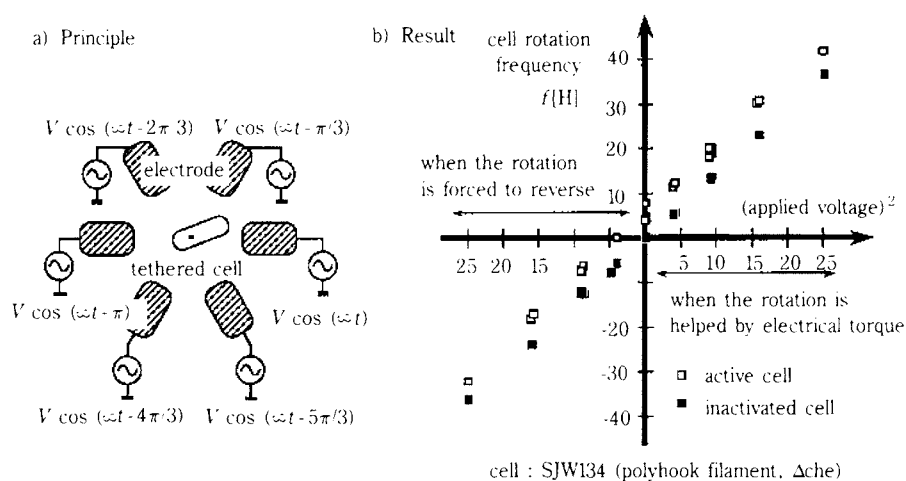


**Fig. 6** Measurement of bacterial motor characteristics using electrorotation

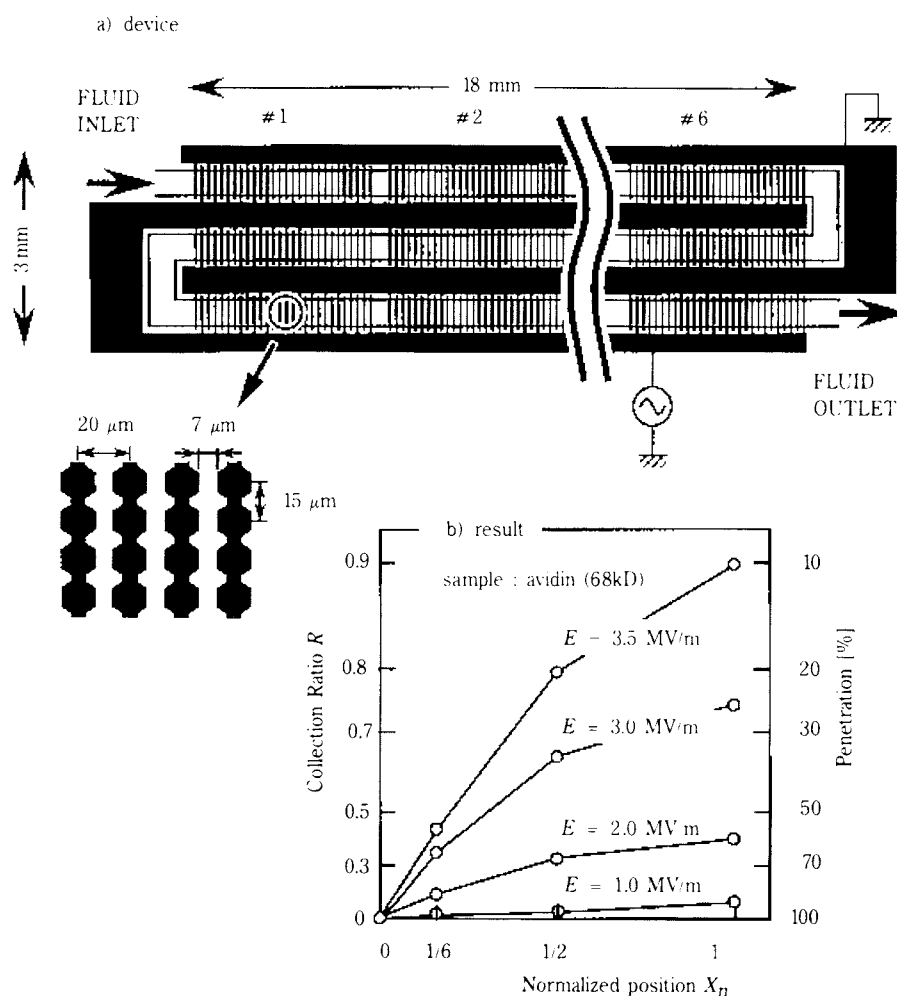


Fig. 7 Dielectrophoretic filtration of protein molecules

The penetration is measured by the fluorescent intensity at the inlet (normalized position  $X_n = 0$ ), 1/6 from the outlet ( $X_n = 1/6$ ), at the middle ( $X_n = 1/2$ ), and at the outlet ( $X_n = 1$ ) of the channel, taking the field strength as the parameter (Figure 7 b). This figure shows that about 90% of the protein is filtrated at  $E = 3.5$  MV/m. We named such a device “dielectrophoretic chromatography” [14].

These molecular DEP experiments are conducted in a non-conducting medium. The use of physiological solution was prevented by an excessive Joule heating even with microfabricated electrodes. A possible solution may be the use of even smaller nm-scale electrodes.

### 3.3 Stretch-and-positioning of DNA

In order to allow an easy external access to arbitrary position, a DNA strand should be stretched straight, and immobilized onto a particular location on a substrate. This can be realized by the process

schematically illustrated in Figure 8 [16]. DNA solution is fed onto a gap between metal thin-film electrodes vacuum-evaporated on a substrate. Under an absence of field, DNA takes randomly-coiled conformation due to thermal agitation as depicted in Figure 8 a). When the field is applied, electrostatic orientation occurs at every part of the DNA strand, and as a result, it is stretched straight (Figure 8 b). Very high intensity field is created at the edge of the planer electrodes, so the DNA is pulled into this region by DEP, until one end touches the electrode (Figure 8 c). Flow of medium driven by electrohydrodynamic (EHD) effect helps DNA motion towards the electrode edge. When an electrochemically active metal, such as aluminum, is used as the electrode material, the DNA end in contact with the electrode is permanently anchored there, presumably by a covalent bond. The anchoring is strong enough to sustain hydrodynamic force exerted by a moderate medium flow. We named this process “stretch-and-

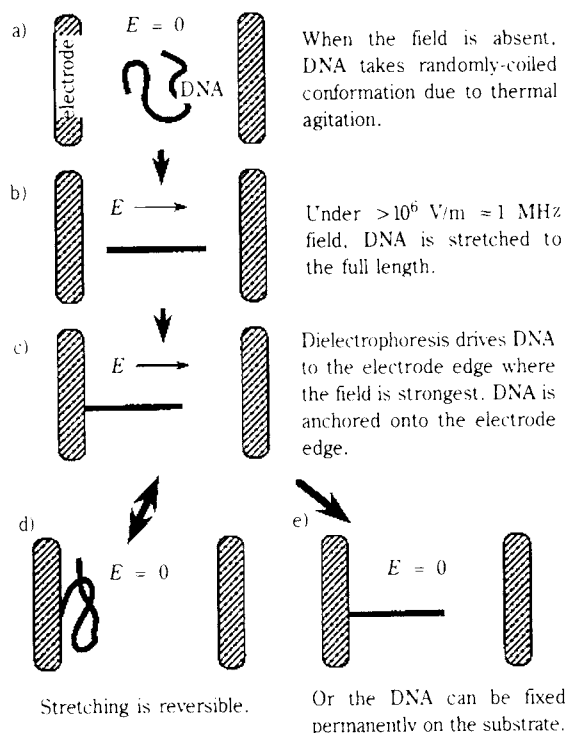


**Fig. 8** The electrostatic stretch-and-positioning of DNA

positioning of DNA" [17]. The stretching is reversible, and the DNA springs back to random-coil conformation when the field is removed, still one end securely anchored on the electrode (**Figure 8 d**). On the other hand, if one can immobilize the other end onto the substrate, the stretched shape is maintained even after removal of the field. A few methods have been developed for the anchoring of this end, including the use of avidin-biotin binding, or the use of the floating-potential electrodes, as described later.

Under the field strength in excess of  $10^6$  V/m, a DNA strand is stretched to its full length, 0.34 nm/base or 3 kb/ $\mu$ m. An apparent application is for DNA assay by length measurement, in which DNA size can instantaneously be determined within optical resolution just by measuring the stretched length of fluorescent-labeled DNA (**Figure 9 a**). Or the restriction sites of restriction enzymes can readily be determined (**Figure 9 b**). The stretched DNA can be cut at arbitrary position by an irradiation with an ultra-violet (UV) laser (**Figure 9 c**). This implies that DNA can be chopped from one end into fragments, which are small enough to be analyzed by electrophoretic methods. The advantage of this method over conventional sequencing using restriction fragments is the global spatial resolution: the position of the fragment in the original long strand is clear.

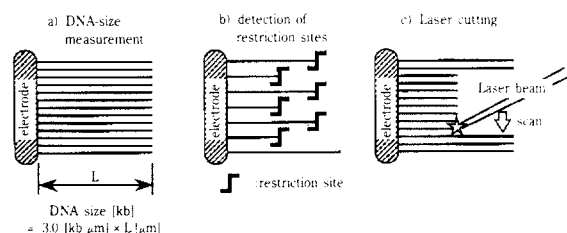


**Fig. 9** Applications of electrostatic stretch-and-positioning of DNA

### 3.4 Site-specific immobilization of the stretch-and-positioned DNA

Another application of the electrostatic stretch-and-positioning is for the time- and space-resolved observation of the dynamics of DNA interacting enzymes. In ref.[18] is reported the visualization of RNA polymerase sliding along a DNA strand. Here, one end of stretched DNA is anchored on the electrode edge, and the other end is fixed onto the electrode by biotin-avidin binding. It is important that the strand is held at both terminus only, and the reminder part is not in contact with the substrate, so as to let the enzyme freely move along the strand. We call this "site-specific" immobilization of DNA.

The site-specific immobilization can be realized also with the electrode system with adjusted gap length if the sample DNA size is known in advance. The device depicted in **Figure 10** has two outermost electrodes connected to power supply, and in between are placed thin strip electrodes which has no electrical connection (floating-potential electrodes). As a stretched DNA bridges over two adjacent gaps, fully stretched straight DNA is obtained if the gap length is equal to the DNA length, and loosely stretched ones are obtained if the gap is slightly smaller.

### 3.5 Molecular surgery

The stretch-and-positioning allows access to arbitrary position on a DNA strand, so that space-resolved chemical modifications (molecular surgery), such as dissection or chemical modifications, becomes possible. **Figure 11** depicts two applications of the concept. **Figure 11 a**) is the dissection of DNA, where a DNA cutting enzyme (DNase) immobilized on a laser-manipulated bead or on a scanning probe tip is pressed against an arbitrary position to cut the DNA. This method will provide chemically-defined cut-end, in contrast to the laser cutting method where the damage and the resultant chemical structure is unpredictable. Dissected fragments in this method might be picked up by a avidin-coated probe, if the

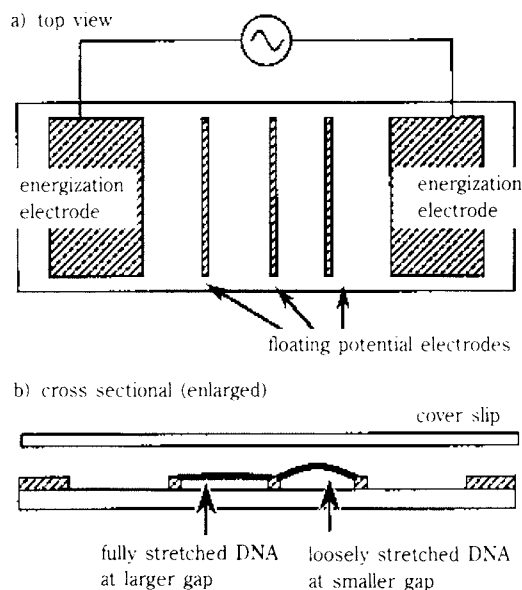


**Fig. 10** Floating-potential electrode geometry for site-specific immobilization of DNA with variable margin

fragment is biotinated prior to dissection. The method also can be used for biophysical studies of the functional and dynamic interactions of enzymes.

The most important point in realizing the molecular surgery is how to immobilize DNA, in such a way that does not hamper enzymatic activity. If the DNA is adsorbed onto the electrode all along its length, the enzyme cannot bite on the DNA, and is hindered to interact. DNA must be held with some clearance to the substrate surface, preferably at both ends only, so that DNA can go into the active site of the enzyme. Another point is the conformation of DNA. Some enzymes require special conformation of the target. For instance, RNA polymerase acts at the kinked part of DNA. This conformation is necessary to tear open the double strand and expose the bases

inside. The enzyme will not work on DNA with perfectly straight conformation. This requirement is dependent on the enzyme, so it may or may not be the case with DNase. The floating-potential electrode geometry, depicted in **Figure 10** gives both the clearance and the margin.

**Figure 12** shows the cutting of DNA with a DNase-immobilized particle [19]. In the fig., two floating-potential electrodes runs vertically, and there are two DNA molecules bridging over the electrodes (**Figure 12 a**). At the instance when the bead touches the upper DNA, it is cut (**Figure 12 b**). In this shot is seen that the left half of the cut strand is shrinking back to the electrode. The right half has already sprung back and disappeared. Next moment (**Figure 12 c**), the left half also disappears. The lower DNA is also cut by the contact of the bead (**Figure 12 d**).

**Figure 11 b**) proposes the local PCR, where the temperature of a particular portion is cycled by micro heating device so that the local sequence can be copied. As the number of replicated molecules expected by the local PCR is estimated to be so small that we do not have a method to effectively detect the replicated DNA fragments, the concept of space-resolved temperature rise is demonstrated using bacterial flagella as the object. A flagellum consists of non-covalently bond monomer units of flagellin. It normally takes helical shape, but a temperature rise changes the binding state between monomers, by which the shape of a flagellum drastically changes, and when the temperature is further elevated above 60 °C, it dissociates into monomers. The morphological change, as well as the dissociation, is directly observable under a dark-field microscope.

A laser-manipulated latex bead containing fine iron powders is used as the heater, so that light refraction in latex provides trapping force, while absorption at

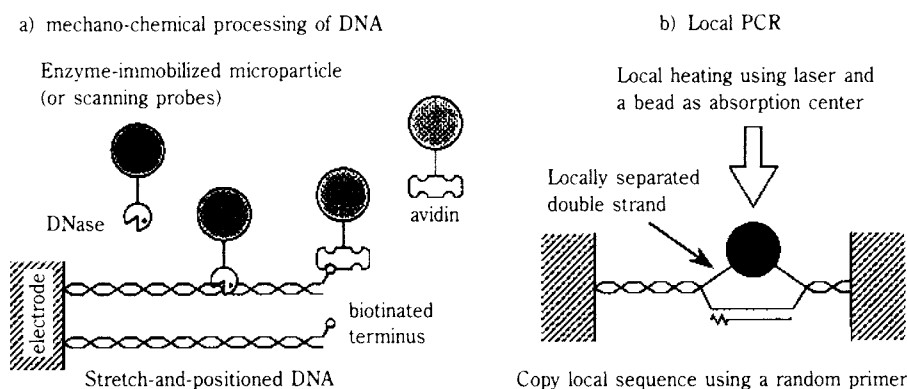


**Fig. 11** Molecular surgery (conceptual)

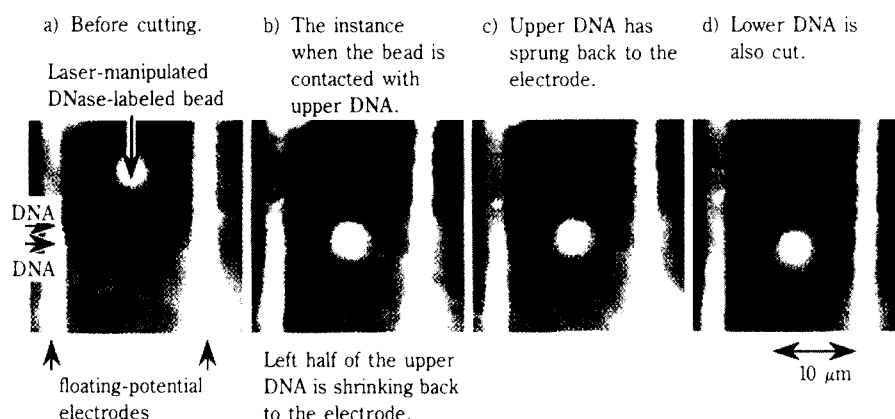


Fig. 12 Cutting of the stretch-and-positioned DNA with a laser-manipulated DNase-labeled bead

iron powder provides heating. The diameter of the bead is  $2.8\ \mu\text{m}$ , and is irradiated with 170 mW YAG laser. **Figure 13 a)** shows the target flagellum. When the bead is pressed against it, the dissociation occurs, and the flagellum is cut at this position (b). This result proves that the temperature rise above  $60\ ^\circ\text{C}$  is achieved with c.a.  $1\ \mu\text{m}$  resolution. With the laser power reduced to 90%, the temperature rise is not high enough to cause dissociation, but still adequate for the morphological change. The bead is contacted with the flagellum of fig. c), by which local transformation is induced, and the flagellum is kinked at this position as shown in fig. d).

### 3.6 Use of single-stranded DNA

In all above experiments, DNA used are double-stranded. The use of single-stranded DNA, in which the bases are exposed and more accessible, seems superior for sequence reading purposes. For instance, binding of a fluorescent-labeled single-strand fragment of known sequence to a stretch-and-positioned single-stranded DNA, observed under a fluorescence microscope, will provide a location of complementary sequence with the optical resolution. A problem we encountered in developing this scheme is that a single-stranded DNA does not stretch under an electrostatic field. This is attributable to hydrophobic interactions among bases, or formation of intra-strand pairs. Therefore we tried to make single-strand, by enzymatically removing one of the strands of double-stranded DNA. The double-strand DNA is first stretch-and-positioned and anchored at both of its termini on the substrate, so as not to cause steric hindrance for the removal of one of the strands with an exonuclease. However, as soon as the exonuclease is added, anchoring came off. The single-stranded portion of DNA, having only one backbone, was not

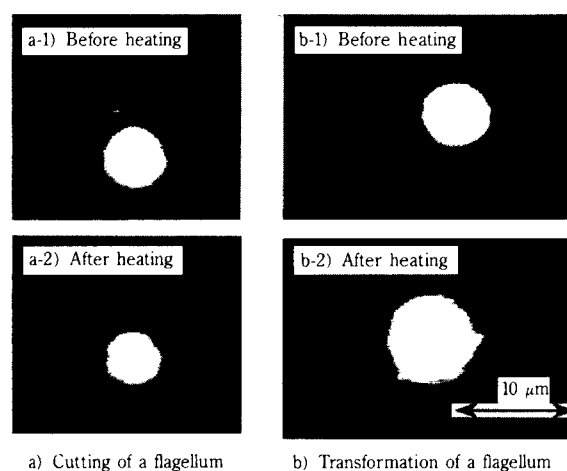


Fig. 13 Local conformation change and dissociation of a flagellum by laser-induced pin-point temperature rise

strong enough to support hydrodynamic force exerted on the entire strand. A method to securely support one of the strands, with the interval short enough to minimize hydrodynamic load, and still not causing hindrance to the exonuclease activity, needs to be developed for the utilization of the single-stranded DNA.

## 4. Conclusions

Recent advances in 1) the electrostatic- and the laser-manipulation methods, 2) microfabrication, and 3) observation methods of nm-sized objects such as the high-sensitivity fluorescent imaging or the scanning probe microscopy, are considered to be the technical seeds for the manipulation of bioparticles. The precise control of the position, the orientation, and the motion of the particles allows the access to individual particles, or even of a particular location of

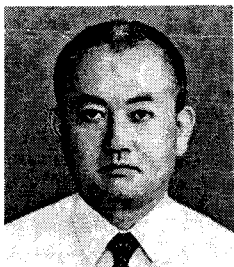
the particle. Time- and space- resolved observation and manipulation of a bioparticles thus made possible has wide applications in biotechnology, from the basic research of dynamic behavior of molecular interactions to the practical applications in high-speed sequencing.

## Acknowledgment

The authors gratefully acknowledge collaborations and valuable discussions of Prof. Senichi Masuda of Tokyo Univ., Mr. Osamu Kurosawa and Mr. Toshiyuki Nanba of Advance Co., Mr. Takatoki Yamamoto of Kyoto Univ., Prof. Nobuo Shimamoto of the National Institute of Genetics, Prof. Sinichi Aizawa of Teikyo Univ., Prof. T.B. Jones of Rochester Univ., Dr. Seiichi Suzuki of Seikei Univ., and financial support from the Advance Company, the Ministry of Education (Grant-in-Aid for Scientific Research; 072411004), and Toyota Physical and Chemical Institute.

## References

- 1) H.A. Pohl: "Dielectrophoresis", Cambridge University Press (1978)
- 2) T.B. Jones, *Electromechanics of Particles*, Cambridge University Press (1995)
- 3) R. Pethig: "Application of a.c. electrical fields to the manipulation and characterisation of cells", in *Automation in Biotechnology*, I. Karube ed., p.159-185, Elsevier Science Publishers (1991)
- 4) W.M. Arnold and U. Zimmermann: "Electro-rotation: Developments of a technique for dielectric measurements on individual cells and particles", *J. Electrostatics*, Vol. 21, p.151-191 (1988)
- 5) Y. Huang, X-B. Wang, J.A. Tame and R. Pethig: "Elektrokinetic behavior of colloidal particles in travelling electric fields: studies using yeast cells", *J. Phys. D*, 26, p.1528-1535 (1993)
- 6) T. Müller, A.M. Gerardino, T. Schnelle, S.G. Shirley, G. Fuhr, G. De Gasperis, R. Leoni and F. Bordon: "High-frequency electric-field trap for micron and submicron particles", *IL NUOVO CIMENTO*, Vol. 17 D, N.4, p.425-432 (1995)
- 7) M. Washizu and T.B. Jones: "Generalized Multipolar Dielectrophoretic Force and Electrorotational Torque Calculation", *J. Electrostatics*, Vol. 38, No.3, p.199-212.
- 8) M. Washizu and T.B. Jones: "Multipolar dielectrophoretic force calculation", *J. Electrostatics*, vol. 33, pp. 187-198 (1994)
- 9) S. Masuda, M. Washizu and T. Nanba: "Novel Method of Cell Fusion in Field Constriction Area in Fluid Integrated Circuit", *IEEE Trans. IA*, Vol. 25, No.4, p.732-737 (1989)
- 10) Masao Washizu, Toshiyuki Nanba and Senichi Masuda: "Handling of Biological Cells Using Fluid Integrated Circuit", *IEEE Transaction IA*, Vol. 26, No.2 p.352-358 (1990)
- 11) M. Washizu and K. Nakada: "Bearingless micromotor using negative dielectrophoresis", *Proceedings of Annual Meeting of Institute of Electrostatics - Japan*, p.233-236 (1991) (in Japanese).
- 12) Masao Washizu, Yuichi Kurahashi, Hirokazu Iochi, Osamu Kurosawa, Shin-ichi Aizawa, Seishi Kudo, Yukio Magariyama and Hirokazu Hotani: "Dielectrophoretic Measurement of Bacterial Motor Characteristics", *IEEE Transaction IA* Vol. 29, No.2, p.286-294 (1993)
- 13) M. Washizu, S. Suzuki, O. Kurosawa, T. Nishizaka and T. Shinohara: "Molecular Dielectrophoresis of Bio-polymers", *IEEE Transaction IA*, Vol. 30, No.4 p.835-843 (1994)
- 14) Masao Washizu, Seiichi Suzuki and Kiyoshi Moro: "Dielectrophoretic Filtration of Protein Molecules in a Fluid Integrated Circuit" *Proceedings of Annual Meeting of Institute of Electrostatics - Japan*, p.27-32 (1993)
- 15) S. Suzuki, T. Yamanashi, S. Tazawa, O. Kurosawa and M. Washizu: "Quantitative analysis on electrostatic orientation of DNA in stationary AC electric field using fluorescence anisotropy", *conf. rec. IEEE/IAS '95 ann. meet.*, p.1374-1382 (1995)
- 16) M. Washizu and O. Kurosawa: "Electrostatic Manipulation of DNA in Microfabricated Structures", *IEEE Trans. IA*, Vol. 26, No.6, p.1165-1172 (1990)
- 17) M. Washizu, O. Kurosawa, I. Arai, S. Suzuki and N. Shimamoto: "Applications of Electrostatic Stretch-and-positioning of DNA", *IEEE Transaction IA*. Vol. 31, No.3, p.447-456 (1995)
- 18) H. Kabata, O. Kurosawa, I. Arai, M. Washizu, S.A. Margason, R.E. Glass and N. Shimamoto: "Visualization of single molecules of RNA polymerase sliding along DNA", *Science*, Vol. 262, p.1561-1563 (1993)
- 19) M. Washizu, T. Yamamoto, O. Kurosawa, S. Suzuki and N. Shimamoto: "Molecular Surgery of DNA Using Enzyme-Immobilized Particles", *T. IEE Japan (Denki Gakkai Ronbunshi)*, Vol. 116-E, No.5, p.196-202 (1996) (in Japanese)

**Author's short biography****Masao Washizu**

Masao Washizu received the doctoral degree in electrical engineering from the University of Tokyo in 1981. He was a research engineer at Toshiba Corporation from 1981 to 1985. He became an associate professor at the Department of Electrical Engineering and Electronics, Seikei University in 1987, and a professor in 1995. From 1996, he is a professor at the Department of Mechanical Engineering, Kyoto University. His primary research interest is in the application of electrostatics to bioengineering, including the electrostatic manipulations of biological objects using micro-machined structures. He is a senior member of Institute of Electrical and Electronics Engineers (IEEE), a member of Institute of Electrostatics Japan, Applied Physics Society of Japan, Biophysical Society of Japan and Institute of Electrical Engineers Japan.

# Mixing of Particulate Solids<sup>†</sup>

Karl Sommer

Technische Universität München\*

Lehrstuhl für Maschinen- und Apparatekunde

## Abstract

*Solids mixing refers to the blending of particulate components differing in one of their properties. To compare mix and mixer the theoretical standard deviation  $\sigma$  is defined as the mixing quality. To simulate the stochastic mixing process the Fokker-Planck-Equation is used. Similar simulations described in the literature up to now, in which the transport coefficient is determined from the throughput, are not generally valid. It could be shown with the modified method that the mixing results depend only on the relationship between the residence time and the fluctuation time of the feed material streams.*

*A model, based on a suggestion of Schulze, is useful to simulate deterministic silo mixers. The experiments confirm the results of the simulations.*

## 1. Introduction

The mixing of solids is one of the oldest and most frequently performed of all chemical engineering operations. With increasing automation of engineering processes in all material transformation sectors, the application of scientific principles to such operations is of increasing importance [1, 2, 3].

Solids mixing refers to the blending of at least one solids component with another, whereby the particulate components differ in at least one of their properties. The definition of mixing efficiency often differs depending on whether one is a manufacturer or customer of mixed materials and mixers. One should therefore specifically define "mixing efficiency" if this parameter is to be used to assess the quality of a mixed material. While solids mixing has been accomplished for centuries in batch operations, just as in other unit operations (e.g. stirred tank reactions, tubular reactors, combustion chambers, etc.), there is now a strong tendency to conduct solids mixing in a continuous fashion.

## 2. Mixing efficiency

The determination of mixing efficiency is a statistical problem and is coupled with the problem of sample collection. The goal of mixing is, of course, to distribute the various components as completely as possible throughout the material. When the component concentration at localised points (i.e. in collected samples) differs from the overall mix composition,

mixing is considered poor, whereas if it is close to the mix composition, good mixing has been achieved. Because it is irrelevant whether the concentration of the sample deviates positively or negatively from the nominal concentration, the mean quadratic deviation is a good measure of mixing efficiency [4, 5]. In statistics, this is called the square of the standard deviation  $\sigma^2$ . This is the theoretical variance of all possible samples in the mixer, and for a given mixture,  $\sigma^2$  is a characteristic parameter that depends on the sample size. The mixing efficiency  $\sigma^2$  therefore "improves" as the sample size increases [6]. If the sample size is of the same order as the particle size of at least one of the solids in the mixture, then  $\sigma^2$  for the best case of mixing approaches a limiting value  $\sigma_z^2$ . This limiting value is a function of the sample collection conditions [6].

## 3. Powder mixing mechanisms

### 3.1 The Fokker-Planck Equation

Assuming that mixing arises from random motion of individual particles, Fokker and Planck developed the following differential equation which is based on the resulting random concentration changes that originate in the mixer:

$$\frac{dc(x)}{dt} = -u \cdot \frac{dc(x)}{dx} + D \cdot \frac{d^2c(x)}{dx^2} \quad (1)$$

This equation is identical in form to Fick's 2nd Law of Diffusion. It describes the concentration change at a given position in the mixer and includes two

\* Weihenstephan, 85350 Freising-Weihenstephan, Germany

<sup>†</sup> Received 19 July 1996

parameters: the transport coefficient  $u$  and the dispersion coefficient  $D$ .  $D$  is a measure of the random motion in the mixer and depends on the mobility of the individual particles. The transport coefficient  $u$  corresponds to the convective flow present in the mixer. However, it is not set equal to the throughput of the mixer, and is thus also relevant for the case of batch mixing.

### 3.2 Batch mixing

According to Equation (1) there are two separate sources of mass flow: convective flow and dispersive (or diffusive) flow. In a batch mixer, these separate flows can work against each other, resulting in demixing [7]. **Figure 1** shows the experiments carried out by Müller [7]. Demixing was brought about by the difference in transport characteristics between iron and quartz (straight line) and between iron and limestone (dotted line). In the first experiment, at the beginning the diffusion and transport streams were in the same direction and in the second, in the opposite direction. The empirical coefficients of variation reflect the course of events predicted in the model. Hence, the first experiment gave rise to a homogenous distribution and then to demixing, and a random homogeneous distribution was not attained at any time in the second experiment.

Demixing can also occur when no convective transport processes are present. This results because the dispersion coefficient is a function of concentration (or location). Because the dispersion coefficient is strongly coupled with the particle mobility, it has a longer residence time for the component in the zones with smaller dispersion coefficients. Statistically, this results in demixed zones within the mixer.

Without convective transport and assuming a constant dispersion coefficient  $D$ , the Fokker-Planck Equation reduces to:

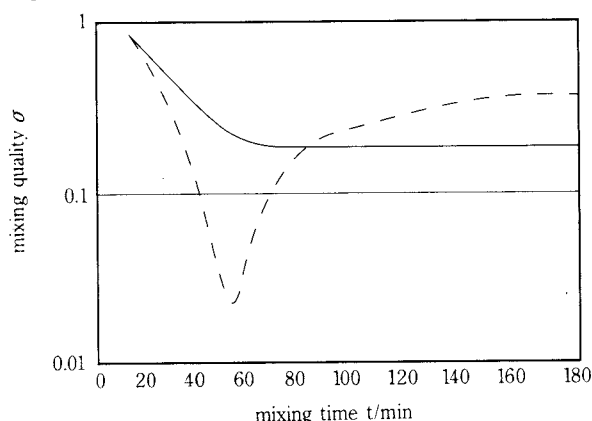


**Fig. 1** Demixing tendency caused by convective flow in a batch mixer [7]

$$\frac{dc(x)}{dt} = D \cdot \frac{d^2c(x)}{dx^2} \quad (2)$$

This is the well-known form of Fick's 2nd Law of Diffusion. It can be written in dimensionless form with  $\lambda = x/L$  and  $\tau = t/T$  as follows:

$$\frac{dc(\lambda)}{d\tau} = + \frac{d^2c(\lambda)}{d\lambda^2} \quad (3)$$

$T = L^2/D$  is a characteristic time formed from a characteristic mixer length  $L$  and the dispersion coefficient  $D$ . For the sample case of a closed barrel mixer of length  $L$ , the equation can be solved in closed form [7]. Rigid walls are assumed as boundary conditions, i.e. there is no material flow at  $x = 0$  and  $x = L$  over the wall. The initial condition is that the component to be considered is highly concentrated on one side of the mixer.

If the variation coefficient  $\sigma/\mu$ , related to the mean value  $\mu$ , is used to represent the mixing efficiency, one obtains the following simple formula:

$$\frac{\sigma}{\mu} = \sqrt{2} \cdot e^{-\left(\frac{\pi}{L}\right)^2 \cdot D \cdot t} \quad (4)$$

The equation predicts what is observed in practice: as the dispersion coefficient increases, mixing occurs more rapidly.

Experimental results from Müller [17] are depicted in double logarithmic form in **Figure 2** as an example of dispersive mixing. The system consisted of 300-400  $\mu\text{m}$  copper particles mixed with the same size nickel particles of concentration  $c_o = 7.67 \cdot 10^{-3}$ . From the slope of the initial line, one obtains a dispersion coefficient of  $D = 1.1 \text{ cm}^2/\text{s}$ . This coefficient is practically independent of the length/diameter ratio

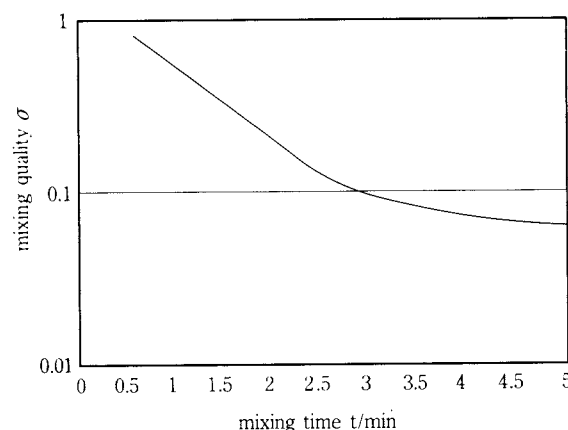


**Fig. 2** Mixing quality as a function of time for purely dispersive mixing [7]

of the mixer. After a sufficiently long mixing time, sample collection error becomes the dominant influential parameter and the measured points begin to asymptotically approach a constant value. The centre of gravity of one of the components was initially near the wall (due to the initial boundary conditions), and after the mix process, was exactly in the centre of the mixer, indicating that it is now homogeneously distributed. Thus, even without convective transport, the centre of gravity of a component shifts solely due to dispersive transport.

#### 4. Continuous mixing of the two material streams

##### 4.1 Depiction of the mixing process

At the inlet to an axial barrel mixer, two material streams converge into the mixer such that no back-flow occurs. The material streams are mixed at the entrance and at each point in the mixer radially (i.e. ideal cross-flow mixing). Generally, a retaining weir is positioned at the end of the mixer and the excess material flows out over it. The degree of fill of both components at the weir is designated  $\phi_a$ . Due to the dispersive and/or convective transport processes, both of the material streams, which are homogenous in the radial direction, are conveyed to the opposite end of the mixer. As discussed in the introduction, one of the primary requirements of continuous mixing is to damp out concentration oscillations resulting from periodic injections of material.

Each of the material streams can be described by the Fokker-Planck Equation:

$$\frac{d\phi_1(x)}{dt} = -u_1 \cdot \frac{d\phi_1(x)}{dx} + D_1 \cdot \frac{d^2 \phi_1(x)}{dx^2} \quad (5a)$$

$$\frac{d\phi_2(x)}{dt} = -u_2 \cdot \frac{d\phi_2(x)}{dx} + D_2 \cdot \frac{d^2 \phi_2(x)}{dx^2} \quad (5b)$$

Here,  $\phi_1(x)$  and  $\phi_2(x)$  correspond to the masses of components 1 and 2, respectively, per differential mixer volume. They are therefore proportional to the local degree of fill of each component and are normalised by the reference degree of fill  $\phi_a$  at the exit.

In general, both material streams have their own unique dispersive and convective transport coefficients. However, if both streams consist of nearly identical or very similar substances and differ, for instance, only in their colour, the coefficients for the two materials may be assumed to be equal (i.e.

transport coefficient  $u_1 = u_2 = u$ , and the dispersion coefficient  $D_1 = D_2 = D$ ).

As was seen in the batch case, the transport coefficient  $u$  is a property of the mixer. In most investigations and literature reports,  $u$  is set equal to the mean material transport. This assumption is, however, not valid in all cases. It may be approximately fulfilled when one of the material streams dominates, conveying the other stream without significantly dispersing it. Such a situation occurs frequently when the primary mass flow is a fluid that, upon entering the mixer, displaces a fluid that is already present in the mixer. However, in particular for the mixing of two powder streams, the above assumption is not valid, and therefore both Fokker-Planck equations must be considered.

##### 4.2 Boundary conditions for continuous mixing of two components

The two mass streams to be mixed enter the mixer at one end ( $x = 0$ ). At this end, no material is allowed to exit the mixer. Both or either of the components individually are subject to fluctuations.

The time-dependent deviation of the concentration from the mean is a measure of the heterogeneity of the mixture, and is expressed by the variance  $\sigma_0^2$  or standard deviation  $\sigma_0$ , or by the variation coefficient  $\sigma_0/\mu$ .

The mixed material is discharged over the retaining weir. In the literature, a convective discharge  $u\phi_a(L)$  is often postulated. However, once again, this boundary condition is only valid for the case in which one of the material streams dominates with purely convective flow.

The boundary conditions for the retaining weir are: if the transport (dispersive or convective) causes the degree of fill at the end of the mixer to rise above the given discharge height, the overflow (which has a concentration corresponding to this location and time in the mixer) is immediately discharged. The result is a constant local degree of fill at the end of the mixer, in accordance with requirements.

The discharged material is also subject to other more minor fluctuations. As in the case of the inlet flow, the heterogeneity of material exiting the mixer can be characterised by a variance or variation coefficient. Based on conservation of mass, at steady state the mean value of the output concentration must be equivalent to the mean value at the entrance  $\mu$ .

The goal of mixing is obviously to reduce the heterogeneity of the entrance material  $\sigma_0$  to produce

a quality product. The ratio  $\sigma/\sigma_0$  is a measure of the effectiveness of the mixing process.

## 5. Simulation of a continuous stochastic mixing process

The simulation of continuous mixing using Equation (5) reveals an unexpectedly strong dependence on the dispersion coefficient (**Figure 3**).

It is well known in batch mixing that a larger dispersion coefficient leads to more rapid mixing (Equation 4). One expects the same to be true for continuous mixing. The dispersion coefficient is also associated with back-mixing, which is intuitively expected to be necessary for successful mixing. The simulation indicates that this expectation is not completely correct. Depending on the value of the transport rate  $u$ , the mixed material can be either accelerated or decelerated as the dispersion coefficient increases. An analysis of the mass distribution in the mixer shows that the magnitude of the dispersion coefficient has no influence when the convective transport in the mixer is adequate to convey the material. There is thus no variation in concentration or degree of fill within the mixer and thus no dispersive influence. At low transport rates, the degree of fill decreases to the end of the mixer and the dispersive effect supports the mass transport. With shorter residence times, the mixing results become poorer. For larger convective transport rates, the degree of fill increases up to the outlet and a larger degree of dispersion reduces the overall mixer throughput. In this case, the mixing efficiency is improved as the dispersion coefficient increases.

Simulations conducted by varying different parameters show that the most influential parameter is the residence time (related to the characteristic fluctuation time  $T$  of the entrance material streams).

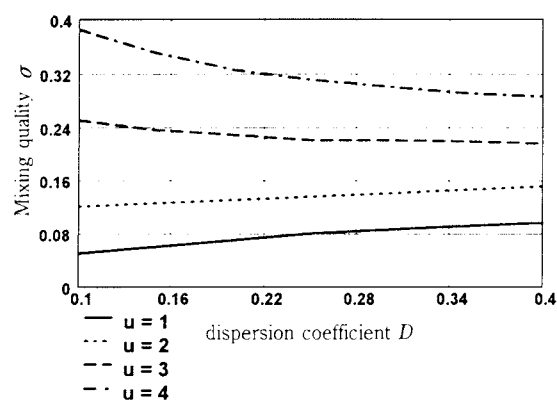


Fig. 3 Mixing quality as a function of dispersion coefficient  $D$  and transport coefficient  $u$

It also indicates that the mixing efficiency falls within a narrow band, which can be completely described by a mastercurve (**Figure 4**) [8].

Unfortunately, there are few accounts in the literature in which practical results have been analysed. Some recent results (shown in **Figure 4**) are available in the work by Weinekötter [9, 10]. These experimental results show surprisingly good agreement with the master curve, and the difference can be explained based on the step oscillation applied at the entrance section, which causes better mix results for “high frequency” components.

## 6. Silo mixing

There is a wide variety of silo mixers that are frequently used for powder mixing. A common feature is that different material streams are mixed in the silo via external (or internal) blending and recirculation. The differences in the flow times within the mixing silo result in a range of residence times, i.e. materials introduced simultaneously at the inlet are conveyed to the outlet at different times, producing a mixture. The mixing effect is increased by circulating the contents several times within the silo. In contrast to a stochastic process, mixing in a silo mixer is very much a deterministic process. Schulze [11] developed a cell / layer model that simulates the processes in a mixer. His derivation results in a vector expression for the time-dependent concentration distribution  $C_k$  in the mixer:

$$C_{k+1} = M \cdot C_k \quad (6)$$

Here,  $M$  is the mixer matrix and contains the residence time spectrum data. The matrix can be used to assess the effectiveness of the silo mixing process.

Using a modification of the above equation, Dauth

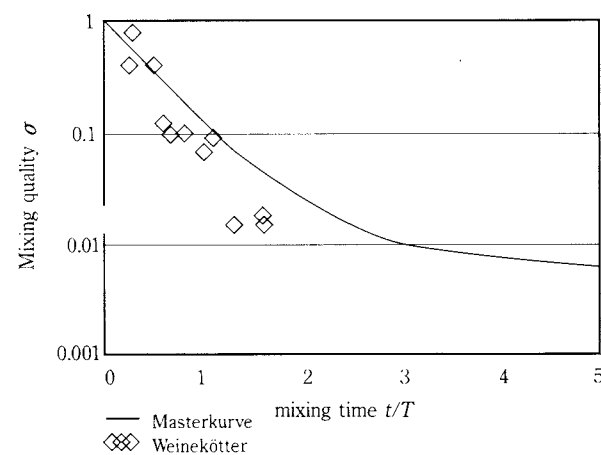


Fig. 4 Master curve for the mixing quality [8]

and Sommer [12] simulated the concentration profile at the outlet of a silo mixer (**Figure 5**). They used a convolution method whereby the entrance conditions were continuously changed (due to recirculation). Analogous to the Schulze equation, the only input to the model is the residence time distribution of the product in the silo, and this can be easily determined via Dirac marking. Comparison of the simulation with mixing results in a plain silo showed excellent agreement through numerous recirculations. It will thus be possible to use simulation to optimise residence time spectra and thereby provide guidance on the proper design of silo mixers.

## 7. Conclusions

The theoretical variance  $\sigma^2$  was defined and proposed as a characteristic parameter to measure the quality of mixers and mixed materials. The empirical variance  $\sigma^2$  is a measure of mixing efficiency with an associated degree of uncertainty and within a given range (confidence interval).

The Fokker-Planck Equation is useful for describing the mixing process and simulating a stochastic mixer with two comparable material streams (in particular, for the blending of powders). The simulation method used in the literature exclusively up to now, in which the transport coefficient  $u$  is determined from the throughput, is not generally valid. In addition, boundary conditions at the outlet must account for the practical case of overflow at the retaining weir.

The commonly held view that a large dispersion coefficient (corresponding to significant recirculation) improves mixing was found to be valid for batch mixing. However, in continuous mixing, the effect of the dispersion coefficient depends on the magnitude

of the “convective” transport rate.

From the simulation, it appears that obtaining sufficiently accurate mix results for practical applications depends only on the relationship between the residence time and the fluctuation time of the entrance material streams. The experiments of Weinekötter confirm this result.

As is the case for stochastic mixers, modern simulation methods can also be used with deterministic silo mixers, both to predict mixing results and provide insight into their design. Such methods provide scientific tools for analysing powder mixing, which, unfortunately, has been almost exclusively an empirical field to date. These techniques thus offer great potential to further advances in this area.

## List of symbols:

$C$	: concentration matrix
$c(x)$	: concentration at point $x$
$D$	: dispersion coefficient
$L$	: length of mixer
$M$	: mix matrix
$t$	: time
$T$	: characteristic time
$u$	: transport coefficient
$x$	: coordinate
$\phi$	: filling rate
$\lambda$	: dimensionless coordinate
$\mu$	: concentration of the total mix
$\sigma_2$	: standard deviation
$\sigma^2$	: variance
$\sigma_0$	: standard deviation in the beginning
$\sigma_z$	: standard deviation of the random mix
$\tau$	: dimensionless time

## Literature

- [1] Harnby N., Edwards M.F., Nienow A.W.: *Mixing in the Process Industries*; Butterworths London 1985
- [2] Sterbacek Z., Tausk P.: *Mixing in the Chemical Industry*; Pergamon Press Oxford 1965
- [3] Koichi Iinoya, Keishi Gotoh, Ko Higashitani: *Powder Technology Handbook*; Marcel Dekker, Inc. New York 1991
- [4] Poole K.R., Taylor R.F.: *Trans. Instn. Chem. Eng* \$2 (1964) T166
- [5] Williams J., Khan M.L.: *The Chem. Eng.* 269 (1973)19
- [6] Sommer K.: *Sampling of Powders and Bulk Materials*; Springer-Verlag New York 1986
- [7] Müller W.: *Untersuchungen über Mischzeit, Mischgüte und Arbeitsbedarf in Mischtrömmeln mit rotierenden Mischelementen*; Dissertation Karlsruhe 1966
- [8] Sommer K.: *Powder Mixing*, Preprints 1st Int. Particle Technology Forum Denver 1994

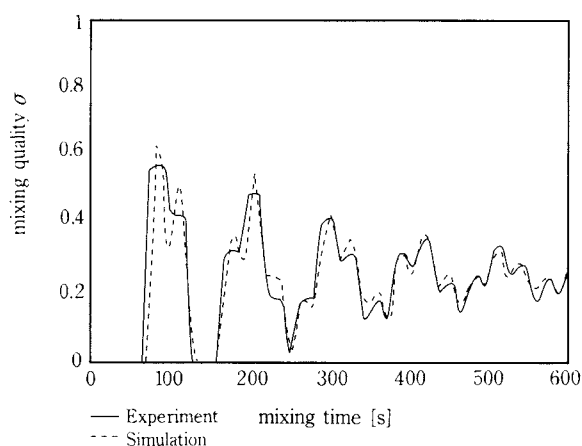


**Fig. 5** Comparison between experiment and simulation of a silo mixer

- [9] Weinekötter R., Gericke H.: Mischen von Feststoffen; Springer Verlag Berlin 1995
- [10] Weinekötter R.: Kontinuierliches Mischen feiner Feststoffe; Dissertation ETH Zürich 1993
- [11] Schulze D.: Schüttgut 1(1995)3 483/486; Schüttgut 1(1995)4 615/618; Schüttgut 2(1996)2 241/247
- [12] Dauth H., Sommer K.: Silo Mixing; Preprints World Congress on Chemical Engineering San Diego; 1996

### Author's short biography



#### Karl Sommer

Karl Sommer, born in Ludwigshafen, Germany, on the 24th June 1943, studied Process Technology with the main point of emphasis on physical systems at the Technical University of Karlsruhe. Upon completion of his studies in 1968, he worked on the academic staff at the Institute for Mechanical Process Technology of the Technical University of Karlsruhe, simultaneously pursuing his doctorate, which he earned in 1974. Thereafter, he worked as scientific assistant at the Institute for Mechanical Process Technology for three years before taking the post of team manager at BASF in Ludwigshafen. In 1977, he qualified as a university lecturer for the branch of study "Mechanical process technology" at the Technical University of Karlsruhe. Since 1982, Karl Sommer has held the chair at the faculty of brewing, foodstuffs technology and dairy science at the Technical University in Munich.

He has also had several works published by Springer Publishers, among them "Probenahme von Pulvern und körnigen Massengütern" in 1979, This work was translated into English and appeared as "Sampling of Powders and Bulk Materials" in 1986.

# Particles Heat Treating in a Pulsating Gas Stream†

A. Parnas

American Combustion, Inc.,\*

## Abstract

The subject of the paper is the application of pulsating flow to the particles heat treating. Pulsation influence mechanisms are segregated by the author into two groups: quasi-steady-state (when, at every point in time, an instantaneous value of the heat transfer rate may be calculated with the equations obtained for steady-state conditions) and unsteady-state which includes the remainder. It is shown that, depending on the process parameters, pulsations can increase, not influence, or even reduce heat transfer. Resonance phenomena and large size particles, for which the influence of gravity is substantial, receive special attention. The heat transfer intensification may be achieved due to increases in both heat transfer coefficient and particle residence time. Longitudinal pulsations (when the pulsation and main flow velocities have the same direction) may be preferable in the unsteady-state range of parameters. Transverse pulsations (when the pulsation velocity is perpendicular to the main flow) can be more effective in the quasi-steady-state range. Nonuniformity of heat treating in pulsating flow, influence of the main flow turbulence, trigger effects, and different methods of pulsation generation, including pulsating combustion, are discussed. In conclusion some recommendations are given for designing practical processes.

## 1. Introduction

The use of a pulsating flow for intensification of heat and mass transfer in gas suspensions was proposed long ago, and the basics of heat treating particles in subsonic pulsating flows were developed in the period of approximately 1945–1970. Hundreds of papers devoted to the subject have been being published, and sometimes it is not easy to differentiate correct and incorrect, new and well-known ideas. The purpose of this work is not to cover all aspects of the problem (a special monograph is needed for this) but only to discuss its basics. The author's personal opinion is presented, and the list of references is short because only articles which illustrate the problem have been included. The author was involved for many years in investigation of unsteady-state heat transfer, heat transfer in pulsating flow, and pulsating combustion phenomena, and he hopes that the paper will help engineers to better understand the mechanisms of pulsation action and to select the proper range of parameters providing profitable results of pulsation usage.

## 2. Basic relationships

Amount of heat transferred by convection from gas to the particle, can be described with the equation:

$$q_p = \int_0^t h (T_g - T_p) dt, \quad (1)$$

As it is seen from equation (1), to increase the heat transferred to the particle one should increase heat transfer coefficient,  $h$ , or/and increase gas temperature,  $T_g$ , or/and increase heat treating time,  $t$ , (residence time of the particles in the apparatus). The value of  $T_g$  may be limited with technological requirements: particle material may be sensitive to temperature, etc. Besides, from an economical viewpoint, it is always preferable to use low cost energy, and, therefore, lower gas temperature. For instance,  $T_g$  cannot exceed the theoretical combustion temperature of a selected fuel. Particle residence time,  $t$ , is also limited because it is inversely proportional to the average velocity of the particle which cannot be lower than the particle terminal (deposition) velocity. Therefore, increase of a heat transfer coefficient,  $h$ , is often the only possible method of increasing heat transferred to the particle.

The dimensionless relationship for the heat transfer coefficient can be obtained with the theory of dimensions. Assuming  $Bi_p$  number is small, gas velocity is

\* Norcross, Georgia, USA

† Received 15 March, 1996

much less than the sound speed, and mass transfer process doesn't significantly influence heat transfer, the following relation may be applied:

$$Nu_p = Nu_p(Re_p, Gr_p, Pr, Sr_p, Kn_p, T_p / T_g, \varepsilon, L/d, a/d) \quad (2)$$

Parameters  $\varepsilon$  and  $L/d$  account for the influence of turbulence. The  $Pr$  number is almost constant for gases and may be excluded from pulsation influence analysis. The  $Gr_p$  number may be also excluded if an influence of gravitational convection is negligible (in the range of  $Re_p > 20$  this is correct if  $Gr_p \ll Re_p^2$ ).  $Kn_p$  number may be excluded for large particles, when  $Kn_p \leq 10^{-3}$ . For small particles, or in the case of heat transfer at low pressure, when the mean free path of gas molecules is comparable with the dimension defining the heat transfer process (thickness of the boundary layer), a gas temperature jump at the surface of the particle and  $Kn_p$  number should be taken into account. With these considerations, the relationship for heat transfer in pulsating flow becomes:

$$Nu_p = Nu_p(Re_p, Kn_p, Sr_p, T_p/T_g, \varepsilon, L/d, a/d) \quad (3)$$

Two parameters ( $Sr_p$  and  $a/d$ ) account for the influence of pulsations in the equation (3). It can be shown that each of them may be replaced with another independent parameter. For instance, the ratio of  $v_a/V_m$  is often used instead of the parameter  $a/d$ .

### 3. Direct and indirect effects

Pulsations can influence heat transfer "directly" and "indirectly." Indirect effects appear when pulsations work like a trigger initiating significant change of the flow near the particle. In these cases the action of pulsations can be sometimes replaced with the other equivalent steady-state action. For instance, the transition of the laminar boundary layer into turbulent boundary layer at the sphere surface can be initiated both with pulsations and with the Prandtl ring.

Among the conceivable indirect reasons of the mean heat transfer change due to flow pulsations, there are following: initiating of the flow stall (when the steady flow was unstalled), displacement of the flow separation location; transition of the laminar boundary layer into turbulent one, displacement of the transition location; change of the vortex movement pattern behind the particle, etc.

### 4. Quasi-steady-state heat transfer

If an amplitude and frequency of pulsations are not large, and if there are no "trigger" effects, heat transfer is quasi-steady-state. It means that at every point in time an instantaneous value of heat transfer rate may be calculated with the equation obtained for the steady-state conditions:

$$Nu_p = Nu_p(Re_p, Kn_p, T_p/T_g, \varepsilon, L/d) \quad (4)$$

where the relative velocity  $(V-u)$  is used in  $Re_p$ . Instantaneous value of  $V$  must be calculated as a geometrical sum of the average (main),  $V_{av}$ , and pulsating,  $v$ , relative velocities. For the quasi-steady-state case equation (4) is further simplified, and an influence of pulsation is taken into account with one, instead of two, dimensionless parameter containing a pulsating velocity amplitude. Assuming the values of  $T_p/T_g$ ,  $\varepsilon$ , and  $L/d$  are the same in pulsating and steady state flows, it is easy to obtain the ratio of the heat transfer coefficients:

$$h/h_0 = (1/P) \int_0^P [(V-u)/(V_0-u_0)]^n dt \quad (5)$$

The values of  $V$  and, therefore, of  $h/h_0$ , depend on the direction of pulsating velocity. For definiteness sake assume the pulsating velocity is Sin function of time, and the  $n = 0.5$ . The last value is usually a good approximation for rounded and not very large particles. If the velocity of pulsations is perpendicular to the main velocity  $V_0$ , formula (5) changes to the following one:

$$h/h_0 = (1/2\pi) \int_0^{2\pi} \{1 + [(V_a - u) \sin x / (V_0 - u_0)]^2\}^{0.25} dx \quad (6)$$

If the directions of the pulsating and main velocities are congruent, the influence of pulsations is described with the formula:

$$h/h_0 = (1/2\pi) \int_0^{2\pi} |1 + (v_a - u) \sin x / (V_0 - u_0)|^{0.5} dx \quad (7)$$

Values of  $h/h_0$  calculated with formulas (6) and (7) are presented on **Figure 1**. It can be seen that perpendicular pulsations (curve 1) substantially increase heat transfer coefficient if a value of an amplitude of relative pulsating velocity is comparable with the main velocity. Longitudinal (congruent) pulsations (curve 2) increase heat transfer only in the range  $(v_a - u)/(V_0 - u_0) > 1.8$ .

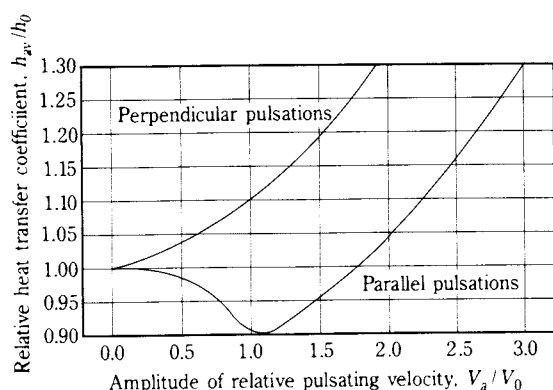


Fig. 1 Influence of pulsations on quasi-steady-state heat transfer coefficient.

To evaluate actual pulsation use benefits, the instantaneous values of relative velocities, and then heat transfer coefficients, residence time, and the average value of transferred heat (formula (1)) must be calculated. There are no universal formulas for such calculations. Usually they must be done numerically with the use of some empirical data. The accuracy of results will depend on a real particles shape and size distribution, parameters of main and pulsating flow, material to gas flow rate ratio, dimensions of apparatus, introduction velocity of particles, and the location of the entrance. Though analytical results may be obtained only with some simplifying assumptions, they proved to be useful as a tool of estimation of the possible benefits of pulsations. Most of the known analytical results are related to the very small ("airborne") particles. In this paper we present some results for the important case of large particles [1]. The following assumptions were made:

1. A constant mass particle is moving vertically upwards entrained by a gas stream oscillating with a period  $P$ . Gas velocity equals  $V_g = V_1 = V_{av} (1+m)$  during the interval  $t_1$  of the cycle period, and  $V_g = 0$  during the interval  $t_2 = P - t_1$ .
2. Gas specific weight is negligibly small in comparison with that of a particle.
3. Collisions of the particle with walls and with other particles are not considered.
4. Drag coefficient of the particle does not depend on the gas velocity and particle orientation.

Expressions for a particle velocity were obtained for the so-called "steady" interval of particle movement (steady in the sense that the particle motion in each successive period does not differ from its motion in the preceding period). Heat transfer then was calculated with a quasi-steady-state assumption

that in each point of time the relation  $Nu \sim |V_g - u|^n$  is valid. As a particle velocity in the upward steady-state flow is  $(V_0 - V_t)$  and  $Nu_0 \sim V_t^n$ , it is easy to see that

$$Nu_{av}/Nu_0 = [(V/V_t - u/V_t)^n + m(u/V_t)^n]/(1+m), \quad (8)$$

and the ratio of particle residence times is:

$$t/t_0 = (V_0 - V_t)/u. \quad (9)$$

Analysis of the obtained solution revealed the minimum mean gas velocity,  $V_{min}$ , required to transport particles in a pulsating flow is less than that velocity in a flow without pulsations (which is the terminal settling velocity of the particle,  $V_t$ ):

$$V_{min}/V_t = (1+m)^{-0.5}. \quad (10)$$

This allows substantial reduction of the pulsation gas flow rate and even the use of the regime with  $V_{av} \leq V_t$ . Due to the possible substantial reduction of the average (mean) gas and particle velocities in a pulsating flow, the gain in the particle residence time may prove to be greater than the possible reduction of the heat transfer coefficient, and then the quantity of the transferred heat may be increased. Heat transfer increase may be also achieved in the opposite case, when the residence time reduces but the coefficient of heat transfer increases. In the work [1] two important cases were analyzed: 1. Equal flow rates ( $V_{av} = V_0$ ), and 2. Equal safety margin for reliable pneumatic transportation [ $V_{av}/V_0 = (1+m)^{-0.5}$ ] in pulsating and steady-state flows. As an illustration, a part of the results of calculations for the case ( $V_{av} = V_0$ ),  $n = 0.8$ , and safety ratio  $V_0/V_t = 3$  are presented on **Figure 2**. It is seen that, while retention time reduces, coefficient of heat transfer and heat transferred to the particle in the pulsating flow increase as compared to the flow without pulsations. Maximum value of transferred heat corresponds to  $m \approx 2$  and slightly reduces if  $m$  increases.

The above examination has been made for the "steady" section of the apparatus. Heat transfer was evaluated also for the so-called accelerating section. For the limiting case, when a particle is introduced in the apparatus with the initial velocity  $u = 0$ , the following formula is valid:

$$Nu_{av}/Nu_0 = (V_{av}/V_0)^n/(1+m). \quad (11)$$

It can be seen from (11) that in the accelerating section heat transfer reduces for both condition  $V_{av} = V_0$

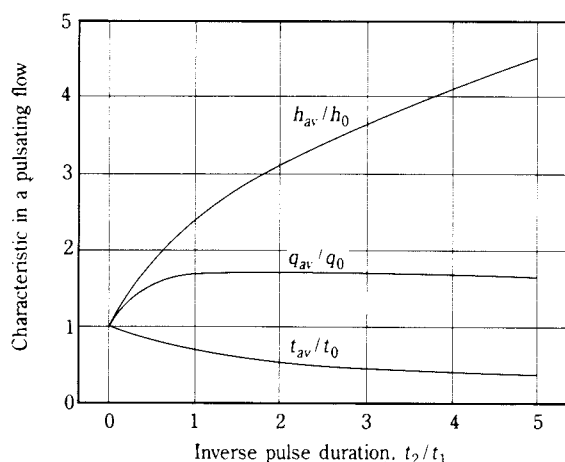


**Fig. 2** Residence time and heat transfer in quasi – steady – state upward pulsating flow.  $V_{av} = V_0$ ,  $V_0/V_t = 3$ .

and condition  $V_{av}/V_0 = (1+m)^{-0.5}$ . Therefore, the employment of the quasi – steady – state pulsating flow may be not profitable if the apparatus is relatively short and, therefore, the length of accelerating section is substantial.

## 5. Unsteady-state effects

As is evident from the foregoing that the substantial heat transfer increase in quasi – steady – state regime can be achieved only if the magnitudes of pulsation and main velocities are of the same order. Two means to generate large pulsations – a special valve – pulsator installation or/and providing for the resonance pulsations – have certain shortcomings. There were many attempts to intensify a process with the small amplitude pulsations, for instance, by applying sound or ultrasound waves to the gas flow. While some results were promising, the other didn't show a change of heat transfer at all. It is obvious that the knowledge of the "critical" pulsation parameters which divide steady-state and unsteady-state pulsation regimes, can help to explain the unsuccessful results and to correctly select pulsation parameters.

Unsteady-state effects may appear when the time of gas parameters change is small, and, therefore, steady-state heat transfer is not achieved. Physically, it can be explained by the well-known phenomena: creation of the hydrodynamic and temperature boundary layers, as well as of the vortex zone behind the body, takes time. The magnitude of this time depends mainly on the shape of the body and on the numbers  $Re_p$  and  $Pr$ . To experimentally define

this time, transient heat transfer of the cylinder with the vortex zone behind it was investigated in the work [2]. A cylinder was selected as a typical bluff body and, therefore, the results of the tests could be applied, at least semi – quantitatively, to other shape bluff bodies (spheres, etc.). In that work parameters of the gas flow changed abruptly, and the time of transition to the steady – state heat transfer regime was measured. The results proved that the transition time may be approximately estimated with the dimensionless number  $Ho \approx 5$ . This value is in a good agreement with the frequency of developing and separation vortices which in the broad range of  $Re$  numbers is defined with the relationship:

$$Sr_p \approx 0.2 \quad (12)$$

To obtain values of critical pulsation parameters, the usual theoretical approach can be used: the steady – state range of hydrodynamic and related to them heat transfer parameters is achieved if the local acceleration member in the Navier – Stokes equation is small in comparison to convective acceleration members [3, etc.]:

$$\partial V_g / \partial t \ll V_g \partial V_g / \partial L. \quad (13)$$

In the case of periodic pulsations the analysis was fulfilled in the work [5]. It can be assumed:  $\partial V_g / \partial t \sim V_g / P$ ,  $\partial V_g / \partial L \sim V_g / d$ . Then the equation (13) transforms into an expression:

$$Sr_p \ll 1. \quad (14)$$

The condition (14) can be refined for the particular cases of pulsations perpendicular and parallel to the main flow velocity. For harmonic pulsations parallel to the main flow, the relative gas velocity is  $[V_0 + v_a \sin(\omega t) - u]$ . If particles are very small, the relative pulsation velocity  $[v_a \sin(\omega t) - u]$  is small, and the situation around the particle is quasi – steady – state. The maximum influence of pulsations may be achieved for the large particles, when  $u \approx 0$ . Then  $\partial V_g / \partial t \sim v_a / P$ , and expression (14) can be replaced with an inequality

$$Sr(v_a/V_0) \ll 1. \quad (15)$$

The other form of the same quasi – steady – state condition can be obtained if to take into account equation  $v_a = 2 \pi a f$ :

$$Sr_p(a/d)^{0.5} \ll 1. \quad (16)$$

If the direction of pulsations is perpendicular to the main velocity, the absolute value of relative gas velocity for the large particles is  $[V_0^2 + v_a^2 \sin^2(\omega t)]^{0.5}$ . If the ratio  $v_a/V_0$  is small, the influence of velocity direction pulsation on the heat transfer is negligible. As  $\partial V_g/\partial t \sim v_a^2/V_0 P$ , the quasi-steady-state condition for perpendicular pulsations is:

$$Sr_p (v_a/V_0)^2 \ll 1. \quad (17)$$

or in the other form:

$$Sr_p (a/d)^{2/3} \ll 1. \quad (18)$$

To experimentally verify relations (17) and (18) and define magnitudes of critical parameters, heat transfer between air flow and a vibrating small size cylinder was investigated in the work [4]. The use of body vibrations, instead of gas pulsations, allowed to accurately measure pulsation parameters: velocity and amplitude. The experiments confirmed the structure of the given above critical parameters complexes. Their values for longitudinal pulsations were defined as follows (it was assumed that deviation from quasi-steady-state heat transfer should be 1%):

$$[Sr_p (a/d)^{0.5}] = 0.03 \sim 0.055, \quad (19)$$

or

$$[Sr_p (v_a/V_0)] = 0.008 \sim 0.019. \quad (20)$$

Expressions (19) and (20) were obtained in the ranges:  $Re_p = 200 \sim 3000$ ,  $Sr_p < 0.12$ ,  $v/V_0 < 0.6$ . The turbulence influence wasn't expressly analyzed though parameter  $\varepsilon$  was measured with a thermo-anemometer. The value of  $\varepsilon$  depended on the flow rate and varied in the range  $2 \sim 6\%$ . Parameter  $L/d$  in the tests was constant. Smaller values in formulas (19) and (20) correspond to the smaller turbulence of the air flow. It can be explained thus: the less are "natural" pulsations of the main flow, the greater is an influence of additional disturbances caused by induced pulsations. The results, probably, may be used in the extended range of  $Re_p$  numbers if the pattern of the gas flow is similar to the investigated one.

Critical parameters for perpendicular pulsations were larger than critical parameters for parallel vibrations. This is in a good agreement with the fact that the acceleration of perpendicular pulsations is less than the acceleration of parallel pulsations of the same amplitude and frequency: it can be shown that their ratio equals  $0.5 v_a/V_0$ . The exact values of critical parameters for perpendicular pulsations were not defined because experiments in the work [4] were conducted at the values of  $Sr_p$  number

close to 0.2, and the maximum of heat transfer related to the vortex separation [5] masked the "direct" unsteady-state-effect.

## 6. Related phenomena

### 6.1 Resonance

Three different resonance phenomena may exist in chambers and ducts filled with a two-phase gas - particles media:

1. Local "gas-particle" resonance, corresponding to the value of  $Sr_p \approx 0.2$ , when a frequency of induced pulsations is close to the frequency of vortexes separation from the particle surface [5]. As the well-developed vortex flow can appear only behind the large particles, when  $Re_p \geq 40 \sim 50$ , and because the values of  $Sr_p$  and  $Re_p$  numbers for different size particles may differ many times in the real polydisperse flows, the possibility of the substantial influence of this kind of resonance is, probably, small.
2. Local "gas-wall" resonance, when a frequency of induced pulsations is close to the frequency of vortexes developing in the gas-wall boundary layer. This resonance influences mainly heat transfer in the area close to the wall and between the wall and gas-particle flow.
3. Large scale acoustic resonance, when a frequency of induced pulsations is close to the one of natural acoustic frequencies of the gas-particle media in the chamber and the ducts. Some experimental investigations [5, etc.] proved that the amplitudes of the resonance pulsations may be very large, even greater than the mean stream velocity. In this case the instantaneous gas velocity vector at certain times can be directed opposite to the mean velocity at the antinodes of the standing waves. Calculations showed [6] that the large amplitude resonance pulsations could substantially increase heat transfer both in the "steady" and accelerating sections of the apparatus.

### 6.2 Turbulence of the main flow

The gas flow turbulence can be treated as "natural" pulsations having a wide range of amplitudes and frequencies. As indicated above, the less are turbulent disturbances of the main flow, the greater is an influence of the induced pulsations. In practical systems an average amplitude of turbulent pulsations usually vary in the range of  $2 \sim 6\%$  of the main flow velocity. To noticeably increase heat transfer (if there are no "indirect" effects) the induced velocity pulsations

should be larger than existing turbulence velocities.

### 6.3 Nonuniformity of heat treating

It is known that small particles, as a rule, are heated faster than the larger ones in a steady – state poly-disperse particle – gas flow. Pulsations can add to this nonuniformity. It can be shown that, if the small and the large particles follow the same hydrodynamic force law, the possible relative increase of heat transferred to the small particles is larger than that to the large particles. Nevertheless, if the goal is to increase heat transfer to the large particles, and overheating of small particles is allowable, the use of pulsations may be justified. Pulsations may also reduce the nonuniformity of heat treating if the difference of particle sizes is so big that their movement is defined by different relations between the hydrodynamic force and relative velocity.

An important cause of nonuniform heat treating can be continuous change of material in the apparatus with the low frequency pulsation flow. As the particles are introduced in different phases of pulsation cycle, they receive different initial velocities, and their residence times and transferred heats are different. The differences can be especially large if particle introduction velocities are directed opposite to the main stream flow [1].

### 6.4 Agglomeration and separation

The increased difference by pulsations in small and large particle velocities, sometimes even reverse movement of a part of particles in some phases of pulsation cycle, increases both a local material concentration and the probability of agglomeration. The possible increase of residence times increases the probability of larger particles (or agglomerated clusters) fall out and separation.

## 7. Basic types of pulsation generators

### 7.1 Pulse valve – interrupter

A simple generator of pulsations is a valve – interrupter of the gas flow. It is usually installed in the gas supply line and made, for instance, as a rotating disk or cylinder with holes. An amplitude of pulsations depends on the size of holes, and the frequency is defined by both the number of the holes and the frequency of rotation. An additional pressure loss and an influence of pulsations on the accuracy of the flow rate measurements are inherent in such pulsators.

### 7.2 Sound generator

Sound waves in gases are longitudinal relatively to the source of the sound. The amplitude of sound waves velocity depends mainly on the sound intensity,  $I$ , and the gas properties: composition, density, and temperature. For the air at atmospheric pressure and temperature  $20^{\circ}\text{C}$ , an amplitude of pulsation velocity is:  $v_a = 0.007$  m/sec at  $I = 100$  db,  $0.069$  m/sec at  $120$  db,  $0.69$  m/sec at  $140$  db, and  $6.93$  m/sec at  $160$  db. The known experimental investigations showed that usually only big amplitude sound waves ( $I > 130 \sim 140$  db) could increase the forced convection heat transfer rate. To protect the maintenance personnel against the high intensity sound, the apparatus must be well insulated.

### 7.3 Pulsating combustion

The period of 15 – 20 years after The World War II was the time when a lot of engineers and scientists investigated pulsating combustion. They tried to develop the new technology of efficient gas and liquid fuel combustion, and to use the high temperature pulsating flow of combustion products for heating, drying and other industrial processes. However, the optimistic expectations, based initially on the German missile pulsating combustion engines experience, were not realized. Additional stresses in structural elements caused by pulsations which are especially large in the case of resonances can substantially reduce the structure endurance limit. Combustion chambers, as well as other parts and structures influenced by pulsations, must be reinforced, and, therefore, their weight and cost increased. This is probably the main reason why pulsating combustion is not used now not only in transport engines, industrial and power plants but, probably, in all types of large scale apparatus. Like in the case of other pulsating generators, the decision of pulsating combustion chamber use should be done in each particular case after complete evaluation of the possible expenses and benefits.

### 7.4 Periodic change of the apparatus cross section area

Pulsations of gas velocity may be organized along the particle path by the periodical change of the channel cross section. Particles decelerate in a large area section of apparatus and accelerate in the small area section. In this case there is no need in a special pulsation generator use. An analysis of such process with vertical transportation of large particles was done in the work [7].

## 8. Cost

### 8.1 Capital investment

The capital investment depends on the particular pulsation generator and apparatus design (or re-design). Though dimensions of the apparatus may be reduced due to increase of heat transfer efficiency in a pulsation flow, some additional equipment must be installed: a generator of pulsations, a damper in the gas line before or after the fan and flow meter, etc. Besides, some money should be invested in the possible reinforcement of the structure.

### 8.2 Expenditure of energy

The use of pulsations usually causes an additional energy consumption. Even if the energy consumption by the pulsation generator itself is small, the possible additional hydraulic pressure losses in the transportation system may be substantial. As a rule, a relative increase of heat transfer coefficient is less than the relative increase of pressure loss. Like in the case of the capital investment, the actual energy consumption depends on the specific type and parameters of the unit and process.

## 9. Conclusion

Though there is no simple method to accurately predict the result of each particular pulsation application, available data allows one to explain the mechanism of pulsation influence, to define the desirable range of pulsation parameters, to estimate anticipated benefits and expenses, and to select the proper type of pulsation generator and other equipment. The following procedure may be recommended for designing a pulsation process. First of all, absolute and relative particle velocities and interphase heat transfer coefficients in the main stream without pulsations should be calculated. The knowledge of the main stream turbulence characteristics is a plus. Then one must evaluate the boundary parameters between quasi-steady-state and unsteady state heat transfer regimes for the particles to be treated. If the quasi-steady-state heat transfer regime is anticipated the transverse pulsations (when the pulsation velocity is perpendicular to the main flow) are usually preferable. Longitudinal pulsations (when the pulsation and main flow velocities have the same direction) may be preferable in the unsteady-state range of parameters. The possibility of trigger effects, large scale and local resonance phenomena should be verified. The total effect of pulsation application can be obtained by calculation of the product of the heat

transfer coefficients and residence times of the particles. After pulsation parameters are defined, pulsation generator and other equipment providing for these parameters may be selected. The final decision can be made after a comparison of all benefits and expenses related to the pulsation use. The expenses depend on the additional pressure loss, possible quality reduction due to secondary effects (agglomeration, etc.), and additional capital investment including the noise suppression and unit structure reinforcement, if necessary.

## Nomenclature

$a$	Pulsation (vibration) amplitude,	mm
$d$	Particle diameter,	mm
$f$	Pulsation (vibration) frequency,	Hz
$h$	Heat transfer coefficient,	W/m <sup>2</sup> /°C
$I$	Sound intensity	db
$L$	Scale of turbulence,	m
$m$	$= t_2/t_1$ - cycle parameter	dimensionless
$n$	Exponent in the relation $Nu \sim Re^n$	dimensionless
$q$	Heat	J/m <sup>2</sup>
$P$	Period of pulsation (vibration)	sec
$t$	Time	sec
$T$	Temperature	°C
$v$	Pulsation (vibration) velocity	m/sec
$u$	Particle velocity	m/sec
$V$	Gas velocity	m/sec
$x$	$= 2\pi ft$ - variable of integration	dimensionless
$\varepsilon$	Intensity of turbulence	dimensionless, %
$\lambda$	Thermal conductivity	W/m/°C
$g$	Acceleration of gravity,	m/sec <sup>2</sup>
$\nu$	Kinematic viscosity of gas	m <sup>2</sup> /sec
$l$	Mean free path of gas molecules,	mm

## Dimensionless Numbers:

$Bi_p$	Biot number,	$hd/\lambda_p$
$Gr_p$	Grashof number,	$gd^3(t_g - t_p)/(t_g + 273)/\nu_g^2$
$Ho$	Dimensionless time number,	$tV/d$
$Kn_p$	Knudsen Number	$l/d$
$Nu_p$	Nusselt number	$hd/\lambda_g$
$Pr$	Prandtl number	$\nu_g c_g e_g/\lambda_g$
$Re_p$	Reynolds number	$Vd/\nu_g$
$Sr_p$	Strouhal number	$fd/V$

## Subscripts:

$a$	Amplitude value
$av$	Average (mean value)
$g$	Gas
$min$	Minimum value

- $o$  Value in the steady – state flow
- $p$  Particle
- $t$  Terminal velocity

## References

- 1) Parnas, A.L., and S.S. Zabrodskiy: Collected articles “Heat and Mass Transfer in Disperse Media”, 79–86, Belarus Academy of Sciences, Institute of Heat and Mass Transfer, Nauka i Tekhnika, Minsk, USSR, 1965 (in Russian)
- 2) Parnas, A.L.: Collected articles “Problems of Unsteady–State Heat and Mass Transfer”, 30–35, Belarus Academy of Sciences, Institute of Heat and Mass Transfer, Nauka i Tekhnika, Minsk, USSR, 1965 (in Russian)
- 3) H. Schlichting: Grenzschicht–Theorie, Verlag G. Braun–Karlsruhe, Germany, 1958.
- 4) Parnas, A.L.: Collected articles “Problems of Unsteady–State Heat and Mass Transfer”, 25–29, Belarus Academy of Sciences, Institute of Heat and Mass Transfer, Nauka i Tekhnika, Minsk, USSR, 1965 (in Russian).
- 5) Parnas, A.L.: Journal of Engineering Physics, 10, 37–44, 1964, Int. Chem. Eng., 213 –217, 2, 1967.
- 6) Zabrodskiy, S.S., and A.L. Parnas: Journal of Engineering Physics, 6, 778 – 782, 1965.
- 7) Elperin, I.T., and A.L. Parnas: Journal of Engineering Physics, 3, 352 – 356, 1966.

## Author’s short biography



### Anatole Parnas

Dr. Anatole Parnas graduated from Moscow Power Institute and Luikov Institute of Heat and Mass Transfer of Belarus Academy of Sciences. His major research interests are related with applications of Theory of Combustion, Thermal/Fluid Science, and Mechanics to various industrial processes: particulate materials heat treating, heat treating of metals, heat transfer and thermal stresses in electronic devices. He also fulfilled some experimental research, analytical and numerical analysis of theoretical problems of heat transfer and mechanics, including unsteady-state convective heat transfer, heat transfer in dispersed media, pulsating combustion, and vibrations and stresses in shafts and plates. Currently he is with American Combustion, Inc.

# Adsorption of Microorganisms to Sand and Diatomaceous Earth Particles Coated With Metallic Hydroxides\*

J. Lukasik, S.R. Farrah

Department of Microbiology and Cell Science, University of Florida\*\*

S. Truesdail, D.O. Shah

Department of Chemical Engineering, University of Florida\*\*\*

## Abstract

*Particles of diatomaceous earth and sand were coated with metallic hydroxides. The coating increased the concentration of metals associated with the particles, their zeta potential, and their ability to adsorb microorganisms in water. The maximum adsorption of microorganisms was achieved using particles coated with a combination of ferric hydroxide and aluminum hydroxide.*

## 1. Introduction

Metallic hydroxides flocs (ferric hydroxide and aluminum hydroxide) have been used to treat water and waste water for many years (1). These flocs have been found to adsorb microorganisms and to remove them from the water following settling or filtration. Metallic hydroxide flocs have also been used in procedures to recover viruses from water as part of detection procedures (11,12). In both applications, efficient adsorption of microorganisms has been observed.

Combining metallic hydroxide flocs with microporous or depth filters has had limited success in producing flow-through filters for adsorbing microorganisms in large volumes of water. The flocs are either not retained by the filters or clog the filters and greatly restrict the flow of water (5,9).

It is also possible to coat sand or diatomaceous earth by using pre-formed flocs of metallic hydroxides or by forming the flocs in solutions that are in contact with the particles (2,3,4,8). Coating particles with a metallic hydroxide by these procedures increases their ability to adsorb microorganism (2,3,8) and metallic ions (4) from water. However, the coating procedure may have to be repeated many times (up to 15 times) or require a relatively long contact time (24 to 36 hrs) to ensure coating (2,3,4,8). Also, the coatings formed may not be stable and may be detached from the particles in contact with water (2,3).

In previous studies, we have found that forming metallic hydroxides directly on the surface of a particle

or inside the fibers of a filter produces a stably modified solid. Also, combinations of metallic hydroxides can be deposited on a particle (5,6).

In this paper, we have expanded our previous studies by including sand and by determining the adsorption of bacteria along with viruses. Both sand and diatomaceous earth particles coated with a combination of ferric hydroxide and aluminum hydroxide efficiently removed bacteria and bacteriophages from water.

## 2. Materials and experimental procedure

Diatomaceous earth (grade 1) was obtained from Sigma Chemical Co., St. Louis, MO. Sand was obtained from local sources and sieved to 50 or 100 mesh. For coating with one metallic hydroxide, the sand or diatomaceous earth was mixed with sufficient solutions of ferric chloride, magnesium chloride or aluminum chloride to cover it for 30 minutes. The specific solutions are given in **Figures 1 and 2** and **Tables 2 and 3**. Excess liquid was drained and the solids were allowed to air dry. The samples were then mixed with approximately 2 volumes of 3 N ammonium hydroxide for 10 min, rinsed with deionized water to remove excess precipitates, allowed to dry and rinsed again. Particles were coated with combinations of metallic hydroxides as described above except that solutions with different concentrations of ferric chloride, magnesium chloride and aluminum chloride were used. Sequential coating of particles was accomplished by treating the particles with either ferric chloride, magnesium chloride or aluminum chloride then forming the corresponding hydroxide as described above and then repeating the procedure using a different salt for the second coating.

\* Journal paper no. R-05459 from the Florida Agriculture Experiment Station, Gainesville

\*\* Box 110700, Gainesville, FL 32611-0700 U.S.A

\*\*\* Box 116050, Gainesville, FL 32611-6050 U.S.A

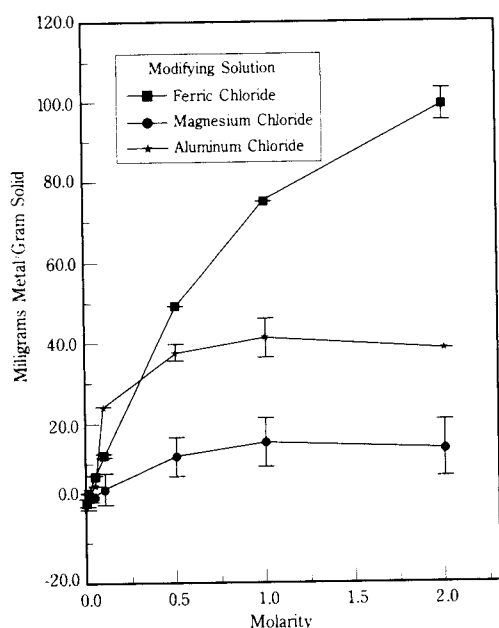


Fig. 1 Metal Composition of Modified Diatomaceous Earth

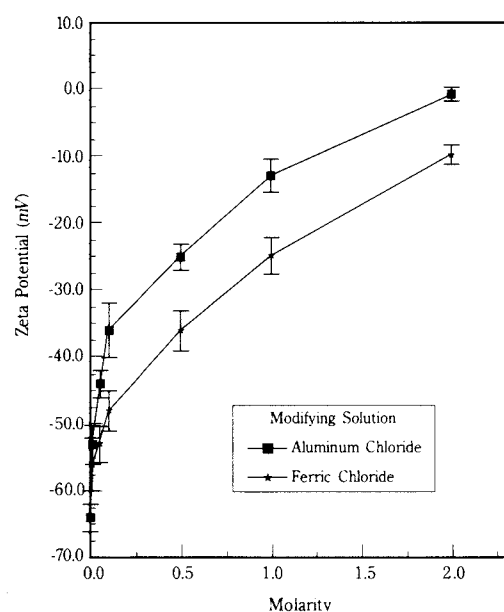


Fig. 2 Zeta Potential (mV) of diatomaceous Earth vs. Molarity of Modifying Solution

Table 1. Comparison of the removal of microorganisms by diatomaceous earth treated sequentially with two metal salts or a single metal salt<sup>1</sup>.

Single Treatment	PRD-1 Removal (Log <sub>10</sub> )	Sequential Treatment Salt #1 → Salt #2	PRD-1 Removal (log <sub>10</sub> )
AlCl <sub>3</sub>	2.54 ± 0.04	0.25M FeCl <sub>3</sub> → 0.1M AlCl <sub>3</sub>	2.95 ± 0.05
FeCl <sub>3</sub>	1.71 ± 0.03	0.25M FeCl <sub>3</sub> → 0.5M AlCl <sub>3</sub>	3.56 ± 0.05

<sup>1</sup> Batch Adsorption experiments were conducted in buffer at pH 7 using 0.5g diatomaceous earth as described in the text.

Table 2. Removal of bacteria and bacteriophages in batch experiments by sequentially treated or untreated sand and diatomaceous earth from seeded pH 7 buffer<sup>1</sup>.

Microorganism	Log <sub>10</sub> Reductions For			
	Untreated Sand	0.5M FeCl <sub>3</sub> → 1M AlCl <sub>3</sub> Treated Sand <sup>2</sup>	Untreated Diatomaceous Earth	0.25M FeCl <sub>3</sub> → 0.5M AlCl <sub>3</sub> Treated D.E. <sup>2</sup>
<i>S. Aureus</i>	0.21 ± 0.03	3.34 ± 0.09	0.33 ± 0.01	3.91 ± 0.09
<i>S. Faecalis</i>	0.29 ± 0.02	2.76 ± 0.07	0.36 ± 0.02	3.31 ± 0.10
<i>E. Coli</i>	0.20 ± 0.02	2.18 ± 0.08	0.34 ± 0.03	2.27 ± 0.06
<i>S. Typhimurium</i>	0.32 ± 0.03	2.33 ± 0.12	0.53 ± 0.07	2.59 ± 0.11
MS-2	0.20 ± 0.01	3.26 ± 0.22	0.22 ± 0.02	5.06 ± 0.21
ΦX-174	0.09 ± 0.006	3.06 ± 0.11	0.13 ± 0.01	3.81 ± 0.12
PRD-1	0.18 ± 0.09	2.78 ± 0.04	0.21 ± 0.05	4.03 ± 0.14

<sup>1</sup> Sand or diatomaceous earth was soaked first in a ferric chloride solution, allowed to dry, soaked in 3M ammonium hydroxide, rinsed and dried, soaked in an aluminum chloride solution, dried, soaked in 3M ammonium hydroxide, then it was rinsed and dried.

<sup>2</sup> Sand or diatomaceous earth was soaked in a ferric chloride solution, allowed to dry, soaked in 3M ammonium hydroxide, rinsed and dried, soaked in an aluminum chloride solution, dried, soaked in 3M ammonium hydroxide, then it was rinsed and dried.

Table 3. Removal and recovery of bacteriophages from water by sand columns or diatomaceous earth filters<sup>1</sup>.

Procedure	Bacteriophages		
	PRD-1	ΦX-174	MS-2
<b>Diatomaceous Earth Filters</b>			
Treated <sup>2</sup>			
Percent Removal	99.934%	99.996%	99.987%
Percent Recovery	34%	40%	45%
Untreated			
Percent Removal	50.12%	27.31%	15.48%
<b>Sand Columns</b>			
Treated <sup>3</sup>			
Percent Removal	61.690%	85.659%	72.683%
Percent Recovery	36%	43%	48%
Untreated			
Percent Removal	8%	11%	14%

<sup>1</sup> Twenty liters of dechlorinated tap water was seeded with indicated bacteriophage and passed through filters containing modified or unmodified diatomaceous earth or through columns containing modified or unmodified sand.

<sup>2</sup> Five grams of unmodified or diatomaceous earth modified sequentially with 0.25M ferric and 0.5M aluminum chloride as described in the text was packed in a series of two 47mm holders with a fiberglass filter sheet.

<sup>3</sup> A 60 × 3 centimeter column was packed with either unmodified or sand modified sequentially with ferric and aluminum chloride as described in the text.

The amount of metal deposited on the particles was determined by first mixing samples of sand and diatomaceous with 5 volumes of 6 N HCl overnight. The solids were separated from the solution by settling (sand) or by centrifugation at 300 g for 5 min

(diatomaceous earth). The composition of the solutions were analyzed using an Inductively Coupled Argon Plasma (ICAP) spectrophotometer. Samples of tap water were also analyzed for metal content before and after passage through filters and columns, using the ICAP spectrophotometer.

The zeta potential of diatomaceous earth particles was measured in 0.02 M glycine 0.02 M imidazole buffer using a Lazer Zee model 501 zeta meter.

The following bacteria were used: *Streptococcus faecalis* (ATCC 19433), *Staphylococcus aureus* (ATCC 12600), *Salmonella typhimurium* (ATCC 19585), and *Escherichia coli* (ATCC 15597). The following bacteriophages and their hosts were used: MS2 (*Escherichia coli* C-3000);  $\Phi$ X 174 (*E. coli*); and PRD-1 (*Salmonella typhimurium*). The bacteria were grown in 3% trypticase soy broth overnight and then diluted 1/1000 in buffer (0.02 M glycine + 0.02 M imidazole) for adsorption studies. Phage stocks were prepared and phage assays done using their host bacteria as previously described (10).

Adsorption studies were conducted by mixing 2 grams of sand or 0.5 grams of diatomaceous earth in buffer (0.02 M imidazole + 0.02 M glycine) with the appropriate virus or bacterium for 5 min. on a reciprocating shaker. The supernatant fractions were assayed after settling (sand) or after low-speed centrifugation (300 g for 5 min for diatomaceous earth). Adsorption was determined by comparing the number of microorganisms in the supernatant fractions with the number in control samples of buffer alone. Unless otherwise stated, adsorption experiments were conducted at pH 7 and room temperature (approximately 25°C).

Bacteria and viruses adsorbed to particles were recovered by mixing the samples with 20 ml of 3% beef extract, pH 7, for 5 min. The microorganisms were separated from the solids by settling or centrifugation, as described above. The fraction recovered was determined by comparing the number of microorganisms in the beef extract with the number adsorbed.

Adsorption of phages in tap water dechlorinated by the addition of sodium thiosulfate was studied using 5 g of diatomaceous supported by fiberglass filters (0.45- $\mu$ m, Filterite Corp., Timonium MD) in a series of two 47-mm holders or approximately 400 grams of sand in 3 by 60 cm columns. Water containing added phages was passed through the filters at 100 ml/min and through the columns at 1,000 ml/min. Adsorbed phages were recovered by mixing the diatomaceous with 20 ml of beef extract or mixing the sand with 200 ml of beef extract as described above.

### 3. Results

Increasing the concentration of the salts used for modification increased the amount of metal deposited on the diatomaceous earth (**Figure 1**). The amount of aluminum or magnesium deposited did not increase much after the concentration of modifying solution was increased past 0.5 M. The concentration of iron deposited on diatomaceous continued to increase as the concentration was increased to 2 M. Higher concentrations of salts were not used since these were hygroscopic and not easily dried.

The addition of the metallic hydroxides increased the zeta potential of the diatomaceous earth particles (**Figure 2**). The zeta potential continued to increase as the concentration of salts used for modification was increased. Similar results were obtained with diatomaceous earth particles treated with magnesium chloride (data not shown).

Changing the zeta potential of diatomaceous earth particles greatly increased the ability of the particles to adsorb bacteriophages in batch tests (**Figure 3**). Increasing the zeta potential to  $-10$  mV permitted a reduction of greater than  $2.5 \log_{10}$  in the numbers of the three phages tested. Data in **Figure 3** were obtained using diatomaceous earth coated with aluminum hydroxide. Similar results were obtained with diatomaceous earth coated with ferric hydroxide or magnesium hydroxide (data not shown).

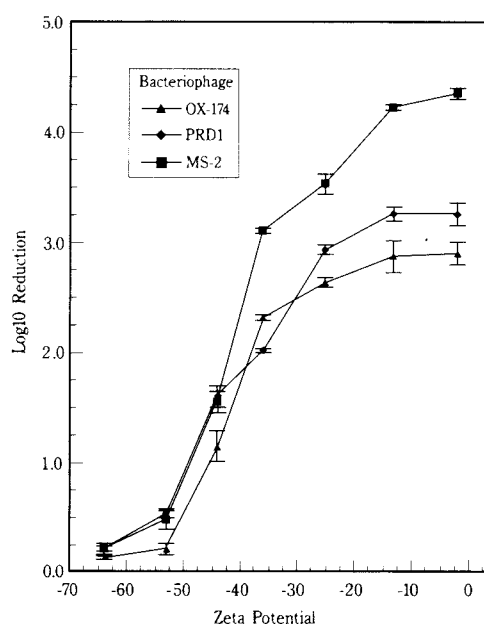


**Fig. 3** Removal of Bacteriophage From Water vs. Zeta Potential of Modified Diatomaceous Earth.

The adsorption of bacteria to diatomaceous earth coated with aluminum hydroxide was similar to adsorption of phages in that increasing the zeta potential increased adsorption (**Figure 4**). However, untreated diatomaceous earth adsorbed more bacteria than phages. Also, the removal of *E. coli* and *S. typhimurium* ( $1.5 \log_{10}$ ) was less than that observed for the phages and for *S. aureus* (greater than  $2.5 \log_{10}$ ).

Only aluminum hydroxide and ferric hydroxide were used in most tests since these have lower solubility constants than magnesium hydroxide or other metallic hydroxides (7). Additional tests were conducted using diatomaceous earth treated with different combinations of aluminum and ferric chloride. Combinations of aluminum chloride and ferric chloride between 0.1 and 2 M were used in combination or sequentially to treat diatomaceous earth and sand particles. Diatomaceous earth sequentially treated with 0.25 M ferric chloride and 0.5 M aluminum chloride adsorbed more virus than did diatomaceous earth treated with a single salt or other combinations of salts. Representative data from these tests is shown in **Table 1**.

In a similar series of tests, it was found that treating sand with 0.5 M ferric chloride and 3 M ammonium hydroxide followed by 1 M aluminum chloride and 3 M ammonium hydroxide adsorbed more microorganisms than sand treated with other combinations (data not shown). Sand or diatomaceous earth treated with the combinations of ferric chloride and aluminum chloride described above adsorbed significantly more of the microorganisms tested than did the untreated materials (**Table 2**). Filters containing diatomaceous

treated with the combination of ferric chloride and aluminum chloride as described above removed greater than 99.9% of the bacteriophages from 20 liters of dechlorinated tap water (**Table 3**). However, less than 50% of the phages could be recovered using 3% beef extract as the eluting solution. Untreated diatomaceous earth removed from 15 to 50% of the phages. Sand columns removed 62 to 86% of the phages in dechlorinated tap water. Untreated sand removed less than 15% of the phages. As with the diatomaceous earth, less than 50% of the phages could be recovered using beef extract.

The concentrations of iron and aluminum in the tap water before filtering and in the effluent from the diatomaceous earth filters and sand columns was less than 0.1 mg/l.

#### 4. Discussion

The ability of metallic hydroxide flocs to adsorb microorganisms has been useful both in treating water and in recovering viruses from water (1,11,12). This has led to studies on their immobilization on filters. Collecting preformed flocs on microporous filters has not led to the development of useful filters. Filters that retain the flocs are subject to clogging (5,6,9). Forming flocs in the presence of particles can result in coating of the particles (2,3,4,8). These coating procedures may not be efficient. Several cycles (15) of floc-formation followed by adsorption may be necessary (4) or long periods (24 to 36 hrs) of contact between the particles and flocs may be necessary to ensure coating (8). Also, the coating may not be stable enough to permit the use of the coated particles in filters used for tap water (2,3). Adsorption of a soluble metallic chloride by particles, followed by drying of the particles and then precipitation of the metals as the hydroxide leads to the formation of stable coatings. Also, coatings with multiple metallic hydroxides can be deposited on the particles (5,6). Our results show that increasing concentration of salt used to modify the particles increases the concentration of deposited metal and the zeta potential of the particles. The reason for the increase in zeta potential after the concentration of metal deposited has become stable is not known.

It is clear that the zeta potential of the modified solids is directly related to the adsorption of both bacteria and bacteriophages. Efficient adsorption of these microorganisms occurs once the zeta potential is raised above approximately  $-30$  mv (for phages) and  $-10$  mv (for bacteria).

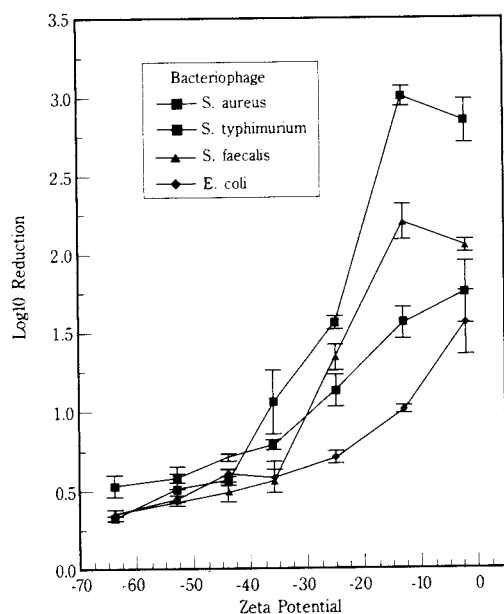


**Fig. 4** Removal of Bacteria from Water vs. Zeta Potential of Modified Diatomaceous Earth.

Coating diatomaceous earth and sand particles with a combination of ferric hydroxide and aluminum hydroxide permitted greater removal than coating the particles with only one metallic hydroxide. Filters and columns composed of particles made with these modified solids removed significantly more microorganisms than did similar filters and columns composed of untreated particles.

Attempts to recover microorganisms adsorbed to the modified particles were only partially successful. Only 50% or less of the microorganisms removed from water could be recovered in the beef extract eluting solution. Improvements in the recovery rate would make the filters more useful for detecting microorganisms in large volumes of water.

None of the metals used for coating diatomaceous earth were detected in effluents from the filters. It does not appear that leaching of the metals from

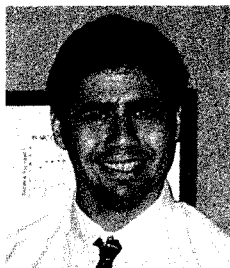
the particles will produce toxic effluents or greatly limit the length of time that the filters could be used.

In summary, we have found that the removal of bacteria and phages can be improved by using diatomaceous earth or sand particles coated with a combination of ferric hydroxide and aluminum hydroxide. Future studies will concentrate on testing the ability of the filters to remove microorganisms from larger volumes of water and on improving procedures for recovering them from the adsorbed particles.

### Acknowledgment

We would like to acknowledge the financial contribution of the Engineering Research Center (ERC) for Particle Science and Technology at the University of Florida, The National Science Foundation (NSF) grant #EEC-94-02989, and the Industrial Partners of the ERC.

### Author's short biography



**Jerzy Lukasik**  
Jerzy Lukasik received his bachelor's degree in Microbiology and cell science from the University of Florida in 1993. Currently, he is working towards the completion of his Ph.D. in Microbiology and cell science. He is also a member of the advanced separations thrust group of the Engineering Research Centers.



**Samuel R. Farrah**  
Dr. Samuel R. Farrah is a Professor in the Department of Microbiology and Cell Science at the University of Florida. He received his B.A. in Science in 1965 and his Ph.D. in Microbiology in 1974 from the Pennsylvania State University. His research interests include detecting viruses in environmental samples and adsorption of microorganisms to solids.



**D.O. Shah**  
At Present Dr. Shah is the director of the Center for Surface Science and Engineering as well as the head of two Engineering Research Centers thrust groups in the area of advanced particle processes. He received his undergraduate training at the University of Bombay and his doctoral degree from Columbia University in 1965 under the direction of the late professor J.H. Shulman a pioneer in the field of Surface and Colloid Science. In 1970 he joined the University of Florida and has received numerous awards in his illustrious career spanning over 25 years. Most recently he was the recipient of the Charles A. Stokes Professorship of Chemical Engineering, Anesthesiology and Biophysics.

**Stephen E. Truesdail**  
At present Mr. Truesdail is working towards the completion of his Ph.D. in chemical engineering at the University of Florida. He is a member of the Engineering Research Center. He received his bachelor's degree in chemical engineering from Purdue University in 1993.

# Relevance of Sol-Gel Methods for Synthesis of Fine Particles †

Helmut K. Schmidt

Institut für Neue Materialien gem. GmbH\*

## Abstract

*Sol-gel techniques are interesting for the synthesis and processing of fine particles if the problems of stabilization of colloidal particles, their agglomeration and the fabrication of green bodies with high density are solved. A new approach for the fine particle fabrication from solution was realized by controlling nucleation, growth and surface reactivity by surface modification through selected organic molecules. A variety of nanopowders (e.g.  $ZrO_2$ ,  $Al_2O_3$ , PZT) have been synthesized, and a scaling-up process has been established. Ceramic green bodies show substantially reduced sintering temperatures.*

## 1. Introduction

Synthesis and processing of ceramic or metallic powders is a very interesting direction with respect to the fabrication of new materials or the improvement of ones already in existence [1]. Inorganic particulate materials are mainly produced in two ways: one is the use of natural raw materials such as quartz,  $CaCO_3$  or  $CaSO_4$ . The other way is to produce them by synthetic processes involving chemistry in the most cases. Examples for this are  $BaTiO_3$ ,  $Al_2O_3$  or  $SiC$ . The powders are used for various purposes such as pigments for lacquers, raw materials for ceramics or as fillers for polymers. Most of the powders obtained from grinding processes possess particle sizes in the micrometer range. To gain smaller particle sizes in the nanometer range, for example, special techniques such as flame pyrolysis (for  $SiO_2$  or  $TiO_2$ ), which is an important technical process, are required. Other techniques such as evaporation and condensation through vapor phases [2], laser pyrolysis, plasma pyrolysis or others are in their infancy. There is an interesting potential connected to very small particle technologies such as very low sintering temperatures and the homogeneous introduction of additives to ceramic powders, for example. In order to exploit the potential of nanoscaled particles, it is necessary to develop appropriate production techniques which are able to fulfill the quality requirements for powders, especially the

prevention of agglomeration. The second important problem to be solved is the processing, which means it is necessary to develop methods to process nanoscaled particles into parts.

Similar ideas have been investigated in connection with sol-gel techniques using so-called sols as intermediates [3, 4]. Inorganic sols consist of nanosized particles suspended in aqueous or non-aqueous solutions stabilized by electrostatic forces. Surface charges obtained by adsorption of OH-groups or protons to the particle's surface prevent the agglomeration. The destabilization of these sols leads to gels with very low solids contents, so that this method is not suitable for ceramic parts fabrication. For these reasons, it was doubted that it is possible to use sol-gel techniques successfully for ceramic parts production (Figure 1).

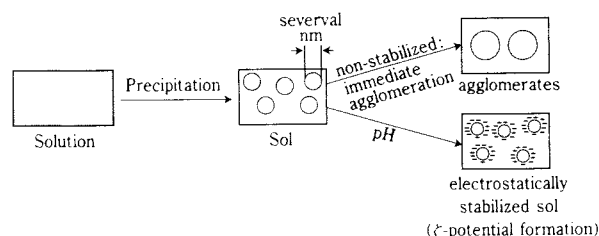


**Fig. 1** Schematic of the sol-gel process as colloidal route based on electrostatic stabilization.

\* Im Stadtwald, Geb. 43 A  
D-66 123 Saarbrücken, Germany

† Received: July 24, 1996

Based on this state of the art, investigations were carried out to overcome the problems of electrostatic stabilization by controlling the surface of the small particles by chemical means, first during the synthesis and secondly for processing. In this paper, a summary is given on the possibilities of fabrication and processing of ceramic fine powders and how to process them to materials.

## 2. General principles

In this chapter, chemical principles for the control synthesis of small particles are described. As it is well known, it is possible to precipitate a variety of materials from solutions. In this case, a nucleation step is necessary to initiate the process. The nucleation rate depends on the free energy of the nucleation step (for overcoming the critical radius for nucleation) and the free energy for the diffusion, which is a function of the temperature, liquid and size of the dissolved components to be deposited. The nucleation rate can be expressed by equation (1) and (2) [5-7].

$$I = A \cdot e^{\frac{-(\Delta G_n + \Delta G_D)}{kT}} \quad (1)$$

$$A = 2n_v \cdot v^{1/3} \frac{kT}{h} \sqrt{\frac{\sigma}{kT}} \quad (2)$$

$\Delta G_n$ : Gibbs free energy for nucleation

$\Delta G_D$ : Gibbs free energy for diffusion

$n_v$ : number of nucleating or crystallizing species per unit volume of the liquid

$v$ : volume per formula unit of the nucleating species

$\sigma$ : interfacial free energy

These equations, of course, are also valid for the growth of particles after the nucleation has taken place, if  $\Delta G_n$  is replaced by  $\Delta G_c$  (Gibbs free energy of condensation or crystallisation). In this case, the surface free energy  $\sigma$  of the growing particle becomes extremely important. These equations do not give any information about mono or polydispersity. To control the dispersity, assumptions have to be made about the interaction of surface active additives. It is assumed that each molecule requires a well defined area for optimal binding. This leads to an energy minimum at a well defined surface coverage and the total surface area of the system then will be controlled by the space requirement of the ligands. Assuming further that the growing system tends to form particles as large as possible, a minimum of the surface free energy should be obtained at a monodispersed particle size with total surface area corresponding to a complete coverage of the formed particles. This was calculated by Strehlow [8] for a Stöber system [9] and could also be experimentally shown with various surface modified systems where particle sizes could be obtained in process techniques not controlling nucleation and growth by La Mer's model [10]. In the optimal case, the Gibbs free energy of the system reaches its minimum in a monodispersed state, as described elsewhere [11]. In order to influence the surface free energy, additives with affinity to the growing particles' surface were used such as complex formers, acids and bases, surfactants or reactive silanes or components reacting to the surface (Figure 2).

Depending on the type of reaction, the growth process can be stopped or continued with different rates. The most interesting reaction type is one which does not stop the growth process but prevents agglomeration. This can be obtained by choosing the appropriate molecule to be bounded or adsorbed to the surface. Functional molecules with the second function can be used to obtain specific surface reactivities for a variety of purposes. If the second function is an inert function (e.g. the alkyl group of carboxylic acids), the interaction between particles is controlled by Van der Waals forces only. Van der Waals forces are weak compared to chemical bonds (ionic or covalent). In very small particles, these types of bonds are present in a rather high concentration per volume unit due to the high surface area and, in general, lead to irreversible agglomeration. The 'reduction' to van der Waals forces as the dominating force, however, leads to easy redispersion in suitable liquids even after drying and allows a

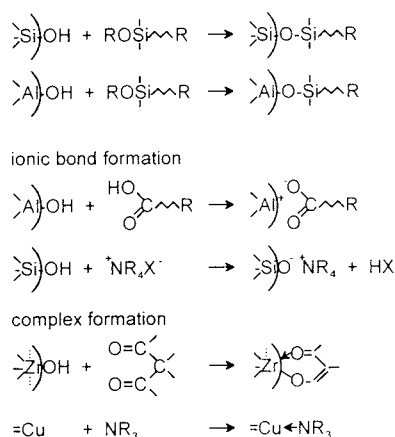


Fig. 2 Examples of surface modification principles with different types of chemical bonds.

dense packing with nano particle systems in green bodies, not obtainable with surface modification [12]. In the case of boehmite with 15 nm particle size, green bodies with densities up to 60% by volume were obtained after drying. This is not possible with electrostatically stabilized sols (gel solids content of 10–20%).

Based on these considerations, a thermodynamical model was developed [11] which postulates that by the appropriate choice and concentration of surface modifiers during a nucleation and growth process, the particle size and particle reactivities can be tailored. In **Figure 3**, an example is shown using zirconia propylate reacted with acetyl acetone and hydrolyzed by water addition. The precipitate “formed” by hydrolysis and condensation is nanoscale, and the particle size depends strongly on the concentration of the  $\beta$ -diketone. As could be shown clearly, the  $\beta$ -diketone concentration dependence of the particle size follows a reciprocal function ( $y = K \cdot 1/x$ ). The particle diameter is rather uniform ( $\approx \pm 1$  nm).

This type of reaction is called controlled growth process (CGP) and can be used for nanoparticle production for single-component systems or multi-component systems, if the nucleation and growth process of the different components is similar under the desired thermodynamical parameters.

Other examples using the interfacial free energy as a tool are microemulsion systems [12, 13, 14]. In this case, the interfacial free energy is decreased to a level such that the emulsified state becomes

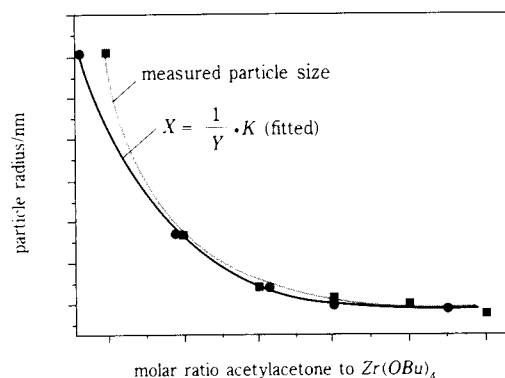


**Fig. 3** Dependence of zirconia particle sizes as a function of the complex former concentration; complex former: acetyl acetone.

stable. For this reason, ionic surfactants are generally used. However, ionic surfactants are very sensitive to the ion strength of the aqueous phase, which, in general, should be the dispersed phase in order to obtain particles by precipitation and from sol solutions. In order to avoid these complications, systems consisting of non-ionic surfactants have been built up [15], and it was possible to demonstrate that stable microemulsions could be obtained, the stability of which is independent of the dissolved salts. The flow chart of this process is shown in **Figures 4** and **5**.

The droplet size of the microemulsion can be adjusted by altering the ratio between the oil phase and the water phase as well as the type and concentration

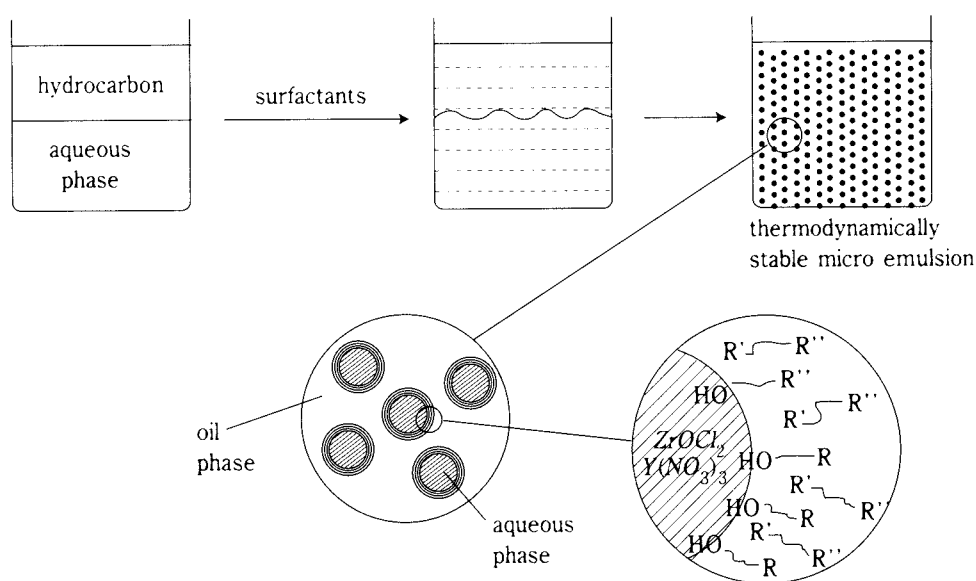


**Fig. 4** Principles for the preparation of a microemulsion with Y/Zr.

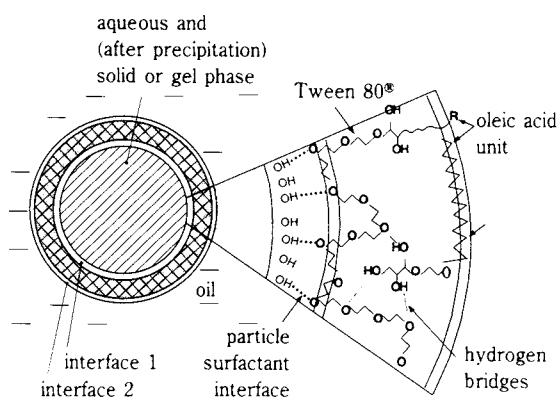


**Fig. 5** Structure of the thermodynamically stable water-in-oil microemulsion.

of the surfactants. The stability of the emulsion ends at the so-called inversion point where the water-in-oil emulsion switches to an oil-in-water emulsion. As shown by Burgard [16] with non-ionic tensides, micro-

emulsions can be stabilized in an up to 45% aqueous phase. The solid particle formation now takes place by adjusting a pH value within the droplets to precipitate the particles. In the zirconia-yttria system, base pH has to be chosen. This can either be obtained by introducing ammonia into the system or by ion exchange with basic ion exchangers and a charge transfer catalyst, for example, quaternaire ammonium bases which transport OH groups into the system. In **Figure 6**, the process routes of the microemulsion and the CGP route are compared.

The volume yield of MEP is remarkably lower, but is a more general route since it is not limited to a few components having similar growth properties. The CGP process has meanwhile been converted to a pilot-scale continuous-flow process with 1 – 2 kg yield powder per hour. The described principles have been used for the fabrication of a variety of powders such as zirconia, yttria-stabilized zirconia, bariumtitanate, PZT or alumina.

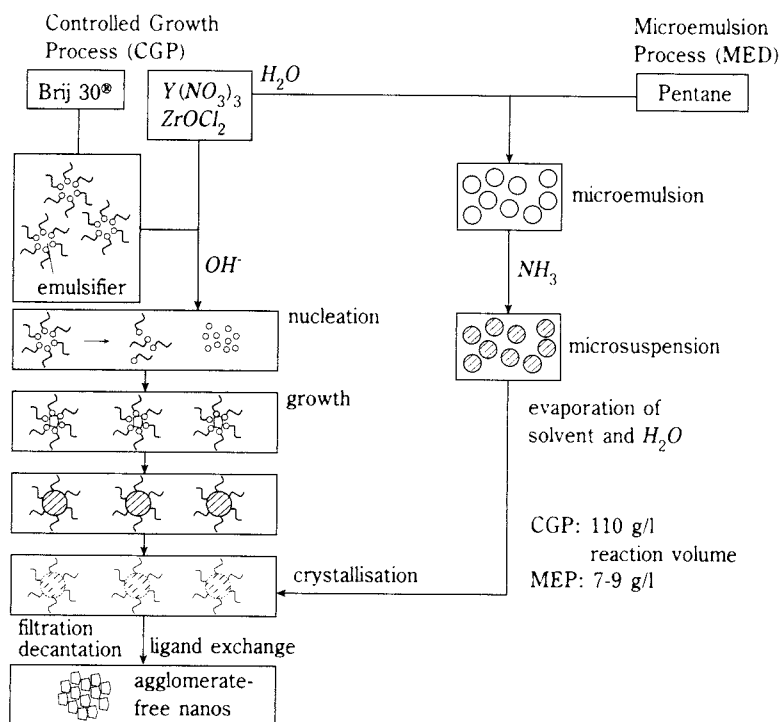


**Fig. 6** Comparison of the CGP with the MEP process and obtainable volume yields.

### 3. Powder Calcination

To obtain well-defined powders, however, the systems have to be crystallized in most cases. In **Figures 7** and **8**, the cleaning and crystallization process of  $5Y\text{-ZrO}_2$  is shown [16]. The cleaning of the nano slurry was carried out by dialysis and the crystallization by hydro-thermal treatment in the presence of  $\beta$ -diketones as surface modifiers.

In **Figures 9**, **10** and **11** [17], several other nano-scale powders produced by the CGP process are shown. As one can see, the powders are either not agglomerated at all or only to a very low degree. In each case, the powders can be redispersed in organic or even aqueous solutions very easily.

**Figure 12a** shows the  $5Y\text{-ZrO}_2$  and **12b** the HRTEM image. It shows that the particles are well crystallized.

Another route has been employed in the case of boehmite. Heavily agglomerated boehmite powder as available from industry can be redispersed by re-fluxing the system for 10 or more hours in acedic or propionic acid [18, 19, 20]. During this process, necks formed between different boehmite crystal-

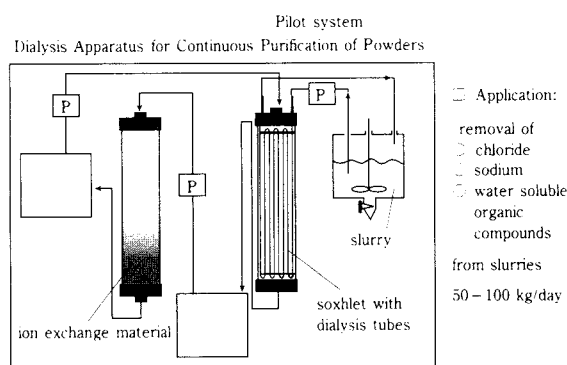


**Fig. 7** Flow chart of the cleaning process. S = storage container for the extraction liquid; P = pumps.

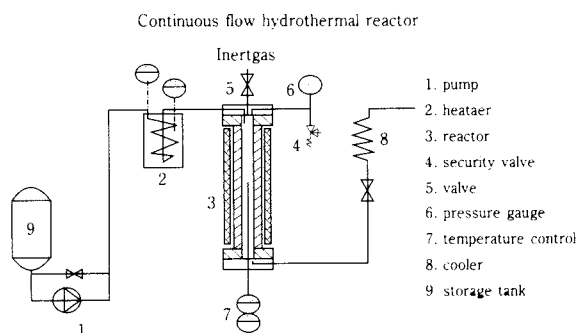


**Fig. 8** Flow chart of the hydrothermal crystallization.

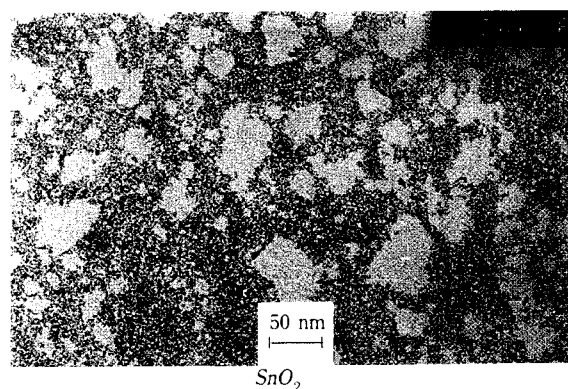


**Fig. 9** TEM micrograph of  $\text{SnO}_2$  produced by the CGP process.

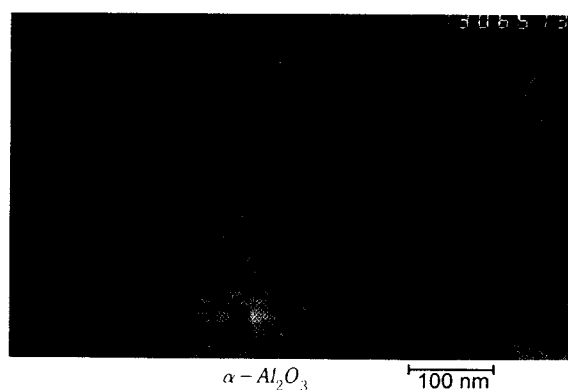


**Fig. 10** TEM micrograph of  $\alpha\text{-Al}_2\text{O}_3$  produced by the CGP process.

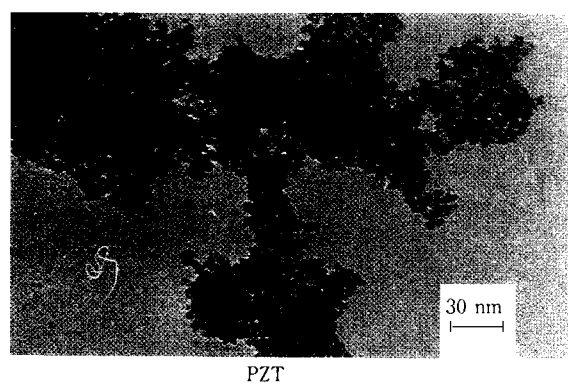


**Fig. 11** TEM micrograph of PZT powder produced by the CGP process.

lites caused by condensation can be dissolved. The deagglomerated particles are shown in **Figure 13**.

After dissolving the necks, the suspension can be filtered using nanofiltration or dialysis, resulting in viscous pastes. These pastes can be redispersed in aqueous or organic solvents such as alcohols. Surface analysis of the dried pastes by DRIFT (**Figure 14**) spectroscopy shows that the boehmite still contains about 3 wt.-% of propionic or acedic acid, which

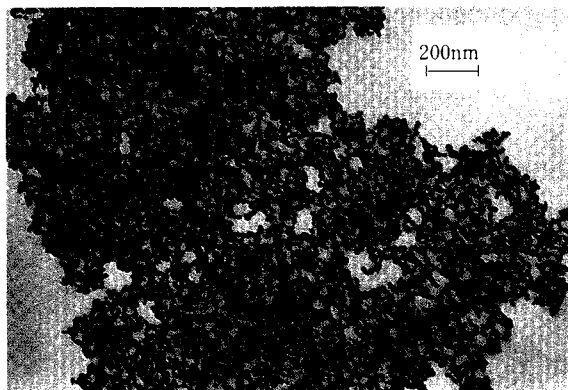


Fig. 12a Electron microscopic images of 5Y-ZrO<sub>2</sub>.

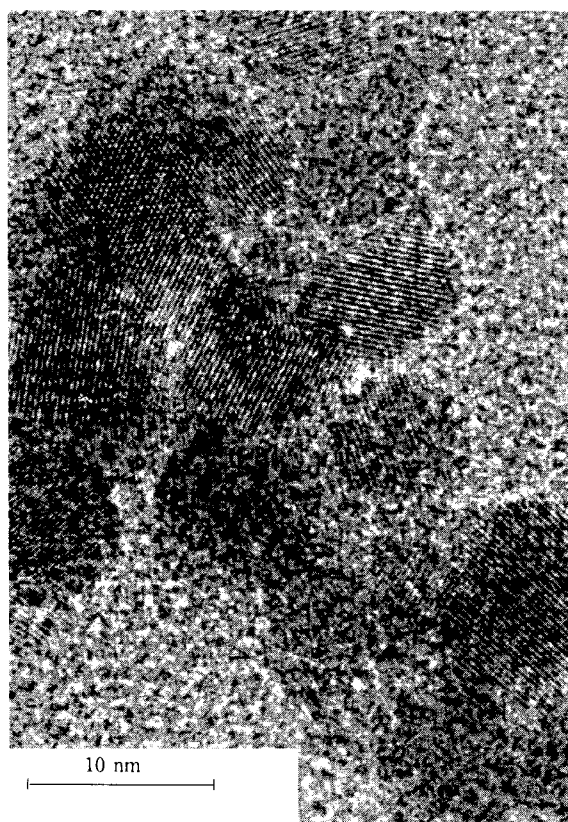


Fig. 12b Electron microscopic images of 5Y-ZrO<sub>2</sub>.

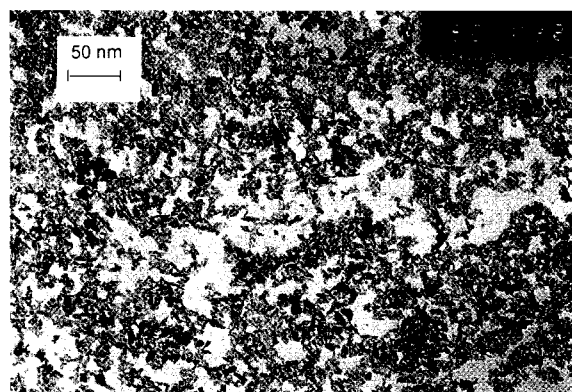


Fig. 13 TEM micrograph of 15 nm boehmite after deagglomeration.

cannot be washed out.

The increase of the solids content in comparison to electrostatically stabilized AlOOH sols does not lead to a gel point, but slowly increases the viscosity. At a solids content of about 40 to 45 vol.-%, the system forms extrudable pastes. At solids contents of about 30% by volume, slips can be formed. Extrusion of these pastes simplified by the addition of about 1 or 2 wt.-% of polyvinyl alcohol leads to shaped bodies such as tubes with solids contents up to 60% by volume after drying. This is an extraordinarily high value which has never been obtained by the simple sol-gel process. This leads to the conclusion that sol-gel techniques, despite many opinions to the contrary, will gain a new potential for ceramic processing. The drawback of sol-gel processes as discussed in the years around 1985 was that sols showed too low solids contents for ceramic parts fabrication since it was only electrostatic stabilization that was used. But with gels of 60% by volume solids contents, ceramic firing with "normal" shrinkage rates can be obtained. Of course, boehmite is not a suitable system for the processing of aluminum oxide parts, but based on these findings, a membrane fabrication process has been developed.

Due to the fact that these nanoparticles can be obtained by rather simple precipitation processes, the costs of these powders are in the range of conventional sub- $\mu$ m powders. There is still a great potential for simplifying the synthesis technique by scaling-up using the rules of chemical engineering.

#### 4. Processing of Nano-Scale Particles

As shown in the previous chapter, it is possible by appropriate surface modification to obtain redispersible nano-scale ceramic powders. In order to process these powders, several important factors have to be considered. One of the interesting potentials of processing nano-scale powders is the option of very low sintering temperatures which can be calculated from the particle radius (calculations for  $\alpha$ -alumina, for example, result in the requirement of having particle sizes below 30 nm to obtain sintering temperatures below 1000°C). Another option is to produce defect-reduced ceramics. This will only be the case if the grain growth during the densification process remains low. In this case, a new strategy for the fabrication of ceramic parts will become possible: to densify the ceramic part without the formation of large defects due to pore formation or large grain formation, and then in a second step to increase the grain growth and to form the desired

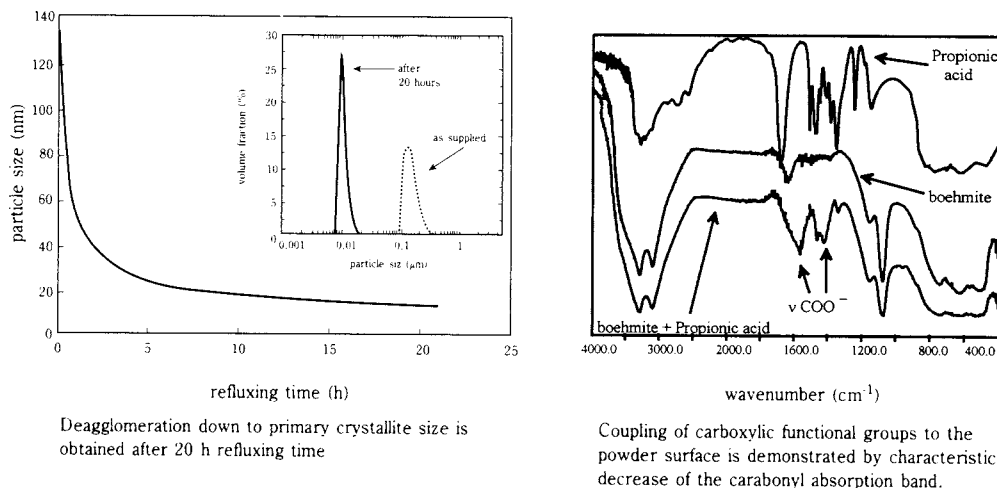


**Fig. 14** Effect of deagglomeration of boehmite using propionic acid and IR spectra of free and adsorbed propionic acid.

microstructure. For low-temperature sintering as well as for defect-free processing, it is necessary that the green body shows a homogeneous pore size, preferably in the lower nano range. In order to keep shrinkage to a tolerable level, a homogeneous green body with sufficient green density is also required.

Another interesting feature of nanoprocessing is to obtain a homogeneous distribution of additives on sub- $\mu\text{m}$  or  $\mu\text{m}$ -size powders. As is generally known, it is extremely difficult or nearly impossible to produce weakly agglomerated particles below 1  $\mu\text{m}$  by mechanical milling, and sintering additives used in low concentrations cannot be homogeneously distributed. If nanoparticles can be attached to the surface of larger particles, the additives can be fixed at the place where they are needed, namely on the particle surface.

A third option for the application of nanoparticulate systems is the field of ceramic micro-systems with the aim of keeping the defect size on the lowest possible level.

As can be easily understood, the control of the particle-to-particle interaction plays the most important role for obtaining sufficient green density as well as for the homogeneity, and is also important for the viscosity of slips. For the control of the particle-to-particle interaction, the concept of "surface lubrication" by adsorption of oligomers or polymers on top

of the particle surface was used for conventional ceramic wet processing. The adhesion of oligomers or polymers on solid surfaces is obtained by a multiple adsorption process in which one and the same macromolecule is able to develop numerous adsorption sites. This leads to a good adsorption of the macromolecules on surfaces even if the adsorption versus desorption equilibrium of one single group is poor. The use of oligomers or polymers in nanoparticle processing, however, does not lead to success because the molecular weight of these components is too high compared to the nanoparticles, resulting in a far too high organic concentration in the green body.

In order to overcome these difficulties, the so-called short organic chain molecule surface modification concept was developed. In this case, strong bonds to the surface have to be present because the concept of multiple adsorption cannot be used due to the existence of only one or two adsorptive sites per molecule. A variety of investigations have been carried out in order to seek appropriate bonding mechanisms to the surface [20, 21]. It was shown that the chemistry of surface ions in nanoparticles does not differ markedly from solution chemistry of ions. If one compares the infrared spectrum of a zirconium alkoxide reacted with a carboxylic acid with a zirconium nanoparticle or a  $\mu\text{m}$  particle surface-modified with a carboxylic acid, the frequency shift of the carbonyl grouping

is identical and resembles the frequency of a carboxylate group (**Figures 15 a and b**).

The identical  $=C=O$  frequency shift leads to the conclusion that the surface chemistry of nano and submicron particle is very similar, but with  $\mu\text{m}$ -size particles, due to the small specific surface area, this is of minor importance. As shown in [22],  $\text{Zr}(\text{OR})_4$  complexed with methacrylic acid (ma) shows exactly the same  $=C=O$  frequency shift as  $\text{ZrO}_2$  nanoparticles loaded with ma. Due to the high surface area of the nanometer particle, the potential of these reactions becomes important and provides an interesting tool for a variety of modifications.

Other investigations, for example, with  $\beta$ -diketones acting as complex formers for ions such as alumina  $3^+$  or titania  $4^+$  or zirconia  $4^+$  can also be used as surface modifiers for nano-particles, and in this case, the same effect can be found, i.e. the shift of the carbonyl frequency to the complexed forms with no difference between the ions in solution and ions on the surface of nanoparticles [22, 23, 24]. Of course, there is a large variety of molecules, for example, short organic molecules with a potential to form strong bonds to the surface. Besides the carboxylic acids and the  $\beta$ -diketones, proteins can be used as well as chelating agents or (if weak complex formers are needed) ether alcoholates [25]. The main purpose of having strong bonds to the surface is to keep the surface modifier on top of the particles and not in the solution in order to avoid disturbing effects from the modifiers.

Another type of surface modifier is constituted by reactive silanes which can be fixed reversibly on a variety of oxidic surfaces as long as stable metal-oxygen-silicon bonds are formed. If that is not the

case, these silanes can be polymerized around the particle by first adsorbing them on the surface and then polycondensing them to a silicate "shell" with functional groupings. This type of surface modification was demonstrated on superparamagnetic iron oxide particles [26]. The model is shown in **Figure 16**. The powder obtained is shown in **Figure 17**.

The described principles can now be used for a variety of different purposes. First, if bifunctional groupings with ionic functions are used, the  $\zeta$ -potential of these particles can be tailored. Tailoring of the surface charge of the nanoparticles opposite to the surface of a large particle leads to a precipitation of the small particles on top of the large particles. This principle can be used for the immobilization of additives. In equation 3, the reaction mechanism for attaching (4 nm) carbon black particles on sub- $\mu\text{m}$   $\text{SiC}$  is shown. Carbon black acts as a reducing agent for the removal of the  $\text{SiO}_2$  layer [27].

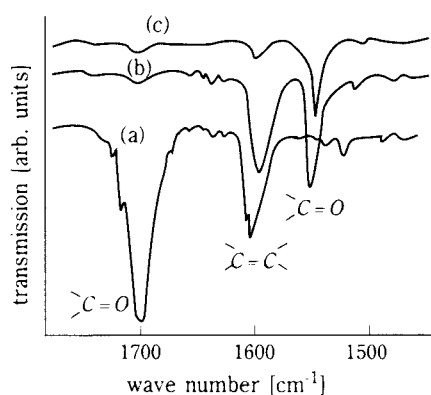
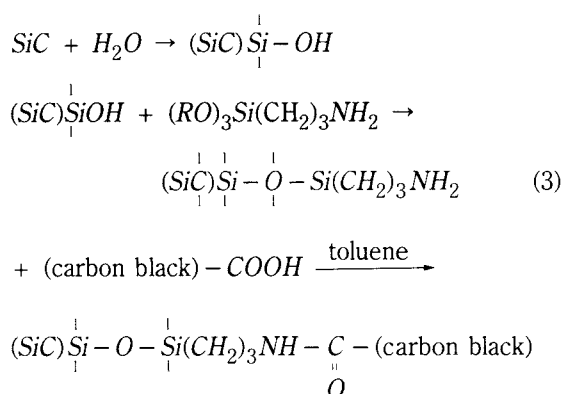


**Fig. 15 a-b** IR comparison of various  $\text{ZrO}_2$  powders loaded with carboxylic acids.

**Fig. 15a** IR spectra of (a) methacrylic acid (ma); b:  $\text{Zr}(\text{OR})_3/\text{ma}$ ; c: after hydrolysis, condensation and polymerization of the ma double bond and two weeks water exposure.

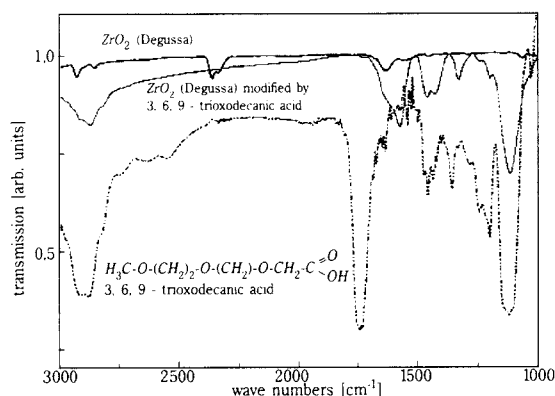


**Fig. 15b**  $\text{ZrO}_2$  submicron powder of Degussa loaded with aliphatic carboxylic acid.

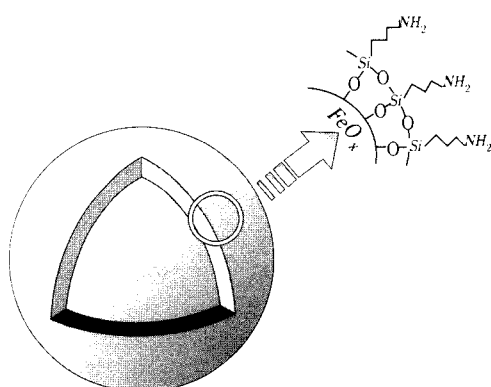


**Fig. 16** Model for the surface modification of superparamagnetic iron oxide particles by the formation of a silicate shell [after 26].

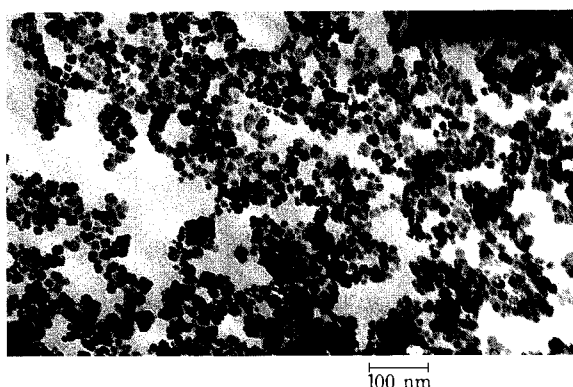


**Fig. 17** TEM micrograph of agglomerate-free nanomagnetite powder.

The effect of the silane modification on the  $\zeta$ -potential of SiC is shown in **Figure 18**. It clearly shows the effect of acid and base grouping containing silanes.

High-pressure slip casting processes were carried out and the carbon black distribution was determined [28] (**Figure 19**) over a wall thickness of 12 mm. No concentration gradient was detected.

Silicon carbide powder UF 15 (500 nm) from ESK Company was used for the experiments. The parts were sintered pressurelessly at 2050°C to full density. The microstructure is shown in **Figure 20**.

In **Figure 21**, the difference between the new processing and conventional ball milling in sub- $\mu$ m high-pressure slip casting is shown. The parts with non-attached carbon black form cracks during firing due to stresses caused by inhomogeneous additive distribution.

Large parts (gas burner tubings of 0.1  $\times$  0.8 m) as well as gas ignitors showing high thermoshock resistance were fabricated.

These results show that by using nano technologies in wet powder processing, substantial advantages

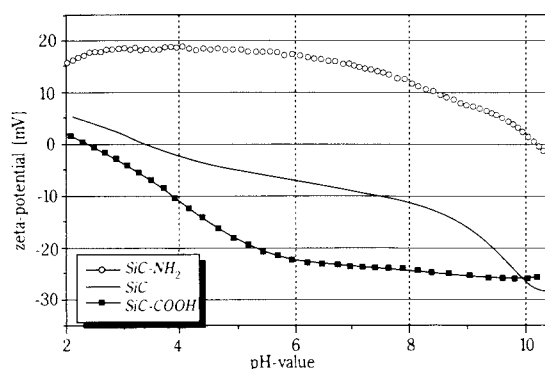


**Fig. 18** Effect of surface modification on the  $\zeta$ -potential of SiC.

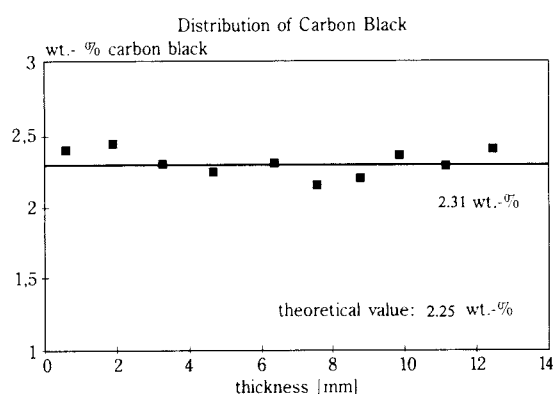


**Fig. 19** Distribution of carbon black in ceramic parts in walls of 12 mm thickness.

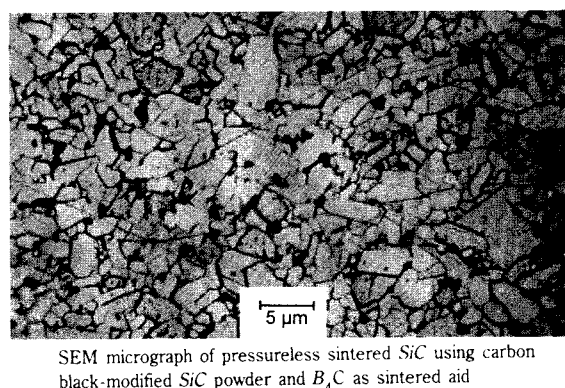


**Fig. 20** Microstructure of pressureless sintered high-pressure slip-cast SiC (density: 99.7% of theoretical density; strength 700 MPa;  $K_{IC}$  2.5 MN/m<sup>3/2</sup>).

compared to conventional techniques can be achieved.

Another example for nano processing was carried out with titanium nitride [29]. Titanium nitride is fabricated by the so-called CVR process (chemical vapor reaction) by reacting titanium chloride with ammonia (H.C. Starck company). The titanium nitride powders as produced are heavily agglomerated with agglomerate sizes up to several hundred nm. In

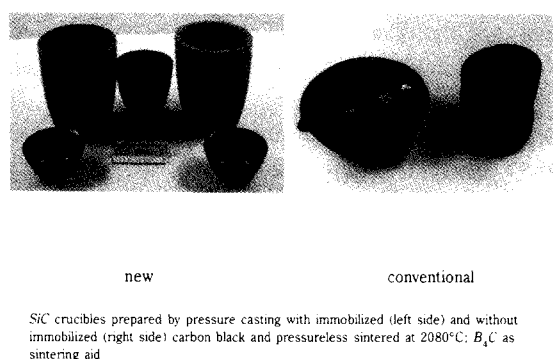


Fig. 21 SiC parts fabricated by two slip casting methods.

**Figure 22**, the effect of dispersing agents is shown as determined by photon correlation spectroscopy.

In order to develop a nano processing technique, a deagglomeration technique was developed. Several dispersion agents were tested.

It clearly shows that guanidino carbonate is the most effective dispersing agent. This is attributed to a complex formation to the titanium  $4^+$  which covers the surface of the titanium nitride in a thickness of about 1 nm, as determined by ESCA profiling. The effect on the  $\zeta$ -potential is shown in **Figure 23**.

The guanidino-carbonate-modified titanium nitride can be processed by combined slip casting and colloidal pressing to ceramic green parts with 60% by volume of titanium nitride and sintered to compact parts at temperatures around 1250°C without using pressure [29]. The hardness of these systems is considerably higher than that of conventionally processed titanium nitride which has to be sintered under pressure at temperatures of more than 2000°C. In **Figure 24**, the effect of the grain size of the sintered parts on the Vickers hardness is shown.

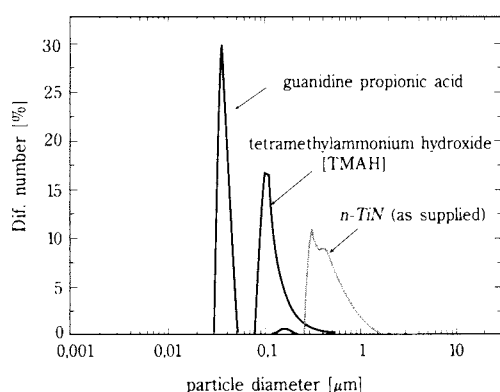


Fig. 22 Effect of different dispersing agents on the disposition of *n*-TiN powder.

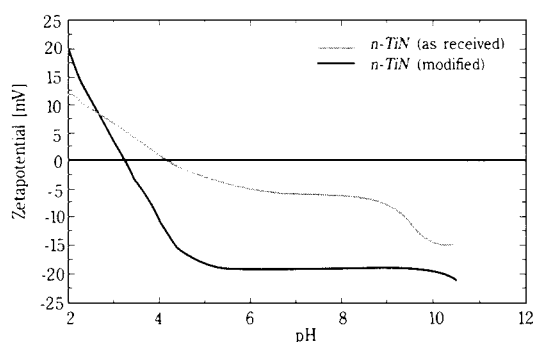


Fig. 23  $\zeta$ -potential of *n*-TiN as received and guanidino-carbonate-modified.

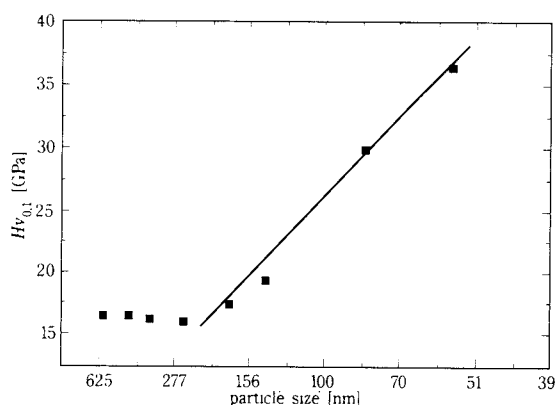


Fig. 24 Hardness of nanocrystalline titanium nitride as a function of grain size.

In **Figure 25**, the sintering behaviour is shown and compared with  $\mu\text{m}$ -sized particles.

One can clearly see that the sintering temperature is substantially lower than that of  $\mu\text{m}$  TiN, but it can also be seen that the grain growth during the densification step up to 1250°C is almost negligible. Above this temperature, rapid grain growth takes place. These systems can be deformed at pressures of 20 MPa at 1150°C.

Similar results have been obtained from *n*-zirconia. The X-ray patterns and the sintering behavior of *n*ZrO<sub>2</sub> (obtained by the CGP process) are shown in **Figure 26 a-b**. The X-ray pattern in **Figure 26a** clearly depicts the nanoparticle size by line broadening.

It clearly shows the decrease of sintering temperatures as a function of the particle size.

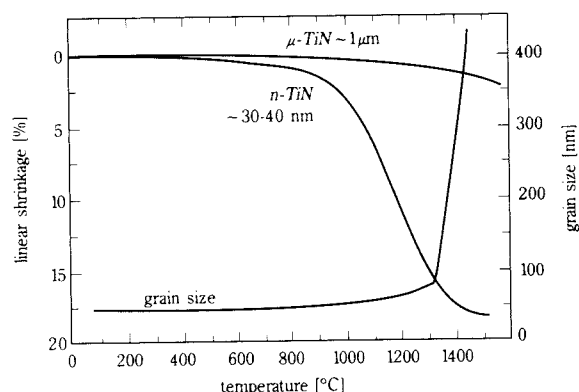


Fig. 25 Sintering behavior and grain growth of  $n$ -TiN.

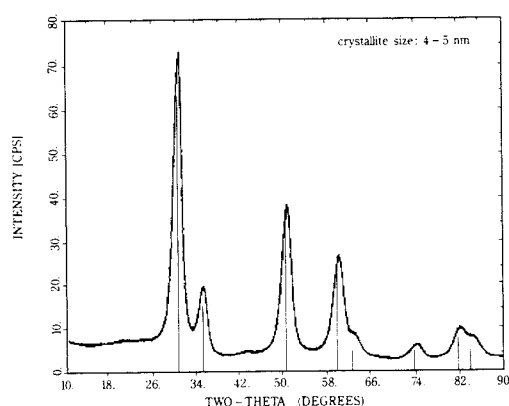


Fig. 26a X-ray patterns of  $n$   $ZrO_2$  obtained by the CGP process, and sintering behavior compared to  $\mu m$   $ZrO_2$  (5Y- $ZrO_2$ , tetragonal full lines).

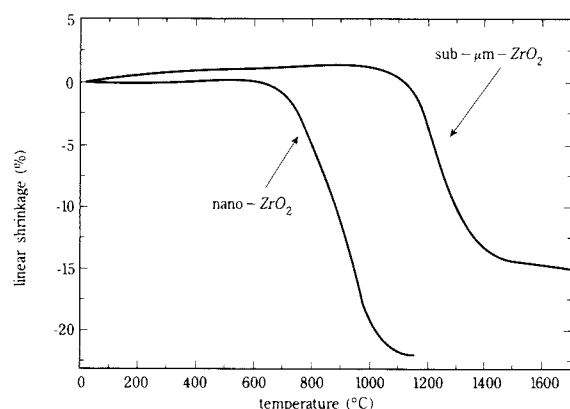


Fig. 26b X-ray patterns of 45 nm  $ZrO_2$  agglomerate size obtained by the CGP process, and sintering behavior compared to sub- $\mu m$   $ZrO_2$  (5Y- $ZrO_2$ , tetragonal).

## 5. Conclusions

A new approach was realized for the chemical synthesis and the processing of ultrafine ceramic powders based on the concept of the control of the surface free energy either in a liquid-liquid system

(MEP) before and after precipitation or in a liquid-solid system (GCP). The crystallization can be carried out by using solid-liquid reaction principles at higher temperatures and higher pressures in closed systems as developed for  $ZrO_2$ . Under these conditions, a crystallization (or recrystallization) process takes place, and fully densified crystalline particles can be obtained (e.g. tetragonal phase in the system 5Y- $ZrO_2$ ). In order to prevent aggregation, surface modification has to be obtained during this process. If surfactants with a medium chain length are used, they have to be exchanged for short organic molecule surface modification agents in order to reduce the overall organic content of the system. For this purpose, a variety of components can be selected showing good surface interaction with the particle. Examples are  $\beta$ -diketones, amines, ether ethonates, complex formers, chelating ligands or proteins. With these systems, it is possible to process the particles by tailoring their  $\zeta$ -potential for modifying larger particle surfaces for the preparation of stable slips or for obtaining high package densities in green bodies composed of nano particles. Another option of these ceramic particles is to use them in particle technologies such as nanoparticle-containing fluids (magneto or electrorheologic) or pharmaceutical applications, or to use them with appropriate surface modification to incorporate them into organic polymer systems to ultimately produce a new type of inorganic-organic nanoparticle-containing composite (Nanomers).

## References

- 1) Brinker, C.J. and Scherer, G. W.: Sol-Gel Science, Academic Press, London (1990).
- 2) Gleiter, H.: Nanocrystalline Materials, Pergamon Press, Oxford (1989).
- 3) Klein, L.C.: Sol-Gel Technology for Thin Films, Fibers, Preforms, Electronics and Specialty Shapes, Noyes Publications, New Jersey (1988).
- 4) *Ultrastructure Processing of Advanced Ceramics*, edited by J.D. Mackenzie and D.R. Ulrich (John Wiley & Sons, New York, 1988).
- 5) *Nucleation*, edited by A.C. Zettlemoyer (Marcel Dekker, New York, 1969).
- 6) James, P., in *Advances of Ceramics*, Vol. 4: Nucleation and Crystallization in Glasses, eds.: J.H. Simmons, D.R. Uhlmann, G.H. Beall, The American Ceramic Society, inc., Columbus/OH (1982), 204
- 7) J. Zarzycki, in *Advances of Ceramics*, Vol. 4: Nucleation and Crystallization in Glasses, eds.: J.H. Simmons, D.R. Uhlmann, G.H. Beall, The American Ceramic Society, inc., Columbus/OH (1982), 204
- 8) Strehlow, P., J. J. Non-Cryst. Solids 107 (1988), 55

- 9) Stöber, W., Fink, A., and Bohn, E.: Colloid and Interface Sci., Vol. 26 (1968), 62-69
- 10) Sinclair, D., La Mer, V.K., Chem. Rev. 44 (1949), 245
- 11) Schmidt, H.: Proc. of Int. Conf. of Werkstoffwoche, 28. – 31.05.96, Stuttgart, Germany
- 12) Schmidt, H., Naß, R., Aslan, M., Schmitt, K.-P., Benthien, T. and Albayrak, S. in: J. de Physique IV, Coll. C7, Vol. 3 (1993), 1251 – 1260.
- 13) Schmidt, H. in: Proc. 8th Int. Workshop on Glasses and Ceramics from Gels. Faro, Portugal, September 1995; ed.: R.M. Almeida, J. Sol-Gel Science and Technology
- 14) Ramamurthi, S.D., Xu, Z., Payne, D.A.: J. Am. Ceram. Soc. 73 (1990), 2760 – 63.
- 15) Richardson, K., Akinc, M.: Ceram. Int. 13 (1987), 253 – 61.
- 16) Burgard, D., Kropf, C., Naß, R., Schmidt, H.: Better Ceramics Through Chemistry, MRS, 346 (1994), 101 – 107.
- 17) Burgard, D.: Master's Thesis, University of Saarland, Saarbrücken, 1992.
- 18) Schmitt, K.-P.: Master's Thesis, University of Saarland, Saarbrücken, 1994
- 19) Färber, K.: Master's Thesis, University of Saarland, Saarbrücken, 1992
- 20) Schmidt, H. and Naß, R. in: Proc. Austceram '94. Eds.: C.C. Sorrell and A.J. Ruys: International Ceramic Monographs, Vol. 1, No. 2, Australasian Ceramic Society, Sydney, 1994, 1065 – 1078.
- 21) Aslan, M., Naß, R., Nonninger, R. and Schmidt, H.: 06.10.1992, Deutsche Patentanmeldung P 42 33 626.0 07.04.1994, Deutsche Offenlegungsschrift DE 42 33 626. A1.
- 22) Popall, M., Meyer, H., Schmidt, H. and Schulz, J. in: Mat. Res. Soc. Symp. Proc. 180 (1990), 995 – 1001.
- 23) Naß, R. and Schmidt, H. in: Ceramic Powder Processing Science; eds.: H. Hausner, G.L. Messing, S. Hirano. Deutsche Keramische Gesellschaft e. V., Köln (1989), 69.
- 24) Livage, J., Henry, M. and Sanchez, C.: Chemistry 18 (1988), 259.
- 25) Kasemann, R. and Schmidt, H.: New J. Chem. 18 (1994), 1117 – 1123.
- 26) Lesniak, C., Schiestel, T., Krause, W., Suyal, N., Schmitz-Stöwe, S., Naß, R. and Schmidt, H.: Proc. of Int. Conf. of Werkstoffwoche, 28. – 31.05.96, Stuttgart, Germany
- 27) Nonninger, R.: Ph. D. Thesis, University of Saarland, Saarbrücken, 1995.
- 28) Aslan, M., Spehr, J., Naß, R., Schmidt, H. and Matje, P.: Proc. of Int. Conf. of Werkstoffwoche, 28. – 31.05.96, Stuttgart, Germany
- 29) Naß, R., Albayrak, S., Aslan, M., and Schmidt, H. in: Advances in Science and Technology 11: Advanced Materials in Optics, Electro-Optics and Communication Technologies. Eds.: P. Vincenzini and G.C. Righini, Techna Srl, Faenza, Italy, 1995, 47 – 54.

### Author's short biography

Dr. Helmut K. Schmidt



#### Short vitae

Prof. Dr. Helmut Schmidt, born 1941 in Haunstetten, Germany  
 1969 Diploma in Chemistry, Technical University Munich  
 1973 Ph. D. Thesis: Heterogeneous Catalysis, Technical University Munich  
 1974 – 75 Post Doc at Free University of Berlin and at Northwestern University Evanston, Illinois/USA  
 1975 Fraunhofer-Gesellschaft, Institut für Silicatiforschung  
 1981 Deputy Director of Fraunhofer-Institut für Silicatiforschung  
 1983 – 1986 Member of the Senate of Fraunhofer-Gesellschaft  
 1984 Head of Division "New Materials and Processes"  
 1986 Call accepted as Director of the Fraunhofer-Institut für Silicatiforschung  
 1990 Call accepted as full professor for materials science and managing director of Institute for New Materials GmbH, Saarbrücken

#### Research fields

Ceramics: submicron and nano range chemical powder processing; shaping techniques (casting, electrohoretic deposition) colloidal processing of ceramis; glasses: sol-gel techniques, optical glasses; colloids in glasses, coatings; inorganic-organic composites: Ormocers, hard coatings, optical waveguide materials (active and passive), micropatterning; nano composites.

**Publications:** 240

# The Brazilian Method for the Determination of Airborne Inorganic Fibres Concentration (Including Asbestos Fibres) – Membrane Filter Method †

**Eng. Rosemary S. Ishii Zamataro\***

*ABRA – Brazilian Asbestos Association – Projects and Control Department*

**Dr. Wagner J. Meirelles\***

*ABRA – Brazilian Asbestos Association – Medical Department*

## Abstract

*This paper reports a historical description of the “Brazilian Method For The Determination Of Airborne Inorganic Fibres Concentration (including asbestos fibres) – Membrane Filter Method” since the creation of the Technical Group Organization for the study of the several existing methods in 1987, until the publication of the definitive method by “ABNT – Associação Brasileira de Normas Técnicas” (Brazilian Association for Technical Standards) in 1994.*

*The Brazilian Method is very similar to the methods from AIA – Asbestos International Association, to NIOSH – National Institute for Occupational Safety and Health, and ISO – International Standards Organization in collecting samples, preparation and analysis. The main differences are the counting criteria which do not consider the fibre aggregate particulate matter.*

## 1. Introduction

The main reason of Brazil’s interest in asbestos and its problems, is that this mineral is one of the national goods in its domestic economy. In 1994, Brazil arises as a great world producer, with 182.000 t./ year production.

This production, exclusively of chrysotile asbestos, is originated from only one mine located in Goiás State, where asbestos is one of the greatest tax incomes in the State. About 60% to 70% of this production is used in the Brazilian market, the remainder being exported, mainly to Japan, Thailand, India and “Mercosul” – The South America Common Market.

## 2. Historical Note

The evaluation of the asbestos fiber concentration in the occupational environment has been introduced in Brazil during the 70’s through a private initiative of some companies that were using asbestos as a raw material.

As there was not a Brazilian methodology for this purpose, the companies chose the “Reference Method For The Determination of Airborne Asbestos Fiber Concentrations At Workplaces By Light Microscopy

(Membrane Filter Method)” RTM1 from the AIA – Asbestos International Association because most of the companies in Europe selected this method for control.

In the mid eighties’, “Fundacentro – Fundação Centro Nacional de Higiene e Medicina do Trabalho Jorge Duprat de Figueiredo”, (Fundacentro – Occupational Medicine and Hygiene National Centre Foundation) linked to the Ministry of Labour, responsible for Governmental Counselling relating to Occupational Hygiene Safety and Health, introduced the measurement of asbestos fiber concentration using the American Methodology of NIOSH – National Institute for Occupational Safety and Health.

In July 1987, by initiative of ABRA – Associação Brasileira do Amianto (Asbestos Brazilian Association) organization that, at this moment, is composed by 60 companies which use and process asbestos, with the purpose of promoting asbestos utilization in controlled and safety conditions, the CEA – Comitê de Estudos do Amianto (Committee for Asbestos Studies) was created. The Committee objectives are to develop studies of general interest on the use of asbestos in safety conditions, as proposed by the Convention 162, of the ILO – International Labour Office, and to collect Brazilian and International information about statistical and technical data, with the main goal of keeping all parts well informed.

\* ABRA – Associação Brasileira do Amianto R. Beira Rio, 57 1º andar Vila Olímpia 04548-050 São Paulo – S.P. Brasil

† Received 15 Feb. 1996

The Committee emphasized the importance of gathering professionals of various fields as: medical doctors, engineers, scientists, lawyers, technical politicians, and people interested in the subject, with partnerships between Government, Business and Workers Unions.

This Committee organized in 1987, as many work groups with the purpose of developing specific studies. The objective of one of these working groups was the elaboration of a Brazilian method for the determination of airborne asbestos fiber concentrations, because all the existing methods presented some differences one from each other, so the comparison between results was not possible to evaluate the most adequate to Brazilian conditions.

This group was mainly composed by technicians involved with governmental and industrial fields and the following fiber evaluation methods were the basis for discussion and experimentation:

- RTM 1 by AIA (Asbestos International Association);
- Method n. 7.400-B by NIOSH (National Institute for Occupational Safety and Health); U.S.A.
- ISO method (International Standards Organization);
- MDHS – 39/2 by H.S.E. (Health and Safety Executive) – England.

After two years of meeting, discussion and experiments, the text of the Brazilian Method was developed by the Technical Working Group and approved by the Workers Labour Union for general use.

In the beginning of 1990 the text was sent to ABNT – Associação Brasileira de Normas Técnicas (Brazilian Association for Technical Standards), organization responsible for the normalization in Brazil. The method was normalized, after one year and a half, with some alterations, into NBR 13.158 – Evaluation Of Airborne Chemical Agents – Airborne Respirable Inorganic Fibers Collection And Phase Contrast Optical Microscopic Analysis – Membrane Filter Method, which became valid from June 30, 1994.

### 3. Characteristics of the Brazilian Method

The Brazilian Method in its essence is an association between the AIA – RTM 1, and Method n. 7.400 – NIOSH. Basically it consists in the standardizing of the systematic sample collection and in establishing criteria for fiber analysis, measurement, and counting. The sample collection consists in the passage of the defined amount of air to be sampled through the membrane filter where the particulate airborne material will be separated.

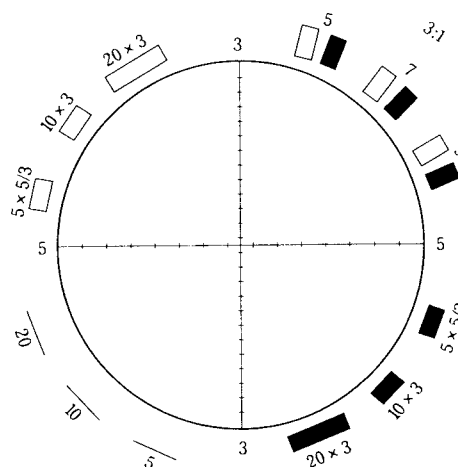
The membrane filter is made from cellulose nitrate or from a mixture of cellulose esters, with  $0.8\ \mu\text{m}$  to  $1.2\ \mu\text{m}$  pore size, filter diameter of 25 mm with a printed grid, available in the general market. The filter holder should be open faced with an extension tube for filter protection made of electrically conductive material, like polypropylene saturated with carbon or metal, for the prevention of the electrostatic attraction of the fibers.

The sampling pump should be portable, with low flowrate and battery operated that allows the running for, at least, 8 hours continuously, with a constant flowrate of  $1.0\text{L}/\text{min.}$ , free from pulsations. The pump flowrate should be calibrated using the prime pattern, (soap bubble method, or another one permissible).

For sample analysis, the filter should be mounted on a microscope stage and cleared with Acetone vapor and Triacetin (Glyceryl Triacetate). For fibers measurement and counting a phase contrast microscope should be used, with 400 to 500 times magnification.

The Brazilian Method specifies and details each step of the sampling collection processes and analysis, advising to each particularity with the purpose of preventing errors and allowing the results reproducibility. Such as the majority number of the methods which use the optical microscopy technique, the Brazilian Method presents a coefficient of variation around 20% in quality control conditions, if 100 fibers are counted.

The Method adopts for counting, the Walton-Beckett graticule, (**Figure 1**) reference G-22 (relation 3:1), diameter of 100 (m for 400 or 500 times magnification used during the microscopic analysis. It is inserted in one of the oculars of the microscope.



“Walton and Beckett” graticule

Fig. 1 “Walton and Beckett” graticule

For sample analysis, the number of fibers counted are those which lay in the interior of the area of the Walton-Beckett graticule, named field. 100 fibers or 100 fields should be counted, or at least 20 fields, even if 100 fibers have been already observed in the fields.

As the effective filtration area of the membrane filter being ( $A$ ), the area of the counting field ( $a$ ), the volume of the sampling air ( $V$ ), the number of the counted fibers ( $nf$ ) and the number of the counted fields ( $ng$ ) are known, it is possible to calculate the fiber concentration ( $C$ ) in the air sampled, by the following equation:

$$C = \frac{nf}{ng} \times \frac{1}{V} \times \frac{A}{a} \quad (1)$$

The measuring units of the above variables should be chosen for the concentration to be expressed in fibers per milliliter (f/ml.).

#### 4. Main differences between the Brazilian method and the AIA and NIOSH methods

The Brazilian Method was established for the inorganic fiber collection and evaluation, including asbestos, with a refractive index different from 1.43, which is the refractive index of the preparation of the membrane filter plus acetone vapor and triacetin.

The companies were already using the AIA – RTM1 method, when Fundacentro, years later, began to use the NIOSH – 7.400 B method.

As there was not a defined method, each one adopted his own, among the several existing methods, but this criteria brought many difficulties in comparing results.

Some companies did not give up the AIA – RTM1 Method, because its counting criteria favoured the companies samplings by bringing a lower result in the concentration of fibers in the occupational environment.

This method considers the diameter of the particle when it is attached to the fibre. If it is bigger than  $3 \mu\text{m}$  the fibre is not counted, while the NIOSH – 7.400 B method omits the attached particle, independently of its diameter size and counts it if the fibre follows the definition criteria.

#### 5. Counting criteria

The reason for counting the fibers aggregated with particles is due to the Brazilian plants conditions, i.e., mainly in the asbestos cement and brakelining sectors, where an expressive amount of particulate

materials among the fibers, is found. This situation raises difficulties to the fibers counting, because no one can not affirm if there is a particulate adherence to the fibers or superposition of it to the fibers.

Concerning to more strict results, the counting criteria relating to the Brazilian Method – ABNT is supposed to count individually the fibers in a bundle, if they can be distinguished separately. If it is not possible identifying them in an individual way, the fibers associated to other particles or to themselves, should be counted as one fiber, following the fiber definition.

A fiber is counted as one, when it presents both defined ends entirely in the interior of the graticule and its diameter should be measured in the non-divided part; the fibers which are gathered to other particles are counted as fibers, independently of the aggregated particle diameter also following the fiber definition that recommends that the respirable fiber diameter be lesser than  $3 \mu\text{m}$ , length longer than  $5 \mu\text{m}$ , and the relation between length and diameter higher than 3:1.

#### 6. Quality control

It is extremely important that reliable and reproducible results should be obtained. Related to this objective there is a participation in international programs of interlaboratorial quality control sponsored by LHCF – “Laboratoire d’Hygiene et des Contrôles de Fibres Minerales” (France) and IOM – “Institute of Occupational Medicine” (Edinburgh). The mentioned laboratories send a set of slides, already prepared, so the technicians count the fibers using an optical microscope. The results are sent to them in order to obtain the due qualification. The LHCF compares the result from the counter, following the average of the results from all the counters participating to the program and classify it according to the standard deviation and variation coefficient. The IOM compares the results from the counter using visual reference counts and Magiscan reference counts, classifying them according to the percentage zone limits.

#### 7. Results

Due to the sensibility inherent to the method, all calculated value of less than 0.1 fiber/ml and all higher value, is rounded off to the first decimal place.

The results showed in **Figure 2** report the Brazilian experience and reality throughout all these

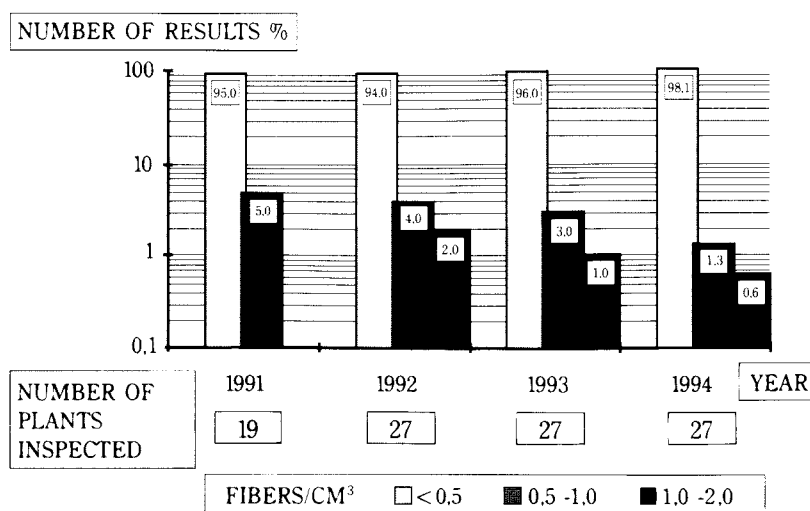


**Fig. 2** Level of airborne chrysotile asbestos fiber concentration evolution in the asbestos cement industries

years, sampled from asbestos cement and brakelining industries, also from other asbestos using industries.

The analysed points were sampled from the operators in order to check the exposure level to which they are submitted.

The measurements realized by ABRA in industries aim to inspect all the industry sectors, and the points are chosen by ABRA technicians and workers at workplaces where there is the possibility of dust formation.

The importance of these evaluations is also to indicate if the collective control measures are efficient enough, and to check the correlation between the exposure level and epidemiological studies (dose-response).

The evaluations are carried out in intervals not higher than six months considering the valid Brazilian health rules for asbestos using factories.

## Conclusion

The Brazilian Method is the result of many years of experience obtained from the Brazilian industries, supported by the institutional and industrial consense among several points of view. The method normalization allows its use without the divergences resulting from the different methods utilization.

The method is available, in English language, in the Documentation Center of ABRA – Associação Brasileira do Amianto.

R. Beira Rio, 57  
Vila Olímpia  
04548-050  
Brasil

1º andar

São Paulo - SP

## Acknowledgements

The authors wish to acknowledge Dr. Viviano Ferrantini for the encouragement and special thanks go to ABRA team for the support of this work.

## Nomenclature

<i>a</i>	Area of the counting field	(mm <sup>2</sup> )
<i>A</i>	Filtration area of the membrane filter	(mm <sup>2</sup> )
<i>C</i>	Airborne fiber concentration in the air sampled	(f/ml)
<i>f</i>	Fibers	
<i>nf</i>	Number of the counted fibers	
<i>ng</i>	Number of the counted fields	
<i>V</i>	Volume of the sampling air	(ml)

## References

- 1) Asbestos International Association – Recommended Technical Method n. 1 (RTM 1). Reference method for the determination of Airborne Asbestos Fibre Concentrations at workplaces by light microscopy (Membrane Filter Method). London, September 1979.

- 2) Asbestos Study Group Meetings. Minutes.
- 3) Brazilian Association for Technical Standards (ABNT) – NBR 13158. Airborne chemical agents evaluation, airborne respirable inorganic fibers collection and phase contrast optical microscopy analysis – Membrane filter method – Method of test. Brazil, May 1994. 15p.
- 4) Committee for Asbestos Studies (CEA) Meetings. Minutes.
- 5) Health and Safety Executive – Methods for the determination of hazardous substances MDHS 39/3. Asbestos fibres in air – Light microscope methods for use with the control of asbestos at work; regulations. England, 1988.15p.
- 6) ISO – Draft International Standard ISO/DIS 8672. Determination of the number concentration of airborne inorganic fibres by phase contrast optical microscopy – Membrane filter method. Germany, 1988.
- 7) National Institute for Occupational Safety and Health – Method 7400. NIOSH Manual of Analytical Methods. United States, May 1989.

### Author's short biography



**Rosemary S. Ishii Zamataro**

Rosemary S. Ishii Zamataro is a chemical engineer graduated in 1976. Her field specialization is Industrial Management by "Fundação Vanzolini", and Occupational Hygiene by Santa Casa Medicine School, in São Paulo, from which she majored in 1994. She worked for 11 years in the asbestos-cement field at the Asbestos and Plastic Research Center of Brasilit S.A. (Saint Gobain Group). She has 17 years experience in the environmental control field. Nowadays she is in charge of the Projects and Control Department of ABRA, whose main objective is to assist the associated industries in relation to the local ventilation exhaust projects and environmental control in order to evaluate the level of worker exposure to asbestos dust.



**Dr. Wagner José Meirelles**

Dr. Wagner José Meirelles, medical doctor, graduated from Ribeirão Preto Medicine School (University of São Paulo). He majored in Occupational Medicine and Hygiene at Santa Casa Medicine School, in São Paulo. For more than twenty years, his main activity has been linked to the environmental and health control relating to workers exposed to asbestos.

# Particle Identification by Image Processing†

Giuseppe Bonifazi and Paolo Massacci

Department of Chemical, Material, Raw Material and Metallurgical Engineering  
University of Rome "La Sapienza"\*

## Abstract

*This paper reviews techniques for obtaining and processing images of particles and objects (irradiation, response, surveying, storage and analysis). It presents the methodologies by which images can be classified and recognised (detection of domains, boundaries, shapes and textures) with a view to developing correlations between the information provided by the images and the physical and chemical properties of the examined particles. It discusses procedures for recognising the boundaries of images of particles, for analysing their properties (geometrical, Fourier series, fractals, etc.) and for recognising the structures and textures of multi-component particles. The instruments used to acquire and store the images and the hardware needed to process the digitized information are described and assessed. The software needed to analyse the data (loading, colour-level correction, enhancement, filtering, thresholding and labelling) are presented. Procedures for classifying vector structures that may be used to characterise images of individual particles (pattern vectors) or classes of particles (feature vectors) are discussed, and those which are used to recognise particles are analysed. Applications of these methodologies and several case studies concerning mineral grains (free and associated), polished sections of minerals, macerals, inorganic and organic materials are described.*

## 1. Introduction

The morphologic characterisation of individual particles, particulate materials, or multi-particle systems entails significant difficulties (Ehrlich et al., 1980), especially when analyses must be performed quickly on a large number of particles (Beddow, 1984).

These difficulties depend upon:

- sampling method;
- complexity of the algorithm used to determine the sample's characteristics;
- time required to process the results;
- representation of the characteristics in a concise form;
- correlation of shape characteristics with chemical and physical data.

In the case of particle populations, it is also necessary to determine the distribution of morphologic characteristics throughout the sample (Luerkens et al., 1987).

Though many morphologic characterisation procedures have been proposed in the past, some more sophisticated than others, none have provided real and practical solutions at the applied level (Beddow, 1986). Procedures are commonly based on the sur-

veying and analysis of characteristics of individual particles and/or of systems of particles such as the boundaries of exposed surfaces or relationships between constituent phases (in the multi-phase particles). Such information can be determined more "easily" through the use of image processing.

The present work examines some investigation techniques and problems related to their application in particle characterisation. The objective may be either the characterisation of a single particle within the system through the definition, surveying and measurement of its specific properties, or the characterisation of the particle system as a whole through the determination of common properties.

The design of an image processing procedure for the characterisation of a particle is never simple or trivial, even at the algorithmic level.

Dependent on the project's objective, various investigation strategies may be adopted and different algorithms can be used which require different running times and which produce information of varying quantity and quality. Such aspects influence the complexity of procedures and could also, in some cases, strongly pre-condition the subsequent practical applications of any investigative approach. Procedures must aim at obtaining the minimum amount of information required for the objective to be reached.

\* Via Eudossiana 18, 00184 Roma, Italy

† Received: 13 December, 1995

## 2. Particle Image

### 2.1. Pictorial image

To determine the characteristics of a particle or of a system of particles, an image has to be produced using either front or back lighting. Using the former, the structure of the object's pictorial characteristics may be projected onto a screen; these depend on the light source and on the response of the object (reflection, refraction, scattering). The latter type of lighting yields a silhouette as a result of the contrast between the shadows generated by the object and the background light.

### 2.2. Digital image

A digital image is a set of pictorial elements  $P(x, y)$ , i.e. pixels, identifiable by the vector  $P(R, G, B, x, y)$  that defines the level of red, green, and blue components (RGB) in the colour of an element with geometric coordinates  $x$  and  $y$ . In the case of a black and white image (B&W), a grey scale value  $GL$  is associated with each pixel; an image of this type can be concisely described by a set of  $P(GL, x, y)$  values. Each pictorial element can also be defined as a function of the surrounding elements by using a scalar, a vector, or a matrix relative to the vector values  $P(R, G, B, x, y)$  for colour images or  $P(GL, x, y)$  for B&W images; plainly, the results will depend upon the direction and distance from the pixel.

### 2.3. Pictorial and digital images correlation

A digital image must be considered as the projection of the pictorial image of a real object. In theory, each element of the digital image  $P(R, G, B, x, y)$  must correspond to a single element of the pictorial image  $P(x, y)$ . The digital image must be considered as a model (imperfect but representative) of the pictorial image, and the latter as a model (also imperfect but equally representative) of the real, three-dimensional object. The digital image provides information in the form of a two-dimensional representation; image quality is a function of the number of pixels adopted in digitalization, since a larger number of pixels yields a higher resolution and hence also more reliable information. Moreover, the sample's initial characteristics are better represented when the sample is correctly prepared and changes in size are minimised.

To determine the characteristics of particles, it is necessary to examine a large number of images. Complex hardware (HW) and software (SW) architectures for the surveying and examination of the

information are required and, what is even more important, an acquisition procedure which is highly standardised with respect to the lighting method must be defined. In fact, changes in the conditions of acquisition can alter the pictorial characteristics of the image, the inevitable consequence of this being a decrease in the quality and reliability of results. This aspect is of particular importance during on-line acquisition and processing on an industrial scale and, more generally, whenever one is operating outside a standard laboratory environment.

### 2.4. Digital image acquisition

A digital image is obtained by transforming (using a converter) the analogue-digital signal from the pictorial form ( $I_p$ ) into an information matrix ( $I_d$ ) which is easily manageable using a computer.

The conversion process depends upon many factors, but primarily on the quality of the HW system that creates the conversion. Not only the electronic HW system, but also the equipment used to acquire a fair view of the sample is very important. Such equipment usually consists of an optical or electron-optical apparatus and of a system with which to light the sample (white light, laser light, IR, X-Ray, fluorescence, etc.).

### 2.5. Digital image processing

A digital image typically consists of a set of three matrices for an RGB colour image and of a single matrix for a B&W image. In order to extract suitable information, one must operate on these matrices as shown in **Figure 1**.

The term image processing refers to the sequence of operations which, when applied to an image sample, produce an image that exhibits characteristics of interest. The term image analysis, on the other hand, refers to the sequence of operations which, when applied to an image sample, yield numerical values that define a pattern vector capable of concisely describing some of the image's characteristics.

The use of a filtration procedure is a typical image processing operation, whereas the determination of a grey-scale histogram for a B&W image, or for the RGB components of a colour image, is a typical operation of image analysis.

In general, the set of numerical matrices that represents a digital image cannot be processed immediately after the conversion. This set of numbers, in fact, contains noise, systematic errors, and also information which is excessive as far as the essence of the characteristics under investigation are concerned.

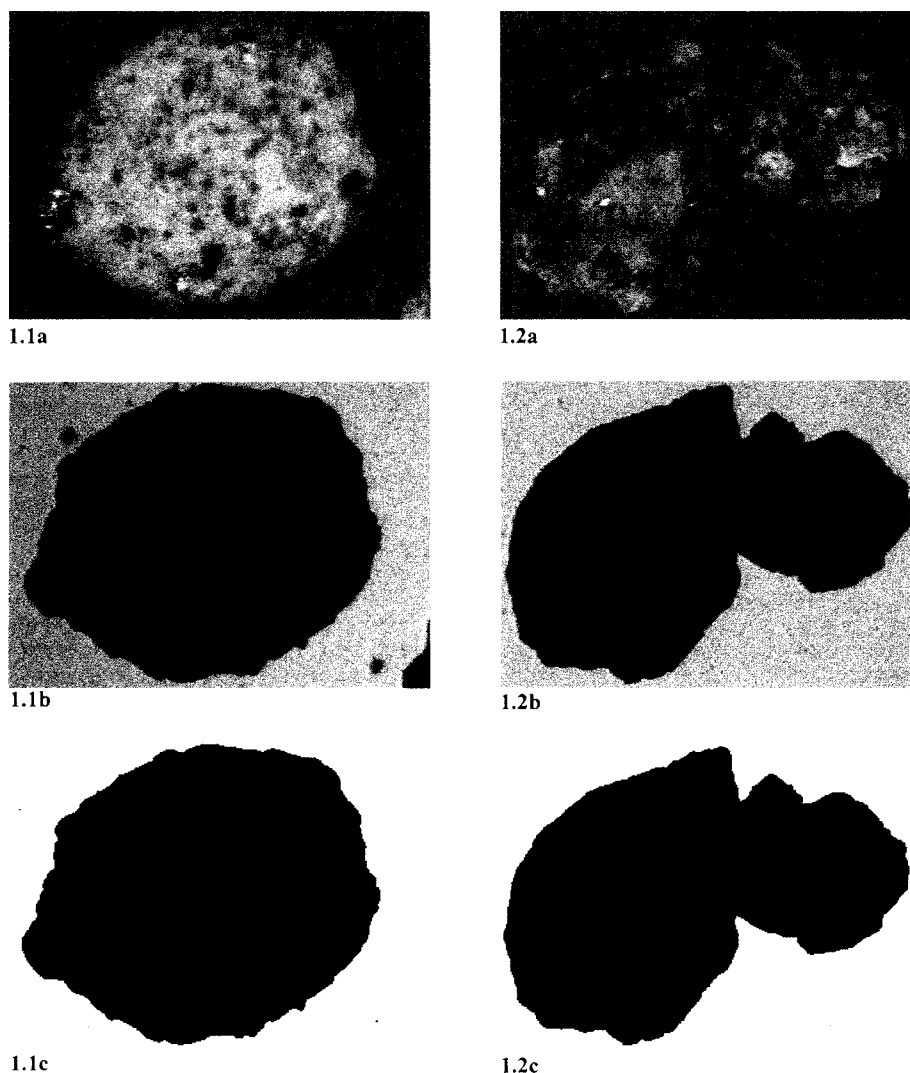


Fig. 1 Digital representation of the pictorial images of two particles acquired under different lighting conditions (1.1a and 1.2a, upper lighting – 1.1b and 1.2b, bottom lighting) and as they result after a thresholding and noise reduction procedure (1.1c and 1.2c).

As a result, the data set must first be subjected to the treatment procedure shown in **Figure 2**.

## 2.6. Hardware

A typical image analysis system consists of a conversion unit ( $I_p$  to  $I_d$ ) and of a unit capable of processing and analysing the images. Naturally, neither the image processing nor the resulting information are conditioned by the analyser, and the study may thus be performed on any computer. That this fact is of particular relevance with respect to the HW characteristics of the computing system (personal and minicomputers) is illustrated in **Figure 3**.

Plainly, such a solution cannot be applied in those cases in which analysis and on-line control are required; in such cases the HW architecture must be perfectly integrated and sometimes even made more powerful by means of a specific processor (DSP) or

boards capable of performing parallel calculations (TRANSPUTERS).

## 3. Information from Digital Images

### 3.1. Pictorial characterisation

The digital images which are produced using the procedure described above may be directly subjected to a segmentation and labelling procedure to identify domains of homogeneous pictorial characteristics (PA) as shown in **Figure 4**. Alternatively, the segmentation phase may be preceded by textural analysis, which transforms the vectors that characterise each pixel into a spatial-tone dependence matrix. Segmentation and labelling, applied to such a matrix, involve the definition of domains on the basis of textural differences (Haralick and Anderson, 1971).

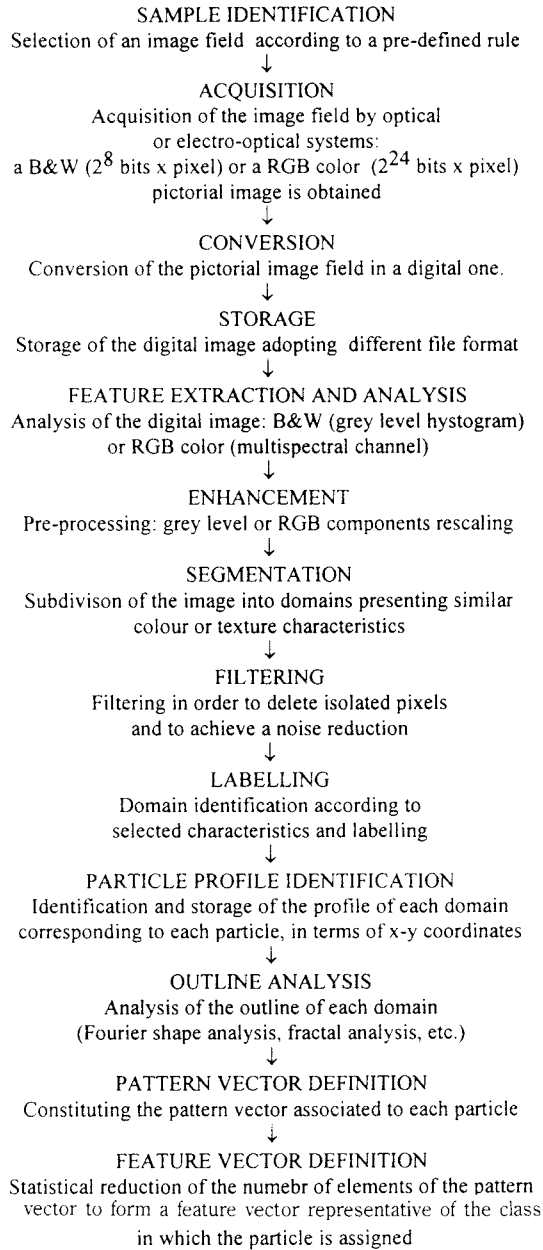


**Fig. 2** Unit operation flowsheet for extracting the distinctive features of a particle, or of a class of particles, following a digital image based approach.

### 3.2. Textural analysis

The pattern of all surface or profile points in a particle image may be considered as the particle texture (Ahuja, 1973). This pattern may be defined as a series of textural parameters capable of representing the statistical properties of the colour-level distribution of the pixels that form each particle (TA) (Andrews

et al., 1972 and Haralick et al., 1973). Using this approach, a series of parameters may be defined as follows:

$R_t, G_t, B_t$	mean values of RGB colour components of a true colour image or mean grey level of a B&W image
$GL_t$	mean grey level of a B&W image
$\sigma_{Rt}, \sigma_{Gt}, \sigma_{Bt}$	standard deviations of the colour components of a true-colour image or standard deviation of the grey level of a B&W image
$\sigma_{GLt}$	standard deviation of the grey level of a B&W image
$L_R, L_G, L_B$	maximum colour level values of an RGB colour image or the maximum grey level of a B&W image
$L_{GL}$	the maximum grey level of a B&W image
$P_{Ri}, P_{Gi}, P_{Bi}$	probability distribution of colour level of an RGB colour image or probability distribution of grey levels of a B&W image.
$P_{GLi}$	probability distribution of grey levels of a B&W image.

As may be observed for the particles shown in **Figure. 5**, these parameters appear to be insufficient to identify particle textures.

It is more useful to consider not only the RGB-colour or grey-level distributions, but also the relative spatial relationships between the RGB colour or grey levels. The definition of parameters that quantify both the distribution and spatial relationships of the RGB colour or grey levels allows for the quantification of some of the textural characteristics of the image such as homogeneity, linear dependencies and contrast. It should be noted that the number of operations required to compute any of these features is proportional to the number of pixels in the image.

The application of a texture-based approach to an RGB colour image requires preliminary processing that changes the colour coordinate system of the image. A widely accepted procedure (Pratt, 1991) is based on the evaluation, for each original pixel  $P(I, S, H, x, y)$  that represents the intensity (I), saturation (S) and hue (H) of each colour of the source image.

The relationships that link the sets are the following:

$$\begin{bmatrix} I \\ V_1 \\ V_2 \end{bmatrix} = \begin{bmatrix} 1/3 & 1/3 & 1/3 \\ -1/6^{1/2} & -1/6^{1/2} & 2/6^{1/2} \\ 1/6^{1/2} & -2/6^{1/2} & 0 \end{bmatrix} \begin{bmatrix} R \\ G \\ B \end{bmatrix} \quad (1)$$

$$H = \tan^{-1}(V_1/V_2) \quad (2)$$

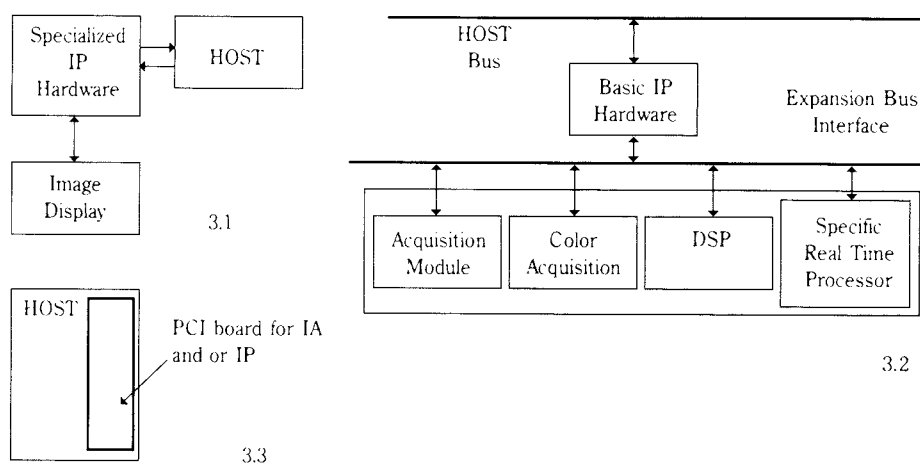


Fig. 3 Different hardware architectures enabling acquisition and processing of digital images, with different flexibility and performances.

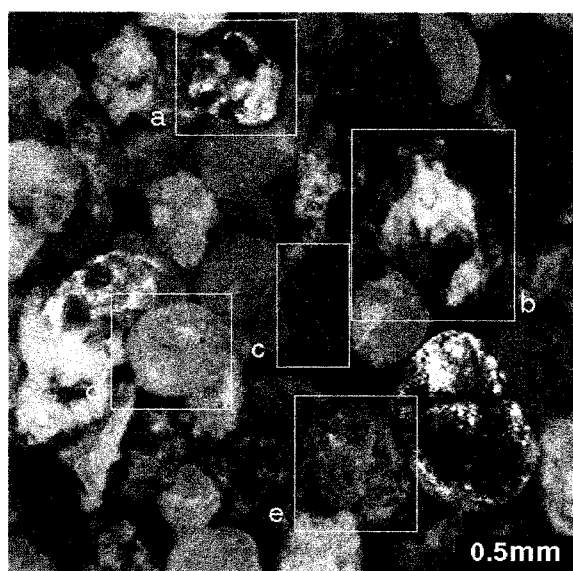


Fig. 4 Digital image of a particulate solid sample in bulk. Each particle of the set can be considered as a domain of different pictorial characteristics.

$$S = [(V_1)^2 + (V_2)^2]^{1/2} \quad (3)$$

where  $V_1$  and  $V_2$  are transformation coefficients.

An example of such a transformation is shown in **Figure. 6**.

Using this procedure, the inner features of the image are enhanced and the subsequent textural analysis results in an improved particle characterisation. For texture evaluation, the definition of suitable colour-level spatial-tone dependence matrices (in the  $I$ ,  $S$ ,  $H$  domain for an RGB colour image or in the  $GL$  domain for a grey-level image) may be carried out.

Considering a B&W image of size  $N_x$  by  $N_y$  (i.e. the number of pixels along the  $x$  and  $y$  coordinates,

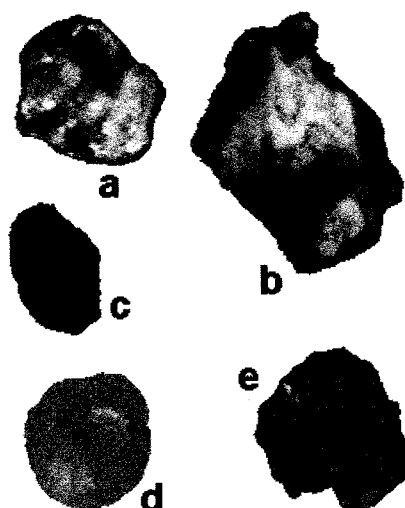


Fig. 5 Each particle presents characteristics of its own, not only related with its dimension and morphology, but also with its inner texture (arrangements of its constituents).

respectively), each pixel may be characterised by a  $P(GL, x, y)$  value and the image defined by the following set:

$$P(GL, x, y) = GL(i, j) \mid (i, j) \in (L_x L_y) \quad (4)$$

where  $L_x$  and  $L_y$  represent the set

$$L_x = (1, 2, \dots, N_x) \text{ and } L_y = (1, 2, \dots, N_y)$$

and where  $GL(i, j)$  is the grey level associated with a pixel having the coordinates  $(i, j)$  that represent the basic information of the image.

For a colour image, the same approach is followed for each component ( $I$ ,  $S$  and  $H$ ).

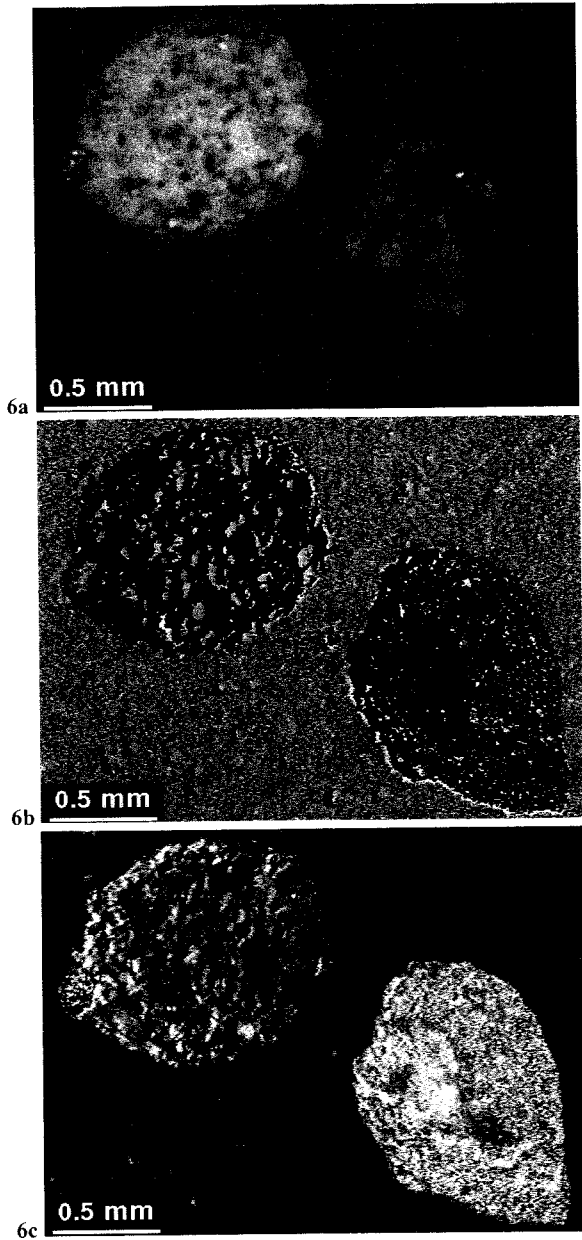


Fig. 6 Color components of the images of the two particles of Figure 1.1 assuming a color coordinate system different from the classic RGB. The images are referred to the intensity (6a), saturation (6b) and hue (6c) values.

If a pixel does not belong to the boundary, a relationship may be defined between the tone level value ( $I$ ,  $H$  and  $S$  for colour images or  $GL$  for grey-level images) of the pixel and that of pixels at known distances ( $d$  pixels) and directions ( $k$ ). The formulation of these relationships allows one to construct a spatial-tone dependence matrix,  $M_k$ , where  $k$  is the direction along which the distance  $d$  is calculated. Thus, if the main directions are  $0^\circ$ ,  $45^\circ$ ,  $90^\circ$  and  $135^\circ$ , the corresponding spatial-tone dependence matrices will be defined in the following manner:

$$M_{0^\circ}(l, m, d) = \# \{ [(p, q), (r, s)] \in (L_y L_x)(L_y L_x) \mid p-r = 0, |q-s| = d, I(p, q) = l, I(r, s) = m \} \quad (5)$$

$$M_{45^\circ}(l, m, d) = \# \{ [(p, q), (r, s)] \in (L_{yz} L_x)(L_y L_x) \mid (p-r = d, q-s = -d) \text{ or } (p-r = -d, q-s = d), I(p, q) = l, I(r, s) = m \} \quad (6)$$

$$M_{90^\circ}(l, m, d) = \# \{ [(p, q), (r, s)] \in (L_{yz} L_x)(L_y L_x) \mid |p-r| = d, q-s = 0, I(p, q) = l, I(r, s) = m \} \quad (7)$$

$$M_{135^\circ}(l, m, d) = \# \{ [(p, q), (r, s)] \in (L_{yz} L_x)(L_y L_x) \mid (p-r = d, q-s = d) \text{ or } (p-r = -d, q-s = -d), I(p, q) = l, I(r, s) = m \} \quad (8)$$

where:

- $l$  = row index of the generic element for matrix  $M_k$  being ( $k=1, \dots, 4$ ),
- $m$  = column index of the generic element for matrix  $M_k$  being ( $k=1, \dots, 4$ ),
- $d$  = distance along the direction  $k$ , defining the spatial relationship of nearby pixels,
- $p$  = row index of the first pixel considered in the image,
- $q$  = column index of the first pixel considered in the image,
- $r$  = row index of the second pixel considered in the image,
- $s$  = column index of the second pixel considered in the image,
- $L_x$  = number of pixels in the image along the  $x$  axis,
- $L_y$  = number of pixels in the image along the  $y$  axis.

The tone ( $l$ ) (colour component or grey level) of the pixel at coordinates  $(p, q)$  is compared with the tone ( $m$ ) (colour component or grey level) associated with the pixel at coordinates  $(r, s)$ . The symbol  $\#$  represents the number of pixel pairs that satisfy the mentioned criteria.

As regards the first of the four matrices, the element  $M_{0^\circ}(l, m, d)$  is equal to the set of ordered pixel pairs  $(p, q), (r, s)$ , whose distance along the  $y$  axis is zero and along the  $x$  axis is  $d$ , and whose tones  $g(p, q)$  and  $g(r, s)$  have the values  $(l-1)$  and  $(m-1)$ , respectively. The matrices  $M_k$  are symmetrical, that is:

$$M_k(l, m, d) = M_k(m, l, d) \quad (9)$$

Normalised spatial-tone dependence matrices are defined as a matrix whose generic element is equal to:

$$M_k^*(l, m, d) = M_k(l, m, d) / T_k \quad (10)$$

where  $T_k$  assumes the following expressions for the main directions  $0^\circ$ ,  $45^\circ$ ,  $90^\circ$  and  $135^\circ$ :

$$T_{0^\circ} = 2(N_x - 1)N_y \quad (11)$$

$$T_{45^\circ} = 2(N_x - 1)(N_y - 1) \quad (12)$$

$$T_{90^\circ} = 2(N_x(N_y - 1)) \quad (13)$$

$$T_{135^\circ} = 2(N_x - 1)(N_y - 1) \quad (14)$$

Using these normalised matrices  $M_k^*(l, m, d)$ , a large series of  $R_{hk}$  texture parameters may be considered. The first nine texture parameters  $R_{hk}$  are:

$$R_{1k} = \sum_{l=1}^{N_g} \sum_{m=1}^{N_g} \{M_k^*(l, m, d)\}^2 \quad (15)$$

$$R_{2k} = \sum_{z=0}^{N_g-1} z^2 M_k^*(l, m, d) \quad (16)$$

where  $z = l + m$

$$R_{3k} = \left[ \sum_{l=1}^{N_g} \sum_{m=1}^{N_g} (l, m) M_k^*(l, m, d)^2 - \mu_x \mu_y \right] / \sigma_x \sigma_y \quad (17)$$

where  $\mu_x$ ,  $\mu_y$  and  $\sigma_x$ ,  $\sigma_y$  are the means and the standard deviations of the  $M_k^*(l, m, d)$  distribution, respectively.

$$R_{4k} = \sum_{l=1}^{N_g} \sum_{m=1}^{N_g} (1 - \mu)^2 M_k^*(l, m, d) \quad (18)$$

$$R_{5k} = \sum_{l=1}^{N_g} \sum_{m=1}^{N_g} M_k^*(l, m, d) / [1 + (l - m)^2] \quad (19)$$

$$R_{6k} = \sum_{l=2}^{2N_g} l M_k^{**}(q, d) \quad (20)$$

$$\text{where } M_k^{**}(q, d) = \sum_{l=1}^{N_g} \sum_{m=1}^{N_g} q M_k^*(l, m, d)$$

$$\text{where } q = l + m \quad (21)$$

$$R_{7k} = \sum_{q=2}^{2N_g} (q - R_{8k})^2 M_k^{**}(q, d) \quad (22)$$

$$R_{8k} = - \sum_{l=1}^{N_g} \sum_{m=1}^{N_g} M_k^{**}(q, d) \cdot \log M_k^{**}(q, d) \quad (23)$$

$$R_{9k} = - \sum_{l=1}^{N_g} \sum_{m=1}^{N_g} M_k^*(l, m, d) \cdot \log M_k^*(l, m, d) \quad (24)$$

where  $N_g$  is the number of distinct grey levels in the image.

Each of the textural parameters  $R_{hk}$  (where  $h=1, 2, \dots, 9$ ) has to be calculated with reference to one of the four matrices  $M_k(l, m, d)$  for  $k=1, 2, 3$  and 4, corresponding to the main directions  $0^\circ$ ,  $45^\circ$ ,  $90^\circ$  and  $135^\circ$ .

As an example, the previously-defined  $R_{hk}$  texture parameters are useful to characterise the roughness of two different ceramic particles as shown in **Figure. 7** and in **Table. 1** (Bonifazi and Massacci, 1988a).

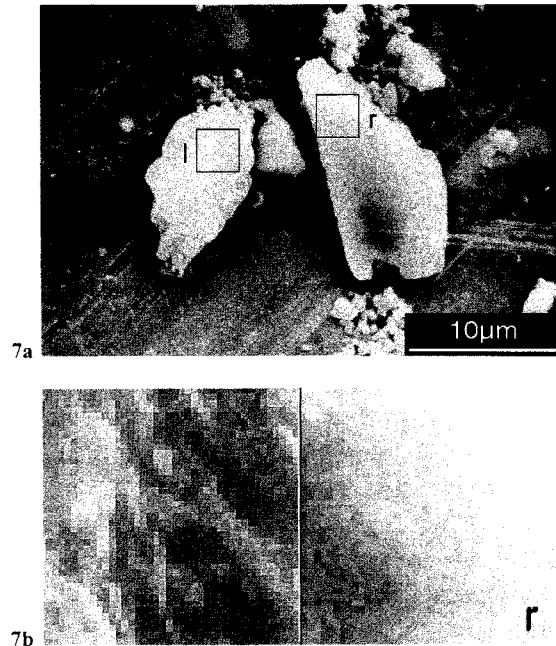


**Fig. 7** Two ceramic particles characterized by a different roughness (7a). The difference of the two sampled domain (*l* and *r* windows) is shown, in pictorial form, after magnification (7b). The first three texture parameters ( $R_1$ ,  $R_2$  and  $R_3$ ) are taken into consideration.

**Table 1** Mean values of the textural parameters resulting from the analysis of the two windows (*i* and *r*) reported in Fig. 7b.

Texture Parameters			
Window	R1	R2	R3
I	4,88E-03	6,18E + 00	3,40E + 06
r	3,84E-03	6,03E + 00	7,25E + 06

### 3.3 Discontinuity

The term discontinuity refers to the variation of the pictorial or textural characteristics of an image. The interconnection of the discontinuity, following a procedure which can recognise linear features (segments, arcs, lines), allows one to define closed or open lines (Bonifazi and Massacci, 1988b). When the closed line bounds a domain characterised by pixels that have the same pictorial characteristics, the boundaries of a particle's phases are identified. If the discontinuity lines are not inside a homogeneous domain, they may be considered to be fractures within the particle or the phase.

The extraction procedure adopted to define discontinuities is usually based on gradientation. A module of the gradient  $P(R, G, B, x, y)$  or  $P(G, x, y)$  is calculated for each pixel; if the module is greater than a threshold value, the examined pixel is considered to be a contour point. The direction of the contour at that point is considered orthogonal to the direction of the gradient. With respect to the  $x$  and  $y$  coordinates, the components of the gradient vectors are

$$\Delta_x = [P(R, G, B, x + \delta_x, y) - P(R, G, B, x, y)] / \delta_x \quad (25)$$

$$\Delta_y = [P(R, G, B, x, y + \delta_y) - P(R, G, B, x, y)] / \delta_y \quad (26)$$

where  $\delta_x$  and  $\delta_y$  are the gradient steps along the  $x$  and  $y$  directions, respectively; they are usually expressed in number of pixels.

The relationships define the components of a vector which describes the local variations. The computation is carried out by iteratively applying the mentioned functions.

All the previously described procedures are applied from a practical point of view, adopting special templates that are able to extract the contour features of a domain set (particles or different phases constituting each particle, fractures or discontinuity lines, etc.).

Different operators capable of generating edge gradients have been examined, such as those by Roberts, Prewitt, Sobel and Frei-Chen (Pratt, 1991); each was found to be incapable of accurately detecting edges in high-noise environments, as sometimes occur when one deals with particles. In such cases, a simple solution is to extend the size over which the gradient is computed. Examples of the different procedures for contour extraction that have been described are shown in **Figures 8 and 9**.

In any case, the identification of gradients on the image is only the first processing step in the identification and characterisation of discontinuities. To achieve the final goal, different analytic techniques may be applied which can help to identify particle boundaries or fractures or lines corresponding to preferential breakage paths, etc.

The procedure described in **Figure 10** allows one to match each image sample with an overlay map showing the directional colour-level gradients (for a given gradient template) that are greater than a suitable threshold value (Bonifazi and Massacci, 1988b).

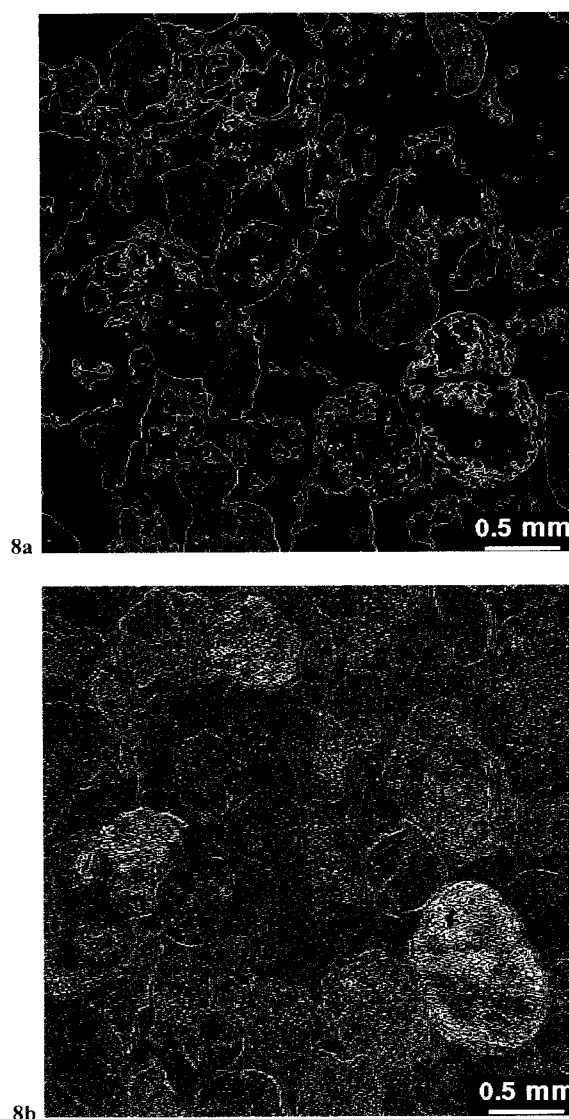


**Fig. 8** Contour extraction procedures applied to an RGB digital image of the bulk particle sample seen in Fig.4 (8a – image obtained by enhancing the spatial amplitude change with a further differential detection; 8b – image by an edge detection procedure adopting a Laplace operator).

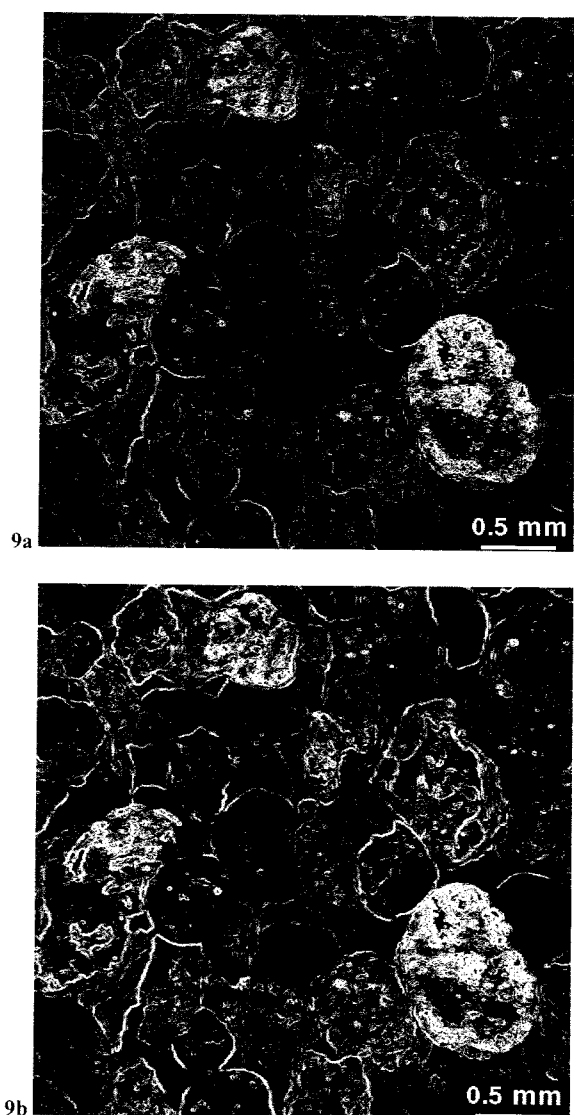


**Fig. 9** Contour extraction procedures applied to an RGB digital image of the bulk particle sample seen in Fig.4 (9a—image obtained by an edge detection procedure adopting a Roberts operator; 9b—image obtained by an edge detection procedure adopting a Sobel operator).

## 4. Particle Shape Analysis

### 4.1. Shape settlement

Classic morphologic analysis is based on the determination of numerical and/or dimension-less values in order to concisely describe the properties of a particle's boundary. Such an approach derives from a procedure that was commonly used in the past, based on determinations performed by an operator, followed by direct observations.

The principle elementary parameters are the following:

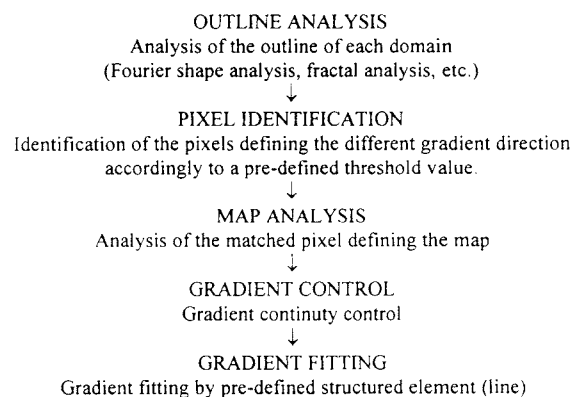


**Fig. 10** Gradient analysis procedure based on "fuzzy set logic" to define an overlay map showing the preferential direction of discontinuities inside a digital image.

- sieve size;
- maximum Feret diameter;
- minimum Feret diameter;
- major axis;
- minor axis;
- equivalent area diameter.

These parameters are not capable of representing the complexity of the morphologic structure of the outline of a particle, even though they require the use of large amounts of data related to the particle's images. An improved definition of a particle's shape may be obtained by Fourier (Luerkens et al., 1987) and/or fractal analysis (Kaye, 1984a) of its outline.

### 4.2. Fourier analysis of a particle's boundary

Two main procedures based on the Fourier analysis of a profile may be applied to the morphologic characterisation of a particle. The first method is based on Fixed Angular Boundary Sampling (FABS) (Beddow and Philip, 1975 and Luerkens et al., 1981) and the second is based on Fixed Boundary Segment Sampling (FBSS) (Bonifazi and Massacci, 1988c).

#### 4.2.1. Fixed Angular Boundary Sampling (FABS)

The boundary of a particle must be described in terms of polar coordinates, assuming the center of gravity as the origin, as shown in **Figure. 11a**. Choosing a fixed angular interval, for example  $2\pi/N$  radians, the shape of a particle's image may be defined by the distances (modules  $R_r$ ) from the origin to the boundary at the number of points,  $N$ . These values may be clearly represented by a suitable Fourier series, with the modules  $R_r$  (where  $r = 1, 2, \dots, N$ ) expressed by:

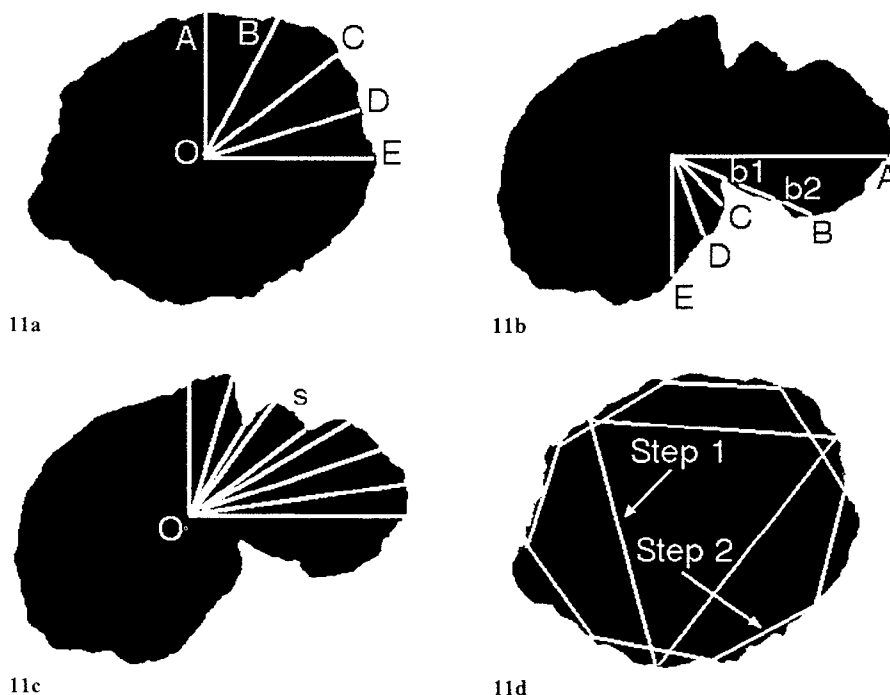


**Fig. 11** Particle profile analysis under different methodologies dependent on concavities or convexities: 11a – Fourier analysis of a particle convex profile: boundary sampling of the particle by constant angle rotating vectors; 11b – Fourier analysis of a particle concave profile: boundary sampling of the particle by constant angle rotating vectors (sampling indeterminacy appears); 11c – Fourier analysis of a particle profile: boundary sampling of the particle by constant step length; 11d – Fractal analysis of a particle profile: sampling polygons of different sides are shown.

$$R_r = \sum_{f=0}^{N-1} c_f e^{[r (2 \pi / N) i f]} \quad (27)$$

It is possible to generate the coefficient  $c_f$  from knowledge of the modules  $R_r$ ; this is done by using the inverse relationship for the  $c_f$  Fourier coefficients:

$$c_f = (1/N) \sum_{i=0}^{N-1} R_r e^{[-r (2 \pi / N) i f]} \quad (28)$$

Both series are cyclic with a periodicity equal to  $N$ ; thus, from the  $N$  measurements determined on a particle's image, the series of the coefficient  $c_f$  (where  $f = 1, 2, \dots, N-1$ ) may be estimated; these are called Fourier coefficients. With regard to discrete Fourier series and transforms, convergence and approximation results are well known and have been extensively used in signal processing and image analysis.

The  $c_f$  coefficients, as previously defined, describe a pattern vector that is representative of the particle's shape.

The angular interval ( $2 \pi / N$  radians) may be varied dependent on the irregularity of the particle's boundary. In other words, if the shape is regular, a relatively wide interval can be adopted, whereas if the shape is highly irregular, a small interval should be

used in order to ensure that the boundary is accurately sampled.

When particle shapes are highly irregular, the angular interval may be decreased, while the number of intervals  $N$  is maintained as a power of two for computational reasons. Furthermore, if the boundary has marked concavities, the distance between the origin and boundary becomes indeterminate; in this case, the smallest distance is considered, as shown in **Figure. 11b**.

#### 4.2.2. Fixed Boundary Segment Sampling (FBSS)

This procedure considers the distance along boundary segments. An example is shown in **Figure. 11c**, considering a particle profile on which a small step of size  $s$  is initially considered and the process is repeated until the final point is located near the initial point.

If the final point does not fall near the initial one, the step size  $s$  is increased and the procedure is repeated. As before, once the boundary has been closed, the coordinates of the points determined by the procedure must be expressed for computational reasons, as a power of two. The coordinates end-

point of each segment may be represented in terms of polar coordinates; in this manner, one obtains the Fourier coefficients. This procedure allows one to represent the boundary of the image more accurately and/or to reduce the number of harmonics required to characterise a given image with specified precision. It avoids, also, any ambiguities as to the definition of the boundary measurements. It should be noted, however, that this technique may require a number of changes in the step size to ensure adequate boundary closure.

### 4.3. Fractal Analysis (FA)

The fractal dimension of a particle's boundary may be defined using the hand and dividers technique on the curve that describes the outline of the silhouette (Kaye, 1984b).

The procedure first involves choosing an arbitrary point on the profile; a pair of dividers is set at some distance (where  $l$  is the step length) and is used to find another point on the curve at the exact same distance from the starting point, as shown in **Figure 11d**. Care must be taken in defining the way in which the dividers are moved, since different protocols may yield different edge points (Kaye et al., 1986).

In a computer-based procedure the next point (while moving along the digitized edge) at the prescribed distance from the starting point is automatically sought. The procedure is repeated to find a third point, fourth point and so on, until there is some closure length from the  $n$ -th point to the starting point which closes an  $n$ -sided polygon. Plainly, this polygon constitutes an approximation of the outline and the perimeter of the polygon,  $P$ , an approximation of the length of the outline (Kaye, 1993).

If the process is repeated by varying  $l$  it is possible to obtain various values of  $P_l$ . Generally,  $P_l$  decreases as larger values of  $l$  are selected and a log-log plot of  $P_l$  versus  $l$  yields a curve with a negative slope  $S$  in a Mandelbrot-Richardson plot (Mandelbrot, 1982). The fractal dimension is defined as  $D_F = 1 - S$  (Kaye, 1993).

The fractal dimension of a classic two-dimensional curve such as a particle's boundary quantifies how irregular or tortuous the curve is. A curve with a fractal dimension of 1 is a straight line, whereas a curve with a fractal dimension of 2 is so re-entrant that it covers the whole area of some part of a plane. Typically, the edges of real particles have fractal dimensions ranging between 1.03 and 1.45.

Sometimes, the plot exhibits more than one slope (**FA1**). The number of slopes (Kaye, 1993), usually 2 (**FA2**) or, more rarely, 3 (**FA3**), is strictly linked to the intrinsic characteristics of the particles (i.e. aggregates, if the particle is an association of different phases) (Kaye, 1994). In this case it is possible to define a texture-fractal and a structure-fractal, the first linked to the dimensions of the constituent elements, the second dependent on the results of their arrangement (Bonifazi et al., 1990).

An example of this approach is reported in **Figure 12**.

## 5. Recognition of Particle Composition

### 5.1. Particle composition via the colour scale

The phase composition of a particle may be obtained by Pictorial Analysis (**PA**) of the image elements by selecting appropriate RGB colour-scale intervals (or grey-scale in the case of B&W images). It has been assumed that a particle consists of phases, each of which has homogeneous pictorial characteristics (some phases are characterised by pixels belonging to identifiable classes of colours).

In order to evaluate the phases that constitute a solid, segmentation and labelling procedures are adopted. The procedures are easily performed for high-contrast images such as, for example, SEM images.

### 5.2. Particle composition via textural properties

A particle's phases are sometimes recognisable if one takes into consideration the spatial relationships between the pictorial elements, i.e. via Textural Analysis (**TA**). The colour tone variations of different

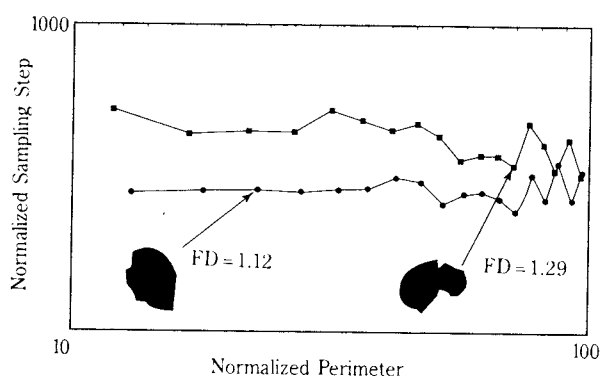


**Fig. 12** Richardson plot showing the perimeter estimates versus the stride length of the particles profile reported in Figures 1.1c and 1.2c, respectively. A structured walked technique is thus applied to evaluate the particle profile characteristics.

phases (i.e. distribution histogram) correspond to different spatial distributions of the colours and, therefore, to different textures.

The method for measuring these parameters has been described above. It is important to assess, with the aim of standardising determinations, the reflection or transmission measurements of the constituent phases. This association allows one to take into account the fact that the absolute distribution of the components of the RGB colours of a phase may be modified by the distribution of colour components in adjacent phases. Each phase is therefore identifiable by a vector of textural and reflective properties.

This approach, based on image analysis, is useful for the characterisation of coals and takes into account not only the reflectivity of the macerals, but also micro-textural characteristics within the macerals themselves (Agus et al., 1994a).

The analytical procedure consists of three steps:

- i) image fields acquisition (in windows related to selected areas) and mapping of information (related to macerals and minerals content of each field);
- ii) determinations of image micro-texture parameters and grey-level histograms (linked to the selected regions of macerals inside each sample image);
- iii) comparison of macerals content of each sample image (mapped using the classic reflectivity approach).

Each sample image and tested area is identified by an alpha-numeric code, while each maceral is defined on the basis of its micro-textural characteristics. This procedure improves the results that may be obtained by analysing the reflectivity characteristics of a coal polished section (analysis of grey levels).

When coal that is characterised by different macerals was examined, promising results were obtained by normalising the textural parameters with respect to the mean grey level of each window considered. Data was normalised by multiplying the textural parameters with the mean value of the grey level corresponding to the same window (Agus et al., 1994b)

The distribution of the normalised textural parameter values is plotted in **Figure. 13**, while in **Figure. 14**, the mean values of the same parameters are presented, considering the  $R_{1k}$ ,  $R_{2k}$  and  $R_{3k}$  normalised textural parameters for the three coordinate axes.

### 5.3. Particle composition via shape properties

A particle's shape is the result of physical and/or chemical actions applied to a solid; these actions carve the surface in various ways according to the nature

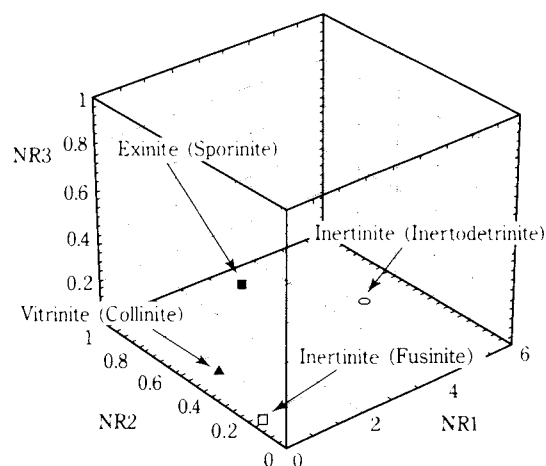


**Fig. 13** Maceral textural parameters (NR1, NR2 and NR3) after normalisation by multiplying for the mean grey level (GL).

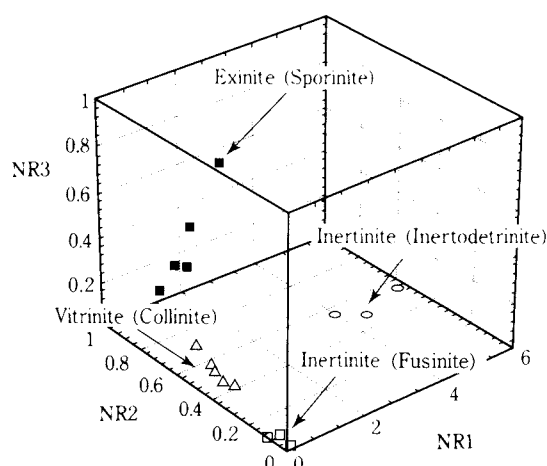
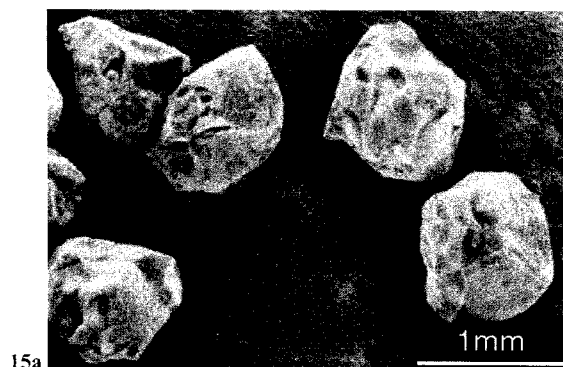


**Fig. 14** Mean values of maceral textural parameters (NR1, NR2 and NR3) after normalisation by multiplying for the mean grey level (GL).

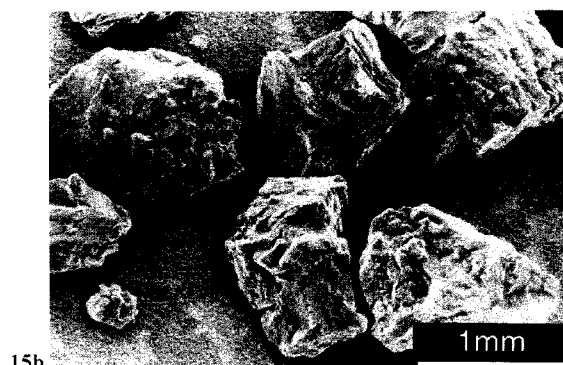
of the phases that constitute the particle. Particles of different mineral composition reveal different pattern characteristics. For this reason, the composition of a particle may be studied starting from a morphologic analysis of the outline of its image and adopting the methods described below.

Taking into consideration the Fourier analysis of the boundary, the particle's composition may be determined by analysing the boundary's shape.

This procedure was carried out on a chromite-olivine ore: as shown in **Figure. 15**, chromite particles and olivine particles present different morphologic characters. Mineral particles were divided into 6 classes of iso-composition in the two component minerals (Bonifazi et al., 1991). The procedure was



15a



15b

**Fig. 15** Scanning Electron Microscopy (BEI – Backscattered Electronic Image) of two particulate solids sample sets, belonging to the same size class, after comminution of a chromite ore. Chromite particles (15a) and olivine particles (15b) present different morphologic characters.

used to determine the distribution of chromite and olivine in a given sample and to precisely define the relative content of each mineral in individual particles. Similarly, promising results have been obtained with other mineral species. This recognition and classification approach, therefore, provides a new technique for determining the shape and size characteristics of particles, as well as their content in terms of their constituent mineral phases.

This method, which involves analysing the shape characteristics of a particle (or its morphologic signature), is much more general than the traditional approaches.

## 6. Particle Characterisation in Stream

Most of the equipment which is used for the continuous characterisation of flowing particles measures the size parameters that are proportional to the volume of the particles. In particular, optical techniques (Allen, 1990) based on the scattering theory (Cornillault, 1972) and Stoke's law are used. Such procedures are based on simple assumptions about

particle shapes and do not provide any information about morphologic structure.

One approach to this problem is based on an optic-system that uses laser light to illuminate the object, thus obtaining the silhouette of a particle in flow. In this way, information related to particle size and morphology is derived.

The optic system acquires and processes the information (particles in a flow stream) contained in a previously sampled portion of the fluid (Castellini et al., 1993); as a result, the sampling procedure can significantly affect the reliability and reproducibility of the results of the experiment. Two different types of applications may be distinguished:

- i) batch analysis (restricted parts and with a defined volume) of fluid samples containing particles;
- ii) on-line flow analysis drawn inside a circuit.

In a batch analysis, the dilution parameter may affect determinations; the sampling procedures and the metric system are relatively straightforward.

In an on-line analysis, the sampling procedure is far more complex as a result of problems related not only to the sampling of the stream (minimisation of noise), but also to the transportation and dilution of the sample. In both batch and on-line analyses, the opacity of the sediment has to be considered. A high sampling rate of fair images is obtained using pulsed illumination of short duration and high intensity.

In order to minimise particle superposition, the fluid-supported particulate solids are fed into a measurement cell that consists of two glass windows separated by a thin copper diaphragm of suitable thickness. The geometric characteristics of the cell, as well as the optic field, depend on the size of the particles.

The optic system consists of microscope-type equipment and a pulsed multi-array semiconductor laser for illumination (a peak power of 1 W with a wavelength of 850 nm on the near-infrared was employed); the laser beam travels along a plastic fibre-optic cable to the cell. A microscope lens of suitable magnification and numerical aperture is used to form the image of a sample on a non-interlaced TV camera. The working distance is greater than the thickness of the diaphragm. A motorised system controls the optics to achieve proper focus.

The digital images may be processed using different strategies, dependent on image type and, most of all, on the process which is used (i.e. batch or on-line analysis); plainly, if operation techniques vary a great deal, batch processing is much simpler (Bonifazi et al., 1993a).

In order to obtain relevant information, suitable focus-enhancement processing of the images must be undertaken. In the case of objects that are small compared to the depth of the field, the image disappears when the object is out of focus. When the depth of the field is very great, unfocusing the image changes the slope, but not the height of the object, because of the large dimension of the latter. For this reason, large particles may also be measured under unfocused conditions. The measurement of a linear dimension on an image reveals an inherent error that depends on the threshold value; if the particle is focused, the error is small because of the sharp slope of the sides. For large particles, more unfocused conditions may be tolerated by considering a constant relative error. **Figure. 16** shows particle silhouettes obtained after thresholding of the image sample and after numerical focusing and enhancement.

## 7. Recognition of particle shape and phase composition of particle set

In industrial processes, particles are present in bulk, which makes it difficult to discriminate individual ones. To describe particle characteristics, therefore, distribution of the properties themselves must be defined in statistical terms. This can be done, alternatively, by:

- i) starting from a colour-level analysis by correlating with the composition of the various phases (Kaye et al., 1995 and Bonifazi and Massacci, 1995);
- ii) starting from a textural analysis by correlating with the grain-size distribution (Bonifazi and Massacci, 1989a).

In the first case, the RGB colour-level distributions are assumed to be characteristic of each particle phase. In order to obtain a pattern vector that is able to describe a class of phases, a set of parameters is extracted:

- mean level values for the three RGB colours;
- standard deviations of the three colour-level distributions.

In the second case, the analysis is carried out adopting the same procedure and algorithm previously described in section 3.2 to characterise individual particle texture. In the case of a bulk of particles, the entire image field has to be analysed and the results assigned to the image sample considered as a whole. In this case, the following parameters assume a particular relevance:

- layout and type of light source;

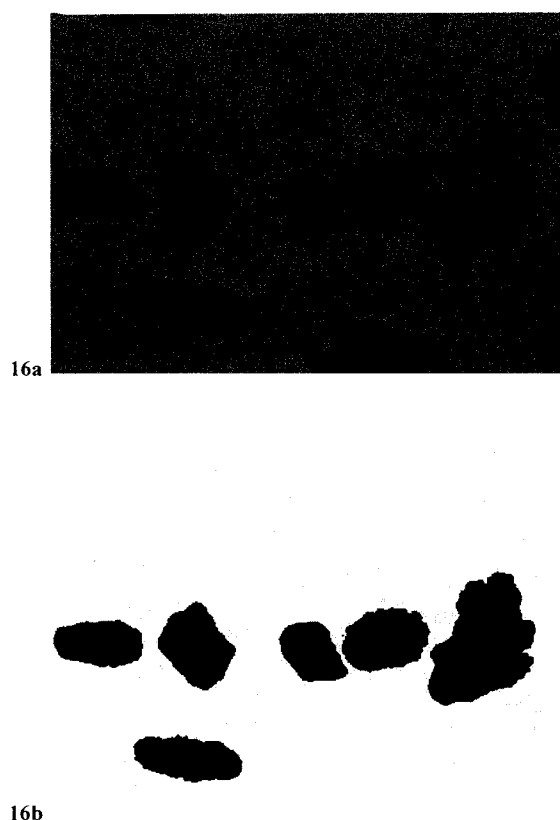


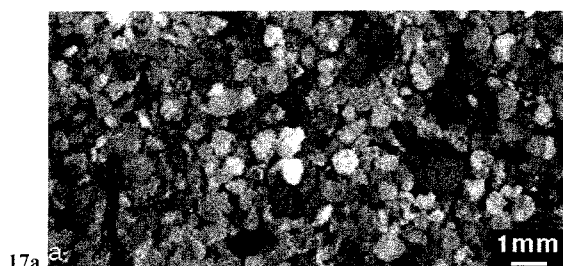
**Fig. 16** Digital image of a set of particles as it appears in a slurry flowing inside a circuit. The opacity of the slurry together with focusing strongly affect the quality of the image and the further processing. 16a: sample image after numerical focusing and a further enhancement. 16b: image after automatic thresholding.

- light intensity;
- shooting distance;
- relative diaphragm opening;
- analogue-digital conversion technique.

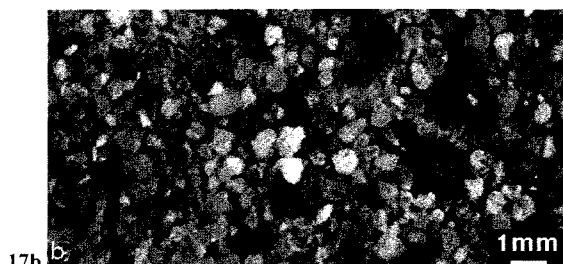
**Figure. 17** and **Table. 2** show an example of this procedure, which takes into consideration various size classes of sands with different mineral compositions. The strong correlation between grain size distribution and texture values is shown in **Table. 3**. The texture parameters corresponding to the four different size classes of the same material are reported in **Figure. 18**.

## 8. Particle Recognition and Classification

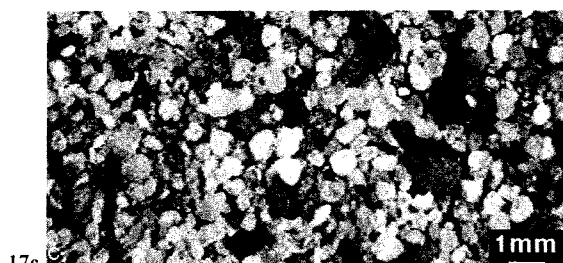
Once the characteristic properties of a particle or of a set of particles are defined (using the techniques described above), the structure of the data must be simplified: a feature vector has to be extracted from the pattern vector obtained from the measurements carried out on particles or on a set of particles present



17a



17b



17c

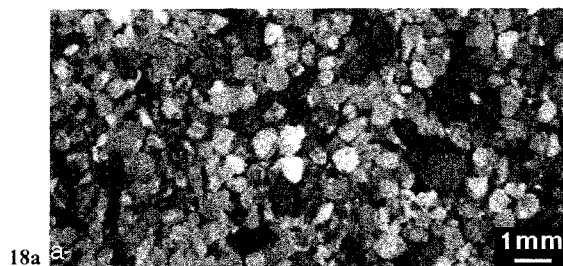
**Fig. 17** Bulk particles characterised by different size composition. The same sample is acquired in different lighting conditions.

**Table 2** Mean values of the textural parameters resulting from the analysis of the three images of the sample set of Fig. 17 acquired in different lighting conditions.

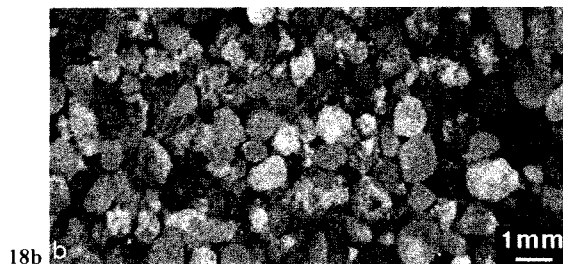
Texture Parameters			
Image	R1	R2	R3
19a	3,23E + 03	2,74E + 00	7,64E + 00
19b	2,37E + 03	3,76E + 00	7,33E + 00
19c	1,12E + 03	9,01E + 00	6,66E + 00

**Table 3** Mean values of the textural parameters resulting from the analysis of the same particle sample set of Fig. 17 acquired under different magnifications.

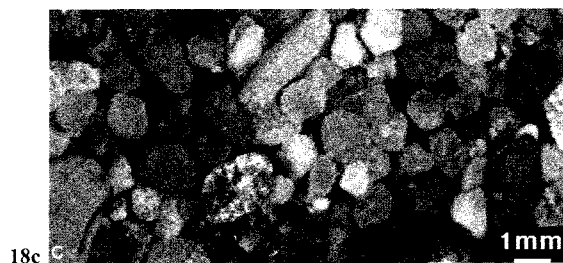
Texture Parameters			
Image	R1	R2	R3
20a	3,27E + 03	2,74E + 00	7,64E + 00
20b	3,84E + 03	2,63E + 00	7,81E + 00
20c	4,03E + 03	2,35E + 00	7,85E + 00
20d	4,87E + 03	1,95E + 00	8,05E + 00



18a



18b



18c



18d

**Fig. 18** Bulk particles. The images concerning the same material are referred to different size classes. The texture values vary accordingly.

in bulk. This is equivalent to reducing the size of the characteristic vector by taking into consideration only the determinant vector elements in the grouping of an individual particle (or of a particle set) within a specific class of characteristics (shape and composition). The problem, therefore, becomes that of analysing the data statistically and can be resolved by adopting various methods.

### 8.1 Feature extraction

The feature extraction algorithm considered in our studies (Bonifazi et al., 1989b) and improved by G. Patrizi, 1981, is the Karhunen-Loeve expan-

sion method (Duda and Hart, 1973). This procedure consists in minimising a mean square error criterion of misclassification, in cases in which the mean vector of the class is used as a classification criterion. The covariance matrix of the pattern vectors is calculated and its eigenvalues and eigenvectors are estimated. The  $e$  eigenvectors corresponding to the largest  $e$  eigenvalues are retained. To form the feature vectors (Garbow et al., 1977), the pattern vectors are pre-multiplied by a matrix formed by these eigenvectors. The procedure was implemented using the standard Eispack routines for the calculation of eigenvalues and eigenvectors (Smith et al., 1976).

The Feature Extraction routine (FE) adopted was successfully adopted for particle classification (Bonifazi et al., 1991a).

## 8.2. Classification Methods (CM)

The most common methods of Classification are based on the measurement of the **Minimum Distance (CMD)** and **Maximum Likelihood (CML)**.

In the training set, the **CMD** procedure is based on the computing of the mean and variance of the features of interest in each sample class. The mean represents the centre and the variance identifies the borders of each class. The classification of an unknown sample is accomplished by computing the distances between the new feature vector and the centre of each reference class; the sample is assigned to a specific class on the basis of these distances.

The **CML** procedure is based on the Bayes theory. An a priori probability for each class has to be established. To correctly classify an unknown sample, one must know the a posteriori probability that the sample with a certain property belongs to one of the considered classes.

These methods do not always allow for the recognition of the particle, particularly when the relationship between the characteristics of the various classes is not linear.

## 8.3. Multi-barycenters method

The **Multi-Barycenters Classification** algorithm (**CMB**) is based on the recognition algorithm of Firschlein & Fischler (1963) whose convergence properties have been studied in detail by Patrizi (1979).

The algorithm has two modes of operation:

- i) a training mode;
- ii) a classification mode.

In the training mode, a set of feature vectors is available that belongs to known classes and the train-

ing set, formed by these vectors, includes members of every class that is considered.

In the classification mode, a feature vector is submitted to the classifier and its class membership is determined by assigning it to the class which corresponds to the barycentre vector nearest to the feature vector.

Given the training set obtained in the training mode, an initial barycenter matrix is formed by finding the average feature vector from all the feature vectors of a given class. The distance of each feature vector from each barycenter vector of each class is then determined. According to the type of application, the distance may be generalised with different weights assigned to different components.

All the feature vectors which are closer to a barycenter vector of a class which is different from that to which the vector should normally belong are marked, and the one among them that is furthest from its proper barycenter vectors is selected to form the seed of a new barycenter vector. All the feature vectors are reassigned to the barycenter vectors of their own class, thus, at every iteration all the barycenter vectors remain the same except for the new class defined by the seed barycenter vector. In this class, the feature vectors are assigned to the different barycenter vectors, according to their distance from each other, to form subclasses.

Once assigned, the barycenter vectors of this class are recalculated as the average of the feature vectors in each subclass. The barycenter matrix will contain an additional column and the algorithm is reiterated by recalculating the distances. The algorithm will eventually converge, on the assumption that the training set satisfies certain non-stringent conditions (Patrizi, 1979).

Given the training set in the classification mode, the algorithm assigns the feature vectors related to a particle of unknown characteristics; it assigns the new particle vector to that class for which the square of the characteristics equation is the smallest.

**Figure. 19** shows the algorithm in structural form.

## 8.4. Neural net method

The simplest version of a neural net (Perceptron) (Mc Culloc and Pitts, 1943 and Rosenblatt, 1958) employs a binary output, organised in three layers, to establish to which class, A or B, a general pattern belongs.

The sensory units are connected to  $N$  units of

# CLASSIFICATION ALGORITHM (Training mode):

*DCL*  $NN$  number of features in the vectors.  
*DCL*  $T$  number of objects in the training set.  
*DCL*  $MM(j)$  number of barycentric vectors of class  $j$ .  
*DCL*  $NC$  number of classes  
*DCL*  $Data(i)$  Vector of features of the object  $i$ .  
*DCL*  $Tracer(j)$  barycentric vector  $j$ .

```

Begin;
  For i = 1,...,T Do;
    For j = 1,...,MM(NC) Do;
      DD(I) = Minj { Distance[data(i),
        tracer(j)] };
    End;
    CLTC(i) = arg { Minj { Distance[data(i),
      tracer(j)] } };
  End;
  For class_of{Data(i) } CLTC(i) Do;
    I* = arg { maxi { DD(I) } };
    Tracer(MM(NC)+1) = Data(I*) U
    class_of{Data(I*)};
    Sort{ Tracer per class };
    Update { number of barycentres
      MM(j) j = 1,...,NC };
    For i = 1,...,T Do;
      P = class_of{Data(i)};
      For j = MM(P-1)+1,...,MM(P) Do;
        J* = arg { minj { Distance{ Data(i),
          Tracer(j) } } };
      End;
      NTracer(J*) = [N(J*)*NTracer(J*)+
        +Data(J*)]/((N(J*)+1);
      N(J*) = N(J*) + 1;
    End;
    Tracer <- NTracer;
  End;
  Otherwise:
    Barycentric_matrix = MB = Tracer;
    Terminate;
  End;
End;
  
```

# CLASSIFICATION ALGORITHM (classifier mode):

```

Begin;
  For j = 1,...,MM(NC) Do;
    J* = arg { minj { MB * v } };
    class_of{v} = class_of{MB(J*)};
  End;
End;
  
```

**Fig. 19** Classification algorithm according to Patrizi (Patrizi, 1979 and 1981).

association or hidden layers. Every associative unit, receiving stimuli from the sensory units to which it is connected, has the role of detecting pattern characteristics. The relative weighted interconnectivity between sensory and associative units is previously fixed and is invariant during training. The connection topology may be undefined or established to impose ties which reflect the understanding of the problem. The decisional unity of the last layer receives the outputs  $Y_{pj}$ , referred to a pattern  $X_p$ , of

all the association units and calculates the output  $Y_p^*$ , creating a weighted sum and applying a threshold mechanism. The training procedure consists of finding, through repeated pattern presentations, a set of values for the weights  $W_i$ , between associative and decisional units, and for the threshold; this yields  $Y_p^* = 1$ , if the pattern  $p$  is of class A, or  $Y_p^* = 0$ , if the pattern  $p$  is of class B.

A schematic representation of a neural net logic is shown in **Figure. 20**.

In general, a neural classifier involves in the first stage a feature vector which represents the  $N$  input information. The values are shown sequentially or are decoded to allow an algorithm to calculate the value and to evaluate the nearest reference pattern. In the second stage, the maximum value is amplified and the lower value is decreased; thus, only the output corresponding to the class which the pattern vector belongs to will be high. The complexity of a net (number of nodes and layers) is a function of the complexity of the problem and the number of elements which constitute each vector fed to the net itself (Hopfield, 1982).

Particles of different mineral composition, which have already been morphologically characterised by a Fourier analysis of the boundary (see section 4.2), are classified with the neural net approach (Bonifazi, 1993b).

## 9. Conclusions

As a result of expanding application, image processing has become an increasingly promising method for the characterisation of particulate solids.

Different kinds of objectives may be pursued:

**a) Particle characterisation and classification by size:** size analysis does not entail particular difficulties in the case of coarse particles, whereas in the case of fine ones, results may be improved through the development of electronic focusing techniques;

**b) Particle characterisation and classification by shape:** the extraction of an adequate feature vector along with the use of adequate recognition algorithms has yielded satisfactory classification results; increased precision in classification by shape may be achieved through the improvement of classification algorithms;

**c) Particulate material recognition by the outline and the inside of the domain of the image:** for many material combinations, components may be satisfactorily recognised through the evaluation

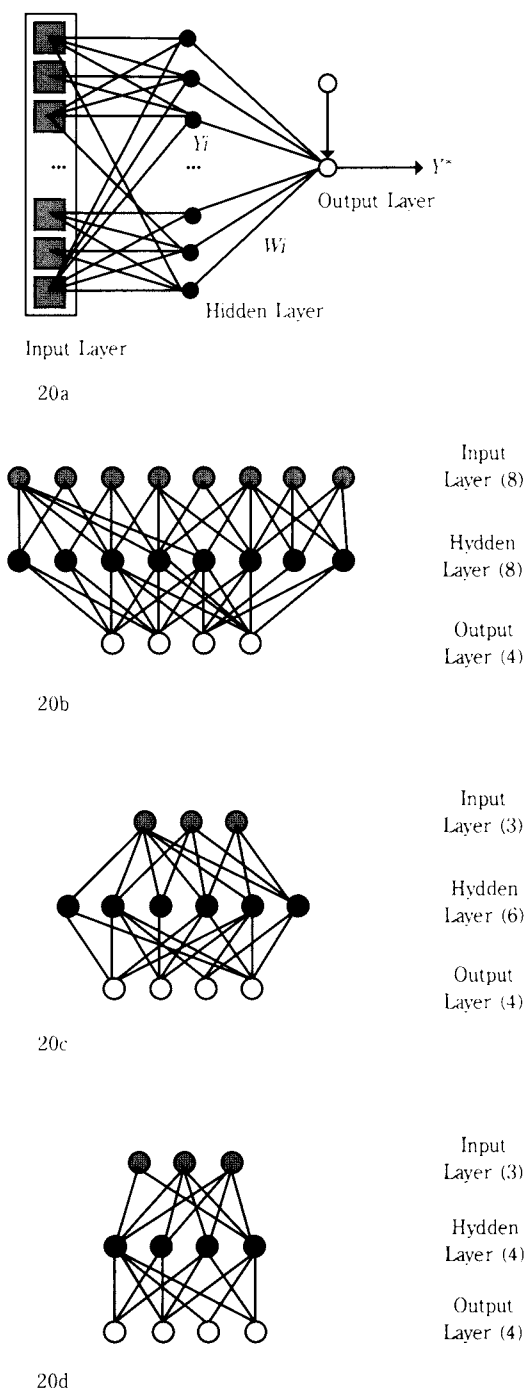


**Fig. 20** General schematic of neural net with a binary output (20a). Three layers are evidenced. The connection topology can be casual or set up with respect to the knowledge status. The connection weights ( $w_i$ ) are fixed. Different neural net architectures are reported in Figs. 20b, 20c and 20d.

of colour and/or textural parameters; for material combinations that are especially difficult to discriminate, new imageacquisition (e.g. lighting type) and signal-analysis (e.g. spectrum distribution) techniques must be developed;

**d) Identification of growth and size reduction laws:** these phenomena may be observed by means of image analysis and may be further investigated through the determination of shape and variation functions; alternatively, particle breakage functions may be described;

**e) Measurements of particle adhesion and removal:** the structure of associated particles may be studied by determining the shape and size of the association under various conditions;

**f) Recognition of particle in bulk:** the colours and textures in images of particles in bulk allow information that may be related to the size distribution and the mineral composition of the set of particles; the improvement of results already achieved depends on the extraction of representative feature vectors starting from the application of adequate statistical methods to data derived from the processing of images;

**g) Measurement of particles in flux:** the first results that have been obtained in the face of such an important problem in the treatment of solids have been satisfactory. Further progress may be achieved through the improvement of optics and intensive processing of the parameters that can be derived from the images.

## Nomenclature Symbols

$c_f$	: F�urier coefficients
$d$	: distance between nearby pixels along the direction $k$
$k$	: direction
$l$	: row index of the generic element for matrix $M_k(l, m, d)$
$m$	: column index of the generic element for matrix $M_k(l, m, d)$
$p$	: row index of the first pixel considered in the image
$q$	: column index of the first pixel considered in the image
$r$	: row index of the second pixel considered in the image
$s$	: column index of the second pixel considered in the image
$x, y$	: coordinate along the x-axis and the y-axis of the image
$GL$	: generic grey-level value in an image
$R, G, B$	: generic red, green and blue colour level values in an image
$L$	: the maximum grey level for a black and white image
$N$	: number of sampling point along a domain profile

$PA$	: a domain characterised by homogeneous pictorial characteristics
$TA$	: a domain characterised by homogeneous textural characteristics
$S$	: slope of the curve on the Mandelbrot-Richardson plot
$D_F$	: fractal dimension
$I_p$	: pictorial image as perceived by our senses
$I_d$	: digital image as digitised by the acquisition stage
$GL_t$	: mean grey level for a black and white image
$GL, i, j$	: grey-level value of the image associated to the pixel of coordinates $(i, j)$
$L_R, L_G, L_B$	: maximum colour level values for a colour image
$L_x, L_y$	: number of pixels in the image along the x-axis and the y-axis
$M_k(l, m, d)$	: spatial-tone dependence matrix
$M_k^*(l, m, d)$	: normalised spatial-tone dependence matrix
$N_x, N_y$	: size of the image along the x and y axis
$P_{GLi}$	: the probability distribution of grey levels for a black and white image
$P(x, y)$	: generic picture element (pixel) of coordinates $(x, y)$
$P(GL, x, y)$	: vector describing the grey-level component of the pixel of coordinates $(x, y)$
$P(I, S, H, x, y)$	: vector describing the intensity (I), saturation (S) and hue (H) colour components of the pixel of coordinates $(x, y)$
$P(R, G, B, x, y)$	: vector describing the red (R), green (G), blue (B) colour components of the pixel of coordinates $(x, y)$
$R_f$	: module of the Fourier series of a particle boundary
$R_{hk}$	: $h^{th}$ textural parameter computed for an assigned direction $k$
$R_t, G_t, B_t$	: mean values of R, G, B colour components for a colour image
$V_1, V_2$	: transformation coefficients
$W_i$	: connection weights between nodes of the layers constituting a neural network
$X_p$	: neural network input pattern
$Y_{pi}$	: neural network output pattern
$Y_{pi}^*$	: decisional unit output, the value result as a weighted sum of $Y_{pi}$

$\delta_x, \delta_y$	: gradient steps along the x and y directions
$\mu_x, \mu_y$	: means of the $M_k^*(l, m, d)$ distribution
$\sigma_x, \sigma_y$	: standard deviations of the $M_k^*(l, m, d)$ distribution
$\sigma_{Rt}, \sigma_{Gt}, \sigma_{Bt}$	: standard deviations of the colour components for an RGB-colour image
$\sigma_{GLt}$	: standard deviation of the grey level for a black and white image

## Abbreviations

<b>BP</b>	particles in bulk
<b>B&amp;W</b>	black and white image
<b>CMB</b>	classification by multi-barycenters algorithm
<b>CMD</b>	classification by minimum distance algorithm
<b>CML</b>	classification by maximum likelihood algorithm
<b>CNN</b>	classification by neural network
<b>FA</b>	fractal analysis of particle boundaries
<b>FABS</b>	Fourier analysis by fixed angular boundary sampling
<b>FBSS</b>	Fourier analysis by fixed boundary segment sampling
<b>FE</b>	feature extraction procedure
<b>FO</b>	flowing object
<b>ID</b>	inside of the image domain
<b>IP</b>	individual particle
<b>OD</b>	outline of the image domain
<b>PA</b>	particle domain characterisation by pictorial analysis
<b>RGB</b>	colour image
<b>SO</b>	standing object
<b>TA</b>	particle domain characterisation by textural analysis

## References

- 1) Agus M., G. Bonifazi and P. Massacci: Coal Structure Characterisation and Analysis by Digital Texture Processing . Int. Jour. of Fuel Processing Technology, Vol. 40, Nos 2 + 3, 361-367 (1994a)
- 2) Agus M., G. Bonifazi and P. Massacci: Image Texture Analysis Based Approach to Characterise and Recognise Coal Macerals. International Journal of Minerals Engineering. Vol. 7, No. 9, 1127-1147 (1994b).
- 3) Ahuja N.: Mosaic models for Image Analysis and Synthesis , Dept. of Computer Science, University of Maryland, College Park - Maryland, USA (1973).
- 4) Allen T.: Particle Size Measurement. Chapman Hall. New York (1990).
- 5) Andrews H.C., A.G. Tescher and R.P. Kruger: Image Processing by Digital Computers , IEEE Spectrum, 9, 20-32 (1972).

- 6) Beddow J.K. and G. Philip: Fourier Analysis-synthesis Method of Particle Shape Analysis. *Plauseeber Pulver-metall* 23 (1), 3 (1975).
- 7) Beddow J.K.: Particle Characterisation in Technology, Vol. II Morphological Analysis, CRC Press, Florida (1984).
- 8) Beddow J.K.: Morphological Analysis: Size, Shape and Texture Analysis, 1st World Congress Particle Technology, Particle Characterisation I, Nuremberg, 31-46 (1986)
- 9) Bonifazi G. and P. Massacci: Texture Analysis for Particulate Characterisation. International Conference on Production and Processing of Fine Particles, Plump-ton (ed.). Canadian Institute of Mining and Metallurgy, Montreal (Canada) (1988a).
- 10) Bonifazi G. and P. Massacci: Description of a Breakage Function by Image Processing. Proceedings of: XVI International Mineral Processing Congress. IMPC'88. Stockholm (1988b).
- 11) Bonifazi G. and P. Massacci: Particle Shape Analysis by means of Image Processing Techniques and Fourier Series. Proceedings of: International Conference on Management and Control of Granular Materials. MCGM'88. Shenyang (China) (1988c).
- 12) Bonifazi G. and P. Massacci: Texture Analysis for Comminution Products Characterisation. Proceedings of: XXI International Symposium on the Application of Computers and Operations Research in the Mineral Industry. APCOM'88. Las Vegas (1989a).
- 13) Bonifazi G., P. Massacci and G. Patrizi: Alternative Feature Selection Procedures for Particle Classification by Pattern Recognition Techniques. Cantoni V., Levaldi S. and Wolf H., (eds.) Recent Issues in Image Analysis, Lecture Notes in Computer Science, Springer-Verlag, Berlin (1989b).
- 14) Bonifazi G., E. Proverbio and E. Traversa: Fractal Description of  $MgAlO_4$  and  $MgFeO_4$  Fine Particle Agglomerates, 10th Congress CHISA-Praha, Czechoslovakia (1990).
- 15) Bonifazi G., P. Massacci and G. Patrizi: Hierarchical Properties of Particle Shape for the Recognition of Powdered Materials. *Int. Jour. of Part. & Part. Syst. Charact.* 8 116-123 (1991a).
- 16) Bonifazi G., F. Francini, G. Longobardi and P. Massacci: On-line Particle Characterisation by Image Analysis Techniques: a Preliminary Approach. AIChE 1993 Annual Meeting and Exhibit, St Louis (MI), U.S.A. (1993a).
- 17) Bonifazi G.: Mineral Particle Characterisation by Use of Neural Network Strategies. Artificial Intelligence in the Mineral Sector. The Institution of Mining and Metallurgy (London) & The University of Nottingham (Nottingham) (1993b)
- 18) Bonifazi G. and P. Massacci: Particulate Solids Characterisation by On-line Colour Analysis. PBS'95 – Powder & Bulk Solids Conference. May 8-11, 1995. Rosemont Convention Centre. Chicago, Illinois – USA (1995).
- 19) Castellini C., F. Francini, G. Longobardi and E. Pampaloni: On-line Characterisation of the Shape and Size of Particles, Part. Part. Syst. Charact., 19, 7-10 (1993).
- 20) Cornillault J.: Particle Size Analyser, *Appl. Opt.* II, 256-268 (1972).
- 21) Duda, R.O. and P.E. Hart: Pattern Classification and Scene Analysis, Wiley, New York (1973).
- 22) Ehrlich R., P.J. Brown, J.M. Yarus and D.T. Eppler: Advanced Particulate Morphology, CRC Press – Florida (1980).
- 23) Firschlein, O. and M. Fischler: Automatic Subclass Determination for Pattern Recognition Applications. *Trans. PGEC*, 12 (1963).
- 24) Garbow B.S., J.M. Boyle, J.J. Dongarra and C.B. Moler: Matrix Eigensystem Routines: Eispack Guide Extension, Springer Verlag, Berlin (1977).
- 25) Haralick R.M. and D. Anderson: Texturitone Study with Applications to Digitized Imagery, Univ. Kansas Centre for Research – Lawrence, USA (1971).
- 26) Haralick R., M.D. Shanmugam and I. Dinstein: Textural Features for Image Classification, *IEEE Transaction System, Man and Cybernetics*, 6, 610-621 (1973).
- 27) Hopfield J.J: Neural Networks and Physical System with Emergent Collective Computational Abilities, *Proc. of the National Academy of Sciences*, 79, 2554-2558 (1982).
- 28) Kaye B.H.: Fractal Description of Fine Particle System in N Dimensional Space, Conference on the Characterisation of Fine Particles – Nuremberg (1984a).
- 29) Kaye B.H.: Fractal Description of Fine Particle System, 81-100 in Beddow, Particle Characterisation in Technology, vol. 1, Applications to Microanalysis, CRC Press. Boca Raton (1984b).
- 30) Kaye B.H., G.G. Clark, J.E. Leblanc and R.A. Trotter: Image Analysis Procedures for Characterising the Fractal Dimension of Fine Particles, 1st World Congress on Particle Technology – Nuremberg (1986).
- 31) Kaye B.H: A Random Walk through Fractal Dimension. VCH – Verlagsgesellschaft, Weinheim (1993).
- 32) Kaye B.H: Chaos and Complexity. VCH – Verlagsgesellschaft, Weinheim (1994).
- 33) Kaye B.H., G. Bonifazi and J. Gratton-Liimatainen: Assessing the Quality of Powder Mixtures using Textural Image Analysis. PBS'95 – Powder & Bulk Solids Conference. May 8-11, 1995. Rosemont Convention Centre. Chicago, Illinois – USA (1995).
- 34) Luerkens D.W., J.K. Beddow and A.F. Vetter: Morphological Fourier descriptors. *Powder Technology* 31 (2), 209 (1981).
- 35) Luerkens D.W., J.K. Beddow and A.F. Vetter: Structure and Morphology, The Science of Form Applied to Particle Characterisation, Powder Technology, 50, 93-101 (1987).
- 36) Mandelbrot B.B.: Fractal Geometry of Nature, W.H. Freeman, S. Francisco, USA (1982).
- 37) McCulloch W.S and W. Pitts: A Logical Calculus of the Ideas Immanent in a Nervous Activity, *Bull*

- Mathematical Biophysics 5, 115-133 (1943).
- 38) Patrizi, G.: Optimal Clustering Properties, *Ricerca Operativa*, vol. 10, 37-60 (1979).
- 39) Patrizi G.: A Pattern Recognition Approach to Judicial Decisions (with reference to industrial property controversies). *European Journal of Operations Research*, vol. 7, N. 2, 133-142 (1981).
- 40) Pratt W.K.: *Digital Image Processing*. 2nd edition. John Wiley Inter science, New York (1991).
- 41) Rosenblatt F.: *Mechanisation of Thought Processes*, Proc. vol. 1, Symposium held in London at National Physical Laboratory (1958).
- 42) Smith, B.T., J.M. Boyle, J.J. Dongarra, B.S. Garbow, Y. Ikebe, V.C. Klema, C.B. Moler, *Matrix Eigen-system Routines: Eispack Guide*, Springer Verlag, Berlin (1976).

### Author's short biography



#### Giuseppe Bonifazi

Giuseppe Bonifazi obtained his degree in Mining Engineering in 1982 at the University of Rome (Italy). At the same University he was appointed Research Assistant in 1983. At the same University he was appointed Assistant Professor of Mining Plants from 1990 to 1992. Actually, from 1992, he is Assistant Professor of Particulate Solids Processing. His research interests are principally concerned with the characterisation of raw ores (texture and structure) and the comminution modelling. From 1986 he started to apply image processing/analyses techniques to characterize and model particulate solid materials.



#### Paolo Massacci

Paolo Massacci obtained his degree in Mining Engineering in 1964 at the University of Cagliari (Italy). At the same University he was appointed Research Assistant in 1964 and Assistant Professor in 1970. In 1975 he was appointed to his present position of Professor of Raw Material Engineering at the University of Rome (Italy), where since 1978 has been Chairman of the Mineral Engineering Division. He is currently member of the Scientific Committee of the International Mineral Processing Congresses, designed as Chairman for the XXI Congress which will be held in Rome in 2000.

His research interests are principally concerned mineral processing, characterization of particulate solids, recycling of secondary raw materials, flotation and comminution.

# Rapid Shape Analysis of Crushed Stone Using Image Analysis<sup>†</sup>

D.A. Broyles, H.W. Rimmer and G.T. Adel

Department of Mining and Minerals Engineering  
Virginia Polytechnic Institute and State University\*

## Abstract

*The shape and texture of construction aggregates are important parameters that have a direct bearing on the strength and durability of their asphalt and concrete end products. Although shape standards may vary throughout the world, nearly every country characterizes shape in terms of elongation and flatness. Typically, a given batch of material is rejected if more than a specific percentage of particles have elongation and flatness ratios which exceed some limit. Present procedures for determining these ratios rely on manual techniques which are tedious and tend to limit the number of samples that can be analyzed.*

*Researchers at Virginia Tech have recently developed a rapid shape analysis system which can determine elongation and flatness ratios for a standard batch of 100 particles in under 10 minutes. The system consists of an image analyzer constructed around a personal computer. Results obtained indicate an excellent agreement between the rapid analysis system and standard manual techniques. In addition, the system is capable of providing two quantitative measures of particle roughness. The development and validation of the analyzer and its measurement procedures are discussed.*

## 1. Introduction

Over two billion metric tons of aggregate (crushed stone, sand and gravel) are produced annually in the U.S. at a value of nearly \$10 billion. Of this tonnage, crushed stone makes up roughly 60% (USBM, 1995). Typically, this material must meet specifications generated by end-users and/or government agencies defining acceptable limits on several material properties including particle size, shape, strength, etc. Of these properties, particle shape may be one of the most important parameters to end-users since poorly shaped particles tend to reduce the strength and durability of road beds, asphalt and concrete.

There are several documented examples indicating the importance of shape and/or product roughness on end-product performance. Barksdale (1989), for example, developed an Aggregate Influence Factor incorporating several shape and roughness parameters to characterize the rutting and resiliency of aggregate bases such as might be used in road beds. Similarly, the use of "well-shaped" material in Portland cement concrete is known to give better workability of the fresh concrete and reduce the

quantity of cement and water needed to obtain a given strength. Unpublished work by Rimmer et al. (1986) on the effects of particle shape concludes that the strengths of standard specimens prepared with aggregate samples obtained from different crushers varies so markedly that the use of a well-shaped stone can permit cost reductions of about 15% through the reduced use of cement in concretes of a given compressive strength. Kojovic (1994) and Ramos, Smith and Kojovic (1994) investigated modifications to the crusher models developed at the Julius Kruttschnitt Minerals Research Centre (JKMRC) in order to predict both particle size and shape. They noted that particle shape, a major quality parameter in the construction aggregate industry, has largely been ignored by researchers.

A number of methods have been used and/or proposed over the years to characterize particle shape. These include everything from various qualitative measures to the use of Fourier descriptors and fractal analysis. The most common qualitative measures and shape factors can be found in a variety of classical texts (Allen, 1974; Orr and Dallavalle, 1960). The use of Fourier descriptors has been examined by several authors including Eppler and Meloy (1980) and Beddow (1988). Finally, fractal geometry has been explored since the late 1970's

\* Blacksburg, Virginia 24061-0239 U.S.A

† Received 16 Oct. 1995

(Kaye, 1978); although it is only beginning to be investigated for shape analysis in the construction aggregate industry (Carr et al., 1994).

Unfortunately, only a few of these methods are routinely used to characterize construction aggregates. The most common of these methods, and the one now accepted as an ASTM standard (ASTM, 1989), involves the measurement of elongation and flatness ratios. Referring to **Figure 1**, the elongation ratio is represented by the length-to-width ratio in the plan view, while the flatness ratio is represented by the width-to-height ratio in the end view. According to the standard ASTM procedure, elongation and flatness ratios are measured using a specially designed caliper, shown schematically in **Figure 2**. This caliper can be set to measure ratios of 2:1, 3:1 or 5:1 depending on various government regulations. Typically, 100 particles are measured and the number and/or weight percent of those particles exceeding a specified limit is recorded. A batch of material is rejected if a certain percentage of particles (e.g., 5%) have elongation or flatness ratios greater than this limiting value. Since this percentage and ratio can vary from state to state, it is possible that a crushed stone product which fails to meet the requirements of one state may be sold in another

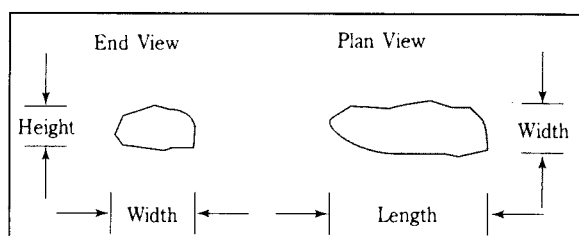
state. Unfortunately, this would require a second analysis at a different caliper setting. Clearly, even at coarse sizes this is an extremely tedious procedure requiring nearly an hour of analysis time per sample. Thus, the number of samples analyzed is greatly limited in a practical situation.

Over the past several years, researchers at Virginia Tech, under the sponsorship of the U.S. Bureau of Mines Generic Mineral Technology Center for Comminution, have developed a rapid shape analyzer based on the use of image analysis technology. This device replaces the tedious manual techniques currently in use in the aggregate industry and is capable of providing the entire flatness and elongation distribution of a sample in a fraction of the time currently required to obtain a single point on the distribution. In addition, the device provides a direct measure of roughness which is not available with current test procedures. The objective of this paper is to describe the development of the rapid shape analyzer, the test work carried out to validate the measurement procedures, and some preliminary applications of the analyzer in characterizing crusher performance.

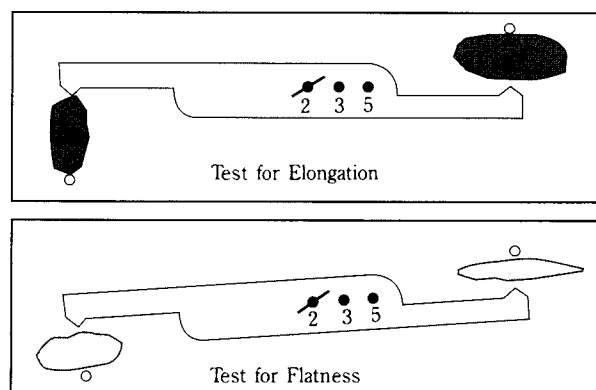
## 2. System Development

Image analysis and computer vision are becoming increasingly common in the world today for identifying and locating objects, analyzing defects and flaws in materials, and positioning robots or robotic arms. In the minerals industry, image analysis has been used for such things as assay determination, particle size analysis and mineral liberation studies. An image analysis system typically consists of a computer, a "frame grabber" board, and a television camera. An image is collected by the television camera and digitized by the frame grabber board. The computer then uses specially designed image analysis software to process the digital image and make measurements on the objects in the image. These measurements can include such things as color, size, area, shape, etc.

A schematic diagram of the rapid shape analysis system is shown in **Figure 3**. As shown, the system consists of a personal computer and monitor, frame grabber board, video monitor and sample presentation stand with dual camera mounts. Crushed stone samples are placed on the multi-level sample stand and positioned so that all samples can be properly viewed in the video monitor. Two cameras or camera angles are used so that both top and side views can be obtained to provide the necessary



**Fig. 1** Schematic diagram of a typical crushed stone particle.



**Fig. 2** Schematic diagram of the ASTM standard procedures for elongation and flatness measurements.

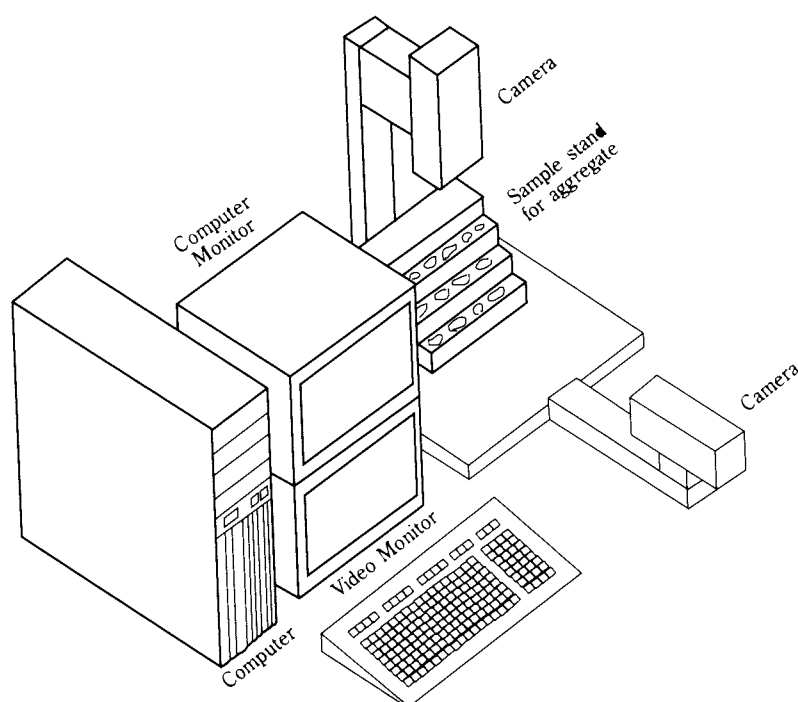


**Fig. 3** Schematic diagram of the rapid shape analysis system.

information for determining elongation and flatness. The camera images are received by the frame grabber board and digitized. The digitized images are then processed, using the OPTIMAS<sup>®</sup> software package marketed by Bioscan, Inc., to produce measurements of the individual particle dimensions. This information is then used to calculate the flatness and elongation ratios, along with two different roughness parameters, for each particle. The software is compatible with Microsoft Windows<sup>®</sup> and the data can be displayed in user-friendly tables and plots.

During the course of the system development work, both single- and dual-camera prototypes were tested. In general, it was found that the dual-camera arrangement gave a higher degree of accuracy; however, it is possible that a single camera on a moveable arm may be a cost-effective alternative in future versions. In addition, a multi-level sample stand was incorporated so that more particles would fit within a single field-of-view than would be possible with a flat stand. With the present design, approximately 20-30 particles of Virginia Department of Transportation (VDOT) Designation 57 (90-100% minus 25 mm, 26-60% minus 12 mm, and 0-3% minus 2.4 mm) can be placed in a single image. Assuming a conservative estimate of one minute to load the sample stand, one minute to process the image and one minute to unload the stand, it should be easily possible to complete 100 measurements of

both elongation and flatness in under 15 minutes, and probably within 10 minutes. The equipment required for the current prototype analyzer was purchased for approximately \$10,000. It is estimated, however, that this cost could be reduced to approximately \$5,000 in a commercial version by using less expensive television cameras and by installing an application version of the software as opposed to a developmental version.

### 3. Testing and Verification

#### Elongation and Flatness

A sample of crushed limestone (VDOT Designation 57) was obtained from the W.W. Boxley Co. Blue Ridge Operation near Roanoke, Virginia, for use in verifying the accuracy of the rapid shape analysis system. Approximately 150 particles were selected from the sample and each particle was hand measured with a micrometer caliper to determine the elongation and flatness ratios. The same set of particles was then measured using the shape analyzer and the results were compared. These comparisons are shown in **Figures 4 and 5** in terms of shape distribution plots (i.e., number percent of particles having elongation or flatness ratios greater than a given value). As shown, the agreement between the caliper measurement and the image analysis measurement is remarkable. The two lines are nearly coincident with,

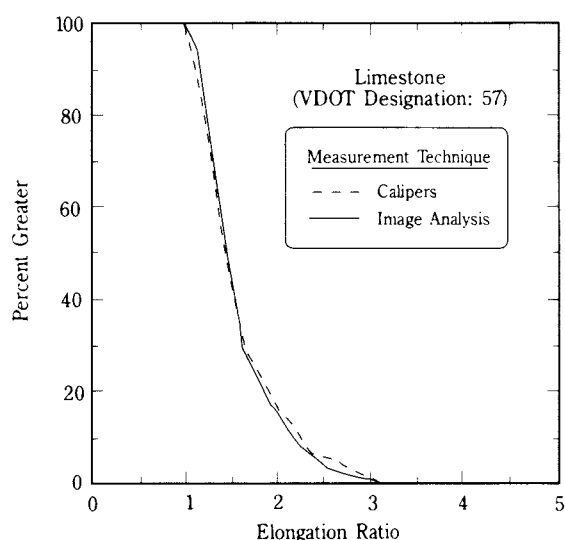


**Fig. 4** Comparison of elongation ratios obtained using image analysis and manual measurement techniques.

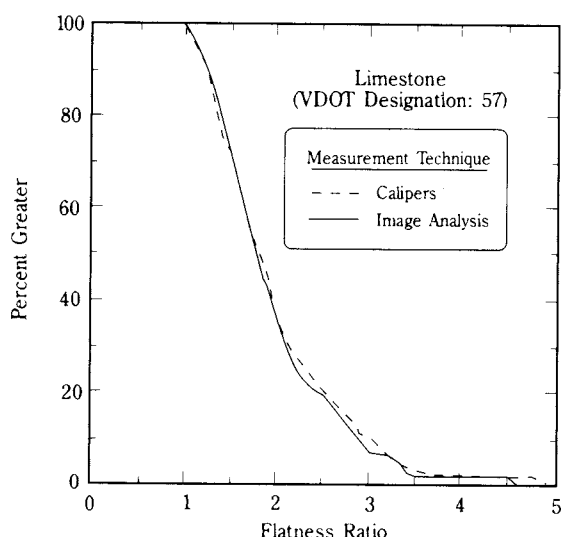


**Fig. 5** Comparison of flatness ratios obtained using image analysis and manual measurement techniques.

perhaps, a slightly greater deviation in the case of the flatness measurement.

It is important to note that the rapid shape analyzer is not limited to providing information at a specific value, such as percentage of particles having an elongation greater than 3, but routinely provides information on the entire shape distribution. Thus, from a single measurement, it is possible to determine the percentage of particles having flatness and elongation ratios greater than 2, 3 or 5, as may be required by various state specifications. Further research may also make it possible to correlate the shape distribution to the strength and durability of

the final end product. For example, it may be possible that two aggregate samples exhibiting the same percentage of flat and elongated particles at some limiting ratio, may very well produce asphalt or concrete products of different strengths due to differences in the overall shape distribution.

### Roughness

In addition to elongation and flatness, the rapid shape analyzer is capable of conducting other useful particle characterization measurements without the need for additional image processing time. One such measurement that has been incorporated into the current design is roughness. At present, there is no direct method for measuring particle roughness in the aggregate industry. Therefore, two parameters have been identified in this work that directly quantify particle roughness. These two parameters are termed "surface irregularity" and "jaggedness".

**Figure 6** illustrates the present implementation of the surface irregularity measurement. The image analysis system begins by locating the centroid of each particle. It then measures the distance,  $R_i$ , from the centroid to the edge of the particle in two-degree increments (**Figure 6a**). If these distance measurements are plotted as a function of the angle,  $\theta$ , the surface irregularity of the particle is transformed into a linear trace (**Figure 6b**). In order to make the measurement independent of particle size, the distance measurements are normalized by dividing by the average radius,  $R_{avg}$ , of the particle (**Figure 6c**). These normalized radii are then digitally filtered to remove surface variations caused by "noise" (**Figure 6d**), and the numerical derivative of the trace is taken to determine the number of peaks and valleys. This number, expressed as a percentage of the total number of possible peaks and valleys (i.e., 179 if every measurement was a peak or valley), represents the surface irregularity of the particle. Mathematically, surface irregularity can be represented using the unit impulse function as:

$$\text{Surface Irregularity} = \frac{\sum_{i=1}^{179} I\left(\frac{d \frac{R_i}{R_{avg}}}{d\theta}\right)}{179} \cdot 100 \quad (1)$$

The jaggedness measurement is used to indicate the amount by which a particle deviates from a perfect sphere. It is calculated using many of the

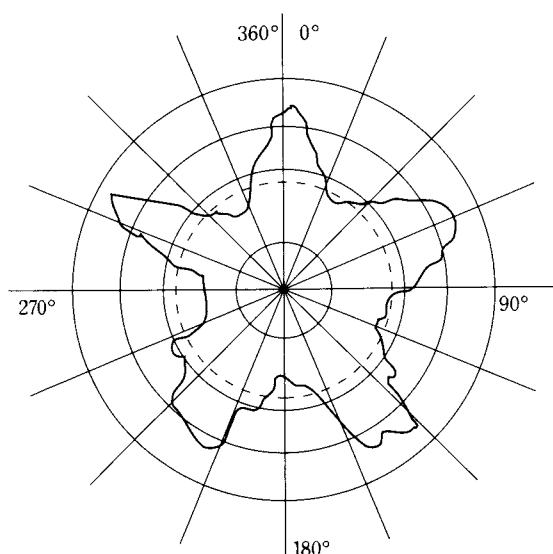


Fig. 6a. Distance from the centroid.

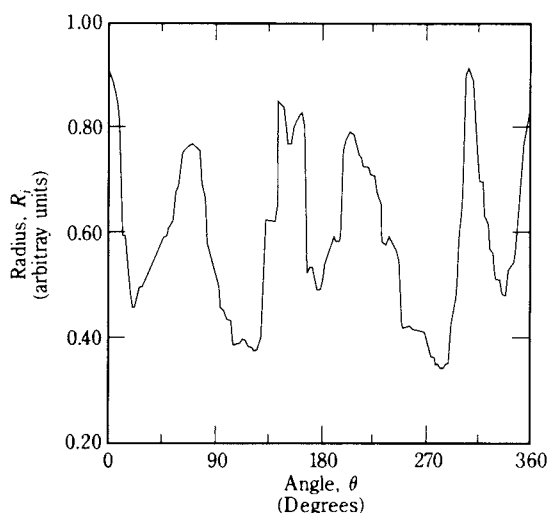


Fig. 6b. Surface irregularity trace.

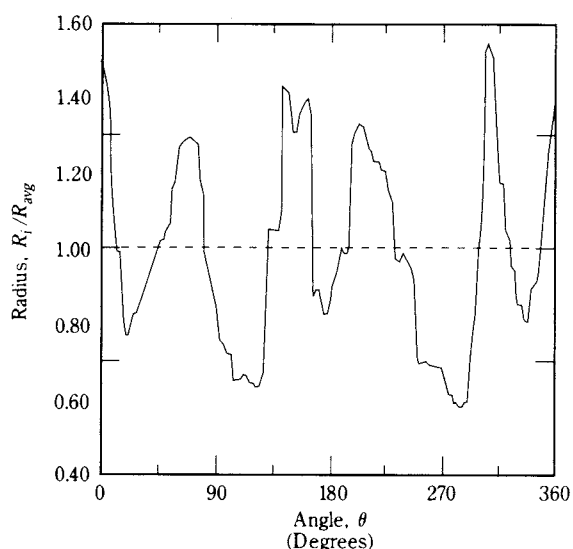


Fig. 6c. Normalized surface irregularity trace.

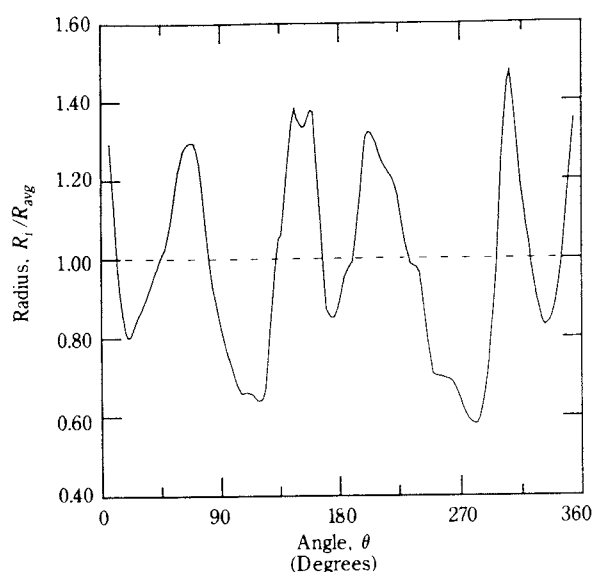


Fig. 6d. Normalized trace after noise removal.









same parameters used for surface irregularity. In this case, the normalized radius,  $R_i/R_{avg}$ , is subtracted from 1. This value provides a measure of the deviation of the radius from the average radius. A perfect sphere should give a value of zero. The individual measurements are then summed over all 180 two-degree increments, and the sum is divided by 180 to give an average measure of the deviation per increment. Mathematically, jaggedness can be represented as:

$$\text{Jaggedness} = \frac{\sum_{i=1}^{180} \left| 1 - \frac{R_i}{R_{avg}} \right|}{180} \quad (2)$$

The implementation of the jaggedness and surface irregularity parameters is illustrated in **Table 1** using several standard shapes. As can be seen, jaggedness values are typically higher for particles which are elongated or have large projections (i.e., particle types 1, 3, 4, 6 and 7). Surface irregularity values are higher for particles which have many small projections (i.e., particle types 2, 6, 7 and 8). Particles such as the star (particle type 4) are jagged but exhibit a very regular surface, while particles such as the gear (particle type 2) have a high surface irregularity but are not considered jagged. The particle illustrated as type 6 is both jagged and irregular, while a perfect circle (particle type 5) shows no jaggedness or surface irregularity.

Although the rapid shape analyzer makes it possible to quantify particle roughness, the utility of these roughness parameters is yet to be determined.

**Table 1. Roughness measurements made on several standard shapes.**

Particle Type	Surface Irregularity	Jaggedness
1. 	5.59	61.76
2. 	24.029	6.34
3. 	3.91	28.26
4. 	2.79	25.35
5. 	0.56	0.74
6. 	11.17	26.34
7. 	9.49	23.30
8. 	6.70	3.88

Obviously, the next step is to correlate these quantitative values to end-product quality. Once appropriate roughness specifications are identified, it may be possible to evaluate crusher and impactor performance in terms of particle roughness.

#### 4. Applications

The use of the rapid shape analysis system to characterize crusher performance is still in its infancy; however, preliminary results have been obtained on the product from a 1.3-meter short-head cone crusher operating on a basalt-type material at the W.W. Boxley Co. Mt. Athos Plant. This crusher is used as the fourth stage of crushing following a primary jaw crusher, a standard cone crusher and another short-head cone crusher. A belt sample was collected immediately following the crusher discharge point, and the material was sized to produce the distribution shown in **Table 2**.

Since the bulk of the sample was primarily in the range from 40-5 mm, four size classes within this range were analyzed using the rapid shape analysis system to produce the results shown in Figures 7-10.

**Table 2. Product size distribution from 1.3-meter short-head cone crusher.**

Size Class (mm)	Weight Percent
+38	0.9
38 × 25	23.1
25 × 19	27.4
19 × 12	23.5
12 × 6.4	11.6
6.4 × 3.3	4.6
-3.3	8.9

As shown in **Figures 7 and 8**, the coarsest particles appear to be more regular in shape, i.e., fewer flat and elongated particles. As size decreases, the percentage of flat and elongated particles increases. Furthermore, the coarsest particles tend to have fewer protrusions as indicated by the jaggedness distribution (**Figure 9**). These results seem to suggest that the coarse particles appearing in the crusher product are subjected to little breakage and simply have their jagged edges removed. The finer particles, which are freshly produced within the crusher, tend to be less regular in shape and more jagged. In terms of surface irregularity (**Figure 10**), there is a general tendency for the particle surfaces to become smoother as size decreases. This sug-

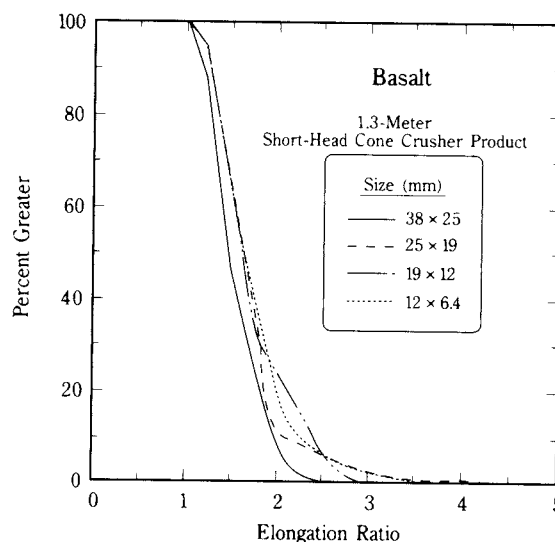


**Fig. 7** Comparison of the elongation distributions as a function of particle size obtained from the product of a 1.3-meter short-head cone crusher.

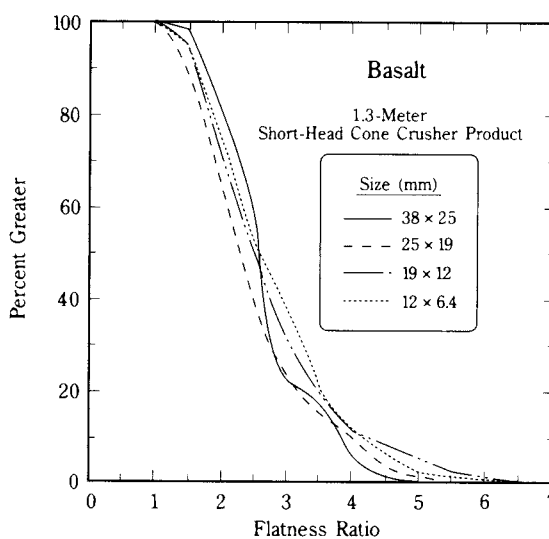


**Fig. 8** Comparison of the flatness distributions as a function of particle size obtained from the product of a 1.3-meter short-head cone crusher.

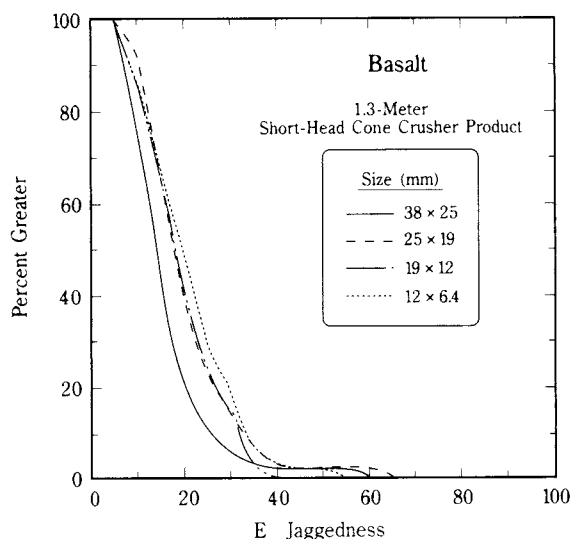


Fig. 9 Comparison of the jaggedness distributions as a function of particle size obtained from the product of a 1.3-meter short-head cone crusher.

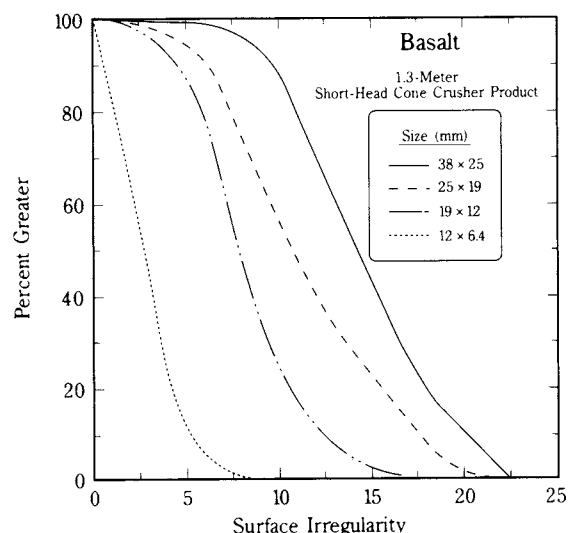


Fig. 10 Comparison of the surface irregularity distributions as a function of particle size obtained from the product of a 1.3-meter short-head cone crusher.

gests that the finer particles are subjected to more breakage and attrition events as they are produced resulting in smoother surfaces. A summary of these findings for specific limiting values of flatness and elongation, surface irregularity and jaggedness is given in Table 3.

Table 3. Summary of shape characterization results for 1.3-meter short-head cone crusher product.

Size Class (mm)	% Flat and Elongated ( $>3$ )	% Jagged ( $>30$ )	% Rough ( $>10$ )
38 x 25	24	6	88
25 x 19	27	13	54
19 x 12	29	13	25
12 x 6.4	41	16	0

## 5. Summary and Conclusions

1. A rapid shape analysis system has been developed for the aggregate industry. The system uses state-of-the-art image analysis technology to determine elongation, flatness and two measures of roughness.
2. The system is capable of analyzing a standard batch of 100 particles in under 10 minutes and provides information on the entire shape distribution as compared to current manual techniques which provide only a single point of the distribution.
3. Results from the rapid shape analysis system were found to be in excellent agreement with manual measurements of elongation and flatness.
4. Two direct measurements of roughness have been proposed and demonstrated with the rapid shape analyzer. At present, there are no other techniques available for direct measurement of roughness.
5. Preliminary analyses of crusher products indicate that the shape analysis system can serve as a useful tool for quantifying the effect of crusher type and operating conditions on particle shape.

## 6. Acknowledgments

This research has been supported by the Department of Interior's Mineral Institute program administered by the Bureau of Mines through the Generic Mineral Technology Center for Comminution under Grant Nos. G1115149 and G1125249. The authors would also like to acknowledge the assistance and cooperation of the W.W. Boxley Co. in providing the samples used in this work.

## Nomenclature

- $I(\ )$  unit impulse function  
 $R_i$  distance from the centroid of a particle to its edge  
 $R_{avg}$  average particle radius (average of  $R_i$  over 180 two-degree increments)  
 $\theta$  direction angle for any particle radius, degrees

## References

- 1) Allen, T., 1974, *Particle Size Measurement*, Chapman & Hall, London.
- 2) American Society for Testing and Materials, 1989, "Standard Test Method for Flat or Elongated Particles in Coarse Aggregate," *Annual Book of ASTM Standards*, D4791-89.
- 3) Barksdale, R.D., 1989, "Influence of Aggregate Shape on Base Behavior," *Stone Review*, April, pp. 10-12.
- 4) Beddow, J.K., 1988, "Morphological Analysis of Particles and Surfaces," *Production and Processing of Fine Particles*, A.J. Plumptre, ed., Pergamon Press, New York, pp. 25-38.

- 5) Carr, J.R., Norris, G.M. and Newcomb, D.E., "Characterization of Aggregate Shape Using Fractal Dimension," National Research Council, Transportation Research Board Record 1278, Washington, D.C., pp. 43-50.
- 6) Eppler, D.T. and Meloy, T.P., 1980, "Applicability of Sophisticated Shape Analysis Techniques to Engineering and Industrial Problems -- Fourier Shape Analysis," *Fine Particle Processing*, P. Somasundaran, ed., AIME, New York, pp. 462-480.
- 7) Kaye, B.H., 1978, "Specification of the Ruggedness and or Texture of a Fine Particle Profile by its Fractal Dimension," *Powder Technology*, Vol. 21, pp. 1-16.
- 8) Kojovic, T., 1994, "Prediction and Control of Aggregate Shape Resulting from Crushing," *Quarrying - A Customer Focus*, Ingersoll-Rand, pp. 247-261.
- 9) Orr, C. and Dallavalle, J.M., *Fine Particle Measurement*, The Macmillan Company, New York, 1960.
- 10) Ramos, M., Smith, M.R., and Kojovic, T., 1994, Aggregate Shape - Prediction and Control During Crushing," *Quarry Management*, November, pp. 23-29.
- 11) Rimmer, H.W., Kebort, L.R. and Harris, G., 1986, "Factors Affecting the Design and Operation of Aggregate Plants," Paper presented to the SME-AIME Fall Meeting, St. Louis, Sept., 14 pp.
- 12) U.S. Department of Interior, Bureau of Mines, 1995, "Crushed Stone and Sand and Gravel in the Third Quarter of 1995," *Mineral Industry Surveys*, Washington, D.C., 7 pp.

### Author's short biography

#### David A. Broyles

David A. Broyles obtained his B.S. (1992) and M.S. (1995) in Mining and Minerals Engineering from Virginia Polytechnic Institute and State University. His M.S. thesis focused on the development of an optical analyzer for measuring the shape of crushed stone particles used in the construction aggregate industry. Mr. Broyles is a member of the Virginia Society of Professional Engineers, the National Society of Professional Engineers and the Society for Mining, Metallurgy and Exploration, Inc. He is currently employed as a mineral processing engineer for Engelhard Corp. in Macon, Georgia.

#### Hugh W. Rimmer

Hugh W. Rimmer is a graduate of Otago (BE, 1963) and Columbia Universities (EngScD, 1972). He taught for several years following graduation, and has worked in process control and metallurgical R&D on the Zambian Copperbelt; in comminution/minerals processing with Allis-Chalmers/Svedala; and in coal and minerals processing R&D at Virginia Tech. He is currently self employed, working on process evaluation/optimization and enterprise computing projects in coal, aggregates and minerals processing.



#### Gregory T. Adel

Gregory T. Adel (Associate Professor, Mining and Minerals Engineering) received his B.S. degree (1978) and M.S. degree (1979) in Metallurgical Engineering from South Dakota School of Mines and Technology. He received his D. Eng. degree in 1982 from the University of California, Berkeley. Following Graduation, he joined the Department of Mining and Minerals Engineering at Virginia Polytechnic Institute and State University as an Assistant Professor. he was promoted to Associate Professor in 1987. Dr. Adel is an active member of the Mineral and Metallurgical Processing Division of the Society for Mining, Metallurgy and Exploration, Inc., serving on a variety of committees. He has approximately 60 publications and 4 patents in areas pertaining to image analysis, optical sensors, mineral and coal characterization, and modeling and simulation of mineral and coal processing operations.



# Studies on the Effect of Moisture Content and Coarse and Fine Particle Concentration on Segregation in Bins<sup>†</sup>

D. F. Bagster

Department of Chemical Engineering, University of Sydney\*

## Abstract

Previous work by the author [1, 2, 3, 4] on particle size segregation in bins has been extended to consider the effect of the concentration of coarse particles. At low coarse concentrations a simplification can be achieved by plotting the non-dimensional concentration of coarse material  $C/C_F$  to summarise the profile. The present study reveals that at high values of  $C_F$ , the coarse feed concentration, the segregation pattern is highly dependent on  $C_F$ .

The addition of small amounts (less than 1%) of water to feed mixtures has a profound influence on segregation behaviour in many cases smoothing what would otherwise be severe segregation patterns with dry materials. Previous study contained speculation that segregation was reduced because the water caused an increase in cohesion of the fines content of the feed which in turn slowed the progress of coarse material relative to fine. Further discussion of this phenomenon is provided here.

## 1. Introduction

The deleterious effect of particle segregation in containers is well-known [5, 6, 7, 8]. In filling bins there is a tendency for coarser particles to separate outward from filling points with a resultant segregation, fine particles in the centre, coarser to the walls. Subsequent withdrawal of the material through a funnel flow hopper below will tend to allow the central material to emerge first with the outer material appearing later. A variation in flow rate and in particle size of discharge can thus readily result.

The same segregation phenomenon on filling can occur in charging a reactor or absorbing vessel and if performance is dependent on particle size or on fluid residence time in the vessel it is obvious that particle size segregation or fluid channelling as a result of it will affect performance.

Potentially most serious of all is the possibility, because of particle segregation, of uneven loading on container walls which possibly could lead to failure of the structure.

In the present study segregation was achieved by using only particles of the same density, by minimising lateral velocity of particles at the feed point and by having no impact velocity at the feed point. A

diagram of the apparatus used in those studies and this is presented in **Figure 1**. Other workers have since used a similar apparatus [9, 10].

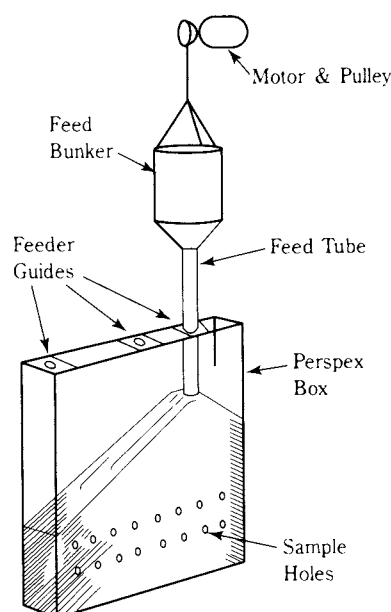


Fig. 1 Schematic Diagram of Segregation Box.

\* Sydney NSW 2006, Australia

† Received 10 June, 1996

It was found that the concentration profiles for varying slope lengths could be correlated using a fractional (dimensionless) slope length, and, at low feed concentrations of coarse particles, the profiles could be correlated with concentration ratios. The latter finding is consistent with there being no interference between coarse particles.

**Figure 2** presents typical results. When the fine fraction in the feed was reduced in particle size a reversal of profile resulted, **Figure 3**, indicating that, relatively speaking, the coarse particles were retarded in their flow down the slope. At high feed concentrations the wall region tended to have a flat, high concentration profile of coarse material, **Figure 4**. It was therefore concluded that segregation patterns in bins are dependent in a complex way both on feed concentration of coarse powder and, through some mechanism or other, on the fineness of the fine powder.

Measurements of the cohesion of the various fine fractions (including one to which a small amount of water was added) showed that even a very mildly cohesive powder has a very marked effect on segregation profile, with cohesion of about 0.25 kPa

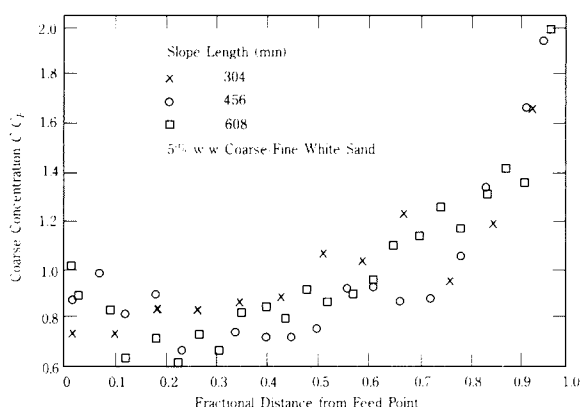


**Fig. 2** Segregation Patterns with Relatively Coarse Fines.

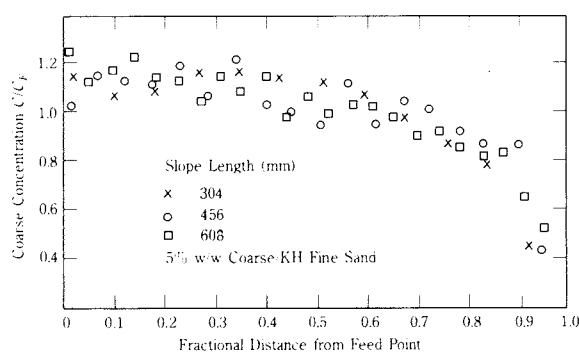


**Fig. 3** Segregation Patterns with Relatively Fine Fines.

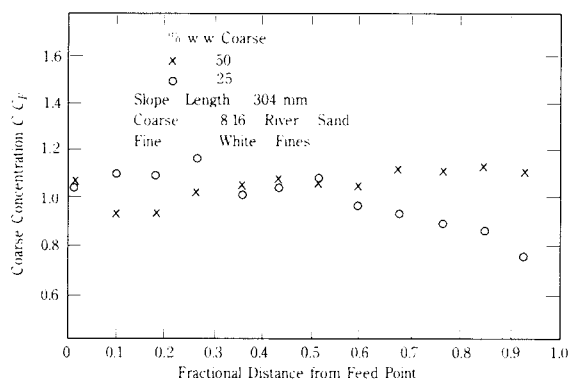


**Fig. 4** Segregation Pattern with High Concentrations of Coarse Material.

(consolidating pressure 6.7 kPa) being associated with a reversal of the commonly discussed profile of coarse accumulation away from the feed point. A further increase to 0.5 kPa almost completely eliminated segregation; **Figure 5**.

The present work is an extension of that study with particular emphasis on;

- (i) the concentration of coarse material in the feed mixture,
- (ii) the size of the fine material and its cohesion as measured in the Jenike type direct shear tester,
- (iii) the effect of added water on the segregation patterns, in particular in relation to cohesion of the fine fraction.

## 2. Experiments and results

**Figure 6** shows the particle size distribution of the various sands employed in the present work with one sand being regarded as relatively coarse (16/30) while three other sands were available to mix with the coarse sand as binary feed mixtures.

The apparatus displayed in **Figure 1** was used

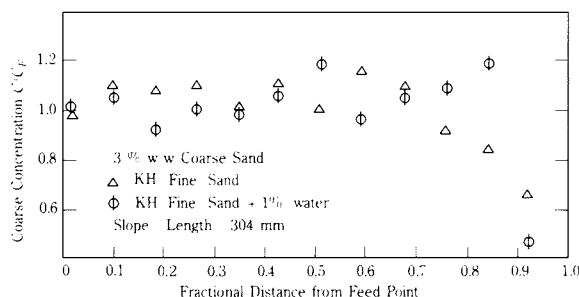


**Fig. 5** Effect of Small Percentage of Water on Segregation Pattern.

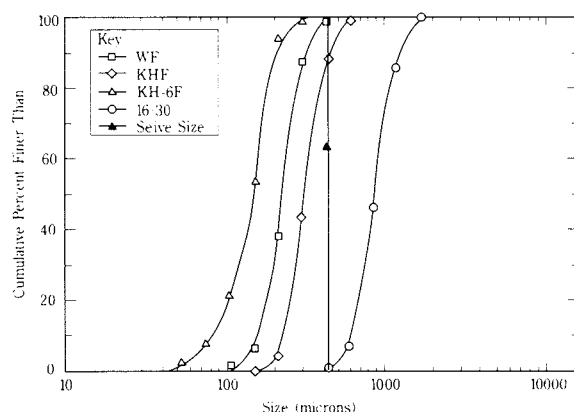


Fig. 6 Particle Size Distributions of Current Study.

as in earlier studies [1, 2, 4]. For the current study the feed was delivered to the central point of the heap in the Perspex bin and samples were taken at 25 mm intervals across the contents of the poured heap at two levels. Allowing for symmetry of the heap when poured centrally there are thus four series of samples which could then be analysed and averaged to produce a good estimate of concentration profiles under various circumstances (eg, for different fine particle size distributions). **Figures 7, 8 and 9** show the dimensionless segregation patterns of  $C/C_F$  each for a range of percentage coarse material ( $C_F$ ) with **Figure 7** having the coarsest fine material with a  $d_{50}$  of 330  $\mu\text{m}$ , **Figure 8** has  $d_{50}$  of 235, while **Figure 9** has 145  $\mu\text{m}$ .

One way of expressing these results is to calculate, for a given segregation pattern, the coefficient of variation or degree of segregation [11].

$$\frac{\sum_{i=1}^N (C_i - C_F)^2}{N-1} \cdot \frac{1}{C_F}$$

where  $N$  is the number of samples across a profile and  $C_i$  is the coarse particle concentration of sample  $i$ . **Figure 10** displays the result of calculating this quantity for all the profiles of **Figures 7, 8 and 9** and it is seen that segregation by this measure is worst at intermediate concentrations of coarse powder.

The result of adding one quarter percent of water to the various fine sands may be found in **Figures 11, 12 and 13** where the fine particle size decreases in that order and where a comparison is visible between dry fine sand and “damp” fine sand on each graph. The decrease in segregation is obvious though

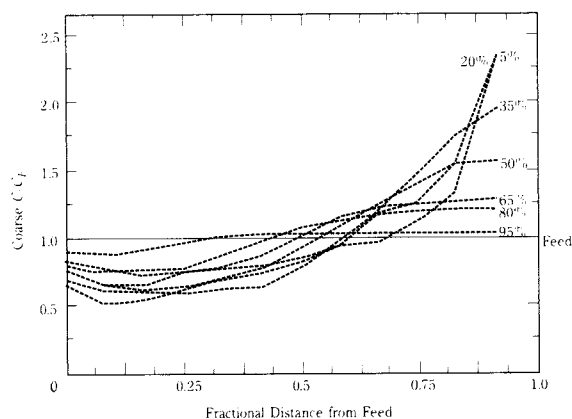


Fig. 7 Dimensionless Segregation Pattern, KH Fine.

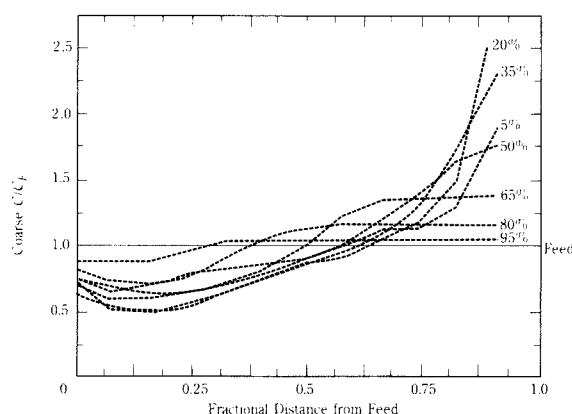


Fig. 8 Dimensionless Segregation Pattern, White Fine.

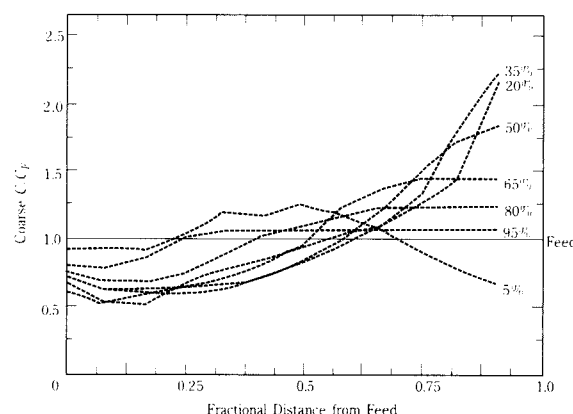
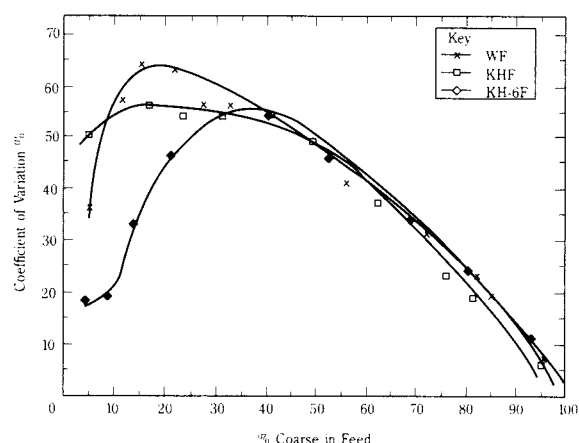


Fig. 9 Dimensionless Segregation Pattern, KH6 Fine.

in the case of White Fines 0.5% proved more effective (**Figure 12**).

**Table 1** summarises various fine particle properties, the  $d_{50}$  sizes, the cohesion as measured by intercept of the linear regression of the yield loci of the material (for an arbitrarily chosen consolidating stress



**Fig. 10** Coefficient of Variation of Segregation Pattern as Function of Coarse Concentration.

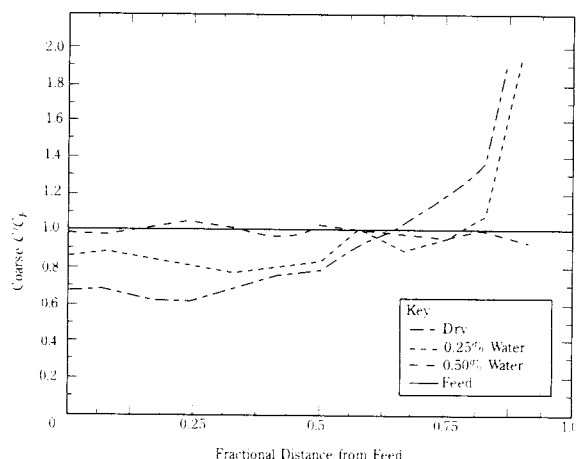


**Fig. 13** Effect of Added Water, KH6 Fine.

**Table 1** Properties of Fine Sands

Designation	KH6 Fine	White Fine	KH Fine
$d_{50}$ $\mu\text{m}$	145	235	330
Moisture Content %	Cohesion kPa		
0	0.12	0.16	0.0
0.25	0.40	0.27	0.27
0.5	0.45	0.48	0.35
1.0	0.40		
Terminal Velocity of $d_{50}$ Sphere m/s (in air)	0.7	1.9	2.7

### 3. Discussion

Drahn and Bridgwater [12] noted a flattening of concentration profile as the percentage coarse material increased from ‘low’ up to 73%. Examining the concentration profiles in the present work it is clear that the device of non-dimensionalising the concentration as  $C/C_F$  is at best an approximation for low concentrations and in the case of the finest powder (Figure 9) a reversal appears similar to the patterns of Figure 3.

Previous work [1] speculated that it was cohesion exhibited by fine particles which retarded the coarse ones in their passage down the slope of the heap as it is poured. This could then lead to a flattened or even a reversed profile. The present work shows little evidence of profile reversal, the outstanding case is Figure 9.

It is, however, worth considering the phenomena which could alter a segregation pattern and cohesion is but one of them: one with a close interaction with particle size and moisture content as can be seen from the cohesion results of Table 1.

Another possibility, not related to moisture content, is that fine particles have lower terminal velocities

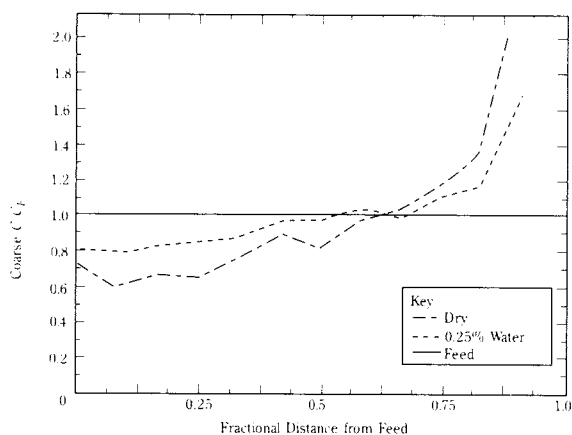


**Fig. 11** Effect of Added Water, KH Fine.

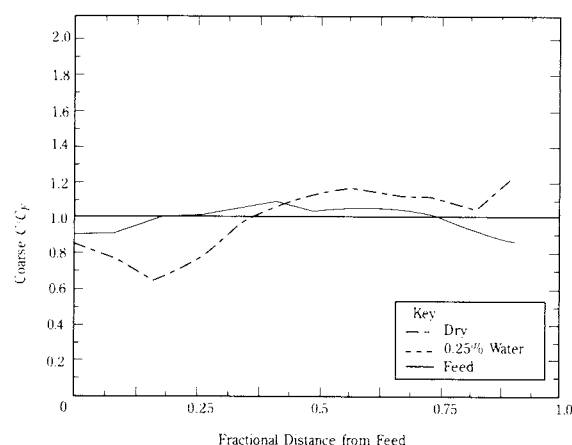


**Fig. 12** Effect of Added Water, White Fine.

of 6.7 kPa) for various percentages of water and the calculated terminal velocity of the  $d_{50}$  size in air assuming a spherical quartz particle.

(either free or hindered) and hence may not settle on the heap as readily. This could lead to their enhanced transport to the wall leading to a profile flattening [11].

Moreover, the concept of the “quasi particle” can be invoked [13, 14, 15, 16] where large particles, under cohesive influences, gather around them smaller ones. Thus large particles can transport smaller ones towards the wall of a bin. The effect will be more pronounced with water present and the end result may be a flattening or perhaps a reversal of the profile.

Whatever the mechanism it may be seen from **Figures 11, 12 and 13** that a small amount of water reduces the segregation from that occurring with dry powders. The addition of moisture to a powder may not be acceptable in some circumstances (for example with highly water soluble product) but could prove beneficial with ores or coal and conceivably could allay a dust problem.

Turning to **Figure 10** which plots degree of segregation as a function of coarse feed percentage, it is seen that maxima occur at intermediate concentrations. This may be viewed as a quantitative picture of the result of the influences which cause or lessen segregation. Some influences tend to enhance the transport of coarse from the feed point, some will tend to retard the progress. The same remark may be made about fine particles.

### Large particles tending to the wall

Brown [17] suggests that vibration during flow will tend to move large particles to the wall more than small ones. Williams [18] also discusses this mechanism while Mathee [19] postulates different frictional resistances for large and small particles.

Brown suggests that protuberances in the surface will stop small particles sooner than large ones. Further he states that small particles near the feed point which are moving slowly will soon stop and hence concentrate near the feed while small particles moving quickly will soon hit large ones and stop.

Dense and/or large particles will sink beneath the line of fall or will roll down the slope [17]. Drahun and Bridgwater [12], however, point out that their experiments do not confirm this.

“If the feed were directly onto the slope, such as was usual in the inclined plane work, the collisions Brown considered would be too weak to cause the displacements implicit in his reasoning. His analysis could be applicable to pouring with a free-fall height,

although he ignored the possibility of small particles being carried down the slope by bounding. A high free-fall height has been found to cause reversal of the distribution of ‘sinkers’ ”.

Williams [20] suggests that small particles will tend to percolate down into a bed and it may be that the large ones will reach the periphery by default.

Drahun and Bridgwater [12], Mathee [19] and Syskov and Tsz Lyan [21] all allude to a rolling mechanism as a major mechanism for large particles to reach the far part of a bin. In particular Drahun and Bridgwater point out that there are always some large particles near the wall even though the major concentration of them may not be there.

### Small particles tending to the wall

There are several feasible mechanisms whereby the trends discussed above may be reversed. Reference has been made already in this Discussion section to the possible influence of cohesion [1, 2], to quasi particles carrying fines with them [13, 14, 15, 16] and to slowly settling fines which may transport to the wall. Concerning the last factor Table 1 gives the terminal velocity of the  $d_{50}$  particles. The particle size distributions contain many smaller (and of course more slowly settling) particles. Small particles inherently will fall through air more slowly and the effect of many together is aggravated by air percolated effects. See for example Reference [22].

Drahun and Bridgwater [12] refer to the possibility of small particles bouncing down a slope (in contrast to Brown’s argument [17] that small ones will be stopped).

Finally, Lawrence and Beddow [8] reported a reversal of the usual segregation pattern (with the coarse to the wall) with a volume of fines greater than 60%. They considered that the small number of large particles simply could not get through the matrix of fines.

## 4. Conclusion

The phenomenon of segregation is becoming more complex the deeper the study. It appears that non-dimensional groups are not able to correlate the phenomena. The segregation patterns resulting when mixtures of particles are poured on to a heap are strongly dependent in a complex fashion on the concentration of coarse material in the feed.

It is worth noting that the author [4] found no speed effect in feeding material on to a heap and

this was held to be a simplification enabling some generalisations to be made about the segregation phenomenon. However, the particles studied at that time were coarse and it may be that with fine particles there are interstitial air effects producing a feed rate effect. Lawrence and Beddow [8] and Syskov and Tsz Lyan [20] found the extent of segregation decreased if the pouring time decreased.

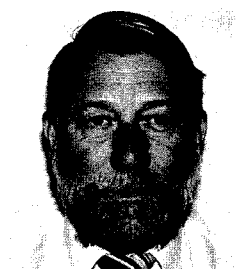
It is the intention of the author to further the study of particle segregation paying particular attention to;

- (i) the scale of the apparatus,
- (ii) the feed rate on to a heap,
- (iii) the concentration of coarse particles, and,
- (iv) by no means least, the segregation patterns resulting with particles much finer than those studied to date.

#### Literature cited

- 1) Bagster, D. F, The Influence of Cohesion on the Segregation Patterns in Bins. Int. Conf. Bulk Materials Storage Handling and Transportation, Newcastle, 1983, 203-206.
- 2) Bagster, D. F, I E Aust, Mech. Eng. Trans, ME9 (1984) 45-48.
- 3) Bagster, D. F, Kirby, P. L, and McFadyen, C, A New Approach to Segregation of Particles in Bins. 7th Aust. Chem. Engng. Conf, Newcastle, 1979, 217-220.
- 4) Bagster, D. F, A Study of Severe Segregation in Bins. 8th Aust. Chem. Engrg Conf, Melbourne, 1980, 190-194.
- 5) Williams, J. C, Powder Technol, 15 (1976) 245.
- 6) Harris, J. F. G, and Hildon, A. M, Ind Eng Chem, Proc Des, 9 (1970) 363-367.
- 7) Williams, J. C, and Kahn, M. I, The Chem Engineer, No 269 (1973) 19-25.
- 8) Lawrence, L. R, Beddow, J. K, Powder Technol 2 (1969) 253-259.
- 9) Mosby, J, Postec. Newsletter, No 12 (1993) 19.
- 10) Yu, A. B, Cowgill, D, Wong, P. L. M, Standish, N and He, Q. L, Stockpiling Behaviour as Observed in a Model Experiment. 5th Int. Conf. Bulk Materials Storage, Handling and Transportation, Newcastle, 1995, 451-455.
- 11) Richards, J. C (Ed), The Storage and Recovery of Particulate Material, IChemE, London (1966).
- 12) Drahun, J. A, and Bridgwater, J, Powder Technol, 36 (1983) 39-53.
- 13) Meissner, H. P, Michaels, A S, and Kaiser, R, Ind Eng Chem, Proc Des 3 (1964) 202-205.
- 14) Furui, T, Kawazu, M, Sugawara, K, Fujiwara, T, Kagawa, M, Sawamura, A, and Uno, S, Technology for Preparation of Raw Materials to be Sintered. Nippon Steel Technical Report. No 18, 1977.
- 15) Rankin, W. J, Roller, P. W, and Batterham, R. J, Quasi-particle Formation and the Granulation of Iron Ore Sinter Feeds. Aust IMM/ISI Japan Joint Symposium 1983, 1-16.
- 16) Sherrington, P. J, J. Powder Bulk Solids Technol, 7 (1983) 1-6.
- 17) Brown, R. L, J. Inst. Fuel, 13 (1939) 15-19
- 18) Williams, J. C, Univ Sheffield Fuel Soc J, 14 (1963) 29-34.
- 19) Matthee, H, Powder Technol, 1 (1968) 265-271.
- 20) Williams, J. C, Chem Processing, 11 (1963) 56-58.
- 21) Syskov, K. I, and Tsz Lyan, Coke and Chemistry. USSR, 2 (1960) 5-9.
- 22) Nedderman, R. M, Tzn, U, Savage, S. B and Houlaby, G. T, Chem Eng Sci, 37 (1982) 1597-1609.

#### Author's short biography



#### David Bagster

David Bagster graduated in engineering from the University of Queensland and gained a PhD in chemical engineering from the University of Cambridge. After ten years in the sugar industry he joined the Department of Chemical Engineering at the University of Sydney. David Bagster's research interests are in particle mechanics, mineral processing and risk analysis.

# Dust Explosions †

Piotr Wolański

Warsaw University of Technology, Institute of Heat Engineering\*

## Abstract

*When mixed with air many natural or artificial types of dust may explode with an energy several times higher than the equivalent mass of TNT. The origin of the dust and its basic properties, which are important from the point of view of a dust explosion, are discussed in the paper. Special attention is focused on the problems of mixture formation, ignition and the subsequent flame propagation. Methods of evaluation of the structure and burning velocities for laminar and turbulent flames are given. Conditions for flame acceleration and transition to detonation are also discussed. Finally, the influence of both inert and reactive particles on homogeneous and dust mixture explosions is presented.*

## 1. Introduction

Even though the first dust explosion was reported in Italy in the 18th century [1], a serious approach was taken to the problem only at the beginning of the 20th century when a coal dust explosion killed more than a thousand miners in France [2]. Many other dust explosions occurred during this century in mining and in other branches of industry such as the grain industry, textile, food processing, metallurgical, pharmaceutical and others. It is so because a typical organic dust may explode with an energy 3-5 times higher than the equivalent mass of TNT.

Studies on coal dust explosions have been carried out since the beginning of this century in many countries, and large-scale testing facilities have been built in the USA, France, Poland, Germany, the UK, Japan and in other countries. Coal dust testing facilities were amongst the first to be used to research industrial dust explosions.

Research of dust explosions accelerated in the seventies due to the rapid growth of powder technologies and the explosion hazard associated with them. More basic work in the area of dust explosions is still being carried out in different university laboratories. Since the seventies, special meetings devoted to dust explosions are occasionally organized in different countries, and since 1984, International Colloquia on Dust Explosions have been organized every two years, initially in Poland, and subsequently elsewhere.

In this paper, the basic parameters responsible for dust explosions will be discussed. The diagram, showing the most important parameters which influence a dust explosion, is presented in **Figure 1** [3]. It shows that the most important parameters are the dust properties, the parameters of dust mixture, the ignition source and the explosion space characteristics. The development of a dust explosion is very strongly related to these parameters.

## 2. Dust properties

Dust may be the main product or a by-product in many different industries. For example, in a coal mine, dust is usually the by-product, but in many power plants, pulverized coal is the main fuel. Similarly in some grain industries, where dust is the by-product in the elevators used during storage of the grain, in the mills, it is the main product in the form of different flours. A lot of dust is also produced in the food, pharmaceutical and metallurgical industries. A typical natural dust which is very often used in dust explosion research is lycopodium, the spores of mosses.

In this paper we will discuss only dusts which require a gaseous oxidizer for combustion and explosion. So, to be explosive, a dust should be combustible. During an explosion the dust burns rapidly and releases a large quantity of heat. A dust of high combustion heat is potentially more explosive. But a high heat of combustion is only one of the parameters which cause a dust to be considered as potentially explosive. For rapid combustion, a dust should have a large specific surface which will appertain if the

\* 25 Nowowiejska Str., 00-665 Warsaw, Poland

† Received: 11 June, 1996

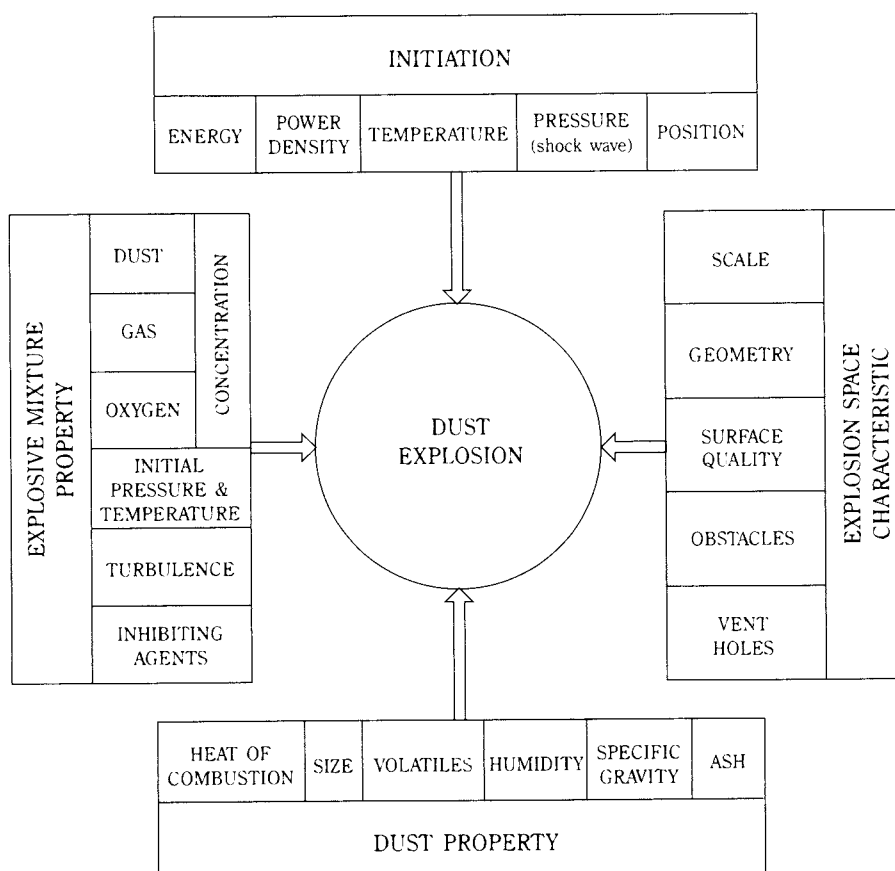


Fig. 1. Major factors influencing dust explosion.

dust particles are very small and porous. For most organic substances, a dust is susceptible to rapid combustion if the particles are less than 300  $\mu\text{m}$  in diameter. Even more explosive is dust with particles of less than 100  $\mu\text{m}$  in diameter. Very important, and sometimes most critical, for a dust explosion is the content of volatile substances. Organic dusts with a large volatile content are usually very explosive, even with a relatively moderate heat of combustion. Moisture and ash contents, bulk density and electrostatic properties also affect the explosive properties of dust. Typical properties of average industrial dusts are shown in Table 1.

Table 1. Typical properties of average industrial dust

Dust parameter	Typical value	Maximum value
Heat of combustion, MJ/kg	15-30	~ 60
Volatile content, %	20-80	100
Particle size, $\mu\text{m}$	10-100	up to 300 and more
Moisture, %	5-20	up to 50 and more
Ash (mineral content), %	5-25	up to 80 and more

### 3. Mixture formation

A dust is explosive in air (gaseous oxidizer) only when its concentration is within the so-called 'explosive limits' which define the concentration range for which a self-sustained flame propagation is possible. For obvious reasons, the limits are called the minimum and the maximum explosive concentration. The minimum explosive concentration is usually more easily defined than the maximum. For fine organic dust, the minimum explosive concentration is usually in the range of 0.05-0.15  $\text{kg/m}^3$ , while the maximum one is often of an order of kilograms of dust per cubic metre.

Within the explosive limits, combustion of a dust-air mixture within a closed vessel results in a significant pressure rise. At the lower limit, the combustion can produce a pressure rise of an order of 2-3 bar. The maximum explosive pressure is much higher and the pressure rise can be in the range of 6-10 bar. Close to the maximum explosive limit the pressure rise is usually slightly higher than that at the lower explosive

limit. A typical graph showing the pressure rise in a closed vessel as a function of the dust concentration is shown in **Figure 2**.

For the same kind of dust, the explosive concentration varies with particle size and with moisture content. The explosive concentration range narrows when the mean particle diameter or the moisture content increases. The explosive concentration can also be changed by increasing or reducing the oxygen content of the air. When the oxygen concentration is reduced, the explosive concentration range of the dust will be narrower. For many organic types of dust, the mixture will no longer be explosive if the oxygen concentration of the air is reduced to 11%. A detailed description of the minimum explosive concentration was presented by Wolanski [4].

During experimental studies of dust explosions, the dust is usually dispersed by a strong air blast or is dropped from the container with the help of a specially designed feeder. In such cases, the dust concentration is controlled by the selection of a required amount of dust to be dispersed by an air blast or by the calibration of the feeder which is used to create the dust cloud. The uniformity of the dust dispersion depends significantly on the size and shape of the enclosure (vessel), the dispersing nozzles, the air pressure and the duration of the pulse. In order to ensure a relatively uniform dust dispersion, especially in a large vessel, an advanced dispersion system and accurate timing is necessary. Only for small vessels may a relatively simple dispersion system be used.

In small vessels, the uniformity of the dust dispersion may be tested by optical methods, but in large volumes, local measurements of the dust concentration are necessary. Recent measurements of dust dispersion in large silos and filters show a strong influence of centrifugal forces on the stratification of the dust and on the non-uniformity of the dust

concentration [5].

Usually, the dispersion of the dust induces initial turbulence in the mixture created. The intensity and scale of the turbulence depends mainly on the dispersion system and less on the type of dust dispersed. The largest turbulence occurs during the dispersion process and thereafter, the turbulence decays. However, the ignition cannot be delayed until the turbulence intensity has decayed completely since, in normal conditions, much of the dust will have already fallen to the bottom of the chamber. Thus most experiments are carried out in turbulent conditions. Only vibrational or fluidized bed feeders enable laminar or quasi-laminar conditions to be established in tubes.

In real industrial conditions, most of the dust clouds are created by convective flow or by the blast wave, which is created by primary explosion. Thus, the conditions are very similar to those used in the evaluation of explosive properties in laboratory conditions.

#### 4. Ignition

Dust may be ignited in many different ways such as by electrical or mechanical sparks, hot elements, and external radiation. When uniformly heated, the so-called 'self-ignition' of a dust cloud can be observed. Evaluations of the critical ignition parameters for dust mixtures have been made for a long time and many data are available.

Usually, a determination of the minimum electrical energy necessary for ignition, the minimum ignition temperature of the dust layer and the self-ignition temperature of the dust cloud is made for an explosive dust. It was found that for a fine dry dust, the minimum energy of an electrical spark which can cause ignition may be of the order of millijoules. The minimum ignition energy usually coincides with a dust concentration close to that which gives the maximum explosive pressure. When the dust concentration varies from the optimum, the ignition energy increases and can be very large at both limits (**Figure 3**). Practically speaking a 10 kJ chemical igniter is a reasonable energy to use for testing a dust.

The ignition energy depends not only on the concentration of the mixture but also on the characteristics of the igniter. The minimum ignition energy is usually found using sparks with a duration of the order of milliseconds. "Short" or "long" sparks are less effective [1]. It is obvious that the minimum ignition energy changes significantly with the dust parameters

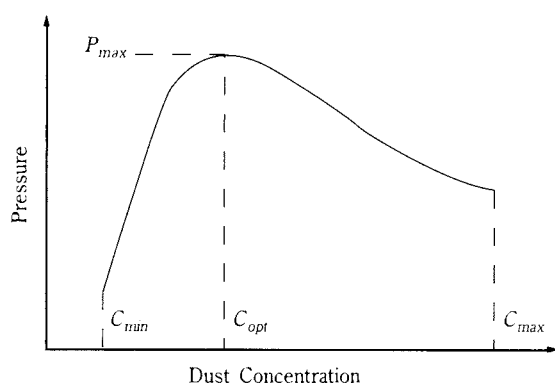


**Fig. 2** Dependence of explosion pressure on dust concentration.

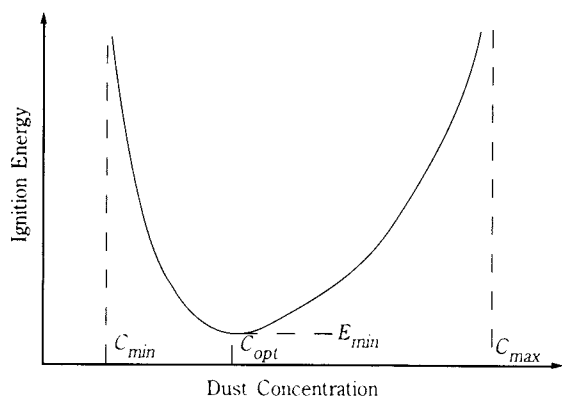


**Fig. 3** Dependence of ignition energy on dust concentration.

such as particle size and humidity. If the mean particle size increases by 100% and the moisture content increases by 10%, the minimum ignition energy can be increased by two orders of magnitude. The minimum ignition energy is also significantly greater in turbulent mixtures when compared to laminar or quasi-laminar mixtures.

The self-ignition temperature of the dust cloud for many types of organic dust is most often in the range of 600-800 K and is usually higher than the ignition temperature of a layer of the same dust. It should be stated, however, that this temperature depends critically on the size and shape of the test equipment used for its evaluation. For example, the ignition temperature evaluated in the Golbert-Greenwald furnace is usually 100-150 K higher than that evaluated in the furnace, one metre long, of Wrocław University of Technology. Information about these temperatures is available in the literature but it should be applied to industrial conditions with great care.

For a better understanding of dust ignition and flame propagation, some research is focused on the radiative ignition of dust. Ignition by laser light and visible radiation are important, since radiation plays a significant role in the mechanics of flame propagation, especially for metallic dusts.

Many data on the ignition of dust mixtures may be found in the literature [1], [3], [6]-[9].

## 5. Structure and burning velocities of dust flames

Dust flames have been studied for many years but despite this, there is only a partial understanding of the dust flame structure, and data on the burning velocity are limited. The best understanding was achieved only for dust flames made of very small and

easily volatilized particles. Such flames are very similar in nature to gaseous flames. For dust flames with polydispersed particles of a relatively large mean diameter, the flame structure is more complicated than that of a gaseous flame, even in laminar conditions.

Laminar flames are usually studied in vertical tubes. The dust-air mixture is created by supplying dust from the top of the tube or by a fluidized bed feeder placed at the bottom of the tube. In both cases laminar or quasi-laminar conditions are obtained. After the whole tube is filled with the dust mixture, the combustion is initiated by an electrical spark and the flame propagation in the tube is monitored. In order to obtain a constant velocity of flame propagation, the bottom of the tube should be kept open.

With the help of Schlieren or interferometric measurement, the thickness of the preheated zone of the laminar dust flame can be measured whilst the total flame thickness is usually measured with the help of direct photography. Typical Schlieren pictures showing the preheated zone and combustion region are presented in **Figure 4** while the direct picture of similar flames is shown in **Figure 5**. Data illustrating the preheated zone thickness and the total flame thickness for two different types of organic dust are shown in **Table 2**. It is seen that the total flame thickness of laminar dust flames is about three orders of magnitude higher than that of gaseous flames.

To evaluate laminar burning velocities for a dust-air mixture, two different methods are usually used. In the "direct" method, the burning velocity is calculated as difference between the flame propagation velocity and the particle velocity just ahead of the flame front. In the "tube" method, the relationship between the flame propagation velocity and the burning velocity is evaluated from measurement of the tube cross-sectional area and the flame area. A more detailed description of such measurements can be found in many publications on this subject [10]-[13]. A typical dependence of the laminar burning velocity of the dust mixture on the dust concentration is shown in **Figure 6**.

Measurements of the turbulent burning velocity of dust-air mixtures are usually performed in a constant volume chamber. However, measurements may be considered to be reliable only if they were performed in relatively large vessels of one cubic metre or more, since the thickness of the dust flame is usually also quite large [12], [14]. The best measurements of turbulent burning velocity were obtained by using the simultaneous measurements of the pressure

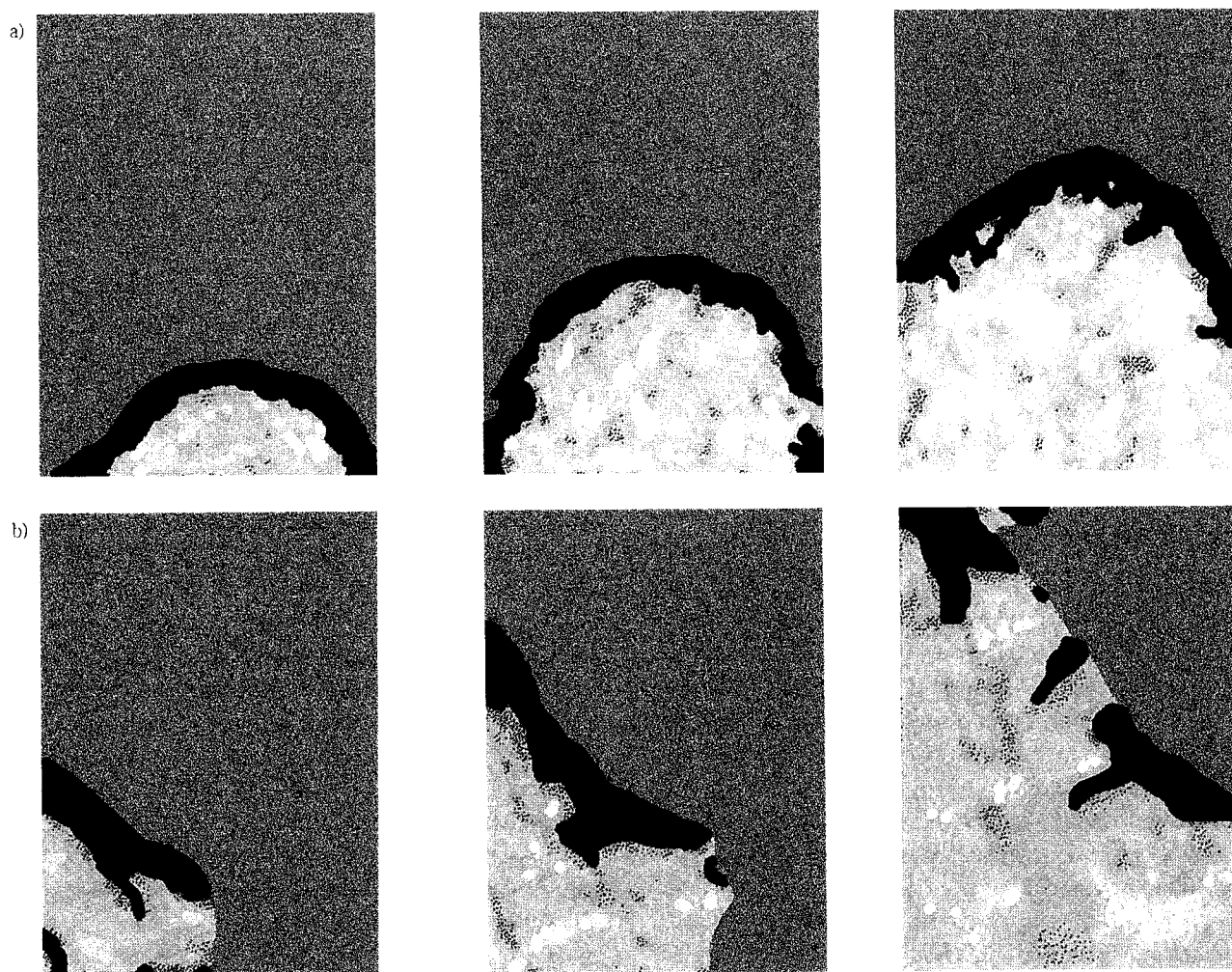


**Fig. 4.** Computer-enhanced Schlieren pictures of lycopodium-air laminar flame (a) and wheat dust-air laminar flame (b) clearly showing preheated zone area and combustion regions

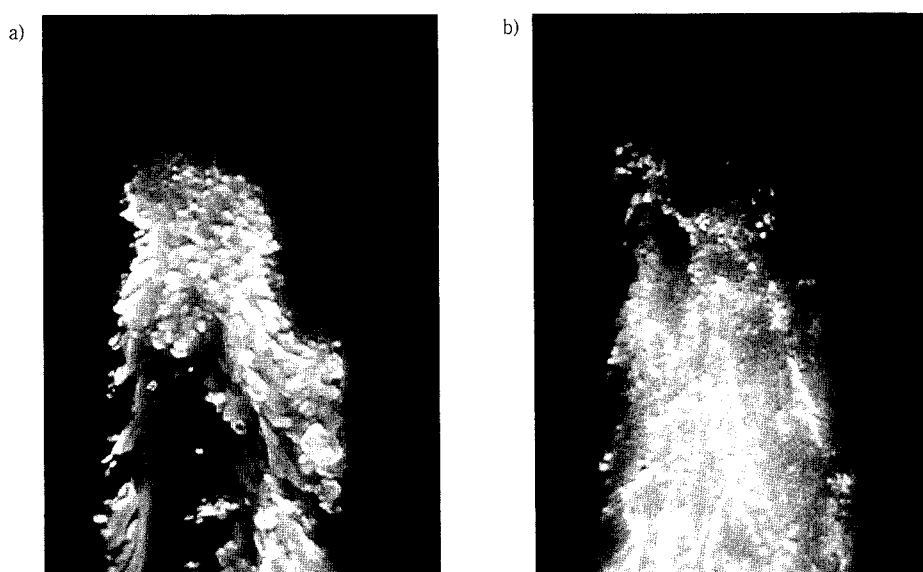


**Fig. 5.** Direct picture of laminar dust flames: a) lycopodium,  $c = 0.048 \text{ kg/m}^3$ , b) wheat dust,  $c = 0.15 \text{ kg/m}^3$

**Table 2.** The thickness of the preheated zone and total flame thickness for laminar flames of lycopodium and wheat

Dust	Dust concentration [kg/m <sup>3</sup> ]	Preheated zone thickness [m]	Total flame thickness [m]
Lycopodium	0.030	0.006-0.01	0.95
	0.038	0.006-0.01	0.85
	0.048	0.005-0.009	1.05
	0.066	0.006-0.016	1.25
Wheat	0.12	0.012-0.031	1.42
	0.15	0.007-0.036	1.57
	0.17	0.007-0.013	1.65

variation inside the chamber and of the flame front position. Such measurements should be performed for different turbulence intensities and scales. A typical relationship between both the turbulent and laminar burning velocities and the turbulent intensity is shown for wheat and lycopodium dusts in **Figure 7**. Such relationships can easily be integrated into computer models of dust explosions. It should be noted, however, that this relationship may only be used for the simulation of dust explosions on a large scale where the extent of the explosion is much bigger than the total flame thickness.

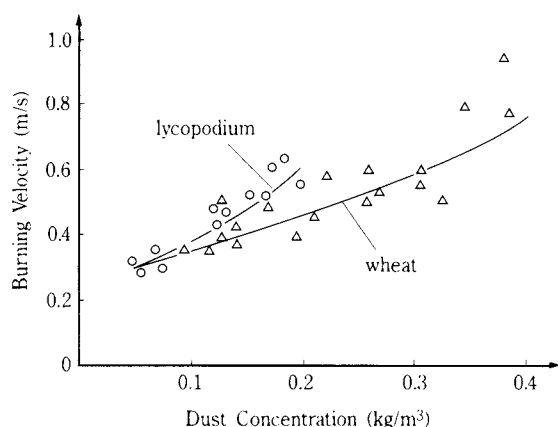


**Fig. 6** Typical dependence of the laminar burning velocity of dust-air mixtures on dust concentration

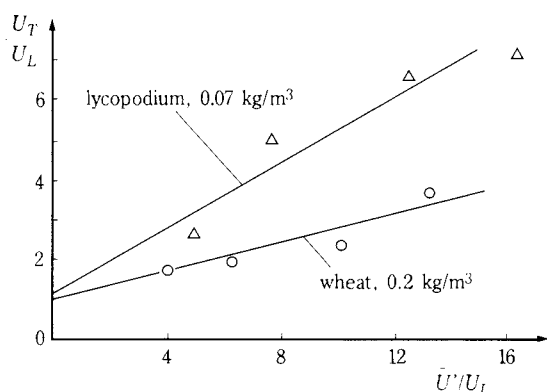


**Fig. 7.** Ratio of turbulent burning velocity to laminar burning velocity as a function of ratio of turbulent intensity to laminar burning velocity  $\bar{U}'/U_L$  for wheat and lycopodium dusts

## 6. Accelerating flames

Accelerating flames propagating in ducts, tubes, channels or galleries have been studied experimentally for many years in different laboratories and also in both large surface and underground facilities. A large number of experimental data is available and the general behaviour of such flames is relatively well understood [1], [2], [15]. Despite this, the accurate prediction of the development of a dust explosion in a channel is difficult. This is due to the problems of mixture formation which for dust mixtures, is very closely connected to the flame propagation, the acceleration of the flame and the eventual transition from deflagration to detonation. A transition from deflagration to detonation is possible even for mildly explosive types of dust.

The condition necessary for the acceleration of the flame is the creation of convective flow just ahead of the propagating flame. This induced flow is produced by the expansion of the combustible products. For a typical mixture with a dust concentration close to the flammable limit, the density ratio across the flame is at least three, but for a stoichiometric mixture it may be eight or even more. The fast combustion of the mixture produces a rapid expansion of hot products of combustion and thus creates pressure waves which propagate ahead of the flame front. Such pressure waves induce a convective flow. The convective flow favours further dust dispersion and increases the turbulence of the mixture. The increased turbulence intensifies the burning velocity and a further acceleration of the flame is observed. The acceleration of the flame in such a process is related to the reactivity of the mixture.

**Figure 8** shows the propagation of the flame in the gallery of the Experimental Mine "Barbara" for different initial concentrations. At the low concentration,  $c = 0.05 \text{ kg/m}^3$ , the flame propagates some distance from the strong ignition and is then eventually quenched. At the highest concentration, a small acceleration of the flame can even be seen. It may be that this concentration, equal to  $0.075 \text{ kg/m}^3$  is the limiting concentration which allows a self-sustained flame propagation. These results are similar to those obtained in vertical tubes.

In short channels, that is a 100-metre-long surface gallery where the dust was only dispersed for 60 m, only a limited acceleration of the flame was observed at the low dust concentration. When the dust concentration was increased, the flame accelerated to as much as a few hundred m/s. A static pressure rise greater than 2 bar was also observed. However,

in a longer gallery, a significant flame acceleration was recorded at a relatively low concentration. **Figure 9** shows the variation of the flame position with time in the 400-metre-long underground gallery of the Experimental Mine “Barbara” for different grain dust concentrations, ranging from 0.1 to 0.2 kg/m<sup>3</sup>. The highest concentration used in the experiments was still lower than stoichiometric and about half the concentration at which the maximum values of the explosive parameters were obtained in a constant volume chamber. At a concentration of 0.1 kg/m<sup>3</sup>, the flame propagates basically with a constant velocity of the order of one hundred m/s. For a grain dust concentration of 0.15 kg/m<sup>3</sup>, a continuous acceleration of the flame was observed up to about three hundred m/s and the pressure rose to four bar. However, at a concentration of 0.2 kg/m<sup>3</sup>, a very rapid flame acceleration was

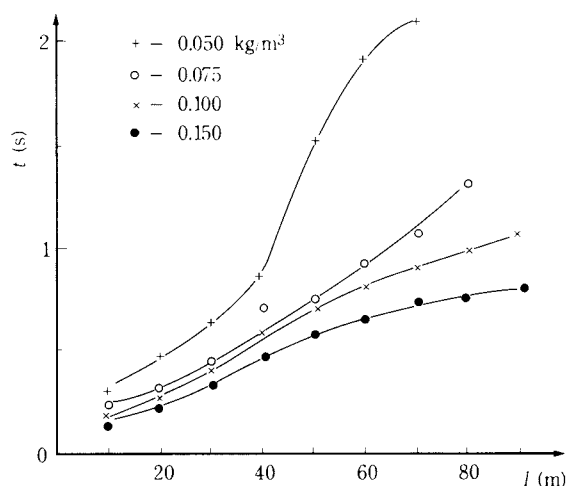


**Fig. 8** Diagram showing variation of the flame position with time along a 100-metre-long gallery for different grain dust concentrations. Initiator – 10 m<sup>3</sup> of CH<sub>4</sub>-air mixture; length of dust zone: 60 m

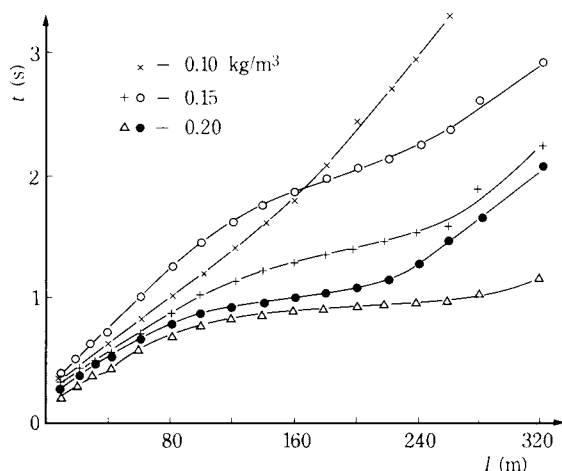


**Fig. 9** Variation of the flame position with time in a 400-metre-long underground gallery for different dust concentrations; length of dust zone: 200 m

observed. In one case the flame reached a velocity of nearly seven hundred m/s and a pressure of 5.6 bar. In another case, a transition to detonation was recorded. The transition from deflagration to detonation was observed close to a distance of 200 m from the initiator that is at the end of the dust zone. The velocity measured at the transition was about 2000 m/s. The pressure could be estimated from the damage caused to the gallery to be about 50 bar. Such conditions are typical for a transition from deflagration to detonation. Even higher transition parameters were measured by Gardner et al. [16], who recorded a velocity of 2800 m/s and a pressure higher than 80 bar. From such experiments it can be inferred that even for organic types of dust, a detonative combustion is possible in real industrial conditions. If it happens, it may cause very serious damage.

For most organic dust mixtures, the measured detonation velocity is in the range of 1450-1650 m/s and the corresponding pressures in the detonation front are in the range of 15-30 bar. However, as already illustrated, very dangerous conditions arise during the transition from deflagration to detonation. Detonation itself is the most dangerous mode of combustion of a dust-air mixture but, fortunately, many conditions have to be met to initiate it. And for this reason it does not occur very frequently in uncontrolled explosions in industry.

## 7. Influence of inert particles on flame propagation

It is well known that the addition of fine inert particles is a very good method of suppressing dust explosions. Barriers of fine stone dust are commonly used in mines for the suppression of methane, dust or hybrid mixture explosions [2]. However, the addition of an insufficient amount of inerting particles may result in the acceleration of flames in ducts [18], [19]. A similar and even stronger effect is obtained when relatively large inert particles are added to a combustible mixture. The addition of such particles may result in acceleration of the flame, faster transition to detonation and an extension of the lower limit of detonation [20, 21].

For gaseous mixtures, the mechanism of flame acceleration is strictly related to the microscale turbulence. Such turbulence increases the rate of reaction and speeds up the flame propagation. For a very high velocity, when shock waves are generated, non-isentropic interactions of the shock waves cause additional energy dissipation and thus the temperature

is increased. The increase in temperature of the reacting mixture further speeds up the flame propagation and the probability of a transition to detonation. Local heating of the gaseous mixture in the region of bow shocks associated with the particles is also important. This can eventually lead to the formation of so-called "hot spots" and ignition of the mixture ahead of the propagating flame.

Studies of the influence of inert particles when added to reactive particles were conducted by Klemens et al. [22]. It was found that unlike in gaseous mixtures, the addition of inert particles does not have a discernible effect on the probability of detonation, but does increase the maximum temperature and pressure. This pressure rise is higher for larger inert particles. In all cases the addition of inert particles causes a temperature rise in the detonation front of as much as  $400 \div 600\text{K}$ . The addition of inert particles always decreases the detonation velocity. For an obvious reason, the same concentration of small inert particles causes a larger velocity deficit than that for larger particles. This relationship is shown in **Figure 10**. As with gaseous mixtures, increased addition of inert particles hinders the transition to detonation and significantly decreases the propagation velocity of the flame. A very large addition of inert particles eventually quenches combustion. Inert particles of smaller diameter are more efficient in impeding the transition to detonation and in inhibiting ignition. The greater effectiveness of smaller particles is basically due to greater heat and momentum transfer.

## 8. Conclusions

Many organic and inorganic types of dust are very explosive when mixed with air. The explosive energy of a typical industrial dust can be higher than the explosive energy of the equivalent mass of TNT.

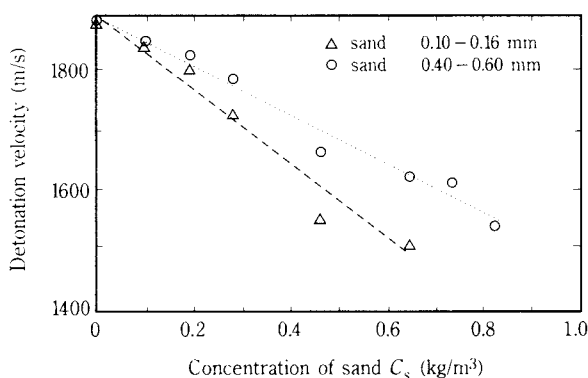


**Fig. 10** Influence of inert sand particle concentration on detonation velocity of flax dust with concentration  $0.91 \text{ kg/m}^3$  in 95%  $\text{O}_2$ , 5%  $\text{N}_2$  atmosphere

For this reason, an uncontrolled dust explosion usually causes significant damage and may result in serious injuries. This is due to the fact that even at the limiting concentration, a dust explosion creates a significant pressure rise.

Many organic and some metallic kinds of dust are also easy to ignite and, once ignited, the flame which is formed may accelerate. This can eventually result in a transition to detonation. The detonation velocity for dust-air mixtures is usually in the range of  $1450\text{-}1650 \text{ m/s}$  and the pressure rise in the detonation front may be as high as 30 bar. The highest pressures, up to 82 bar, were recorded during a transition from deflagration to detonation. The addition of inert particles always results in a decrease of the detonation velocity, but the temperature and pressure in the detonation front may be even higher.

Dust explosions are usually very complicated in nature and detailed studies are necessary to fully explain of the phenomena observed and to better predict their initiation and development. In this paper only the most important aspects of dust explosions were mentioned.

## References

- 1) Eckhoff, R.K.: Dust Explosions in the Process Industries, Butterworth-Hinemann, 1991.
- 2) Cybulski, W.: Coal Dust Explosions and Their Suppressions, Warsaw, 1975.
- 3) Wolański, P.: Explosion Hazards of Agricultural Dust, Proceedings of the International Symposium on Grain Dust, Manhattan, KS, 1979, pp. 422-446.
- 4) Wolański, P.: Minimum Explosive Concentration of Dust-Air Mixtures, Proceedings of the Sixth International Colloquium on Dust Explosions, Deng Xufan, P. Wolański, (Ed.), Northeastern University Press, Shenyang, 1994, pp. 206-219.
- 5) Hanert, F., Vogl, A.: Measurement of Dust Cloud Characteristics in Industrial Plants, Dust Explosion Protecting People, Equipment, Buildings and Environments, Conference Documentation, IBC, London, 1995, pp. 12-63.
- 6) Field, P.: Dust Explosions, Elsevier, Amsterdam, 1982.
- 7) Wolański, P.: Grain Dust Explosion and Control, Warsaw University of Technology, Warsaw, 1993.
- 8) Van der Wel, P.G.J., Lemkowitz, S.M., Leschonski, S., and Scarlett, B.: Ignition of Dust Clouds Using Pulsed Laser Beams, Proceedings of the Sixth International Colloquium on Dust Explosions, Deng Xufan, P. Wolanski (Ed.), Northeastern University Press, Shenyang, 1994, pp. 125-140.
- 9) Itagaki, H., and Matsuda, T.: Thermal Ignition of Activated Carbon Dusts, Proceedings of the Sixth International Colloquium on Dust Explosions, Deng

- Xufan, P. Wolański (Ed.), Northeastern University Press, Shenyang, 1994, pp. 141-145.
- 10) Proust, C.: Experimental Determination of the Maximum Flame Temperature and of the Laminar Burning Velocities for some Combustible Dust-Air Mixtures, Proceedings of the Fifth International Colloquium on Dust Explosions, Pultusk near Warsaw, 1993, pp. 161-184.
  - 11) Mazurkiewicz, J., Jarosiński, J.: Temperature and Laminar Burning Velocity of Cornstarch Dust-Air Flames, Proceedings of the Fourth International Colloquium on Dust Explosions, Porabka-Kozubnik, 1990, pp. 82-94.
  - 12) Wolański, P. (Ed.): Investigation of Flame Structure During Laminar and Turbulent Burning in Dust-Air Mixtures, Dust Explosions, Protecting People, Equipment, Buildings and Environment, Conference Documents, London, 1995, pp. 168-224.
  - 13) Pedersen, L.S., Van Wingerden, K.: Measurement of Fundamental Burning Velocity of Dust-Air Mixtures in Industrial Situations, Dust Explosions, Protecting People, Equipment, Building and Environment, Conference Documents, London, 1995, pp. 140-167.
  - 14) Tezok, F.I., Kauffman, C.W. Sichel, M., and Nicholls, J.A.: Turbulent Burning Velocity Measurements for Dust-Air Mixtures in a Constant Volume Spherical Bomb, Dynamics of Reactive Systems, Part II: Modelling and Heterogeneous Combustion, Progress in Astronautics and Aeronautics, Vol. 105, 1985, pp. 184-195.
  - 15) Bartknecht, W.: Explosions, Course, Prevention, Springer-Verlag, New York, 1981.
  - 16) Gardner, B.R., Winter, R.J., and Moore, M.J.: Explosion Development and Deflagration-to-Detonation Transition in Coal Dust/Air Suspensions, Twenty-first Symposium (International) on Combustion, The Combustion Institute, 1986, pp. 335-343.
  - 17) Alexander, C.G., Harbaugh, A.S., Kauffman, C.W., Li, Y.C., Cybulski, K., Dyduch, Z., Lebecki, K., Sliz, J., Klemens, R., Wolański, P., Zalesiński, M.: The Establishment of Dust Detonation, Archivum Combustionis, Vol. 13, 1993, No. 3-4, pp. 261-269.
  - 18) Jarosinski, J., Klemens, R., and Wolański, P., Investigation of inert particles influence on gaseous flame structure near the lean flammability limit, Proceedings of the First International Colloquium on Explosibility of Industrial Dusts, Baranów, 1984, pp. 8-10.
  - 19) Góral, P., Klemens, R., and Wolański, P., Mechanism of Gas Flame Acceleration in the Presence of Neutral Particles, Progress in Astronautics and Aeronautics, Vol. 113, 1987, pp. 325-335.
  - 20) Wolański, P., Liu, J.C., Kauffman, C.W., Nicholls, J.A., and Sichel, M., The Effect of Inert Particles on Methane-Air Detonation, Archivum Combustionis, Vol. 8, 1988, pp. 15-32.
  - 21) Woliński, M., Wolański, P., Gaseous Detonation Processes in Pressure of Inert Particles, Archivum Combustionis'', Vol. 7, 1987, pp. 353-370.
  - 22) Klemens, R., Kapuscinski, M., Woliński, M., and Wolański, P., Investigation of Organic Dust Detonation in the Presence of Chemically Inert Particles, Combustion and Flame, Vol. 99, 1994, pp. 742-748.

### Author's short biography



Prof. P. Wolański graduated from Warsaw University of Technology (1966) and obtained his doctorate (1971) and habilitation (1979) in the field of combustion. Since graduation he has been working at The Institute of Heat Engineering of Warsaw University of Technology. He is a specialist in the fields of dust explosions, combustion in engines and detonation. He has worked as a visiting scientist and as a visiting professor at The University of Michigan and at The Institute of Theoretical and Applied Mechanics of the USSR Academy of Sciences in Novosibirsk. He has been an organizer and co-organizer of seven International Colloquia on Dust Explosions. He is currently President of The Polish Combustion Institute.

### P. Wolański

# Preparation of Microcapsule Toner and Their Properties<sup>†</sup>

Masato Tanaka, Isao Imura, Natsukaze Saito,  
Hideaki Tominaga

Department of Chemical Engineering, Faculty of Engineering, Niigata University\*

## Abstract

Microcapsule toners were prepared in two steps: fine core particles and the wall of the capsule were prepared in the first and the second steps, respectively. The core material was stearic acid in which carbon black was dispersed. The wall material was the fine polystyrene beads prepared by the soap-free polymerization.

In the experiment, operating conditions, such as the volume fraction of stearic acid and the impeller speed and the mixing time in the preparation of the first O/W dispersion, were changed stepwise.

It was investigated that how the operating conditions affected the properties of microcapsule toners, such as the size distribution, the mean size and the contents of ferrite powder and the wall material.

The mean size of the toner decreased with the increase of the impeller speed and the mixing time ( $D_{AV} \propto N r_1^{-1.2}$ ,  $D_{AV} \propto t_1^{-0.48}$ ). The content of the wall material increased with the polymerization time.

## 1. Introduction

The toner, the developer used in electronic copiers, is intensively researched for the purpose of saving energy in the manufacturing process and copying process and enhancing picture quality.

For example, active developments are focused on polymerized toner which offers a balance in particle size, fixing performance, separation performance, charging property and other conditions presented at the time of preparation, and microcapsule toner that is said to be effective in saving energy in copying process. The toner manufactured by the suspension polymerization and emulsification polymerization, which are manufacturing methods of polymerized toner, has been fundamentally and systematically studied in regards to the effects of polymerization conditions and stirring conditions on the toner properties (particle size distribution, mean particle size, fixing performance, electric charging property, etc.)<sup>1-5)</sup>.

On the other hand, there has been little basic research into microcapsule toner, although many patents are disclosed<sup>6-8)</sup>.

Therefore, in the present study, the effects of

preparation conditions on fundamental characteristics of microcapsule toner (particle size distribution, film thickness structure, controllability of film thickness, etc.) were studied, proposing a model microcapsule toner of a simple structure, as a first step.

## 2. Structure of model microcapsule toner

The structure of microcapsule toner we attempted to prepare in the present study is shown in **Figure 1**. The core material is stearic acid, and coloring matter is dispersed therein. Fine particles of the core material are covered with magnetic powder (first microcapsule). The first microcapsule is further covered with ultra-fine polymer particles (second microcapsule).

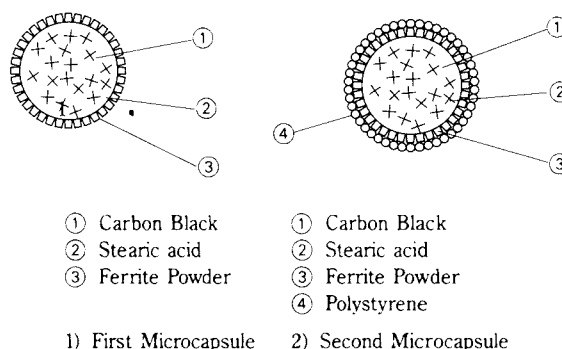


Fig. 1 Structure of model microcapsule toner

\* 2-8050 Ikarashi, Niigata City, Japan 950-21 JAPAN

<sup>†</sup> This report was originally printed in *SHIKIZAI KYOKAISHI* **67**, 624 (1994) in Japanese, before being translated into English by KONA Editorial Committee with the permission of the editorial committee of the Japan Society of Colour Material.

### 3. Experiment

#### 3.1 Reagent

The higher fatty acid used as core material is stearic acid (SA, Kanto Chemical Co.), and its density and melting point are  $940 \text{ kgm}^{-3}$  and  $70.1^\circ\text{C}$  respectively. The coloring matter dispersed in this core material is carbon black (CB, Asahi Thermal of Asahi Carbon Co.). Principal properties include a mean particle size of  $87 \text{ nm}$ , specific area of  $2.4 \times 10^4 \text{ m}^2\text{kg}^{-1}$ , oil absorption of  $2.9 \times 10^{-4} \text{ m}^3\text{kg}^{-1}$ , and pH of 9.2. The magnetic powder is strontium ferrite ( $\text{SrO} \cdot \text{Fe}_2\text{O}_3$ ) of  $0.9 \mu\text{m}$  in size (FP, Dowa Mining Co.).

The outermost polymer of the second microcapsule is polystyrene (PS), which was generated and coated by soap-free polymerization of styrene (ST, Kanto Chemical). The polymerization initiator is potassium persulfate (KPS, Kanto Chemical).

#### 3.2 Preparation of first microcapsule

Figure 2 shows how the first microcapsule was prepared. First, a beaker containing a specified amount of stearic acid (SA) was immersed in a thermostatic oven kept at  $75^\circ\text{C}$ , and the stearic acid was melted. A specified amount of carbon black ( $W_{CB}$ ) was added and mixed to prepare a core substance (oil phase).

On the other hand, a specified amount of ferrite powder ( $W_{FP}$ ) was suspended to prepare a continuous water phase (ion-exchange water). In this continuous water phase, a specified amount ( $\phi_1$ ) of

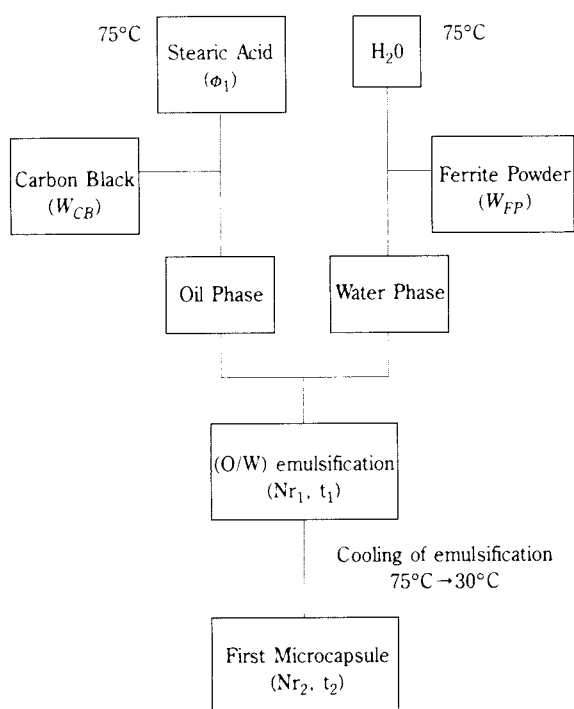


Fig. 2 Schematic representation of first microcapsule preparation

the prepared oil phase was added and stirred at high speed ( $Nr_1$ ) until finely broken up. In this breaking operation, the ferrite powder suspended in the continuous water phase has a contact angle of  $\theta = 68^\circ$  to the liquid-liquid system, and hence adheres on the surface of the fine stearic acid particles whereby forming a coating layer<sup>1-4,9)</sup>. Afterwards, by cooling the O/W dispersion to  $30^\circ\text{C}$ , the stearic acid was solidified, and the first microcapsule was prepared. By solidifying the stearic acid, the adhesive strength of the ferrite powder is extremely enhanced. In this operation, the impeller speed ( $Nr_2$ ) and mixing time ( $t_2$ ) were fixed.

This operation was executed by changing the content (volumetric fraction  $\phi_1$ ) of the stearic acid when preparing the O/W dispersion, and impeller speed ( $Nr_1$ ) and mixing time ( $t_1$ ) for breaking the core substance in steps.

Basic conditions are shown in Table 1, and operating conditions in Table 2.

#### 3.3 Preparation of second microcapsule

Figure 3 shows how the second microcapsule was prepared. The ultrafine particle polymer layer for composing the capsule wall was formed by soap-free polymerization. That is, a specified amount of potassium persulfate ( $C_{KPS}$ ) is used as a water-soluble polymerization initiator, and is dissolved in a specified amount of ion-exchange water in continuous liquid phase. Herein, a specified amount of styrene (SS), preliminarily being rid of polymerization inhibitor, was added, and soap-free polymerization was started at a specific impeller speed ( $Nr_3$ ) and polymerization temperature of  $70^\circ\text{C}$ . After a certain time ( $t_3 = 3 \text{ hrs}$ ), the polymerization temperature was lowered to  $60^\circ\text{C}$ , the first microcapsule was added and polymerization was continued further. This operation was executed by changing mixing time ( $t_4$ ) after adding the first microcapsule in steps. The basic conditions are shown in Table 3, and operating conditions in Table 4.

Table 1 Experimental conditions for preparing the first microcapsule

Volume fraction of stearic acid	$\phi_1 = 0.05$
Amount of carbon black added	$W_{cb} = 20 \text{ wt\%}$ of stearic acid
Amount of ferrite powder added	$W_{FP} = 50 \text{ wt\%}$ of stearic acid

Table 2 Operating conditions for preparing the first microcapsule

Impeller speed for preparation of (O/W) emulsion	$Nr_1 = 83.3 \sim 200 \text{ s}^{-1}$
Mixing time for preparation of (O/W) emulsion	$t_1 = 3 \sim 90 \text{ s}$

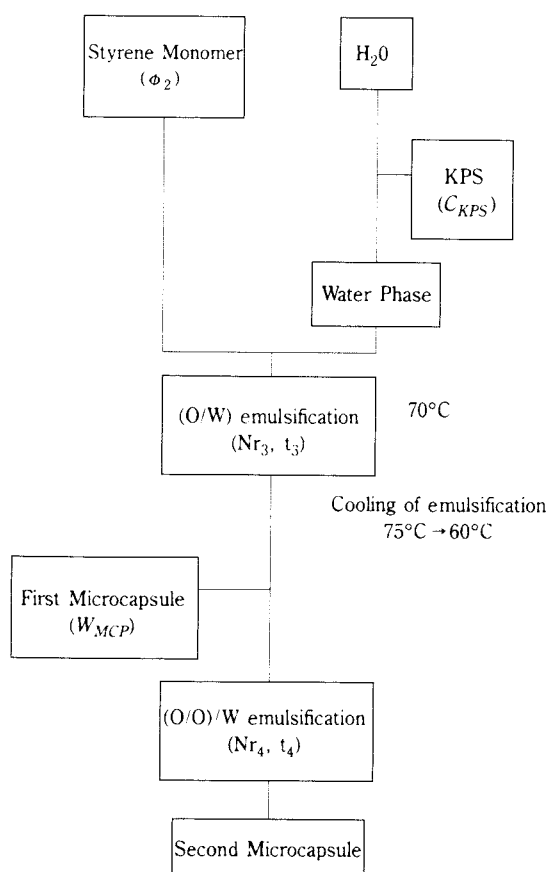


Fig. 3 Schematic representation of second microcapsule preparation

Table 3 Experimental conditions for preparing the second microcapsule

Volume fraction of the first microcapsule	$\phi_2 = 0.05$
Concentration of initiator	$C_{KPS} = 10 \text{ wt\% of monomer}$
Impeller speed for the second emulsion	$Nr_3 = 3.3 \text{ s}^{-1}$
Impeller speed after adding the first microcapsule	$Nr_4 = 3.3 \text{ s}^{-1}$
Mixing time for preparation of the second emulsion	$t_3 = 21600 \text{ s}$

Table 4 Operating conditions for preparing the second microcapsule

Mixing time after adding the first microcapsule	$t_4 = 1800 \sim 21600 \text{ s}$
---	-----------------------------------

### 3.4 Evaluation of properties of microcapsules

#### 3.4.1 First microcapsule

##### (i) Particle size distribution and mean particle size

The first microcapsule was photographed, particle size was directly measured, and distribution was obtained. As the mean particle size, the surface average diameter was calculated with the following formula.

$$D_{AV} = \frac{\sum(N_t d_t^3)}{\sum(N_t d_t^2)} \quad (1)$$

Wherein,  $N_t$  and  $d_t$  are the number and particle size of microcapsules existing in a range of each diameter respectively.

##### (ii) Yield

The yield ( $Y_1$ ) of microcapsule was defined and calculated with the following formula.

$$Y_1 = \frac{\text{Amount of first microcapsule produced}}{\text{Initial weight of (SA + FP + CB)}} \quad (2)$$

##### (iii) Weight fraction of FP

A specific amount of the first microcapsule was weighed precisely, and it was charged and dissolved in a specific amount of hydrochloric acid (11:3N). A specific amount was sampled from this solution and diluted in ion-exchange water, and the absorbance (wavelength 334 nm) was measured with a spectrophotometer (UV-160, Shimadzu Corporation). The value was compared with a prepared calibration curve (ferrite dissolved concentration vs. absorbance), and the FP concentration was determined.

By using the thus obtained adhering amount, the weight fraction of FP,  $F_{FP}$ , was defined as follows.

$$F_{FP} = \frac{\text{Weight of adhering FP}}{\text{Weight of first capsule}} \quad (3)$$

##### (iv) Microscopic observation

The general image and surface of the prepared microcapsule were observed with a scanning electron microscope (SEM).

#### 3.4.2 Second microscope

##### (i) Weight fraction of PS ultrafine particles

A specific amount of the second microcapsule was weighed precisely and added to in a specific volume of tetrahydrofuran, and the PS and core substance SA were dissolved. Then, the CB and FP in the core substance were settled and separated, and dried and weighed. A specific mount of the supernatant was sampled and subjected to liquid chromatography (DSC-50, Shimadzu Corporation), and the molecular weight distribution and component ratio of each the PS and SA were determined. From the second microcapsule weight and solid matter (CB and FP) weight, the weight of the dissolved substances (PS and SA) was calculated. From this value and component ratio, the adhering amount of PS was determined. By using this adhering amount, the weight fraction of PS,  $F_{PS}$ , was defined with the following formula.

$$F_{PS} = \frac{\text{Weight of adhering PS}}{\text{Weight of second capsule}} \quad (4)$$

(ii) Weight fraction of *FS*

Considering the dissociation of *FP* would probably occur in the second microcapsule preparation process, the amount of adhering *FP* was determined in the same way as mentioned in 3.4.1, and the weight fraction  $F_{FP2}$  was defined with the following formula.

$$F_{FP2} = \frac{\text{Weight of adhering FS}}{\text{Weight of second microcapsule}} \quad (5)$$

(iii) Molecular weight and degree of polymerization of *PS* ultrafine particles

It was presumed that the distribution of *PS* in the above-mentioned molecular weight distribution of *PS* and *SA* occurred 35 minutes before peak, and the weight-average molecular weight determined from that distribution was defined as the molecular weight  $M_w$  of the *PS* adhering to the second microcapsule. Furthermore, supposing the molecular weight of *ST* to be 104, the degree of polymerization  $n$  of the adhering *PS* was calculated from the following formula.

$$n = \frac{M_w}{104} \quad (6)$$

(iv) Microscopic observation

The general image, surface and cross section of a prepared second microcapsule were observed with a scanning electron microscope.

## 4. Results and discussion

### 4.1 Effects of volumetric fraction of stearic acid

With an impeller speed of  $Nr_1 = 7.5 \text{ s}^{-1}$  in the first emulsion system, the effects of a volumetric fraction  $\phi_1$  of *SA* on particle size distribution, mean particle size  $D_{AV}$ , yield  $Y_1$ , and *FP* weight fraction  $F_{FP}$  of the first microcapsule were studied. Results are shown respectively in **Figures 4, 5, 6 and 7**. Particle size distribution shifted to the larger size side as the volumetric fraction of *SA* increased. As a result, the mean particle size and volumetric fraction both increased. Generally, in the liquid-liquid dispersion, as the volumetric fraction of dispersed phases increases, the chance of junction between liquid drops increases, and hence the drop diameter increases<sup>9-11)</sup>. The dependence of mean drop diameter on dispersed phase volumetric fraction is expressed with the following formula.

$$\frac{D_{AV}}{D_1} = k_1 (1 + k_2 \phi) We^{-3/5} \quad (7)$$

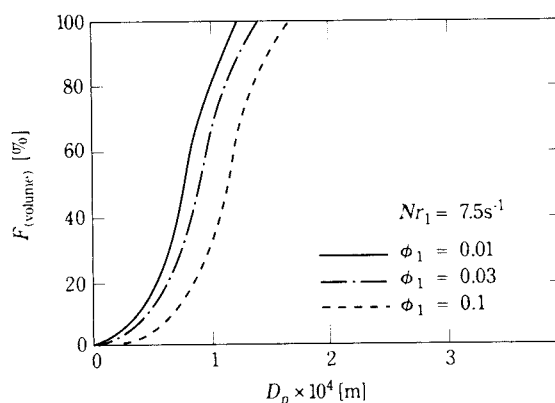


Fig. 4 Effect of the volume fraction on the size distribution

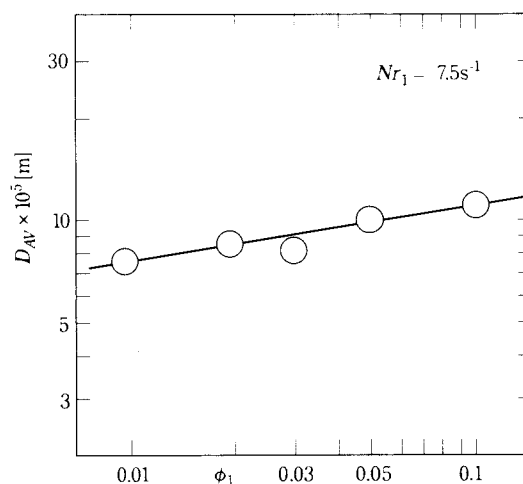


Fig. 5 Effect of the volume fraction on the mean size

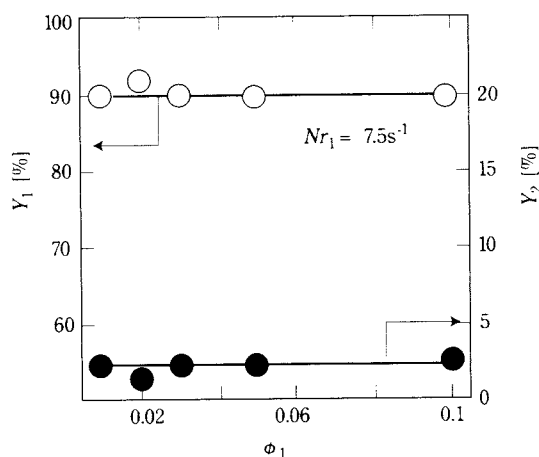


Fig. 6 Effect of the volume fraction on the yield

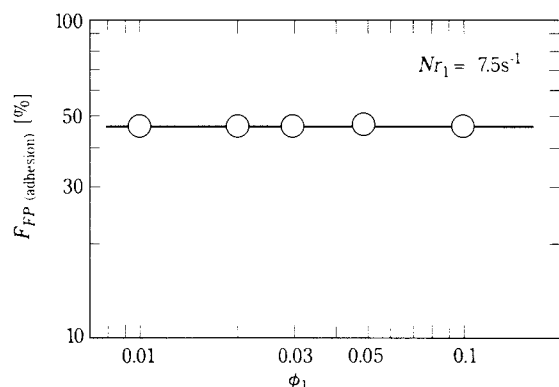


Fig. 7 Effect of the volume fraction on the content of ferrite powder

Wherein,  $D_1$  and  $We$  are impeller diameter and mixing Weber number, respectively. Values of constants  $k_1, k_2$  reported so far are  $k_1 = 0.047$  to  $0.081$ , and  $k_2 = 2.5$  to  $5.4$ . As in this experiment, in the SA disperse phase where  $FP$  acts as dispersion stabilizer and  $CB$  is mixed, it is known that  $k_1 k_2 = 0.19$ , which coincides with the results.

In the preparation of the first microcapsule, aside from first microcapsule, hollow capsules were produced. The wall of this microcapsule was composed only of  $FP$ , and it was very brittle. Therefore, this hollow capsule is considered to be formed of  $FP$  which adhered to bubbles that were trapped while preparing first emulsion system. If left still after forming the first microcapsule, the hollow capsule floats and can be separated.

The yield  $Y_1$  of the first microcapsule and yield  $Y_2$  of hollow capsule are not affected by the volumetric fraction of SA and are nearly constant ( $Y_1 = 90\%$ ,  $Y_2 = 2\%$ ). The weight fraction  $F_{FP}$  is constant (48%) for the most part even if the volumetric fraction of SA increases. These results are attributable to the fact that the initial addition of  $FP$  is constant (50%) in respect to SA content, and that yield is almost constant. The weight fraction of  $FP$  does not coincide with the initial condition, which is because hollow capsules were formed.

#### 4.2 Effects of impeller speed

With a volumetric fraction of SA of  $\phi_1 = 0.05$  and mixing time  $t_1 = 3$  s, the effects of impeller speed ( $Nr_1$ ) in preparing the first emulsion system on particle size, distribution, mean particle size, yield, and  $FP$  weight fraction were investigated. Results are shown in Figures 8, 9, 10, and 11 respectively.

It was known that particle size distribution shifted to the smaller size side as the impeller speed in-

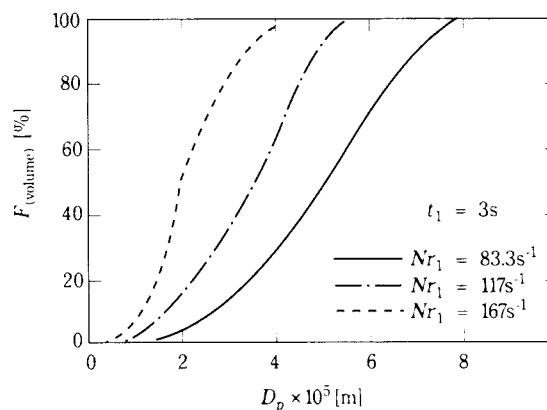


Fig. 8 Effect of the impeller speed on the size distribution

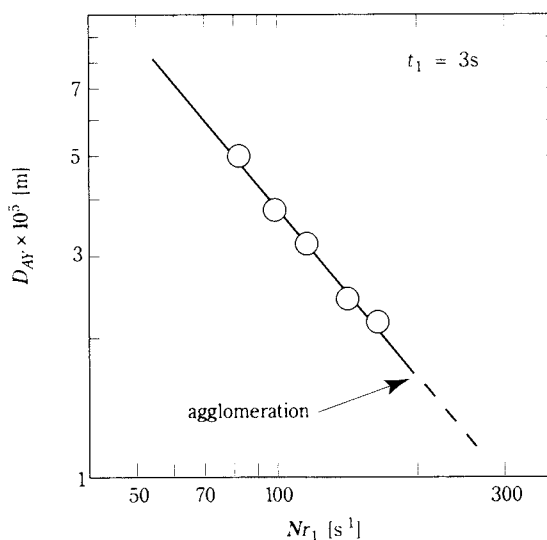


Fig. 9 Effect of the impeller speed on the mean size

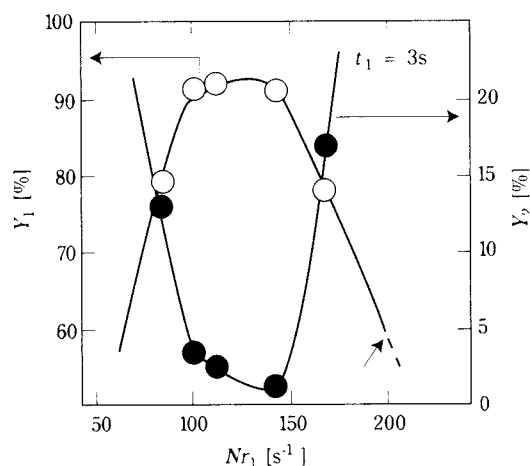
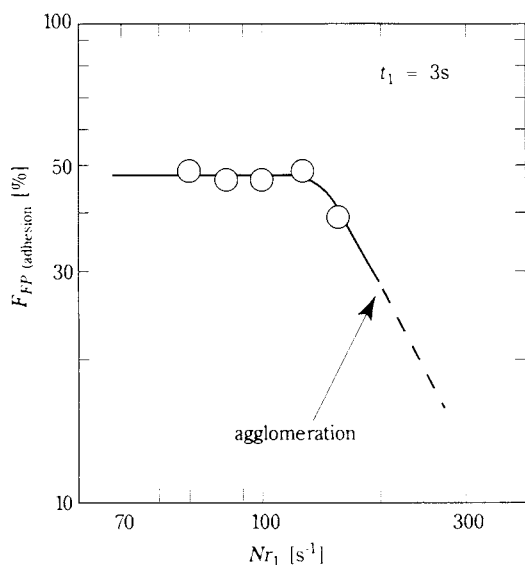


Fig. 10 Effect of the impeller speed on the yield



**Fig. 11** Effect of the impeller speed on the content of ferrite powder

creased, while distribution width became narrower, and liquid drop separation was promoted dominantly<sup>12-14</sup>). As a result, the mean particle size decreased along with impeller speed. At  $Nr_1 = 200 \text{ s}^{-1}$ , however, particles agglomerated. The dependence of mean particle size on impeller speed in the region of decreasing particle size is expressed as  $D_{AV} \propto Nr_1^{-1.2}$ . This dependence coincides with the dependence of mean drop diameter on the impeller speed in the liquid-liquid dispersion formed under breaking. This is because breaking dominants in the range of low SA volumetric fraction and high impeller speed. On the other hand, yield is extremely affected by impeller speed. That is, the first capsule yield  $Y_1$  increases with impeller speed, and it is nearly a constant value at  $Nr_1 = 100 \text{ s}^{-1}$  or more ( $Y_1 = 93\%$ ), but to the contrary, if  $Nr_1 \geq 150 \text{ s}^{-1}$ , it is decreased extremely. By contrast, the yield  $Y_2$  of the hollow capsule shows a nearly opposite dependence of first capsule yield. This is because bubble inclusion increases as impeller speed increases, thereby increasing production of hollow capsules<sup>15,16</sup>).

The weight fraction of FP drops when the hollow capsule yield increases and drops even further as the impeller speed which leads to agglomeration is approached. This is because the adhesion favorable to the first capsule decreases.

#### 4.3 Effects of mixing time

Under mixing conditions of an impeller speed of  $Nr_1 = 83.8 \text{ s}^{-1}$  and SA volumetric fraction of  $\phi_1 =$

0.05, the effects of mixing time on particle size distribution, mean particle size, FP weight fraction and yield were investigated. Results are shown in **Figures 12, 13, 14, and 15** respectively.

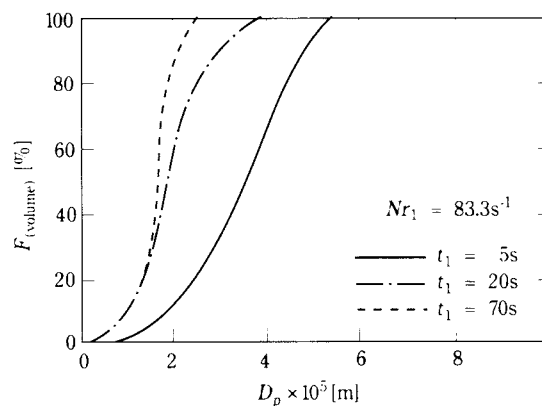


**Fig. 12** Effect of the mixing time on the size distribution

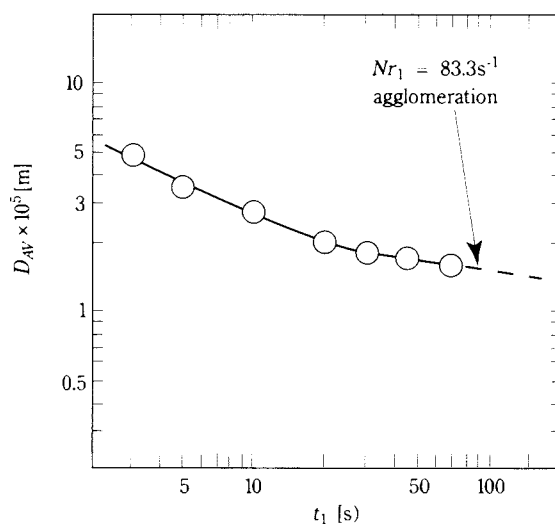


**Fig. 13** Effect of the mixing time on the mean size

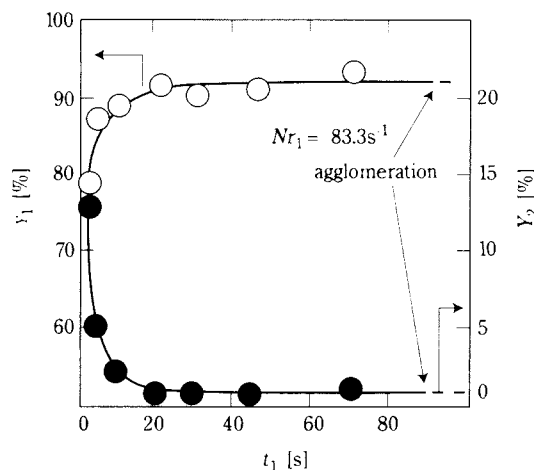


**Fig. 14** Effect of the mixing time on the yield

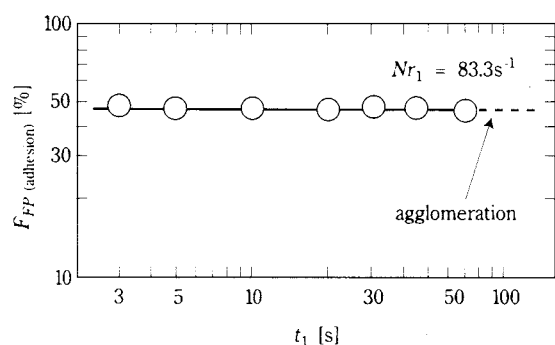


Fig. 15 Effect of the mixing time on the content of ferrite powder

Particle size distribution shifted to the smaller size side and became narrower as mixing time became longer. The change in mean particle size corresponding to the shift in particle size distribution presented a dependence of  $D_{AV} \propto t_1^{-0.48}$  up to  $t_1 = 20$  s, and a dependence of  $D_{AV} \propto t_1^{-0.17}$  at  $t_1 > 20$ . It suggests that, under the condition of  $Nr_1 = 83.3 \text{ s}^{-1}$ , the mean particle size is close to the equilibrium value when  $t_1 = 20$  s.

The yield of the first capsule increased abruptly along with mixing time, and was nearly constant ( $Y_1 = 93\%$ ) around  $t_1 = 20$  s. By contrast, hollow capsules decreased abruptly along with mixing time, and yield was nearly constant ( $Y_2 = 1.0\%$ ) around  $t_1 = 20$  s. At  $t_1 \geq 20$  s, particle size distribution and mean particle size approached equilibrium values, and yield was also stationary. Hence, the sudden decrease in hollow capsules was attributed to destruction at high speed mixing, if the hollow capsule is once formed. The weight fraction of *FP* was constant from start to end ( $F_{FP} = 49\%$ ).

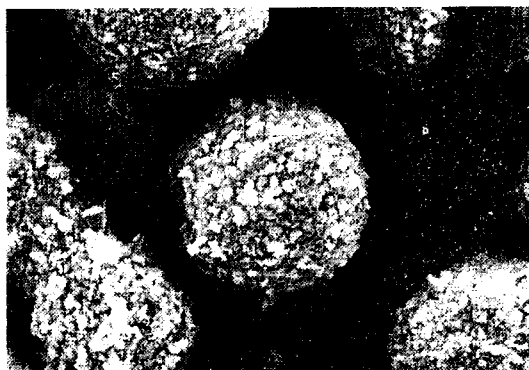
#### 4.4 Microscopic observation

Figure 16 shows SEM pictures of the entire first microcapsule and its surface. It is learned that the first microcapsule is nearly spherical, and that the surface is covered densely with multiple layers of *FP*. It was also found that the *FP* is fixed by *SA*.

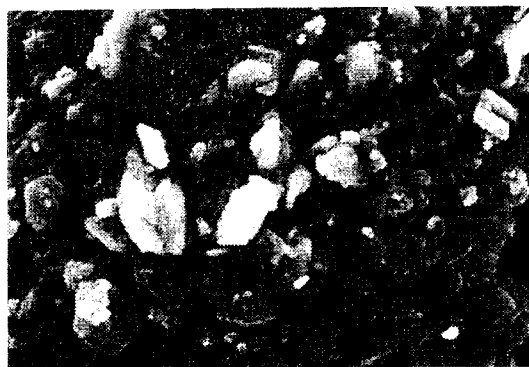
#### 4.5 Effects of mixing time in preparation of second microcapsule

The effects of mixing time  $t_4$ , after the addition of the first microcapsule, on weight fraction of adhering *PS*, *FP* weight fraction, *PS* weight-average molecular weight, and degree of polymerization were studied. Results are shown in Figures 17, 18, and 19 respectively. The fraction of adhering *PS*,  $F_{PS}$  increased from 19% ( $t_4 = 33$  min) to 30% ( $t_4 = 5.5$  hr) along with mixing time. The increasing tendency reached

nearly stationary level at  $t_4 = 2$  hr. This is because particle generation and growth were terminated by



20KU X2,000 10 μm 040106



20KU X10,000 1 μm 040106

Fig. 16 SEM photographs of the first microcapsule

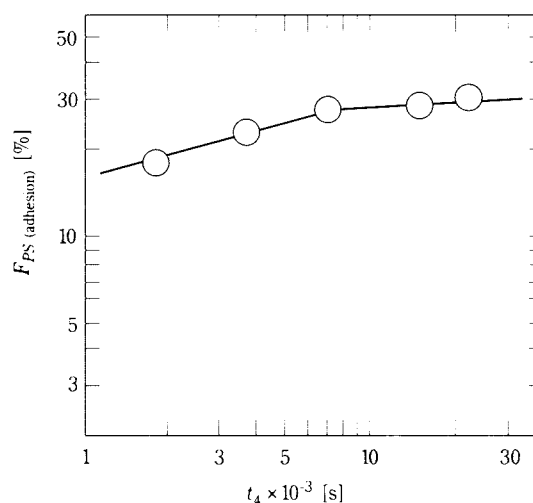


Fig. 17 Contents of *PS* beads

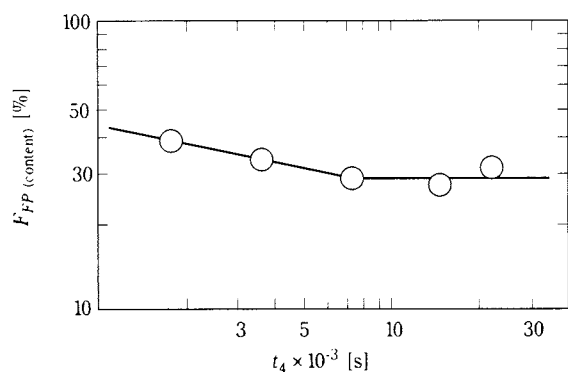


Fig. 18 Contents of ferrite powder

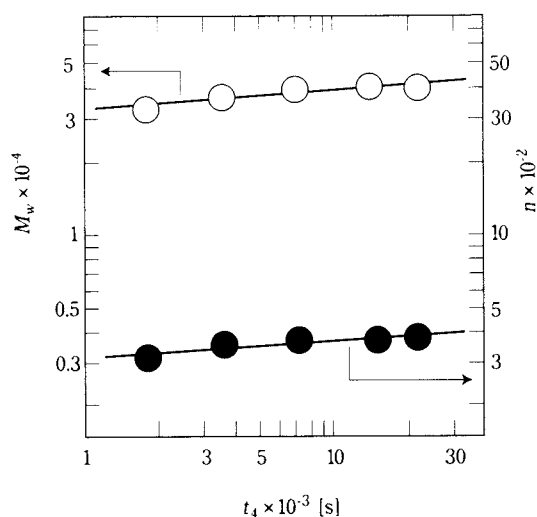


Fig. 19 Weight average molecular weight and average degree of polymerization of PSbeads

the addition of a monomer and initiator.

The adhering weight fraction of *FP* decreased along with mixing time, being nearly constant at  $t_4 = 2$  hr. It corresponds to the transition process of adhering weight fraction of *PS*. Looking at the rate of increase in the adhering weight fraction of *PS*, it means that the *FS* adhering weight did not change. Therefore, in the formation process of the second microcapsule, it was confirmed that the dissociation of *FS* did not take place substantially. The molecular weight of the *PS* ultrafine particles increased along with mixing time, but finally it was about  $(3 \text{ to } 4) \times 10^4$ . The degree of polymerization was found to be in a range of  $(3 \text{ to } 4) \times 10^2$ .

#### 4.6 Microscopic observation

Figure 20 shows SEM pictures of the entire appearance, surface and cross section of the second microcapsule. As can be seen in the pictures, the

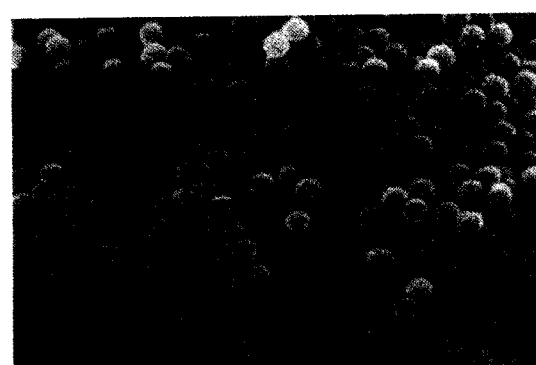


Fig. 20 SEM photographs of the second microcapsule

capsules are nearly spherical, the surface is covered with *PS* ultrafine particles, and the *PS* film is composed of multiple layers. It was investigated whether *PS* ultrafine particles would dissociate or not when the suspension system of the second microcapsule was irradiated with ultrasonic waves. No such dissociation was observed. Hence, it is learned that the adhesive layer of the *PS* ultrafine particles is formed by fusion.

#### References

- 1) M. Tanaka, K. Hayashi & T. Kojiya: Shikizai, **62**, 271 (1989)
- 2) M. Tanaka & K. Hayashi: Kagaku Kogaku Ronbunshu, **15**, 1144 (1989)
- 3) M. Tanaka & K. Hayashi: Shikizai, **63**, 321 (1990)
- 4) M. Tanaka, J. Saito, K. Hosogai & I. Kimura: Kagaku Kogaku Ronbunshu, **18**, 330 (1992)
- 5) M. Kamiyama, K. Koyama and Y. Sano: *J. Appl. Polym. Sci.*, **50**, 107 (1993)
- 6) T. Kondo: Latest Microcapsule Technology, Sogo Gijutsu Center (1987)
- 7) Japanese Laid-open Patent 5-46942
- 8) Patent Specification Collection "Microcapsule Toner," Hi-Tech Research (1994)

- 9) M. Tanaka, K. Hosogai, T. Yuda, I. Kimura & N. Saito: *Shikizai*, **65**, 484 (1992)
- 10) Y. Mlyneck and W. Resnick: *AIChE J.*, **18**, 122 (1972)
- 11) C.A. Coulaloglou and L.L. Tavlarides: *AIChE J.*, **22**, 289 (1976)
- 12) K. Hosogai and M. Tanaka: *Can. J. Chem. Eng.*, **70**, 645 (1992)
- 13) B. Weinstein and R.E. Treybal: *AIChE J.*, **17**, 304 (1973)
- 14) H.G. Yuan, G. Kalfas and W.H. Ray: *Macromol. Chem. Phys.*, **31**, 215 (1991)
- 15) M. Tanaka, T. Iseki & H. Yoshimura: *Kagaku Kogaku Ronbunshu*, **11**, 668 (1985)
- 16) M. Tanaka and T. Izumi: *Chem. Eng. Res. Des.*, **65**, 195 (1987)

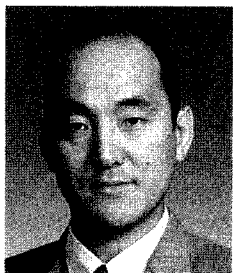
### Author's short biography



#### Masato Tanaka

Dr. Masato Tanaka is professor of Department of Chemical Engineering of Niigata University.

His major research interests are polymer particle size control in suspension polymerization, preparation of composite particles composed of inorganic and polymeric materials, preparation of various microcapsules.



#### Isao Kimura

Dr. Isao Kimura is Associate Professor of Center for Cooperative Research at Niigata University. His major research interests are preparation of particulate composites constituted of organic/inorganic/metallic compounds and preparation of high-performance, particulate materials utilizing optical activity of titanium dioxide.

# Control of Dispersion of Agglomerated Particles in Water by Electrostatic Repulsion Force†

Yasuo Kousaka, Yoshiyuki Endo, Takahiro Horiuchi  
and Yoshiyuki Sasaki

Dept. of Chem. Eng., Osaka Pref. Univ.,\*

## Abstract

The effect of electrostatic repulsion force arising from the surface potential  $\Psi$  and the double layer  $1/\kappa$  around a particle on dispersion or de-agglomeration of agglomerated particles in water is discussed.

Several suspensions of PSL (polystyrene latex) particles in an agglomerated state where  $\Psi$  and  $1/\kappa$  are respectively controlled by the pH and the electrolyte concentration  $C_e$  were prepared. They were accelerated in a convergent nozzle to give an external force on particles and agglomerated particles were dispersed into primary particles. PSL particles thus dispersed were observed with an optical microscope. It was found that the dispersion of agglomerated particles were enhanced with an increase of  $\Psi$  and  $C_e$  under a constant external force or a constant flow rate in the nozzle. It is well understood that the dispersion of particles with higher surface potential  $\Psi$  is much easier. It is, however, intuitively curious that the dispersion of agglomerated particles in higher electrolyte concentration  $C_e$  is much easier, since coagulation is usually enhanced in such a higher  $C_e$  suspension. The experimental results may be applied to control the dispersion of agglomerated particles in water.

## 1. Introduction

Particles suspended in liquid are controlled by enhancing their surface potential in order to prevent agglomeration, or by reducing the thickness of electrical double layers to promote agglomeration as is the case of filtration or settling. Once agglomerated, however, it is hard to disperse the particles completely only utilizing electrostatic repulsive force. For dispersion, it is necessary to apply some sort of mechanical force to the agglomerated particles. Several papers have been reported about the dispersion phenomenon of agglomerated particles in a state, in which electrostatic repulsive force can be almost ignored, when subjected to mechanical force exerted by accelerated flow or shearing flow of the fluid itself<sup>1-4, 8)</sup>.

In this study, agglomerated particles were dispersed under the conditions where electrostatic repulsive force, van der Waals force and mechanical force (herein, separating force acting on agglomerated particles by accelerated flow of fluid) are exerted, and the effects that factors dominating the electrostatic repulsive force (surface potential of particles

and thickness of electrical double layers) had on particle dispersion were investigated using 1.1  $\mu\text{m}$  polystyrene latex (PSL) particles. Research<sup>5, 7)</sup> has been done into fiber cleaning (dissociation of adhered particles from fibers) and it is related to the present paper, but these studies were limited to qualitative discussions using potential energy curves. They did not evaluate the dispersion phenomenon by the adhering and separating forces acting among particles as is discussed in this paper.

## 2. Theoretical discussion

### 2.1 Adhesion force among particles

The total potential energy  $V_t$  acting between two spherical particles of the same size in a liquid, and the interactive force  $F_{a0}$  between two particles, are given in the following equations according to the DLVO theory<sup>9)</sup>.

$$\begin{aligned} V_t &= V_v + V_e \\ &= d_p [-A/24h + \pi\epsilon\Psi^2 \ln \{1 + \exp(-\kappa h)\}] \\ &\quad (h \ll d_p, 1/\kappa \ll d_p) \end{aligned} \quad (1)$$

$$\begin{aligned} F_{a0} &= -dV_t/dh \\ &= F_v + F_e = d_p [-A/24h^2 + \pi\epsilon\kappa\Psi^2 \exp(-\kappa h) / \\ &\quad \{1 + \exp(-\kappa h)\}] (h \ll d_p, 1/\kappa \ll d_p) \end{aligned} \quad (2)$$

† This report was originally printed in *Kagaku Kougaku Ronbunshu*, **21**, 372 (1995) in Japanese, before being translated into English by KONA Editorial Committee with the permission of the editorial committee of the Soc. Chemical Engineers, Japan.

\* Sakai 593, Japan

Here,  $V_v$  is the van der Waals potential energy,  $V_e$  is the electrostatic potential energy,  $F_v$  is the van der Waals force,  $F_e$  is the electrostatic repulsive force,  $d_p$  is the diameter of the spherical particle,  $h$  is the distance between particles (distance between particle surfaces),  $A$  is the Hamaker constant for a particle in liquid,  $\epsilon$  is the dielectric constant of the liquid,  $\Psi$  is the surface potential,  $1/\kappa$  is the electrical double layer thickness, which is approximately  $3 \times 10^{-10}/(zC_e^{1/2})$  in aqueous solution at 298K,  $z$  is the ionic valence, and  $C_e$  is the electrolyte concentration. In equations (1) and (2), delaying effects<sup>10)</sup> are ignored.

**Figure 1** shows calculation results of the total potential energy  $V_t$  between two spherical particles of the same size (PSL particles with primary particle size of 1.1  $\mu\text{m}$ ), and interactive force  $F_{a0}$  between two particles. Particle agglomeration in a disperse system can be explained as peak height on a potential energy curve when particles approach each other from an infinite distance, as shown in **Figure 1** (a). But once agglomerated, to disperse the particles, it is necessary to look from the closest state of particles (in a bonded state, with total potential curve sinking to the primary minimum) and to consider how the force necessary for increasing  $h$  varies. In this study, the distance between particles was defined as  $h = 0.4$  nm, but the definition will be discussed later. Differentiation along the potential energy curve by  $h$  in **Figure 1** (a) results in the interactive force between particles in **Figure 1** (b). When the inclination of the potential energy curve is maximum (positive), the maximum attractive force (negative) acts between two particles. For example, in **Figure 1** (a), the potential energy of curve ① rises to a maximum (positive) at  $h = 0.4$  nm. At this time, in **Figure 1** (b), the maximum attractive force ( $-4.8 \times 10^{-9}$  N) acts on the particles. The agglomerated particles in this state are not separated unless an external force exceeding this attractive force is applied.

First, suppose the surface potential  $\Psi$  of a particle varies. In **Figure 1** (a), with the electrolyte concentration  $C_e$  being constant, when particle surface potential  $\Psi$  is raised (from curve ① to ②), the total potential energy  $V_t$  is changed from a negative to a positive value, and the interactive force between particles  $F_{a0}$  at  $h = 0.4$  nm decreases (from curve ① to ②), so that particles may be dispersed with a smaller external force. Thus, if the potential energy becomes positive in curve ② in **Figure 1** (a), since an attractive force remains active between particles in curve ②, an external force exceeding the attractive force is needed to disperse the particles. The action

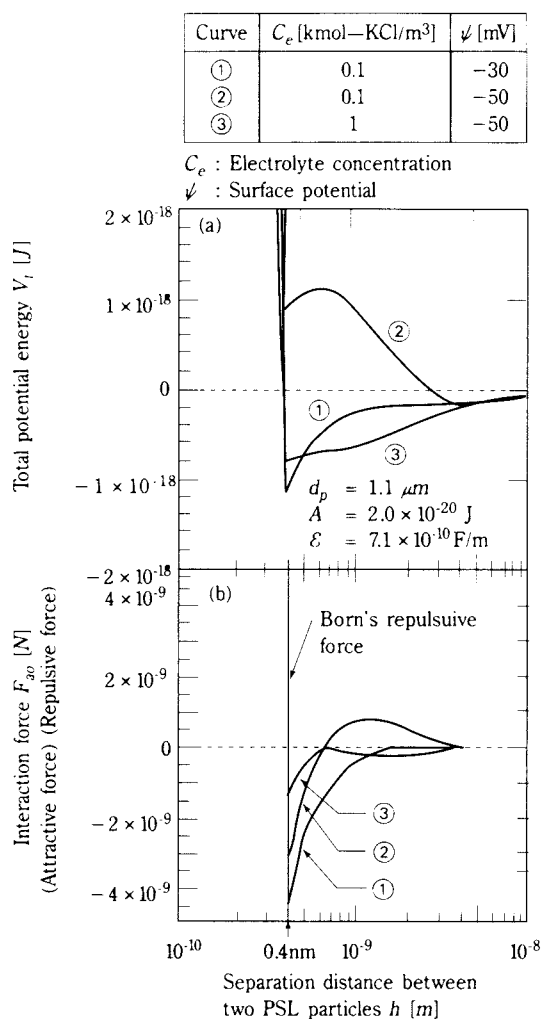


**Fig. 1**

of such an external force can surpass the peak potential energy in curve ②, so that the particles are separated.

Next, suppose the electrolyte concentration  $C_e$  varies while surface potential  $\Psi$  remains constant. Particles initially dispersed are more likely to agglomerate when  $C_e$  is higher because the electrical double layer  $1/\kappa$  is thinner. Here, one may tend to think that agglomerated particles are difficult to disperse when  $C_e$  is higher. However, once agglomerated, regardless of the circumstances or conditions surrounding agglomeration, when placed in a state of high  $C_e$ , the interactive force between particles  $F_{a0}$  is smaller when  $C_e$  is higher (from curve ② to ③) as is seen from **Figure 1** (b). Hence, if the same external force is applied to two kinds of agglomerated particles ( $h = 0.4$  nm) in the curves of this diagram, it is theoretically expected that particles of higher electrolyte concentration  $C_e$  on curve ③ are dispersed easily. That is, though higher

electrolyte concentration  $C_e$  in the disperse system enhances particle agglomeration, a curious phenomenon that once-agglomerated particles can be separated with a smaller force in the same condition. This is an example of PSL particles with a particle size of  $1.1 \mu\text{m}$ . This case discusses the effects of surface potential  $\psi$  and electrolyte concentration  $C_e$  (electric double layer thickness  $1/\kappa$ ). This tendency is not changed theoretically if the particles and electrolyte are changed. The ease with which particles agglomerate by Brownian motion can be usually judged by the magnitude of the maximum total potential energy, but to separate once-agglomerated particles, we must take note of both the magnitude of external force and its action time. The action time is the time required to move the particles relatively to the maximum value position of the potential energy. This is usually considered to be a very short time. Accordingly, in the dispersion operation for separating the bonded particles, we must pay attention to the force acting between the particles, not to the total potential energy.

## 2.2 Evaluation of dispersion and separating force acting on agglomerated particles in accelerated field

Suppose we want to disperse agglomerated particles by fluid acceleration, passing agglomerated spherical particles of the same density and size through a convergent nozzle. Assuming agglomerated particles to be separated into two, the separating force acting on particles at this time is given in the following equation<sup>3,6)</sup>.

$$F_d = \{0.119 d_v^2 \rho_f u_r^2 (\kappa_1^0 - D_v \kappa_2^0) + 2.07 (\eta \rho_f u_r^3 d_v^3 D_v^3)^{1/2} (\kappa_1^0 - D_v^{3/2} \kappa_2^0) + 9.05 \eta u_r d_v^2 D_v (\kappa_1^0 - D_v \kappa_2^0)\} / (D_v^3 + 1) \quad (3)$$

Here, subscripts 1 and 2 relate to two particles after separation (respectively particle 1 and particle 2),  $\rho_f$  is fluid density,  $d_v$  is volume equivalent diameter,  $\eta$  is fluid viscosity,  $u_r$  is the relative velocity of a particle to fluid,  $\kappa^0$  is dynamic shape factor, and  $D_v \equiv d_{v1}/d_{v2}$  ( $\leq 1$ ).

Whether the agglomerated particles are dispersed or not by the separating force defined in equation (3) is determined by the magnitude between the separating force  $F_d$  and the interactive force between particles  $F_a$ . Hence, by the following dispersability<sup>3)</sup>, the disperse state of agglomerated particles is evaluated.

$$DS \equiv F_d / F_a \quad (4)$$

Herein, agglomerated particles are dispersed if  $DS > 1$ , and not dispersed if  $DS < 1$ .

## 3. Method of experiment

The particles used in the experiment were PSL particles made by Japan Synthetic Rubber Co. (primary particle size  $d_p = 1.1 \mu\text{m}$ ). In this particle suspension (primary particle concentration  $\approx 5 \times 10^{13}$  particles/ $\text{m}^3$ ), KCl (0.05, 0.1, and 0.10  $\text{kmol}/\text{m}^3$ ) was added as electrolyte, and pH was adjusted to 2.5 (near the isoelectric point) by adding an aqueous solution of  $\text{HNO}_3$  and stirring gently at room temperature for 24 hours. In this state, almost all particles are agglomerated, which consist of 5 to 10 primary particles. Afterwards, by changing the pH of the particle suspension by adding  $\text{NH}_4\text{OH}$  and  $\text{NaOH}$  aqueous solution, samples with different levels of surface potential  $\Psi$  were prepared. Immediately after pH adjustment, the samples were presented to the following dispersion experiment.

Figure 2 shows the experimental setup for dispersing agglomerated particles by the same acceleration method used in previous paper<sup>3,4)</sup>. The prepared sample was charged in the reservoir in Figure 2, and sent into the convergent nozzle by pressurization with high pressure nitrogen gas (max. 11 MPa, abs). The agglomerated particles were dispersed by accelerating liquid flow in the nozzle. The mean flow velocity of the particle suspension in the throat of the nozzle was 10, 50, and 90 m/s. The liquid guided into the beaker was sampled on a glass slide, and the disperse state of about 1000 to 2000 particles was observed under an optical microscope.

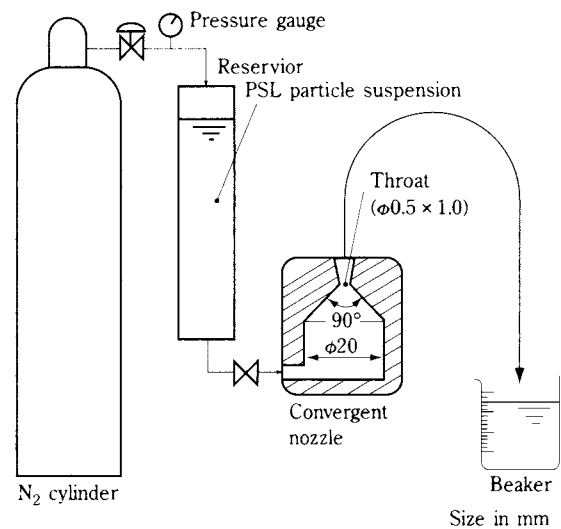


Fig. 2

#### 4. Results and discussion

**Figure 3** shows the  $\zeta$  potential of PSL particles measured with the LEZA-600 by Otsuka Electronics Co. As seen in the figure, the  $\zeta$  potential differs depending on the electrolyte concentration  $C_e$ . This is because, as shown in **Figure 4**, the elevation of  $C_e$  reduces electrical double layer thickness  $1/\kappa'$ , indicated by broken line, while particle surface potential  $\Psi$  is constant. This lowers potential on the sliding surface, that is,  $\zeta$  potential ( $\zeta'$  in the figure). Generally, the surface potential  $\Psi$  used in calculating electrostatic repulsive force [ $\Psi$  in equations (1) and (2)] is not measurable and is replaced by a measurable  $\zeta$  potential. However in this paper,  $\zeta$  potential when the electrolyte is not added is used as the surface potential. That is, from **Figure 3**, the values for surface potential  $\Psi$  at pH 4, 5 and 7 are represented by  $\zeta$  potentials of -30, -40, and -50 mV at  $C_e = 0$ .

**Figure 5** shows observation results of PSL agglomerated particles. The state before dispersion is shown in (a) and that after dispersion in (b). These photographs clearly show the dispersion state of particles. From these results, the number fractions of agglomerated particles and single particles were determined.

Results on dispersion are shown in **Figure 6**. The ordinate represents the fraction of concentration of agglomerated particles composed of primary particles of  $N_p$  pieces (including  $N_p = 1$ ) to the concentration of total primary particles. In both **Figure 6** (a) and (b), the diagrams show the result of dispersion under constant (90 m/s) flow velocity in the throat  $u_{th}$

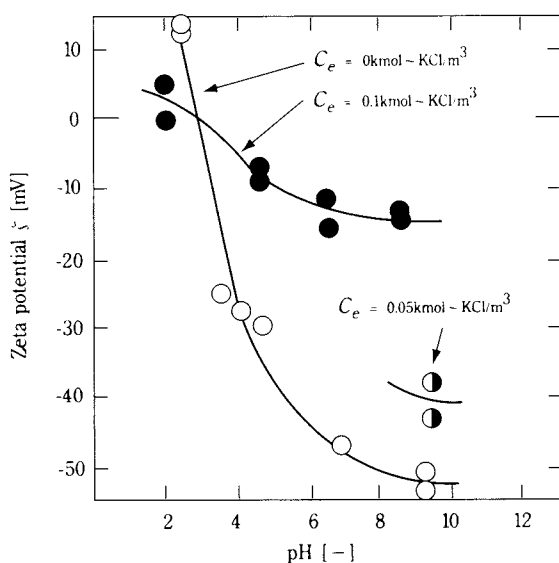


**Fig. 3**  $\zeta$  potential of PSL particles

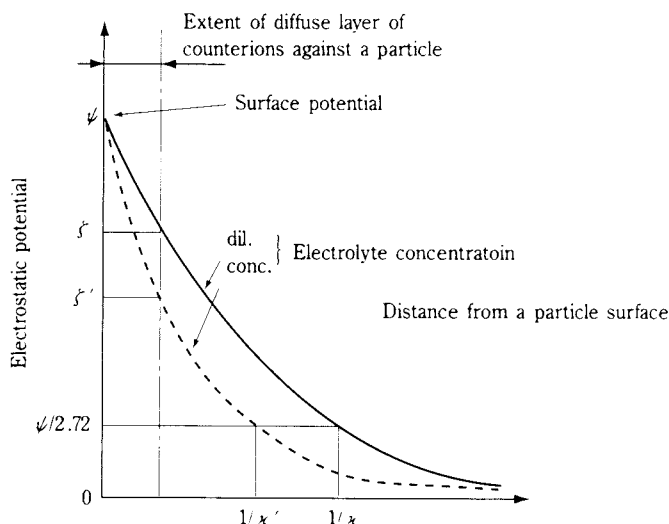


**Fig. 4** Electrostatic potential around a spherical particle

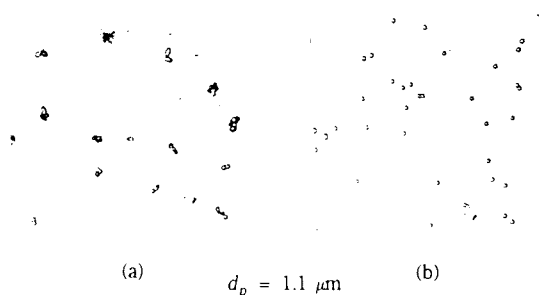


**Fig. 5** Photomicrographs of PSL particles before (a) and after (b) dispersion ( $d_p = 1.1 \mu\text{m}$ )

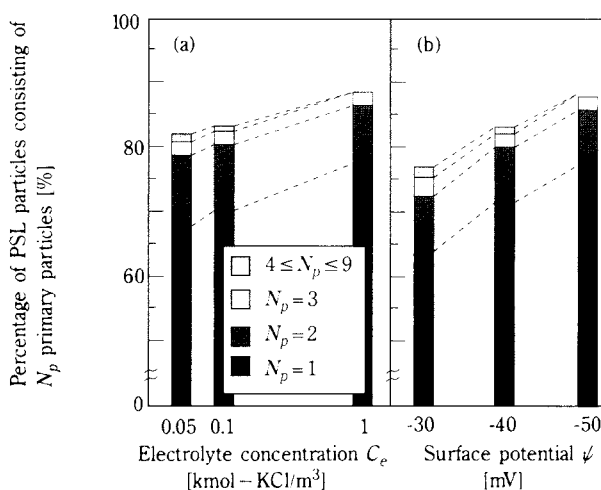


**Fig. 6**

(mean velocity in the throat of the convergent nozzle shown in **Figure 2**). By solving the equation of motion for particles in the convergent nozzle,  $u_r$  (relative velocity of particle and fluid) is obtained in an arbitrary agglomerated state<sup>3</sup>). From this  $u_r$ , the

separating force  $F_d$  in equation (3) can be determined. Since  $u_{th}$  is constant, **Figure 6** shows the results of experiments in which the separating force  $F_d$  acting on particles in the same agglomerated state was constant. The agglomerated particles are dispersed well when the electrolyte concentration  $C_e$  is high as seen in **Figure 6** (a), or when surface potential  $\Psi$  is high as seen in **Figure 6** (b). That is, particles of  $N_p = 1$  are increased. This result qualitatively coincides with the fact that, as mentioned in the theoretical discussion, the interactive force between two particles  $F_{a0}$  becomes smaller and the agglomerated particles are dispersed more easily when the electrolyte concentration  $C_e$  and surface potential  $\Psi$  are higher. In particular, the result in **Figure 6** (a) is a curious finding which supports the theoretical discussion that what is easy to agglomerate is easy to disperse, and it seems to be applicable in the control of particle dispersion.

**Figure 7** sums up experimental findings at various levels of pH, electrolyte concentration  $C_e$  and flow velocity in the throat  $u_{th}$ , in terms of dispersability  $DS$  as defined in equation (4). The abscissa denote the percentage of singlets, that is, the number of primary particles to the total number of primary particles including the primary particles in agglomerated particles. The ordinate represents the dispersability determined theoretically for triplets in triangular form (agglomerated particles consisting of three primary particles) that are theoretically the hardest to disperse<sup>3)</sup>. The solid line in the figure shows the

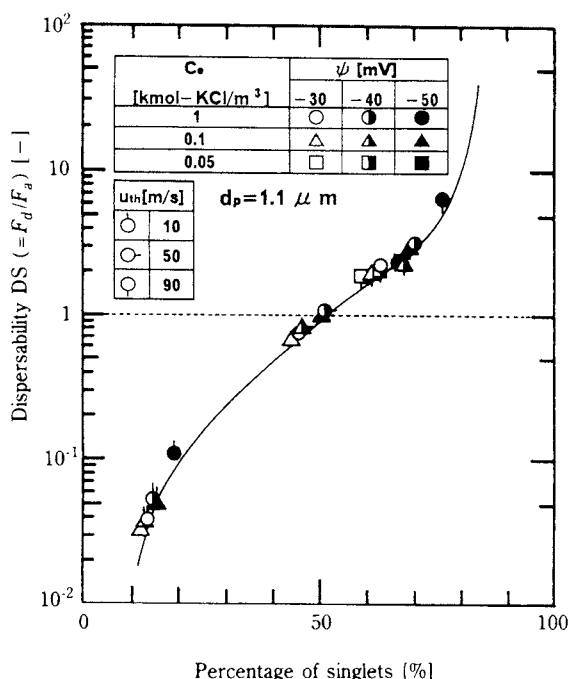


Fig. 7 Dispersability  $DS$  against percentage of singlets

dispersion of agglomerated particles in a liquid from the previous report<sup>3)</sup>, in which only van der Waals force  $F_v$  is acting as the interactive force between particles  $F_a$  (dispersion using the same apparatus as in **Figure 2** and PSL particles of about 1.1 to 5.2  $\mu m$ , assuming distance between particles to be  $h = 0.4$  nm). In this experiment, an electrostatic repulsive force  $F_e$  of about 0.12 to 0.74 times the van der Waals force  $F_v$  is acting on particles. Even in such a case, if the interactive force between particles  $F_a$  including the electrostatic repulsive force  $F_e$  is used to obtain dispersability  $DS$ , it can be expressed with the same correlation curve as in the case of van der Waals force alone (solid line in diagram). Instead of  $h = 0.4$  nm, if we assume the distance between particles to be 0.6 nm, for example, the interactive force between particles  $F_{a0}$  becomes smaller as is understood from equation (2) and **Figure 1** (b). Therefore, in **Figure 7**, the value of  $DS$  increases, and the result of the present experiment and the result of the previous report (solid line in diagram) both rise. The manner of elevation is, however, not uniform but fluctuates significantly. This fact suggests that the assumption of  $h = 0.4$  nm is not a serious error. Results in **Figure 7**, in which the particle surface potential  $\Psi$  and electrical double layer thickness  $1/\kappa$  are varied in different levels, seem to support, to a certain extent, the theoretical discussion based on the DLVO theory.

## 5. Conclusions

The following conclusions were made based on dispersion results from PSL agglomerated particles (primary particle size being 1.1  $\mu m$ ), whose interactive force between particles was controlled by varying the surface potential  $\Psi$  and electrical double layer thickness  $1/\kappa$ , and whose containing fluid was accelerated in a convergent nozzle.

- 1) Agglomerated particles were easier to disperse when electrolyte concentration  $C_e$  and particle surface potential  $\Psi$  were higher. The results of dispersion experiments could be summarized by dispersability  $DS$  ( $F_d/F_a$  ratio wherein  $F_d$  is the separating force acting on agglomerated particles, and  $F_a$  is the interactive force between particles derived in consideration of electrostatic repulsive force and van der Waals force).
- 2) When electrolyte concentration  $C_e$  was higher, it was curious to see that particles in a disperse system were agglomerated more easily in general, while once-agglomerated particles were, to the contrary, more easily dispersed. This would imply

that result could be applied to control dispersion of agglomerated particles.

## Nomenclature

$A$	= Hamaker constant	[J]
$C_e$	= electrolyte concentration	[kmol/m <sup>3</sup> ]
$DS$	= dispersability ( $\equiv F_d/F_a$ )	[-]
$D_v$	= volume equivalent diameter ratio ( $\equiv d_{v1}/d_{v2} \leq 1$ )	[-]
$d_p$	= primary particle diameter	[m]
$d_v$	= volume equivalent diameter	[m]
$F_a$	= adhesion force	[N]
$F_{a0}$	= adhesion force between two spherical primary particles	[N]
$F_d$	= separation force	[N]
$F_e$	= electrostatic interaction force	[N]
$F_v$	= van der Waals force	[N]
$h$	= separation distance between two spherical particles	[m]
$N_p$	= number of primary particles consisting of a coagulated particle	[-]
$u_r$	= relative velocity of a particle to fluid	[m·s <sup>-1</sup> ]
$u_{th}$	= fluid velocity at throat	[m·s <sup>-1</sup> ]
$V_e$	= electrostatic potential energy	[J]
$V_t$	= total potential energy	[J]
$V_v$	= van der Waals potential energy	[J]
$z$	= valence of ion	[-]
$\epsilon$	= dielectric constant	[F·m <sup>-1</sup> ]
$\zeta$	= zeta potential	[V]
$\eta$	= viscosity of fluid	[Pa·s]
$1/\kappa$	= electrical double layer thickness	[m]

$\chi^0$	= dynamic shape factor	[-]
$\rho_f$	= density of fluid	[m <sup>-3</sup> ]
$\Psi$	= surface potential of spherical particle	[V]

## <Subscripts>

1	= particle 1
2	= particle 2

## Literature Cited

- 1) Higashitani, K., N. Inada and T. Ochi: *Colloids and Surfaces*, **56**, 13-23 (1991)
- 2) Higashitani, K., N. Tanise, A. Yoshida, A. Kondo and H. Murata: *J. Chem. Eng. Japan*, **25**, 502-507 (1992)
- 3) Horiuchi, T., Y. Kousaka and Y. Endo: *Kagaku Kogaku Ronbunshu*, **20**, 708-716 (1994)
- 4) Horiuchi, T., Y. Kousaka and Y. Endo: *Kagaku Kogaku Ronbunshu*, **21**, 224-227 (1995)
- 5) Imamura, T: *J. Chem. Soc. Japan*, 943-947 (1975)
- 6) Kousaka, Y., Y. Endo, T. Horiuchi and T. Niida: *Kagaku Kogaku Ronbunshu*, **18**, 233-239 (1992)
- 7) Lange, H.: "Solvent Properties of Surfactant Solutions," Edited by K. Shinoda, pp117-188, Marcel Dekker Inc., New York (1967)
- 8) Lee, Y.J., D.L. Feke and I. Manas-Zloczower: *Chem. Eng. Sci.*, **48**, 3363-3372 (1993)
- 9) Ross, S. and I.D. Morrison: "Colloidal Systems and Interfaces," pp.248-249, John Wiley and Sons, New York (1988)
- 10) Russel, W.B., D.A. Saville and W.R. Schowalter: "Colloidal Dispersions", p. 135, Cambridge Univ. Press, Cambridge (1989)

## Author's short biography



### Yasuo Kousaka

The author is Professor of Chemical Engineering Department at Osaka Prefecture University since 1979. His major research interests are dynamic behavior of aerosol particles, sizing techniques of aerosol particles and powders, and dispersion of aggregate particles in air and water. He is currently the president of the Society of Powder Technology, Japan, and vice president of Japan Association of Aerosol Science and Technology.



### Yoshiyuki Endo

The author is Associate Professor of Chemical Engineering Department at Osaka Prefecture University since 1996. His research interests are almost same as those of Professor Kousaka.

# Preparation of a Oxide Superconductive Composite using Aerosol Process Technology †

Yasumasa Takao\*, Masanobu Awano\*,  
Yoshitaka Kuwahara\*\* and Yoshio Murase\*

## Abstract

*Composite particles of oxide superconductor were prepared using two kinds of aerosol processes, which were one used an electrostatic force and the other used a vibro-fluidized bed CVD reactor. The composite particle was constructed of an oxide superconductive core particle coated with fine particles and/or a thin film, of which secondary phases acted as magnetic flux pinning centers and sintering aids, etc. The microstructure control of composite particle and the enhancement of the pinning properties of sintered bodies were discussed.*

## 1. Introduction

Oxide superconductive composites are solution for improving performance of oxide superconductors. Materials (additives) used for producing oxide superconductive composites include some sintering aids, metals and oxides. These composites help improve critical current density by dispersing magnetic flux pinning centers, or help increase strength<sup>1)</sup>. Silver (Ag) is popular additive for producing oxide superconductive composites, since it can improve the pinning characteristic, and because of the auxiliary effect resulting from the drop in melting point, it improves ductility, is not readily reactive with superconductors, and facilitates the supply of oxygen at high temperature<sup>2)</sup>. These merits can be improved by furthering homogenizing sub-component particles.

To achieve this, it may be effective to use composite particles with a controlled microstructure. Aerosol processes enable continuous supply of highly-pure ultrafine particles and are thus a good method for producing such a microstructure<sup>3)</sup>. Aerosol means either the particles are distributed at low concentration or they are gathered and fluidized at high concentration. Both systems can be used for producing composites, though the selection should depend on the expected features of the composite to be produced.

We therefore studied two production methods. In the first, we controlled the charge applied to the separate dispersed particle systems of the supercon-

ductor particles and sub-component particles. This enabled us to control of composite structure (number of particles adhered, etc.) using the electrostatic force (Coulomb's force) that acts on the charged particles. This is called electrostatic mixing. In the second, we produced a particle comprising a submicron superconductor particle core filmed with a thin layer of sub-component. We used a vibro-fluidized bed CVD reactor that enabled continuous production of composite particles at a uniform temperature and concentration. This is called the vibro-fluidized CVD reactor process. We used silver (Ag) particles produced by mist pyrolysis for the sub-component dispersed particle system in the vibro-fluidized process. Note that Ag production by CVD with conventional delivery is often limited by the low volatility and low thermal stability of the precursors. Aerosol delivery provides a viable alternative route to conventional delivery. The electrostatic mixing and the vibro-fluidized CVD reactor process offer a high degree of controllability in producing composite particles, and dispense with the need to compensate for the difference in solubility between the core and subcomponents, unlike the coprecipitation process. We carried out a microscopic examination on the structure of the composite particles obtained by these processes using an electronic microscope. The sintered body made of these composite particles were also microscopically observed and evaluated.

## 2. Method of experiment

### 2.1 Producing composite particles by electrostatic mixing

This process, enabling a continuous production of composite particles, consists of a subprocess which

\* Ceramic Sci. Dept., National Ind. Res. Inst. of Nagoya (1-1, Hirate-cho, Kita-ku, Nagoya 462)

\*\* Structural Formation Process Dept., National Ind. Res. Inst. of Nagoya

† This report was originally printed in J. Soc. Powder Technology, Japan. **32**, 144 (1995) in Japanese, before being translated into English by KONA Editorial Committee with the permission of the editorial committee of the Soc. Powder Technology, Japan.

supplies an aerosol of the dispersed particle system, and another subprocess which charges the particles and controls their motion using an electrostatic force. This process enables us to accurately form the composite particles (e.g.: control the number of adhering particles) by controlling factors which significantly effect the electrostatic process such as charging voltage (**Figure 1**).

The subprocess for aerosol supply uses the mist pyrolysis method that enables us to produce a chemically-uniform aerosol of ultra-fine particles even from a superconductive material made of multiple components<sup>4</sup>). The aerosol, produced using an ultrasonic nebulizer (vibration frequency: 1.7 MHz), was a liquid aerosol of nitrate solution (prepared as  $Ba : Y : Cu = 2 : 1 : 3$  in atomic ratio) having a concentration of 0.05 mol/l. The aerosol was fed into the reaction zone (having a heating element of 800 mm in length and 27 mm in inside diameter, 950°C) with the aid of the oxygen carrier gas (1 l/min.), where ultra-fine particles of yttrium-based superconductive material ( $Ba_2YCu_3O_{7-x}$ ) were produced. The aerosol was retained in the reaction zone for about 30 seconds. During this time, the aerosol of the sub-component was produced in the other reaction zone. Sub-components we used were  $Ag$  and  $BaZrO_3$ . The  $Ba_2YCu_3O_{7-x}$ - $Ag$  composite was mainly used to verify the contribution of electrostatic mixing to furthering homogenization of  $Ba_2YCu_3O_{7-x}$  and  $Ag$ , since  $Ag$  is well distinguishable from superconductive materials in SEM observation at low magnification. The concentration of the  $Ag$  solution was 0.04 mol/l. The flow of the oxygen carrier gas was adjusted to 3 l/min. and 6 l/min. so that the number of particles could be changed. The  $Ba_2YCu_3O_{7-x}$ - $BaZrO_3$  composite was used to verify the improved characteristics of the sintered body produced from the composite

particles. Verification focused on the properties of the pinning center as studied in our previous paper<sup>5</sup>). The aerosol produced was a liquid aerosol of a solution made by mixing a barium nitrate solution (0.005 mol/l) with  $ZrO_2$  in such a manner that the ratio of  $Ba$  to  $Zr$  was 1:1. The flow of the oxygen carrier gas was 3 l/min.

The aerosols of the superconductive component and sub-component were then fed into a charging unit. In this stage, argon gas was fed into the transfer lines between the reaction zone and charging unit in order to homogenize the aerosol, prevent particles from adhering to walls, and charge the particles (argon gas is ionized, and ions are produced). The charging unit comprised a cylindrical charger (Masuda Laboratory Co.) of 35 mm in inside diameter and 70 mm in length. The charger uses a bi-directional monopolar ionic charging method capable of charging up to the saturation level at short charging time<sup>6</sup>). Charging (main) voltage was controlled between 0 and 20 kV<sub>pp</sub> at a constant excitation voltage of 5k V<sub>pp</sub>/20 kHz. The static electricity applied to the superconductive aerosol was negative, while that applied to the sub-component aerosol was positive. From the charging unit, the particles were soon fed into a common line and then to a mixing unit (electric field of 50 mm in inside diameter and 130 mm in the length) under an AC electric field of 20 kV<sub>pp</sub> and 200 Hz. The mixing unit increases the amplitude of the particle flow in the direction perpendicular to the main flow so that the Coulomb effect can be raised. Note that the voltage (V<sub>pp</sub>) from an AC source is given as the peak voltage between the electrodes. The composite particles produced by the mixing unit were collected onto a disc (SUS304) of 150 mm in diameter by a 10 kV DC corona discharge type electrostatic precipitator.

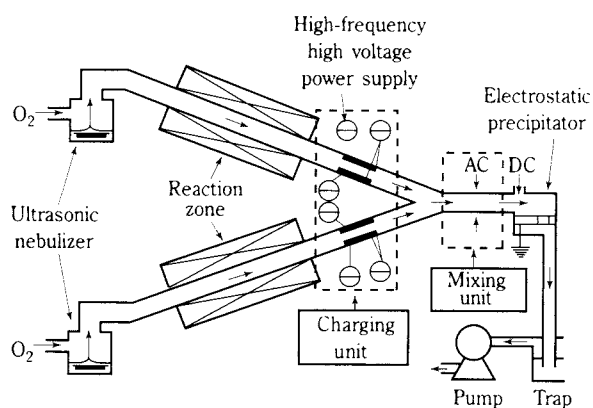


**Fig. 1** Scheme of the process for preparing the composite particle using electrostatic force

## 2.2 Producing composite particles using a vibro-fluidized CVD reactor

The system used for this study comprises a vibro-fluidized CVD reactor that fluidizes submicron particles, and the unit for the purpose of supplying  $Ag$  aerosol by mist pyrolysis for aiding the sintering process (**Figure 2**). This system can produce a comparatively large volume of composite particles.

The submicron particles of a superconductive material are produced by spray drying<sup>7</sup>). The reaction zone is a tube of 24 mm in inside diameter with a heating zone of 300 mm in the length. The tube has a distributor plate (Nikkato Co.) on the inside which functions as a porous filter made from alumina

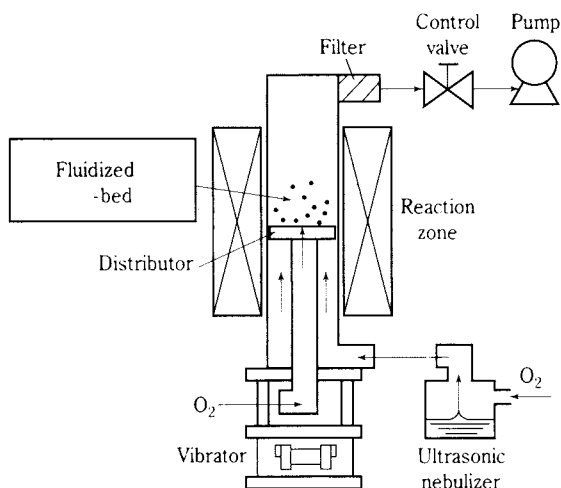


Fig. 2 Scheme of the process for preparing the composite particle using vibro-fluidized bed CVD reactor

particles of  $200\ \mu\text{m}$  in diameter. The distributor plate is supported by the fluidized gas feeding pipe in the reaction tube. Ag aerosol is fed into the reaction tube but outside the gas feeding pipe. The carrier gas for the Ag aerosol also functions as a sheath gas to avoid the fall of particles from the plate, and as an aid for re-fluidizing the particles adhering to the wall of the tube. The reaction tube is fixed to an assembly with an eccentric motor (3,000 rpm) and a spring-coupled vibrator for vertical and twisting vibration. Several dozen grams of superconductive material in particle form are placed on the plate and fluidized by the force of the oxygen fluidizing gas (0.5 l/min.) and by controlling discharge pump exhaust.

The Ag aerosol is a liquid aerosol of nitrate solution of 0.5 mol/l sprayed with an ultrasonic nebulizer (2.4 MHz). The Ag liquid aerosol is fed onto the fluidization bed with the aid of the oxygen carrier gas (9.5 l/min.). The temperature of the reaction zone is set to  $900^\circ\text{C}$ . Ultra-fine particles of Ag produced by the thermal decomposition of the aerosol are processed into  $\text{Ba}_2\text{YCu}_3\text{O}_{7-x}$ -Ag composite particles by thermal treatment and vibro-fluidization.

### 2.3 Evaluation

The composite particles were evaluated by XRD analysis, SEM, and TEM observation. The composite particles produced by the electrostatic mixing process were sintered at  $930^\circ\text{C}$  for 20 hours after CIP treatment at 200 MPa, and then annealed in an oxygen flow at  $500^\circ\text{C}$  for 40 hours to produce the sintered body of the composite particles. The sintered body was used for observing the microstructure using EPMA, measuring critical temperature ( $T_c$ ) and critical current density ( $J_c$ ) using the four-probe method,

and measuring magnetic hysteresis loops at 77 K using SQUID.

## 3. Results and discussion

### 3.1 Composite particles produced by electrostatic mixing

#### 3.1.1 Controlling the microstructure of composite particles

This study aims to investigate the uniformity of dispersion of sub-component particles in a superconductive matrix, using several kinds of composite particles each comprising a different coat of sub-component particles (Figure 3). In the production of composite particles, it is necessary to control of the number of sub-component particles that adhere to the surface of the superconductive (core) particle and/or to film the core particle with a thin layer of sub-component. (An example of this former is to adhere sub-component particles charged to +4 to the core particles charged to -4 at a sub-particle/core-particle ratio of 1:1, or to adhere sub-component particles charged to +1 to the core particles charged to -4 at a sub-particle/core-particle ratio of 4:1.) In the process of producing composite particles, it is important to control microstructure of the composite particles besides ensure homogeneity and productivity.

First, we studied the composite status for two cases: mixing two different non-charged aerosols; and mixing two different charged aerosols. The latter case served to investigate the effect of charging voltage on the composite status. Figure 4 shows how the composite status varies in response to the change in charging voltage. For both cases, Ag was used as the sub-component at a flow rate of 3 l/min. It was assumed that each particle has been charged to the maximum level (saturation level) that is determined by the voltage of the charging unit (this assumption is justifiable, because particles were retained in the charging zone for longer time than that required for reaching saturation). This study used submicron superconductive particles and Ag particles having a diameter about one-tenth that of the superconductive particle. The diameter of the sub-component particles may be too small to maintain its function as a magnetic flux pinning center. However, considering the production feasibility and other factors, the size selected is believed to be reasonable. All the production conditions, including the concentration values of solutions and the parameters of the mist pyrolysis method, were determined based on the selected diameter of

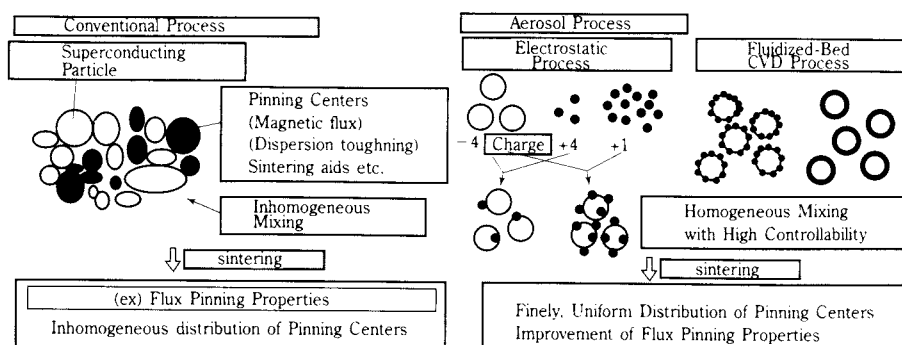


Fig. 3 Scheme of development of oxide superconductive composite using conventional process, and aerosol process

the sub-component particles.

Figure 4(a) shows the case for non-charged particles. Figure 4(b) shows the case for both superconductor and Ag particles charged to  $5\text{ kV}_{pp}$ . Figures 4(c) and 4(d) show the case for both particles charged to  $20\text{ kV}_{pp}$ . As clearly shown in Figure 4(a), both non-charged superconductive particles (large gray) and Ag particles (small white) show non-uniform agglomeration. As can be seen in Figures 4(b) and 4(c), charging the particles and increasing the charging voltage, agglomeration is eliminated, which uniformly disperses both superconductive and Ag particles. This improvement is likely because the electrostatic repulsion between particles was charged to same polarity<sup>8)</sup>. Figure 4(d) shows that Ag

particles have adhered to a  $\text{Ba}_2\text{YCu}_3\text{O}_{7-x}$  particle. This is believed attributable to the electrostatic agglomeration<sup>8)</sup>.

Next, we studied the ability to control the number of sub-particles adhering per core (superconductive) particle (Figure 3). One possible method for increasing the number of sub-particles per core particle, that we applied, was to control the electric field intensity in order to relatively reduce the electrostatic charge of the Ag particles, while at the same time, increasing the supply of Ag particles by increasing the flow of the carrier gas (Figure 5). The superconductor particles were fed at  $1\text{ l/min.}$  and charged to a constant voltage of  $20\text{ kV}_{pp}$ . Figures 5(a) and 5(b) are the counterpart of Figures 4(c) and 4(d) respectively,

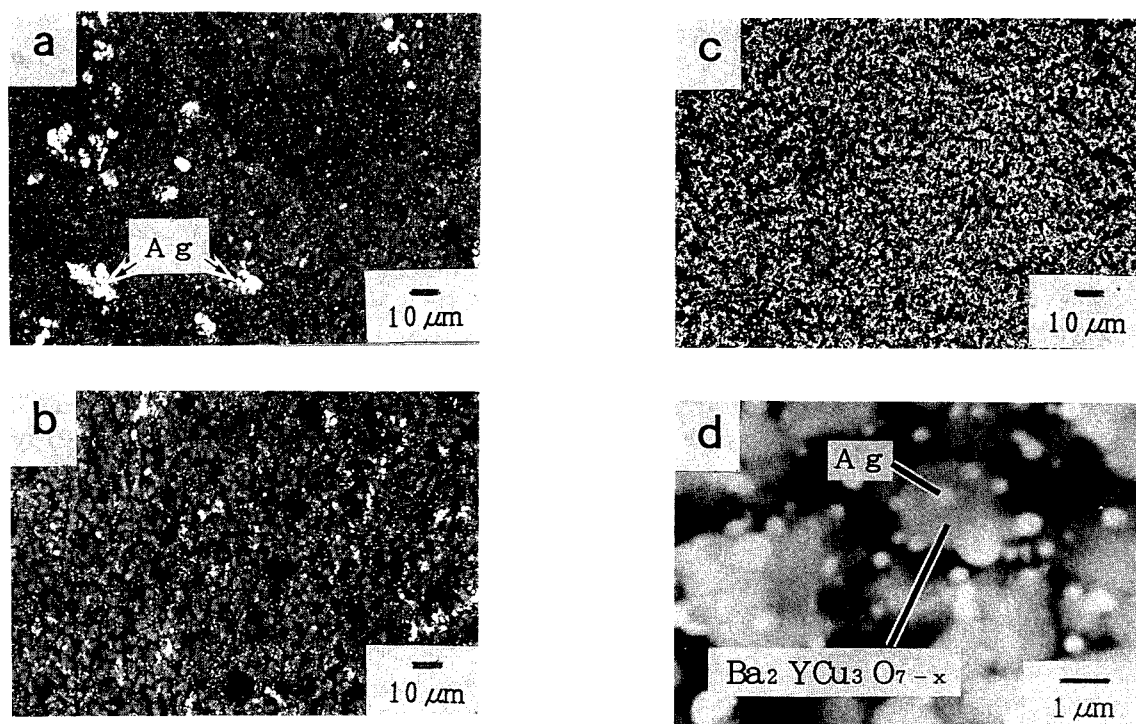
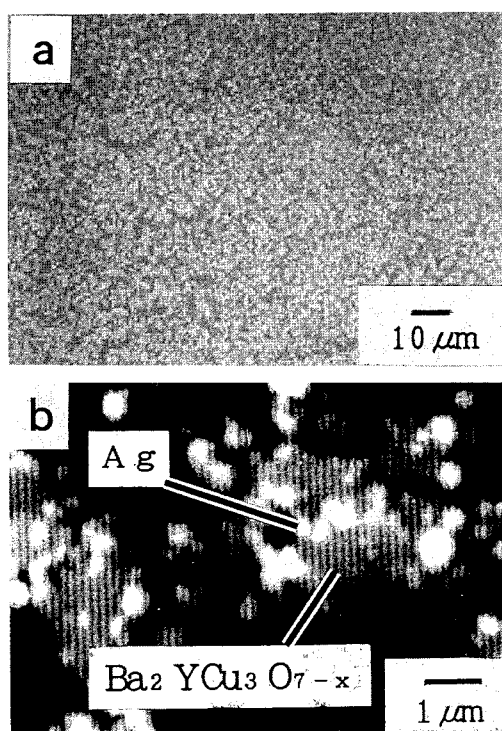


Fig. 4 Scanning electron micrographs of  $\text{Ba}_2\text{YCu}_3\text{O}_{7-x}$ -Ag composite particles:  
a. Uncharged; b.  $\text{Ba}_2\text{YCu}_3\text{O}_{7-x}=5\text{ kV}$ ,  $\text{Ag}=5\text{ kV}$ ; c,d.  $\text{Ba}_2\text{YCu}_3\text{O}_{7-x}=20\text{ kV}$ ,  $\text{Ag}=20\text{ kV}$ .

though the Ag related parameters are different; Ag flow and charging voltage for the cases shown in **Figure 4** and **Figure 5** were 3l/min. and 20 kV<sub>pp</sub>, and 6 l/min. and 5 kV<sub>pp</sub> respectively. **Figure 5(a)** is a micrograph at low magnification and shows that both superconductive and Ag particles are uniformly dispersed as well as the case shown in **Figure 4(c)**. This result indicates that the flow and charging parameters for the case shown in **Figure 5** are also effective for achieving uniform particle distribution. In comparison, **Figure 5(b)** contributes more to the increase in the number of sub-particles adhering to the surface of the core particle than **Figure 4(d)** does. This means that the parameters for the case shown in **Figure 5** are more effective for increasing the number of adhering particles.

It has been concluded that the electrostatic mixing process is capable of controlling the number of sub-particles adhering to the surface of the core-particle. This study used charging voltage and aerosol flow variables to regulate the number of adhering particles. However, other factors such as excitation voltage, AC electric field and particle diameter may also be available as control parameters for composite particle production processes. More quantitative control of the microstructure of the composite particles may be possible by optimizing these parameters.



**Fig. 5** Scanning electron micrographs of Ba<sub>2</sub>YCu<sub>3</sub>O<sub>7-x</sub>-Ag composite particles: Ba<sub>2</sub>YCu<sub>3</sub>O<sub>7-x</sub>=11/min, 20KV, and Ag=61/min, 5KV.

**Fig. 5**

### 3.1.2 Contribution to improvement in micro-structure and properties of a sintered body of composite particles

Though it is an excellent additive, Ag tends to agglomerate by sintering. This means that it is difficult to measure the pinning characteristics and charging effect on sintered composite particle, if Ag is used as sub-component. This study therefore used BaZrO<sub>3</sub>; it shows better dispersion as sub-component<sup>5)</sup>. This study aimed at to clarifying the effect of composite particles on the dispersion of sub-component particles (functioning as the pinning center) in the sintered body of superconductor particles (**Figures 6** and **7**). **Figure 6(a)** shows composite particles obtained when charging the superconductor and BaZrO<sub>3</sub> particles to 20 kV<sub>pp</sub> and 5 kV<sub>pp</sub> respectively. This figure shows that the superconductor particle (large particle at the center) is attached with BaZrO<sub>3</sub> particles (small particles) as is the case using Ag. **Figure 6(b)** shows an example of the sintered body obtained from the powder of non-charged core and sub-particles. **Figure 6(c)** shows the sintered body of the composite particles shown in **Figure 6(a)**. It was revealed that using composite particles contributes to dispersion of the sub-particles in a matrix of superconductor particles. Also revealed was that using composite particles reduces electrical resistivity, improves *T<sub>c</sub>* and *J<sub>c</sub>* values, and improves the magnetic hysteresis (increases magnetization) shown in **Figure 7**.

It has been concluded that using composite particles comprising sub-particles of high controllability enables better uniformity and better microstructure characteristics.

### 3.2 Composite particles produced by vibro-fluidized bed CVD reactor process

It was reported that in fluidizing submicron particles using a vibrator and/or medium, particles gradually self-agglomerate to a size suitable for fluidization<sup>9)</sup>. **Figure 8(a)** shows the spray drying powder before processing with a vibro-fluidized bed CVD reactor. **Figure 8(b)** shows post processed status. Though the vibro-fluidization process helped fluidize the submicron superconductor particles, it also caused the uniformly distributed submicron particles of uniform diameter to change into agglomerates of several dozen microns in diameter. We demonstrated the results shown in the reference<sup>10)</sup> that such agglomerates can be broken up with the pressure of the little finger.

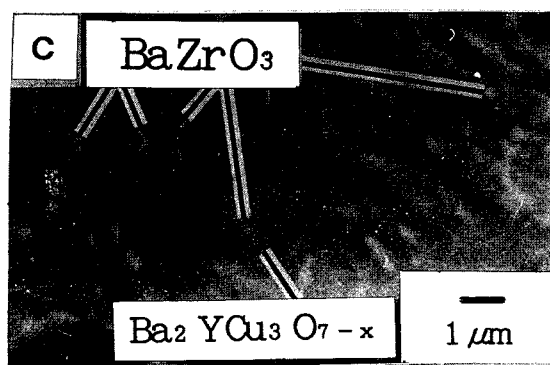
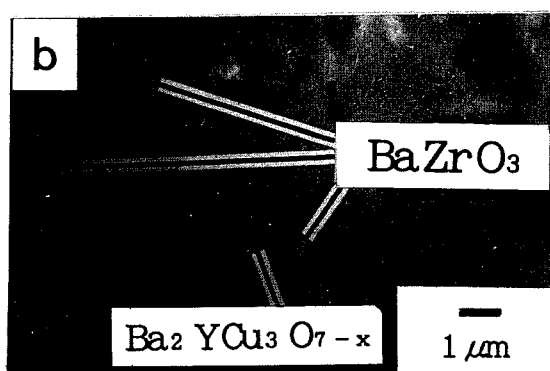
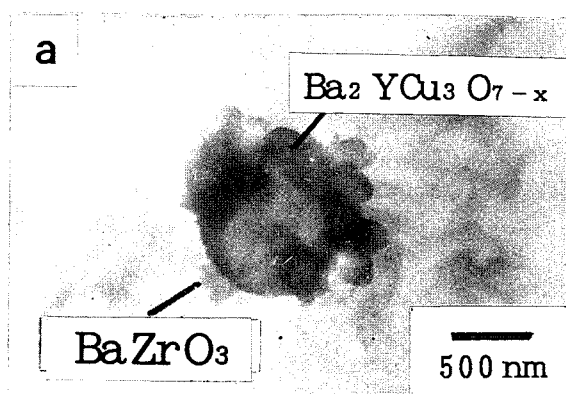


Fig. 6 Transmission electron micrograph of  $Ba_2YCu_3O_{7-x}$ - $BaZrO_3$  composite particles of  $Ba_2YCu_3O_{7-x}$ =20KV,  $BaZrO_3$ =5KV(a), and scanning electron micrographs of composite sintered bodies ; b. Uncharged; c.  $Ba_2YCu_3O_{7-x}$ =20KV,  $BaZrO_3$ =5KV.

**Figure. 9** shows the  $Ba_2YCu_3O_{7-x}$ -Ag composite particles produced by the vibro-fluidized bed CVD reactor process. The reactor was set to 900°C. This temperature is expected to form and partially melt the Ag particles while not effecting the superconductor particles. **Figure. 9** is a transmission electron micrograph and shows the superconductor particles filmed with Ag particles. **Figure. 10** shows examples of EDS profile analysis in which can be seen the successful formation of a thin film of Ag on the sur-

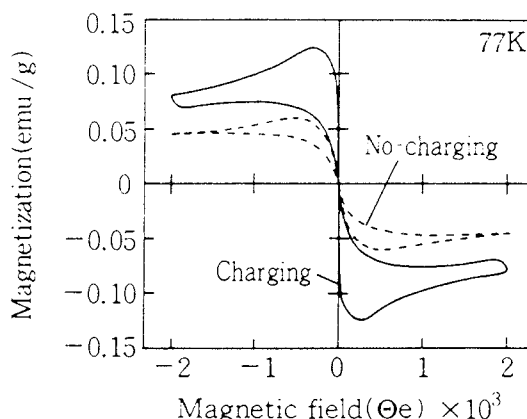


Fig. 7 Magnetic hysteresis loops of the sintered bodies prepared from the composite particles consisting of  $Ba_2YCu_3O_{7-x}$  and  $BaZrO_3$  by the process using electrostatic force : a : No-charging and b :  $Ba_2YCu_3O_{7-x}$  = 20kV<sub>pp</sub>,  $BaZrO_3$  = 5kV<sub>pp</sub>

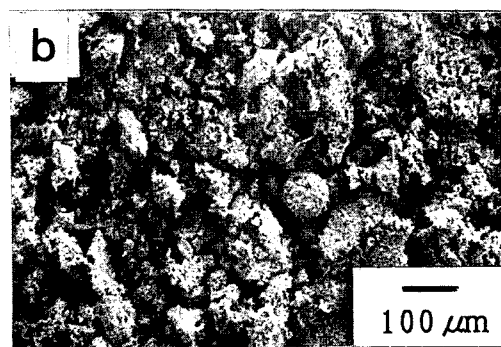
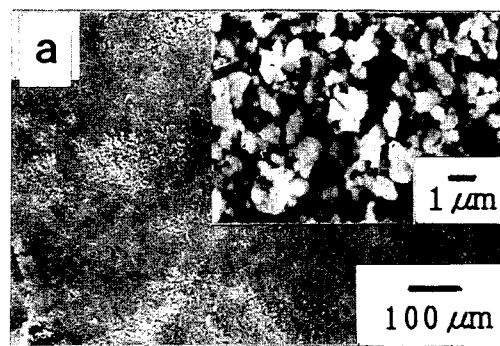
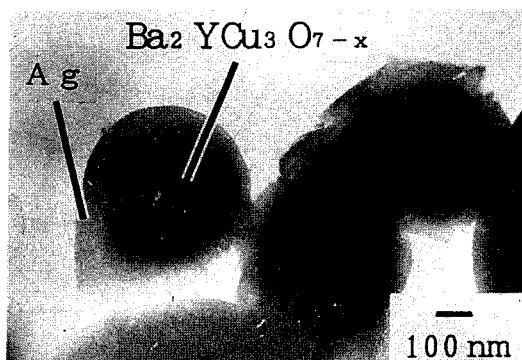


Fig. 8 Scanning electron micrographs of  $Ba_2YCu_3O_{7-x}$ -Ag composite particles of vibrofluidized bed CVD reactor process: a. spray drying powder before processing; b. post processed status.

face of the superconductor particles. Filming the superconductor particles with a thin Ag layer is likely the result of plastic deformation in the Ag particles, this itself caused by the mechanical action of fluidization, and high temperature that causes partial melting. However, since the superconductor particles have been agglomerated to a size of several dozen microns, it is necessary to establish optimum conditions for the reactor process in order that the penetration of Ag particles into the superconductor agglomerates

is easier, or else a method of de-agglomeration.

It can be concluded that this process is a useful option available for improving the performance of superconductors for the following reasons. Composite particles, as shown in **Figure. 9**, can be relatively easily obtained; Ag particles available for this process are an excellent additive (sub-component of the composite); and the process using a fluidized bed may give rise to various advantages in practical use.



**Fig. 9** Transmission electron micrograph of  $\text{Ba}_2\text{YCu}_3\text{O}_{7-x}/\text{Ag}$  composite particles of vibro-fluidized bed CVD reactor process.

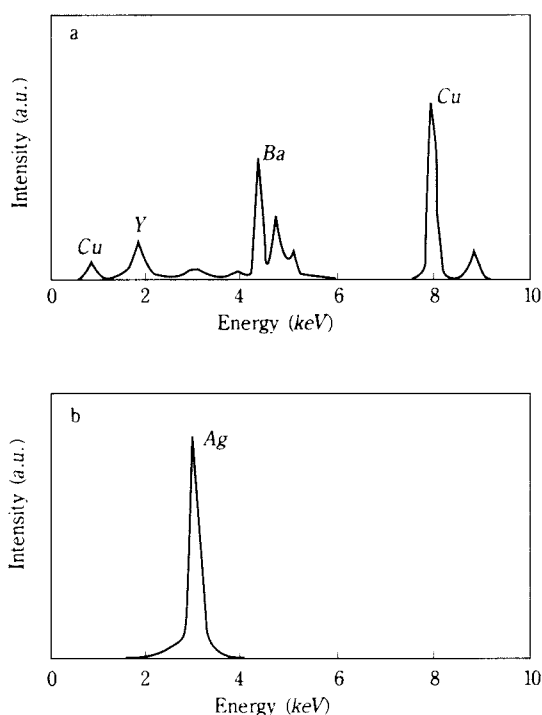


**Fig. 10** EDS profiles for the composite particles consisting of  $\text{Ba}_2\text{YCu}_3\text{O}_{7-x}$  and Ag prepared by the process using vibro-fluidized bed CVD reactor:  
a : profile detected from  $\text{Ba}_2\text{YCu}_3\text{O}_{7-x}$  core particle and  
b : profile detected from Ag layer

## 4. Conclusions

Using an aerosol process in order to obtain better uniformity in the microstructure of the sub-component in the process of producing composite particles provides the following.

- (1) The electrostatic mixing process makes it possible to control the number of sub-component particles adhering to the surface of a superconductor particle by adjusting the charging voltage and other parameters.
- (2) Sintered bodies of composite particles produced by the electrostatic mixing process show better uniformity in the distribution of sub-component particles and better properties of the magnetic flux pinning center compared to those produced from non-charged particles.
- (3) The vibro-fluidized bed CVD reactor process enables the fluidization of submicron superconductor particles and the production of Ag-filmed superconductor particles.

## References

- 1) Oka, T., Y. Itoh, Y. Yanagi, H. Tanaka, S. Takashima, Y. Yamada and U. Mizutani: *Physica C*, **200**, 55 (1992)
- 2) Lee, D. and K. Salama: *Jpn. J. Appl. Phys.*, **29**, L2017 (1990)
- 3) Okuyama, K., H. Masuda and S. Morooka: "Biryuushikougaku", p.147, Oomu-sha (1992)
- 4) Awano, M., Y. Takao, K. Kani and H. Takagi: *J. Chem. Eng. Jpn.*, **25**, 508 (1992)
- 5) Takao, Y., M. Awano and H. Takagi: *J. Ceram. Soc. Jpn.*, **102**, 237 (1994)
- 6) Masuda, S., M. Washizu and T. Ohtani: Proc. 2nd World Congress "Particle Technology", part 1, p.313, Kyoto, Japan (1990)
- 7) Awano, M., M. Tanigawa, H. Takagi, Y. Torii, A. Tsuzuki, N. Murayama and E. Ishii: *J. Ceram. Soc. Jpn.*, **96**, 426 (1988)
- 8) The Institute of Electrostatics Japan: "Handbook of Electrostatics", p.259, Oomu-sha (1981)
- 9) Morooka, S., T. Okubo and K. Kusakabe: *Powder Technol.*, **63**, 105 (1990)
- 10) Kobata, A., T. Okubo and K. Kusakabe and S. Morooka: *Kagaku Kogaku Ronbunshu*, **16**, 543 (1990)

**Author's short biography****Yasumasa Takao**

The author is researcher of National Industrial Research Institute of Nagoya (NIRIN), Agency of Industrial Science and Technology (AIST), Ministry of International Trade and Industry (MITI) since 1990. His research interests are preparation and properties of composite particle prepared by aerosol process.

**Masanobu Awano, Dr. Eng.**

He is senior researcher of NIRIN, AIST, MITI. His research interests are synthesis of oxide superconductor and microstructure control of functional ceramic.

**Yoshitaka Kuwahara, Dr. Eng.**

He is director of structure formation process department, NIRIN, AIST, MITI. His major research interests are evaluation and application of ceramics for structure matrix.

**Yoshio Murase, Dr. Eng.**

He is senior researcher of NIRIN, AIST, MITI. His research interest is preparation of ceramic fine particles.

# Motion of Grinding Media in Axial Direction and its Effect on Comminution in an Agitation Bead Mill†

Yoko Hashi and Mamoru Senna

Faculty of Science and Technology, Keio University\*

## Abstract

Grinding tests were carried out using a model agitation bead mill with a single disc. Four different types of disc were used to examine the effect of the motion of the grinding media in the axial direction. The median diameter of the ground product decreased with increasing axial movement of the grinding media under the same degree of filling of the grinding media and rate of rotation. Contamination in the product from the agitating element and grinding vessel increased with increasing energy input, irrespective of the shape of the agitating disc. Contamination from the grinding media increased with an increase in the axial movement of the grinding media which promoted mutual collision and hence abrasion of the grinding media.

## 1. Introduction

By observing the actual performance in agitation vessels made of transparent material, it turned out that agitation bead mills use shear friction between grinding media and/or vertical compressive force during grinding<sup>3-7</sup>). Motion of the grinding media in an agitation bead mill has been discussed based on the agitation theory<sup>1,2</sup>). The predominating motion of the grinding media in an agitation vessel is circular, while the radial motion is subordinate. The latter is attributed to disc rotation, circulation flow in the axial or vertical direction, and local and irregular motions due to the presence of pin-like structures. Because of these complex motions of the grinding media, it has not been clearly demonstrated what kind of motion predominated in the comminution effect.

There is a view that the particle diameter of the ground product is determined by the input energy, and not by the type of mill or operating conditions<sup>8</sup>). However, this is not very applicable to local regions where the motions of the grinding media are different from each other.

Tenda et al.<sup>7</sup>) measured the circular component of the speed of the grinding media, in a region where grinding operation was highly effective in a vertical type agitation bead mill. They revealed from the experiments using a vessel of 2.2 dm<sup>3</sup> and three different discs—horizontal plate, vertical pin and horizontal pin—that grinding efficiency depends on

the fluctuation amplitude of the grinding media rather than the average velocity or velocity gradient.

We devised a single disc type agitation bead mill that enables simple motion of grinding media and allows independent regulation of radial and axial velocities. Using the model mill, we measured the energy consumption in the grinding vessel, particle size of the ground product and contamination from the grinding media. The main circular motion combined with several subordinate motions of the grinding media was simulated as well.

## 2. Experimental equipment and method

The model mill has a grinding chamber shown in **Figure 1**. All parts contacting with the slurry of the raw material are made of SUS304. The disc is

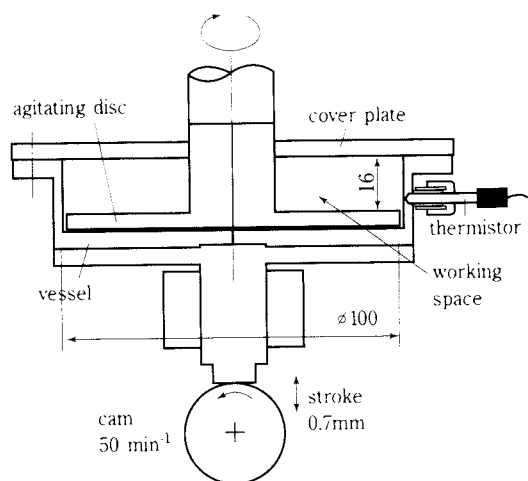


Fig. 1 Scheme of single disc mill

\* 3-14-1 Hiyoshi, Kohoku-ku, Yokohama 223 JAPAN

† This report was originally printed in *Kagaku Kougaku Ronbunshu*, **21**, 502 (1995) in Japanese, before being translated into English by KONA Editorial Committee with the permission of the editorial committee of the Soc. Chemical Engineers, Japan.

connected to the lower end of the driving shaft. The vessel is connected by a rod with a cam which enables a periodical vertical motion. The clearance between the wall of the vessel and the disc edge is less than one-third of the particle diameter of the grinding media so that particles are not captured under the disc. The volume of the grinding vessel refers to the space between the upper plate of the vessel and disc top. The cylindrical part of the vessel has an opening for a temperature sensor and is insulated to avoid heat transfer through the wall. **Table 1** shows the main dimensions of the vessel, operating conditions and the sample specification. **Figure 2** shows the discs we used. The experiment with vessel vertical motion was performed only with the plain disc.

The sample to be ground was a mixture of water and calcium carbonate (NS100 by Nitto Funaka) at a solid volume fraction 0.1. The initial size distribution of the calcium carbonate was  $0.98\ \mu\text{m}$ ,  $5.12\ \mu\text{m}$  and  $14.5\ \mu\text{m}$  in 10%, 50% and 90% cumulative values, respectively. Alumina beads with their diameter ranging from 1.7 mm to 2.0 mm (D2 by Ashizawa Ltd.) were used as the grinding media. They contained about 13% silica. The vessel was filled with the slurry after feeding the required amount of the grinding media. Operation time was 15 minutes. The temperature in the vessel and particle size of the sample were monitored during the operation. A laser diffraction system (Micro-Trac Spa by Leeds & Northrup Instruments) was used for particle size analysis. The concentration of Fe and Al was measured using a fluorescent X-ray analyzing system (3080E2 by Rigaku Electric Equipment Ltd.).

### 3. Motion of grinding medium

According to our previous papers<sup>5,7)</sup>, the tangential component of the motion of the grinding media is more than twice as large as that in either the axial (vertical) or radial direction. In the case with the flat disc and the vessel agitated without vertical movement, axial and radial components are even smaller, as shown in **Figure. 3(a)**. The motion of the grinding media are, therefore, nearly tangential.

In the case of agitating the vessel with the flat disc moving periodically in a vertical direction, the entire grinding media moved in the axial direction periodically, compressing and decompressing throughout the vessel, as shown in **Figure. 3(b)**. The compression frequency was the same with that of the vertical motion.

**Table 1 Apparatus dimensions and operating conditions**

Vessel diameter	100 mm
Vessel length	16 mm
Working volume	117.8 cm <sup>3</sup>
Rotating speed	1350, 1750 min <sup>-1</sup>
Vessel axial slide frequency	50 min <sup>-1</sup>
stroke	0.7 mm
Grinding media	Alumina, 1.7-2.0 mm (Ashizawa, D2)
density	3.5 g/cm <sup>3</sup>
Filling degree	0.4, 0.6
Weight of grinding media	99.0, 148.4 g
Weight of water	87.2, 74.5 g
Weight of powder	26.2, 22.4 g

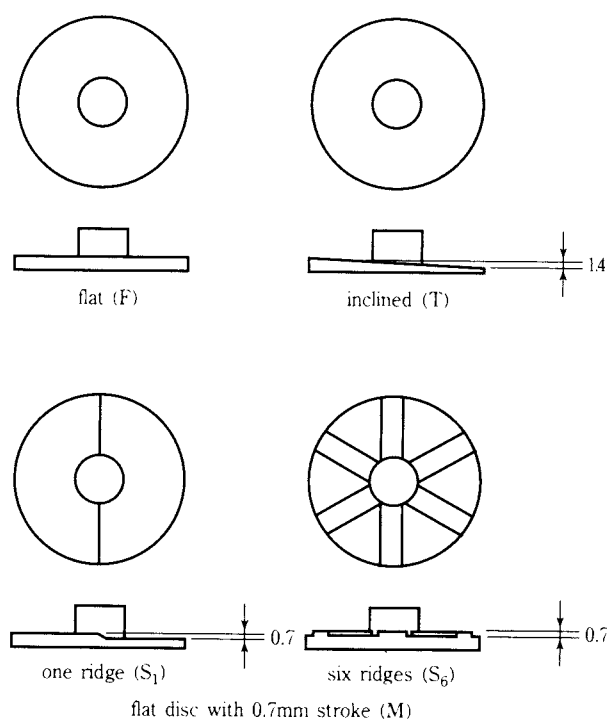


**Fig. 2** Agitating discs

In the case of the inclined disc without vertical motion of the vessel, grinding media were compressed and decompressed periodically. This differed from the previous case with simultaneous compression and decompression, and, depending on the position of the disc, force acted in the tangential and axial directions. The compression/decompression frequency of the grinding media was larger than the rotating frequency of the disc because of the circular motion of the grinding media. The compression/decompression frequency was nearly one-tenth of that of the vessel vertical motion.

With the ridged discs, the direction of the motion of some particles changes suddenly as shown in

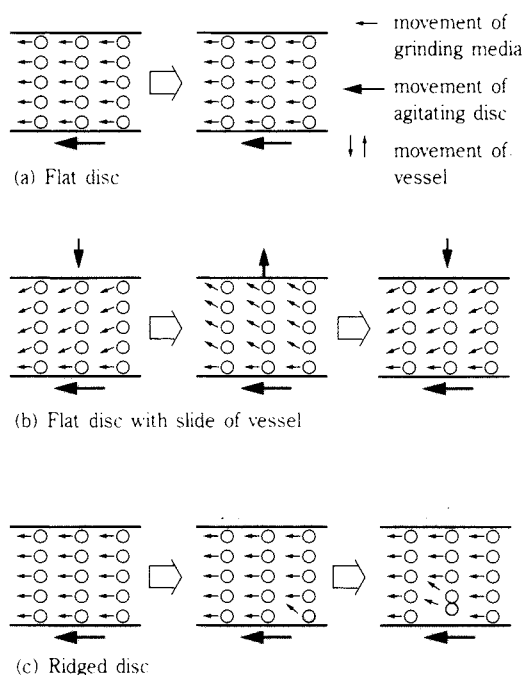


Fig. 3 Movement of grinding media

**Figure 3(c).** The particles then collide with each other, which disturbs media configuration. A disc having six ridges caused an axial motion six times more frequent.

## 4. Results and discussions

### 4.1 Temperature of the sample during the experiment

Since the energy input to the grinding vessel was too small to be evaluated with reasonable accuracy, we measured the temperature rise as an indirect measure of energy consumption. **Figure 4(a)** shows the case with the smallest change in temperature, while the **Figure 4(b)** the largest. The other two cases are in between. The temperature rise due to the type of disc is the largest for S6 (six ridges), followed by S1 (single ridge), T (inclined), M (flat and vertical motion) and F (flat). The rate of temperature rise decreases at higher temperatures as shown in **Figure 4(b)**. This is attributed to energy dissipation by poor heat insulation and thermal conduction through the drive shaft. For the cases with smaller temperature rise, the heat dissipation is small.

The ratio of the heat dissipation to the total heat generation in the vessel per unit time is less than 0.05 for a temperature difference of 5 K. This means that temperature rise is proportional to heat genera-

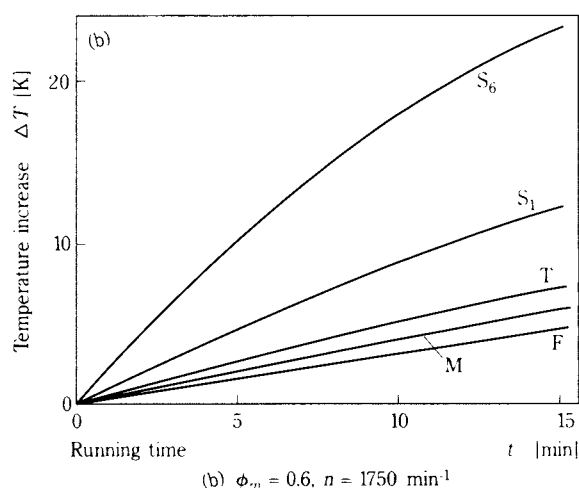
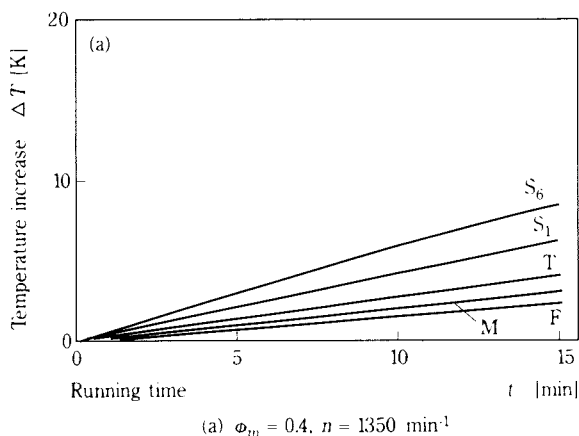


Fig. 4 Temperature increase of slurry

tion within a 5% tolerance.

Most of the energy consumed in the vessel is transformed into heat, while only a small amount of energy is used for grinding. Therefore, the energy consumption is considered proportional to temperature rise within the same 5% tolerance.

### 4.2 Particle size distribution after grinding

**Figure 5(a)** shows the particle size distribution with the smallest load among the four cases. **Figure 5(a)** shows no significant difference among those obtained when using discs F, M and T. The particle size distribution is not affected by rotating speed ( $1350 - 1750 \text{ min}^{-1}$ ) or filling rate ( $0.4 - 0.6$ ). Since energy consumption depends on the type of disc as shown in 4.1, we concluded that the increase in energy consumption does not contribute to the grinding operation. In **Figure 5(b)**, no significant

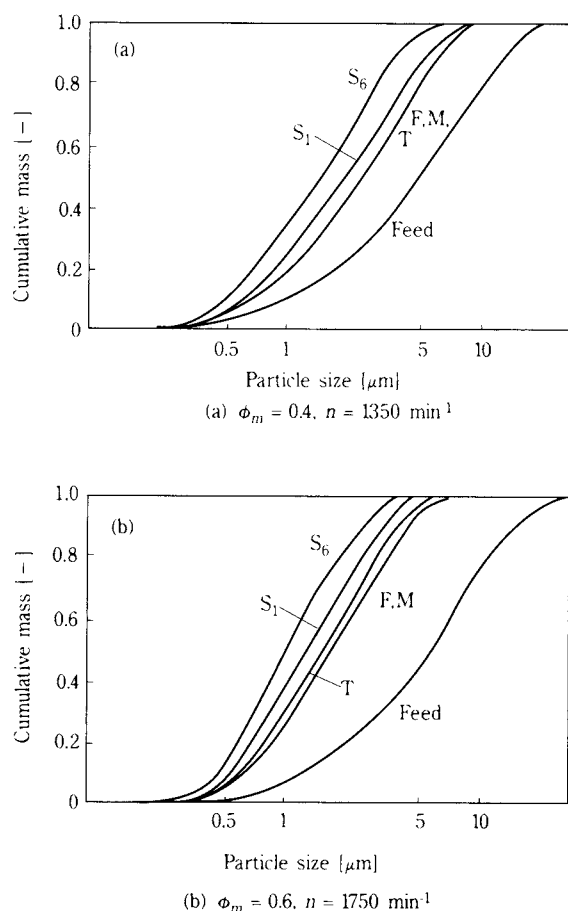


Fig. 5 Particle size distribution of product

difference in the particle distribution is found between discs *F* and *M*, while disc *T* causes a different distribution from others. This means that the inclined disc *T* improves grinding efficiency at a higher filling rates and rotating speed.

Ridged discs result in smaller particles, being capable of abrupt change in the motion of the grinding media and improving the grinding effect significantly.

Figure 6 shows the relationship between particle size and slurry temperature measured five minutes after the start of operation. The larger temperature rise render and a higher filling rate a smaller particle size.

### 4.3 Sample contamination

Figure 7 shows the relationship between iron (*Fe*) concentration and energy input. The *Fe* and *Al* concentrations are normalized with respect to the mass of the slurry. Temperature rise ( $\Delta T_5$ ) up to 2 K rarely causes a change in *Fe* concentration. Above 2 K,  $\Delta T_5$  is proportional to *Fe* concentration. Thus, abrasion is negligible when energy consumption is

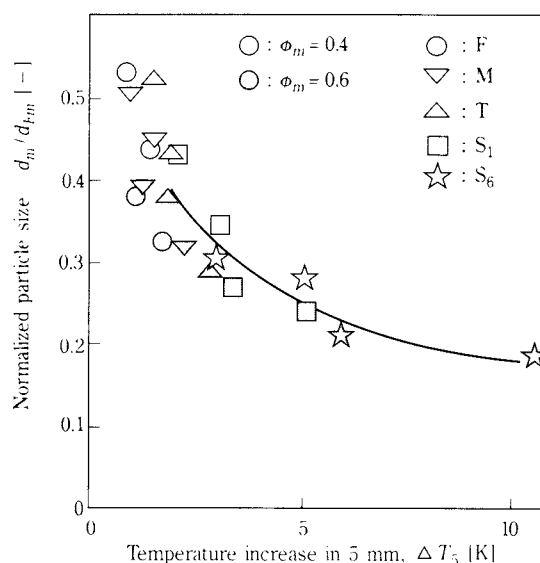


Fig. 6 Relationship between particle size and energy input

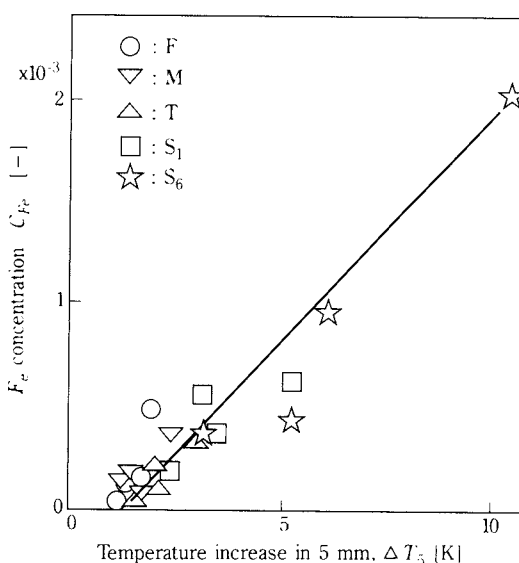


Fig. 7 Relationship between *Fe* concentration and energy input

less than a certain value.

Figure 8 shows the relationship between *Al* and *Fe* concentrations in the sample. Note that aluminum is contained only in the grinding medium. *Al* contamination is therefore attributed to the friction within the grinding media itself and/or between the media and the wall. Iron (*Fe*) contamination is exclusively originated from the machine.

Both *Fe* and *Al* concentrations increase concurrently

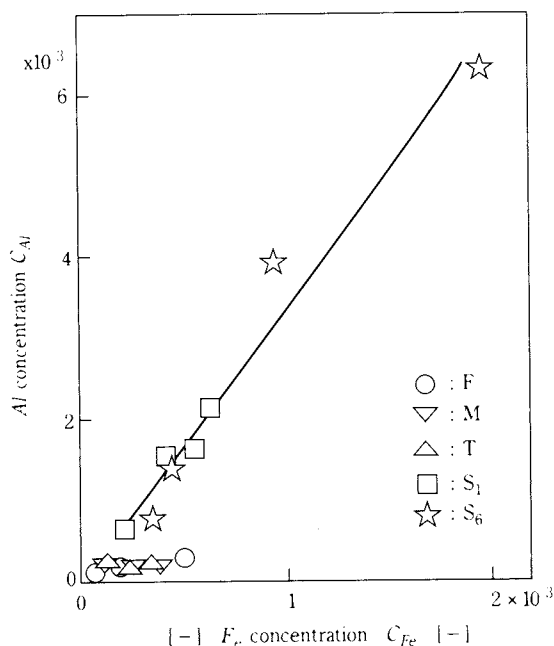


Fig. 8 Relationship between Al and Fe concentration

when using S1 or S6 ridged discs, while only Fe concentration increases in the case of discs F, M or T. This means that using an S1 or S6 disc causes more abrasion between the grinding media or between the media and the machine, as energy consumption increases. Moreover, discs F, M and T rarely increase abrasion even when the energy consumption increases. The relationship between Fe and Al concentration proves that the ridged discs causing sudden changes in the media motion, trigger more frequent and intensive collisions between grinding media. From this result and the particle size distribution described in Section 4.2, we concluded that collisions of the grinding media due to the sudden axial motion promote the size reduction.

Figure 9 shows the relationship between the particle size and Al concentration. It was shown in 4.2 that ridged discs are better than other types of disc in terms of grinding efficiency. However, even with the discs without ridges, the change in the filling rate and/or rotating speed can also improve grinding efficiency to the same level achieved by the ridged disc, judging from the initial/final particle size ratio, 0.3 (Figure 9). Figure 9 also shows that using a non-ridged disc reduces Al concentration at the same initial/final particle size ratio. It is, therefore, recommended to use a non-ridged disc, whenever it suffices in order to avoid product contamination.

Figure 10 shows the relationship between the particle size and the total amount of impurity fraction,

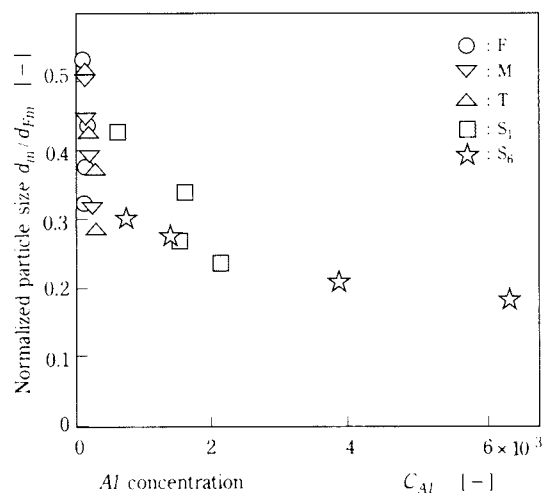


Fig. 9 Relationship between particle size and Al concentration

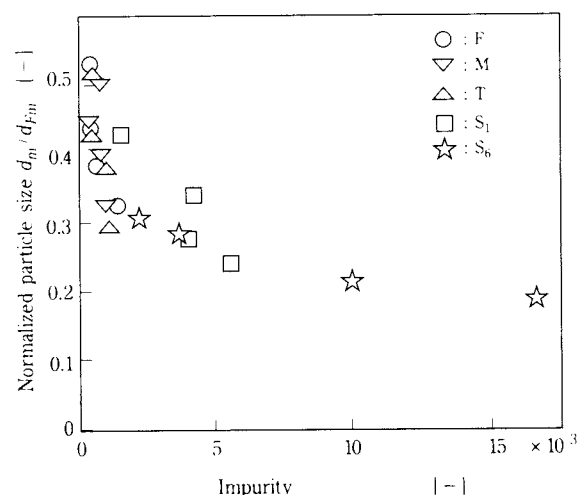


Fig. 10 Relationship between particle size and impurity of slurry

calculated from the Al and Fe concentration. Contamination from the grinding media is dominant as compared with those from the machine, as mentioned previously.

## 5. Conclusion

When powders are ground in an agitation bead mill at constant filling rate and constant rotating speed, a sudden vertical (axial) motion of the grinding media under circular motion promotes size reduction. Contamination from the machine increases with the energy consumption for any type of disc. Contamination from the grinding media increases by using, a ridged disc. It is therefore recommended to use a non-ridged disc as far as the particle size range reached is satisfactory.

## Nomenclature

$C_{Al}$	= relative concentration of <i>Al</i> in product	[–]
$C_{Fe}$	= relative concentration of <i>Fe</i> in product	[–]
$d_{Fm}$	= median particle size of feed	[ $\mu\text{m}$ ]
$d_m$	= median particle size of product	[ $\mu\text{m}$ ]
$n$	= speed of rotation	[ $\text{min}^{-1}$ ]
$t$	= running time	[min]
$\Delta T$	= temperature increase	[K]
$\Delta T_5$	= temperature increase in 5 min	[K]
$\phi_m$	= filling degree of grinding media	[–]

## Literature cited

- 1) Bosse, D.G.: *Official Digest*, **30**, 250-276 (1958)
- 2) Engels, K.: *Farbe u. Lack*, **71**, 375-385 (1965)
- 3) Gondoh, T., M. Toh and Y. Murakami: *Shikizai Kyokaishi*, **62**, 202-207 (1989)
- 4) Gondoh, T., M. Toh, Y. Murakami, Y. Hashi and M. Kusunoki: *ibid.*, **64**, 297-304 (1991)
- 5) Hashi, Y. and M. Senna: *J. Soc. Powder Technol., Japan*, **28**, 738-744 (1991)
- 6) Kaku, M., Y. Murakami, T. Tenda, T. Gondoh, M. Toh and M. Kusunoki: *Shikizai Kyokaishi*, **63**, 3-10 (1990)
- 7) Tenda, T., Y. Kubozono, H. Nishimura, T. Teshiba, S. Komori and Y. Murakami: *ibid.*, **64**, 148-155 (1991)
- 8) Weit, H. and J. Schwedes: *Chem.-Ing.-Tech.*, **58**, 818-819 (1986)

## Author's short biography



### Mamoru Senna, PhD

Graduated from Keio University, Graduate School in 1970, with a promotion to PhD. He has been a visiting scientist from 1972 to 1974 in Technische Hochschule Aachen and from 1980 to 1981 in Technische Universität in Karlsruhe. Since 1988, he is a professor in the Department of Applied Chemistry, Faculty of Science and Technology, Keio University. Enhancement of reactivity of solids by mechanical and irradiational strategy, including soft-mechanochemical synthesis center his research interests.



# Influence of Particle Size of Titanium Dioxide on UV-ray Shielding Property†

Masashi Sakamoto, Haruo Okuda, Hideo Futamata,  
Akihito Sakai and Masaki Iida\*

Ishihara Sangyo Kaisha, Ltd., Research & Development Laboratory\*

## Abstract

*The influence of particle size (0.019–0.24  $\mu\text{m}$ ) of  $\text{TiO}_2$  on UV-ray shielding capability was studied.*

*UV-ray shielding capability of  $\text{TiO}_2$  depended on the wavelength. That is, the smaller the primary particle size was, the greater its shielding capability against around 300 nm of UV-B range was. On the contrary, for the shielding capability against around 350 nm of UV-A range, an optimum primary particle size was found. Furthermore, the optimum primary particle size varied, depending on dispersion strength of the particles in a paint.*

## 1. Introduction

Titanium dioxide is high in refractive index, chemically stable and extremely safe to use. It is widely used as a white pigment. The titanium dioxide used for pigment is generally designed to a primary particle size of 0.2 to 0.3  $\mu\text{m}$  in order to maximize visible light scattering. Ultrafine particles of titanium dioxide are extremely smaller in primary particle size and present characteristic properties not found in the titanium dioxide used for pigment. They have come to be used in various fields, including sunscreen cosmetics, ultraviolet ray (UV-ray) shielding paint, ink, plastics and textiles, automotive metallic paint, and silicone rubber.

In particular, they are intensively used to cut-off UV-rays. And the relationship between the UV-ray shielding effect and particle size, in other words, the optimum particle size for maximizing the UV-ray shielding effect, has been calculated theoretically<sup>1-3)</sup>, but details have not been reported about experimental study.

The authors, using  $\text{TiO}_2$  particles of different primary particle sizes (0.019 to 0.24  $\mu\text{m}$ ), investigated the effects of particle size on the shielding performance of UV-ray (300 to 400 nm), and searched for optimum particle size<sup>4)</sup>. Incidentally, though dispersion of  $\text{TiO}_2$  particles is more difficult when the primary particle size is smaller, the effects of dispersion strength were studied at the same time.

## 2. Experiment

### 2.1 Samples

$\text{TiCl}_4$  was hydrolized by neutralization, followed by calcination, then it was ground by wet process, and treated with hydrous aluminum oxide on its surface (1.5% as  $\text{Al}_2\text{O}_3$  to  $\text{TiO}_2$ ). Eight samples (A to H) of rutile particles  $\text{TiO}_2$  with different primary particle sizes were prepared. The particle size was controlled mainly by changing calcination temperature.

For supplementary experiment (1), pigment type titanium dioxide CR-50 (Ishihara Sangyo Kaisha, Ltd.) and carbon black (MA-100, Mitsubishi Chemical Corp.) were used.

### 2.2 Operation of experiment

#### 2.2.1 Preparation of paint

In a paint system of acrylic resin (Acrydick 47-712, Dainippon Ink & Chemical Inc., solid content 50%)/melamine (Super Beckamine L-117-60, Dainippon Ink & Chemical Inc., solid content 60%) = 4/1, paint samples were prepared by dispersing for 5, 20, 60, and 180 minutes using a paint shaker, with zircon beads of 0.5 mm in diameter as a medium (1400 g/ 100 g  $\text{TiO}_2$ ). A pigment concentration in solid matter (PWC) was 3.3%.

#### 2.2.2 Measurement of transmittance of paint film

The paint was applied to a film (Fujitac Film, Fuji Photo Film Co., Ltd) in a dried film thickness of 5  $\mu\text{m}$  by doctor blade, and baked. Spectral transmittance (300 to 700 nm) was measured using a spectrophotometer (UV-240, Shimadzu Corporation), while a clear resin was applied to a film in a same

\* 1. Ishihara-cho, Yokkaichi-city, Mie-pref., 510 Japan

† This report was originally printed in *SHIKIZAI KYOKAISHI* 68, 203 (1995) in Japanese, before being translated into English by KONA Editorial Committee with the permission of the editorial committee of the Japan Society of Colour Material.

film thickness to be used as blank.

### 2.2.3 Electron microscopic observation

Using a scanning electron microscope (S-800, Hitachi, Ltd.), the primary particle size of  $\text{TiO}_2$  and the dispersion state of  $\text{TiO}_2$  particles in the paint film were observed at an overall magnification of 20,000 times.

### 2.2.4 Measurement of specific surface area

The specific surface area of the  $\text{TiO}_2$  samples was measured using a specific surface area measuring apparatus (FlowSorb II 2300, Micromeritics Instrument Corp.).

### 2.2.5 Supplementary experiment (1)

In the same acrylic/melamine paint system as in 2.2.1, by dispersing for 60 minutes, paints were prepared at  $\text{PWC} = 0.33\%$  of carbon black, and  $\text{PWC} = 2.3\%$  of CR-50.

Besides, these paints were mixed at 1.5/8.5, 3/7, 5/5, 7/3, and 8.5/1.5, and applied to films to a dried film thickness of  $9 \mu\text{m}$ , and baked. Spectral transmittance and reflectivity were measured.

## 3. Results and discussion

### 3.1 Calculation of particle size from specific surface area

The specific surface area of eight samples A to H was measured. Results are shown in **Table 1**. From the measured values, the particle size was calculated by assuming  $\text{TiO}_2$  particles to be perfect spheres. The result coincided well with the primary particle size observed by electron microscope. This calculated value was regarded as the primary particle size of  $\text{TiO}_2$ .

**Table-1** Primary particle size (estimated from S.S.A. \* value)

Item Sample	S.S.A* [ $\text{m}^2/\text{g}$ ]	Primary particle size [ $\mu\text{m}$ ]
A	75.0	0.019
B	49.0	0.029
C	39.7	0.036
D	29.8	0.048
E	19.0	0.075
F	14.9	0.096
G	8.9	0.16
H	6.0	0.24

\*S.S.A, specific surface area

### 3.2 UV-ray shielding capability and particle size

Microscopic observations of the dispersion state of sample paint are shown in **Figure 1**. Extreme agglomeration was noted in paint samples of short dispersion time, and in spite of using sample C where primary particle size was  $0.036 \mu\text{m}$ , many agglomerated particles of even  $0.2$  to  $0.3 \mu\text{m}$  were observed. The longer dispersion time, the more dispersion advanced, and agglomerated particles became smaller and fewer. But even at a dispersion time of 180 minutes, particles were not dispersed completely to the primary particle size, and this tendency was the same in all samples.

**Figure 2** shows changes in transmittance of ultraviolet rays in relation to the primary particle size under strong dispersion. In the wavelength range of 300 to 400 nm, the shorter the wavelength of ultraviolet ray, the lower the transmittance for titanium dioxide of any particle size. The transmittance of ultraviolet rays of 300 nm tends to decline as the primary particle size becomes smaller, and in ultraviolet rays of 325 to 400 nm, minimum values of transmittance were noted. The optimum particle size, from the viewpoint of UV-ray shielding, was

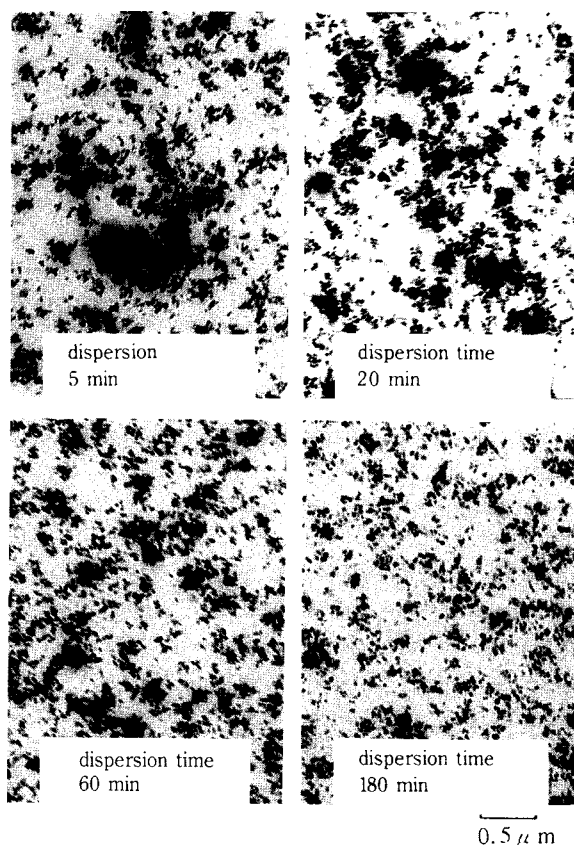


**Fig. 1** SEM photographs of sample C.

found to depend on wavelength. **Figure 3** shows calculation results by P. Stamatakis<sup>1)</sup>. Results in **Figure 2** seem to be very close to these calculation results. Incidentally, **Figure 2** and **Figure 3** are identical in terms of pigment concentration  $\times$  film thickness.

**Figure 4** gives results of reflectance measurements on a black substrate. As a result, reflectance at 300 and 325 nm was considerably low, and there was no maximum value for particle size. But in ultraviolet rays of 350 nm, 375 nm, and 400 nm, maximum values were observed. Reflectance was

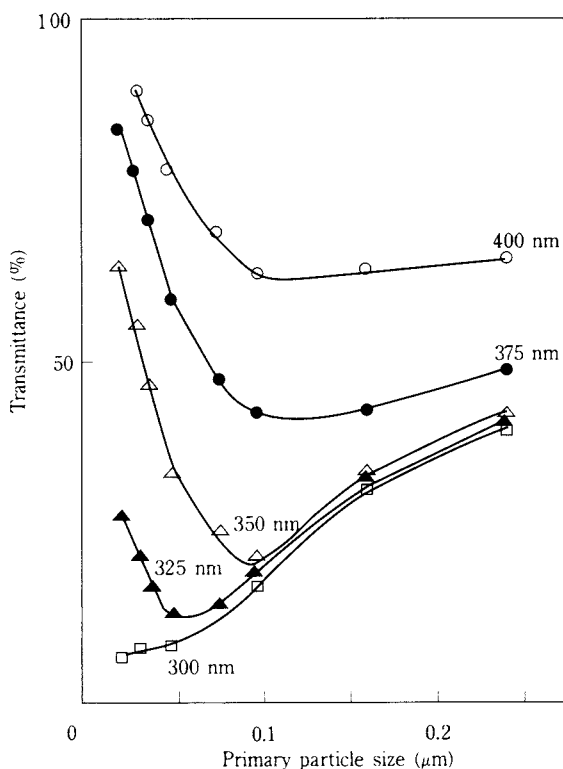


**Fig. 2** Relation between transmittance and primary particle size. (○), 400 nm; (●), 375 nm; (△), 350 nm; (▲), 325 nm; (□), 300 nm. Dispersion time, 180 min.

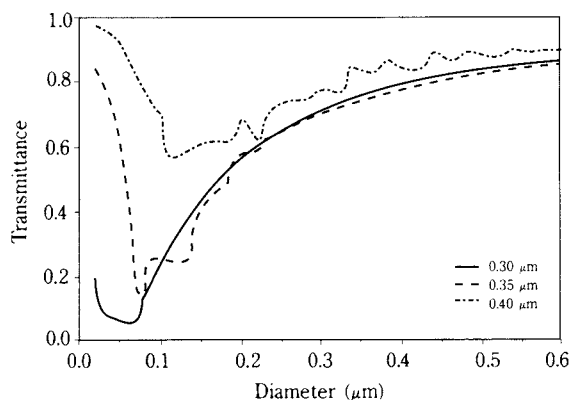


**Fig. 3** Transmittance of a film containing spherical titanium dioxide particles as a function of particle size<sup>1)</sup>.

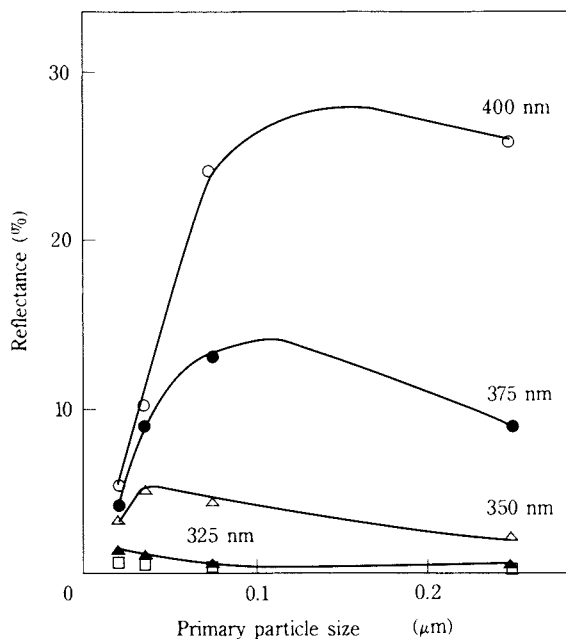


**Fig. 4** Relation between reflectance and primary particle size. (○), 400 nm; (●), 375 nm; (△), 350 nm; (▲), 325 nm; (□), 300 nm. Dispersion time, 180 min.

greater in longer wavelength of ultraviolet rays. Considering this together with the results in **Figure 2**, especially at 400 nm, UV-ray shielding capability seems to depend mostly on scattering capability.

Reflectance measured in this method was influenced by absorption and did not always represent true scattering capability. Roughly speaking, if we assume the reflected light to be scattered at an average point of a paint film thickness  $\times$  1/2, corrected reflectance can be determined with the following formula, subtracting the influence of absorption.

$$\text{Reflectance (corrected value)} = \frac{\text{Measured reflectance}}{\text{Transmittance}} \times 100$$

This equation is plotted in **Figure 5**.

By comparison of **Figure 5** and **Figure 2**, the contribution of absorption and scattering to the UV-ray shielding effect of titanium dioxide may be estimated as follows.

- 400 nm: Shielding capability is mostly due to scattering.
- 375 nm: Effects of scattering and absorption are nearly balanced.
- 350 nm: Effect of absorption is greater, but scattering cannot be ignored.
- 325 to 300 nm: Mostly due to absorption.

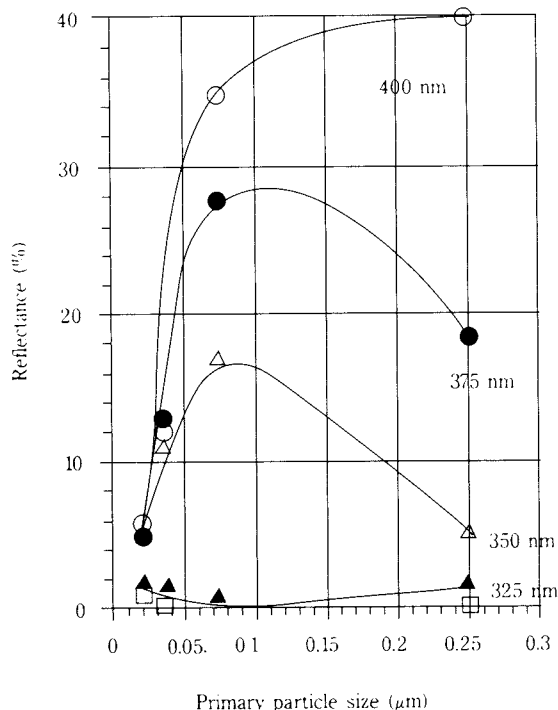


Fig. 5 Relation between reflectance (corrected value) and primary particle size. (○), 400 nm; (●), 375 nm; (△), 350 nm; (▲), 325 nm; (□), 300 nm. Dispersion time, 180 min.

To prove these results further, relationship between UV-ray absorption and particle size was simulated using a following model. The conditions of the present evaluation are PWC = 3.3% and a dry film thickness of 5  $\mu\text{m}$ . Hence, the titanium dioxide weight  $W$  existing in coated film 1  $[\text{cm}^2] \times 5 \times 10^{-4} [\text{cm}]$  (assuming the specific gravity of the coated film to be 1) is obtained as follows.

$$W = 5 \times 10^{-4} \times 3.3 \times 10^{-2} [\text{g}] \quad (1)$$

Also, assuming there are  $n$  spherical particles with mean particle radius  $r [\text{cm}]$ , the projected area  $St [\text{cm}^2]$  is as follows.

$$St = \pi r^2 \cdot n \quad (2)$$

And, assuming the specific gravity of titanium dioxide to be  $\rho$ ,  $W$  may be expressed as follows.

$$W = 4\pi r^3 \cdot \rho \cdot n / 3 \quad (3)$$

From formulas (1), (2) and (3),  $St$  is expressed in the following relation in terms of  $r$ , assuming  $\rho = 4.2$ .

$$St = 2.9 \times 10^{-6} / r \quad (4)$$

From this formula, supposing the projected sections of each particle do not overlap each other (actually

overlapping in part, though), it is required that  $St \geq 1$  in order to cover 1  $\text{cm}^2$  completely. It is thus known from formula (4) that all of 1  $\text{cm}^2$  cannot be covered unless the particle size is  $0.0292 \times 2 = 0.058 [\mu\text{m}]$  or less.

To observe changes in transmittance when the particle size was larger than 0.058  $\mu\text{m}$ , calculations were attempted by approximating the spherical particles to a rectangular shaped object having the same projected sectional area and volume as shown in **Figure 6**.

Seeing the coated film surface from the vertical direction as shown in **Figure 7**, the area occupied by titanium dioxide is supposed to be  $S_1$ , and the area free from titanium dioxide to be  $S_2$ . Hence,  $Ps$  is defined as follows (assuming whole area of coated film to be  $S_{all} = S_1 + S_2$ ).

$$Ps = S_1 / (S_1 + S_2) = S_1 / S_{all} \quad (5)$$

Assuming the volume of total titanium dioxide contained in the coat film to be  $V$ , the transmittance at  $S_1 = S_{all}$  to be  $T_0$ , and the thickness of titanium dioxide at this time to be  $L_{all}$  ( $V/S_{all} = L_{all}$ ), it follows that;

$$\ln T_0 = -\beta \cdot L_{all} \quad (6)$$

Wherein,  $\beta$  denotes the absorption coefficient of titanium dioxide.

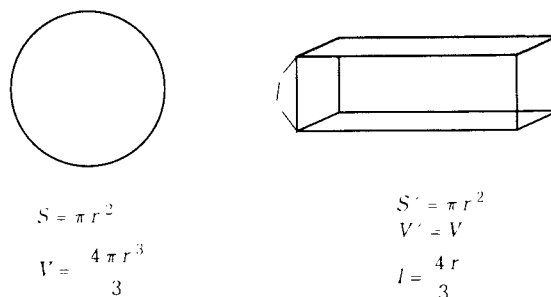


Fig. 6 Schematic model of particle shape conversion

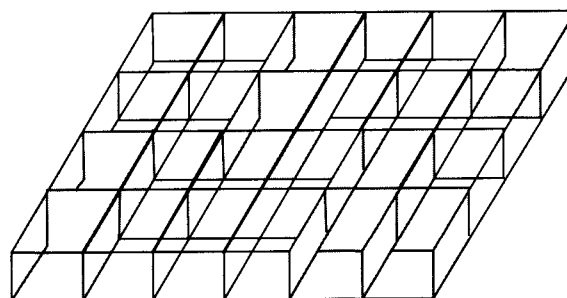


Fig. 7 Occupation model of the film with  $\text{TiO}_2$  particle. (■),  $S_1$ , the area occupied with  $\text{TiO}_2$  particle; (□),  $S_2$ , the vacant area.

If  $0 \leq S_2 < S_{all}$ , assuming the transmittance in  $S_1$  and  $S_2$  parts to be  $T_1$  and  $T_2$ , respectively, mean transmittance  $T$  in  $S_{all}$  is;

$$T = (S_1 T_1 + S_2 T_2) / S_{all} \quad (7)$$

Herein, the absorption and reflection by the base film and resin are ignored, and it follows that  $T_2 = 1$ . From formulas (5) and (7), we obtain the following.

$$T = Ps \cdot T_1 + 1 - Ps \quad (8)$$

Similarly,  $T_1$  is expressed in formula (9).

$$\ln T_1 = -\beta \cdot (V/S_1) \quad (9)$$

From formulas (5), (6), and (9), the following formula is obtained.

$$\ln T_1 = (\ln T_0) / Ps$$

$$T_1 = T_0^{(1/Ps)} \quad (10)$$

Then, from formulas (8) and (10), the following equation is deduced.

$$T = Ps \cdot T_0^{(1/Ps)} + 1 - Ps \quad (11)$$

Plotting for  $Ps = 0$  to  $1$  is shown in **Figure 8**

As seen in this figure, when transmittance  $T_0$  is low at  $Ps = 1$ , that is, when the absorption capability is high, the drop in absorption that occurs when the particle size is increased is very significant, i.e., transmittance is raised notably. In contrast, when transmittance  $T_0$  is high at  $Ps = 1$ , even if the

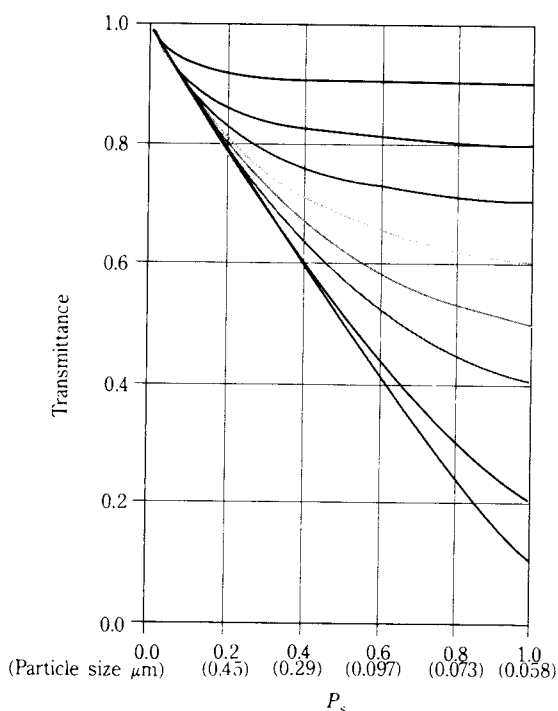


**Fig. 8** Relation between transmittance and  $Ps$ . PWC, 3.3%; dry-film thickness, 5  $\mu\text{m}$ ; calculation model.

particle size is increased somewhat, absorption capability is hardly lowered and transmittance rarely changes.

This result seems compatible with the following phenomena: At around 400 nm, where the absorption capability is low, absorption capability is not raised much, while scattering is lowered, if the particle size becomes smaller. Thus, the maximum UV-ray shielding capability is found with a relatively large particle size. On the other hand, at around 300 nm, where the absorption capability is high, absorption capability rises significantly as particle size becomes smaller, and decrease of scattering capability can be ignored. Thus, UV-ray shielding capability is raised when the particle size becomes smaller.

Effects of dispersion time are shown in **Figures 9** to **11**. **Figure 9** shows relation between transmittance at 300 nm and dispersion time for samples differing in primary particle size. In all cases, transmittance is lowered with an increase of dispersion time. In other words, the smaller the particle size, the higher the shielding capability becomes<sup>6</sup>.

**Figure 10** shows results at a wavelength of 400 nm, which are very similar to the results obtained with a visible light of 550 nm (**Figure 12**).

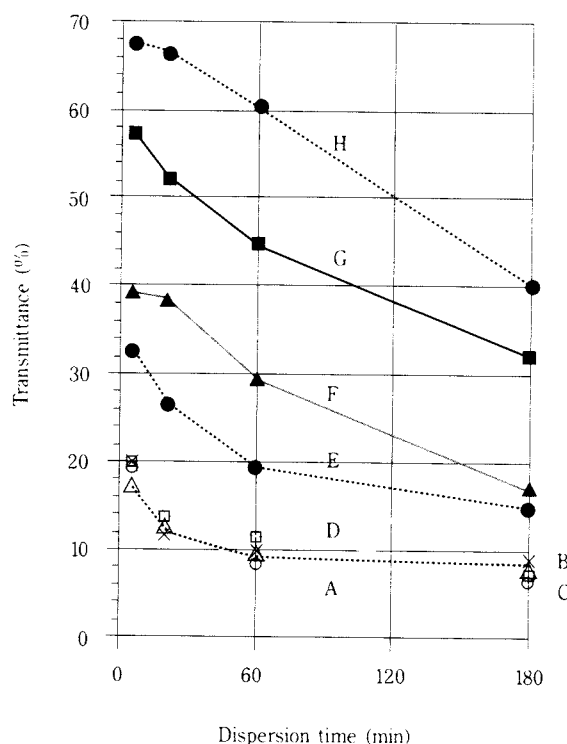


**Fig. 9** Relation between transmittance (at 300 nm) and dispersion time. (○), Sample A 0.019  $\mu\text{m}$ ; (△), Sample B 0.029  $\mu\text{m}$ ; (□), Sample C 0.036  $\mu\text{m}$ ; (×), Sample D 0.048  $\mu\text{m}$ ; (●), Sample E 0.075  $\mu\text{m}$ ; (▲), Sample F 0.096  $\mu\text{m}$ ; (■), Sample G 0.16  $\mu\text{m}$ ; (◆), Sample H 0.24  $\mu\text{m}$ .

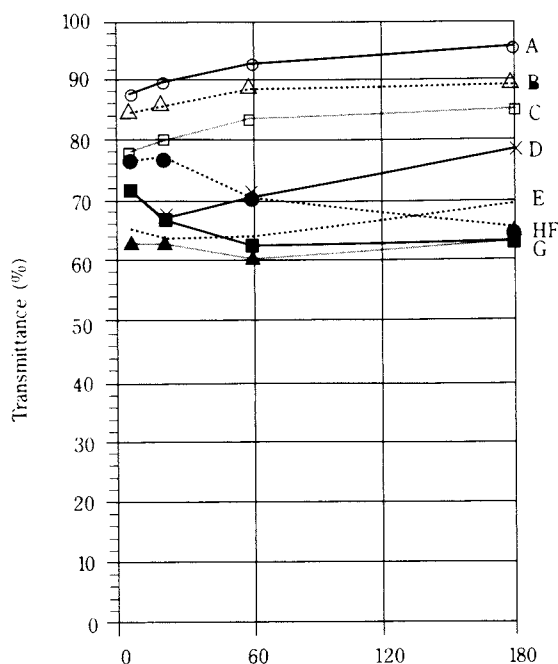


**Fig. 10** Relation between transmittance (at 400 nm) and dispersion time. (○), Sample A 0.019  $\mu\text{m}$ ; ( $\Delta$ ), Sample B 0.029  $\mu\text{m}$ ; ( $\square$ ), Sample C 0.036  $\mu\text{m}$ ; ( $\times$ ), Sample D 0.048  $\mu\text{m}$ ; (●), Sample E 0.075  $\mu\text{m}$ ; ( $\blacktriangle$ ), Sample F 0.096  $\mu\text{m}$ ; ( $\blacksquare$ ), Sample G 0.16  $\mu\text{m}$ ; ( $\blacklozenge$ ), Sample H 0.24  $\mu\text{m}$ .

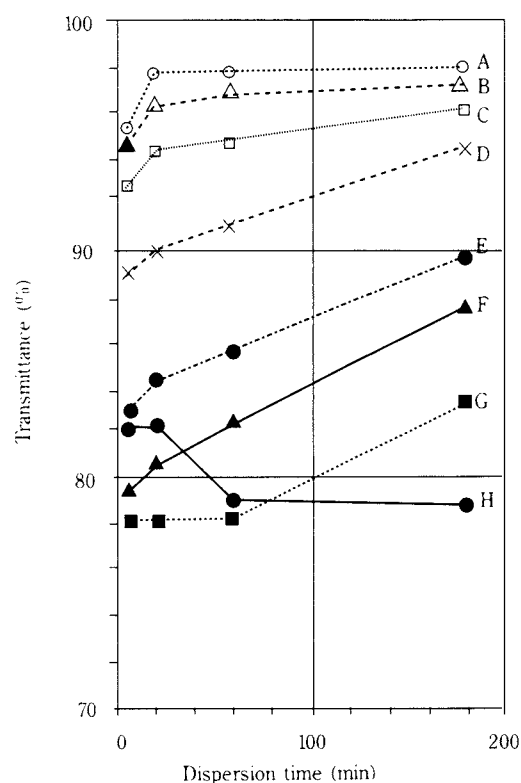


**Fig. 12** Relation between transmittance (at 550 nm) and dispersion time. (○), Sample A 0.019  $\mu\text{m}$ ; ( $\Delta$ ), Sample B 0.029  $\mu\text{m}$ ; ( $\square$ ), Sample C 0.036  $\mu\text{m}$ ; ( $\times$ ), Sample D 0.048  $\mu\text{m}$ ; (●), Sample E 0.075  $\mu\text{m}$ ; ( $\blacktriangle$ ), Sample F 0.096  $\mu\text{m}$ ; ( $\blacksquare$ ), Sample G 0.16  $\mu\text{m}$ ; ( $\blacklozenge$ ), Sample H 0.24  $\mu\text{m}$ .

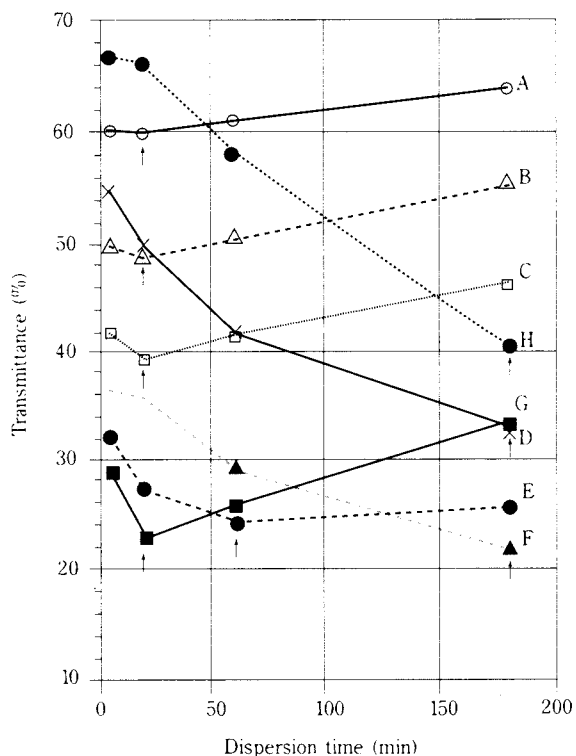


**Fig. 11** Relation between transmittance (at 350 nm) and dispersion time. (○), Sample A 0.019  $\mu\text{m}$ ; ( $\Delta$ ), Sample B 0.029  $\mu\text{m}$ ; ( $\square$ ), Sample C 0.036  $\mu\text{m}$ ; ( $\times$ ), Sample D 0.048  $\mu\text{m}$ ; (●), Sample E 0.075  $\mu\text{m}$ ; ( $\blacktriangle$ ), Sample F 0.096  $\mu\text{m}$ ; ( $\blacksquare$ ), Sample G 0.16  $\mu\text{m}$ ; ( $\blacklozenge$ ), Sample H 0.24  $\mu\text{m}$ .

The shielding capability for visible light of 550 nm is mostly due to scattering. Hence, at a wavelength of 400 nm as well, the majority of shielding capability may be considered due to scattering.

**Figure 11** shows results at a wavelength of 350 nm, in which transmittance is lowered when dispersion time is extended for larger particles of primary particle size of 0.096  $\mu\text{m}$  or more. On the other hand, in samples of a primary particle size of 0.075  $\mu\text{m}$  or less, dispersion time required to minimize transmittance was found. Hence, to shield ultraviolet rays of a wavelength of 350 nm, there seems to be an optimum particle size of titanium dioxide in a range of 0.075 to 0.096  $\mu\text{m}$ .

From the present study, the UV-ray shielding capability of titanium dioxide is confirmed due to the combined effect of scattering and absorption capabilities. Absorption is dominant in ultraviolet rays of short wavelength, while scattering is superior in ultraviolet rays of long wavelength.

Finally, the combined effect of scattering and absorption was studied, the results of which are shown in **Figure 13**. At a wavelength of 550 nm, pigment class  $\text{TiO}_2$  mainly showing scattering charac-

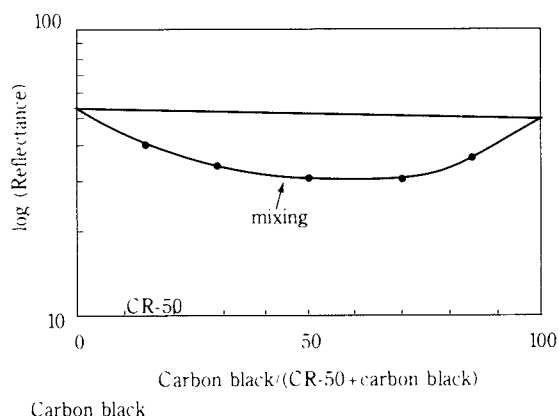


**Fig. 13** Effect of mixing with CR-50 and carbon black on reflectance at 550 nm.

teristics and carbon black mainly showing absorption characteristics were mixed at various blending ratios. The changes in transmittance of the coated film are shown. In either material alone, transmittance is about 50%, but when mixed, evidently, trans-

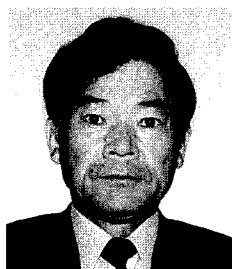
mittance shows less than 50%. In fact, when mixed at 5/5, transmittance was 30% and a significant shielding capability was exhibited.

Ultrafine particles of titanium dioxide have the ability to both absorb and scatter ultraviolet rays, and it is estimated that an excellent shielding capability was demonstrated by their combined effects.

## References

- 1) P. Stamatakis, B.R. Palmer, G.C. Salzman, C.F. Bohren and T.B. Allen: *J. Coat. Technol.*, **62** [10], 95 (1990)
- 2) C.F. Bohren: *Am. J. Phys.*, **55** [6], 524 (1987)
- 3) P.S. Mudgett and L.W. Richards: *Appl. Opt.*, **10** [7], 1485 (1971)
- 4) M. Sakamoto, H. Okuda, H. Futamata & A. Sakai, Collected papers of research meeting of Japan Association of Coloring Matter, 2B-33 (1993)
- 5) K. Kubo, Powder, p. 177, Maruzen (1985)
- 6) K. Shibata, Spectrum Measurement and Spectrophotometer, pp. 21-23, Kodansha Scientific (1974)

## Author's short biography



### Masashi Sakamoto

Graduated, Department of Chemistry, Faculty of Science, Okayama University in 1964. Began to Work for ISHIHARASANGYO KAISHA from 1964. Inagulated a Director in 1996. Now, Deputy General Manager of Technical Research Institute.



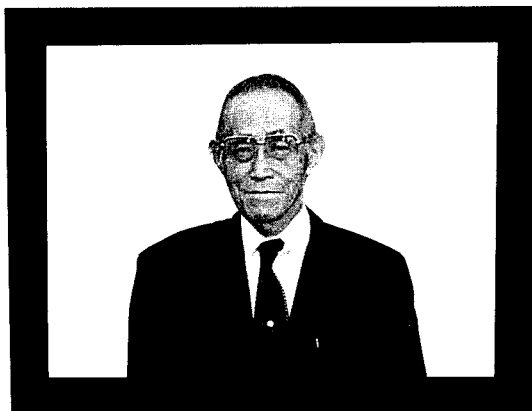
### Information Articles

#### Obituary : Professor Tetsuo Yoshida

Very sad news of the loss of our colleague, Professor M. McLaren (see front article page 1), was followed by another very sad news. Professor Tetsuo Yoshida has passed away on 26th of August, 1996 aged 82. Professor Yoshida was very famous for his research activities on powder technology through his academic carrier mainly in the departments of chemical engineering in Osaka City University, until 1970 and University of Osaka Prefecture until 1978, of which he was emeritus professor. But especially for the reader of this journal, his name never forget as the founder of this KONA journal. When he was the

president of the Council of Powder Technology, Funtai-Gijyutu-Danwakai, in 1983, he proposed to launch this new journal for promoting international exchange of many aspects of information on powder and particle technology. He also played very important role in the establishment of Hosokawa Powder Technology Foundation, and always assumed his leadership, develop this journal, as the first Secretary General of the Foundation, to develop this KONA to internationally recognized journal, His name will remain forever and ever with powder technology, especially with this journal.

(Genji JIMBO, President of the Council)



## The 30th Symposium on Powder Technology

The 30th Symposium on Powder technology, was held on September 5, 1996 in the Tokyo Sanseido Cultural Hall, sponsored by the Hosokawa Powder Technology Foundation and supported by the Hosokawa Micron Corporation.

This symposium centered around functional composite materials for coping with the problems on

resources, environment and energy and the adopted theme was "production and processes on the Latest Functional Composite Materials."

Four lectures were given on the subject. The symposium was a great success with serious participants filling the 150 seat capacity hall.

### The 30th Symposium on Powder Technology

Theme: The Production and Processes of the Latest Functional Materials

#### **Session 1 Characteristics and Applications of Materials Related Clean Energy**

Chairmanship T. Senna (Keio Univeristy)

- |  |   |
|--|---|
| <ul style="list-style-type: none"> <li>● Application of Solid Electrolytes to Resources, Environment and Energy</li> </ul> | <p>Taakashi Hibino<br/>(National Industrial Research Institute of Nagoya)</p>                 |
| <ul style="list-style-type: none"> <li>● Nickel-Hydrogen batteries</li> </ul>  | <p>Osamu Yamamoto<br/>(Central Research Center, Matsushita Electric Industrial Co., Ltd.)</p> |

#### **Session 2 Production of Functional Materials and Related Problems**

Chairmanship H. Tsuji (Osaka University)

- |  |  |
|--|--|
| <ul style="list-style-type: none"> <li>● Production Proceses and Performance of Functional Composite using Powder Materials</li> </ul> | <p>KONA Awardee, Kei Miyanami<br/>(University of Osaka Prefecture)</p> |
| <ul style="list-style-type: none"> <li>● Application of Powder Technology to Production of Functional Materials</li> </ul>             | <p>Toyokazu Yokoyama<br/>(Hosokawa Micron Corporation)</p>             |



## The 5th KONA Award

The 5th KONA Award sponsored by Hosokawa Powder Technology Foundation and given to the scientists or groups who have achieved excellence in the researches related to the basic powder technology, was presented to Professor Kei Miyanami of University of Osaka Prefecture by Masuo Hosokawa, President of the Foundation on January 18, 1996 at the R&D Center of Hosokawa Micron Corporation in Hirakata.

Professor Kei Miyanami's research achievements are related principally to the fundamental mechanism and practical applications of mixing, kneading and granulation of particulate materials as well as the measurement and control of powder processing systems. His remarkable contributions were made also in the research of production processes of functional composites starting the powder materials.

### Correction

In the original research paper entitled "Dispersants in Stirred Ball Mill Grinding" by Yanmin Wang and Eric Forssberg in KONA No. 13 (1995), p.73, there were misplaced symbols in **Figure 8** and should be corrected as follows.

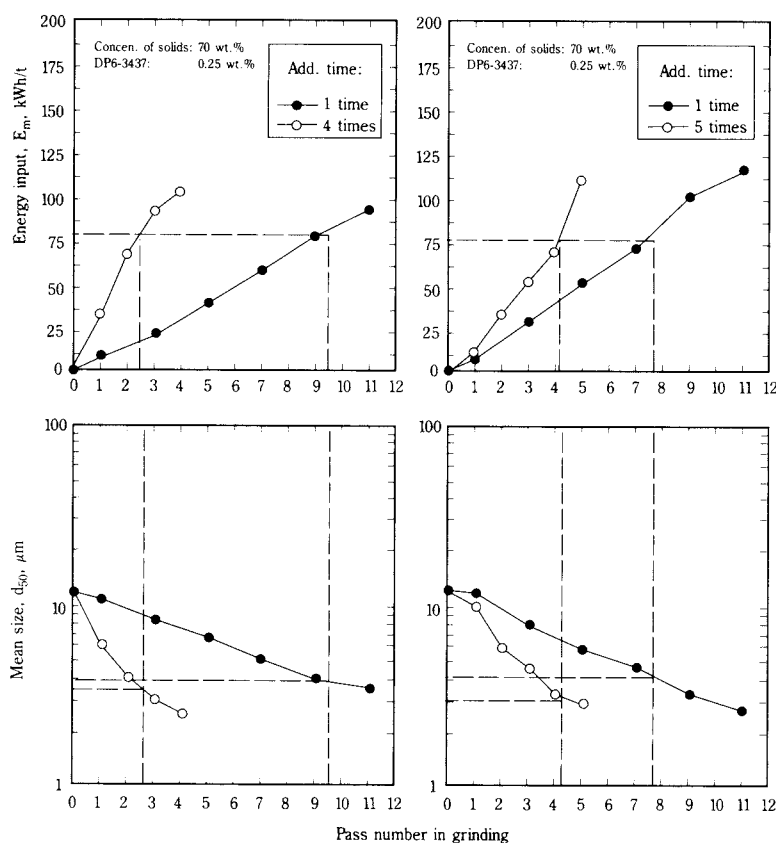


Fig. 8 Energy-size reduction relationships produced by periodic or instantaneous addition of the polymeric dispersants at a slurry concentration of 70 wt. %.



# Academic publication concerning powder technology in Japan (1995)

## Journal of the Society of Powder Technology, Japan Vol. 32 (1995)

Title	Author(s)	Page
< Research Papers >		
• The Dust Explosibility of Several Kinds of Cellulose Derivatives	H. Mukai, H. Muto and Y. Onda	4 – 9
• The Effect of Aggregation on Rheological Characteristics of an Electrorheological Fluid of the Particle Dispersion Type	K. Shimada, M. Iwabuchi, K. Okui and T. Fujita	10 – 15
• The Difference Between 2-D and 3-D Distinct Element Solution of Granular Materials	J. Yoshida	16 – 22
• Morphological Change of Antimony Trioxide Fine Particles through Impaction, Compaction or Grinding	K. Fukui, T. Matsuzaki, K. Gotoh and H. Masuda	23 – 30
• The Surface Properties and Surface-treatment of Iron Carbide Fe <sub>5</sub> C <sub>2</sub>	N. Suzuki, H. Naoi, S. Daimon, T. Arase, A. Endo, T. Kato and H. Utsugi	76 – 82
• Micro Feeding of a Fine Powder Using a Vibrating Capillary Tube	S. Matsusaka, K. Yamamoto and H. Masuda	83 – 88
• Size Segregation of Polydispersed Particles Caused by Vertical Tapping	K. Yubuta, K. Gotoh and H. Masuda	89 – 96
• Preparation of a Oxide Superconductive Composite using Aerosol Process Technology	Y. Takao, M. Awano, Y. Kuwahara and Y. Murase	144 – 150
• The Effect of Particle Shape on the Mechanical Properties of a Powder Bed	M. Otani, H. Minoshima, T. Uchiyama, K. Shinohara, K. Takayashiki and T. Ura	151 – 157
• Microstructural Control of a Oxide Superconductor by a Hybridization Process through Grinding	M. Awano, Y. Takao, Y. Murase, Y. Kuwahara and Y. Kodama	158 – 163
• The Preparation of Micro-porous Cells by the Dissolution of Core Particles within a Core-Shell Type of Composite Powder – The Preparation of Titania or Silica Micro Porous Cells –	A. Towata, A. Tsuge, M. Sando and Y. Murase	164 – 169
• A Study of Antireflective and Antistatic Coating with Ultra-fine Particles	Y. Endo, M. Ono, T. Yamada, H. Kawamura, K. Kobara and T. Kawamura	170 – 175
• Development of an On-line Measuring Apparatus of Particle Size Distribution and Concentration with a Three-stage Classifier	T. Ono, K. Koyata, H. Makino, G.H. Hong, K. Saito, K. Watanabe and K. Iinoya	222 – 228
• Preparation of Composite Particles Constituted of Fine Aluminum Nitride Powder and Polystyrene by Suspension Polymerization	I. Kimura, H. Yoshii, N. Saito and M. Tanaka	229 – 236
• Asymmetric Bin Loads due to Throwing Position	T. Yahiro	300 – 310
• The Effect of Particle Diameter on the Acoustic Properties of a Powder Bed – Sound Absorption Characteristic and Sound Velocity –	Y. Okudira, H. Ando, M. Satoh and K. Miyanami	311 – 318
• Conceptual Design of a New Type Powder Mixer with Fluctuating Air – The Mechanism of Convective Mixing –	K. Shinohara and S. Suwa	319 – 325
• Copper Recycling from Printed Circuit Board Scraps by Shape Separation – Application of Inclined Conveyor Method –	C. Izumikawa, H. Sasaki, H. Ohya, S. Endoh and H. Iwata	378 – 384

Title	Author(s)	Page
• The Recycling of Printed Wiring Board Scraps Using a Shape Sorting Technique – Recovering Copper Components by the Inclined Vibrating Method –	S. Kayanaka, S. Endoh and H. Iwata	385 – 391
• Dense Phase Horizontal Pneumatic Conveyance of Powder by a Mohnno Pump	Y. Morikawa, N. Sugita, M. Matsuda S. Nishimori, M. Maruo, M. Yamashita and H. Maruyama	446 – 452
• The Particle Packing Method and Separation Characteristics in a Liquid Chromatography Column	H. Yoshida, K. Adachi, Y. Issiki, T. Matsumoto, H. Murata, E. Shinoda and Y. Yamada	453 – 458
• Preperation of Microcapsules with the Shell of Two Layers of Organic and Inorganic Films by Spray Drying	N. Yamada, E. Abe and H. Hirosue	459 – 465
• Compression Characteristics of a Mixed Cake in Body Filtration – Evaluation of Equilibrium Porosities by the Internal Void Model –	E. Abe, H. Hirosue and N. Yamada	466 – 471
• Scale-up Performance of Dry Classification Cyclones – Evaluation by Different Particle Size Measurement Instruments –	T. Fuyuki, Y. Yamada, H. Yoshida and K. Inoya	526 – 532
• The Effects of Agitation on the Properties of a Highly Loaded Coal Water Mixture	S. Takao and H. Ozaki	533 – 537
• The Permeabilty of a Magnetic Particle Bed Suspended Magnetically	A. Touda, T. Kawanishi, Y. Hayashi and N. Shimizu	538 – 543
• The Compaction Behavior of Powder at Low Normal Stress	M. Hirota, H. Fujimura, K. Suzuoki M. Suzuki and T. Oshima	544 – 549
• A Method for Predicting the Filtration Characteristics of Body Filtration	E. Abe, H. Hirosue and N. Yamada	550 – 556
• The Effect of Particle Size and Shape on the Possibility of Plug-phase Conveying	M. Futamura	557 – 565
• The Transport of a Dense Phase Powder in a Horizontal Pipe	H. Eitoku, M. Hirota, M. Suzuki T. Oshima, Y. Iwata and T. Matsumoto	606 – 611
• The Separation of Irregular-shaped Fine Particles Using a Rotating Vibrating Conical Disk – Effects of Operating Conditions on Separation Characteristics –	K. Yamamoto, Y. Tamao and M. Sugimoto	612 – 616
• The Effect of Slurry Preparation Conditions on the Characteristics of Spray Dried Granules and their Green Compacts	M. Naito, Y. Fukuda, N. Yoshikawa H. Kamiya and J. Tsubaki	617 – 623
• Preparation and Sinterability of Spherical Calcium Phosphate Particles by Ultrasonic Spray Pyrolysis	T. Ogihara, T. Yanagawa, N. Ogata and N. Mizutani	624 – 628
• The Investigation of the Dispersion of Magnetic Powder and the Adsorption Form of a Binder Resin	Y. Takai, K. Sakamoto and K. Terashita	629 – 633
• The Effect of Planetary Mill Treatment on the Synthesis of Barium Hexaferrite Powder	M. Narita, O. Abe and F. Ikazaki	634 – 638
• The Amorphization Process of Titanium Oxide During Planetary Ball Mill-treatment	Y. Suzuki, O. Abe and F. Ikazaki	639 – 643
• A Wet Classification Process of Suspension	N. Furuno	644 – 648
• The Change in the Water Vapor Affinity of Fine Particles Loaded with Trimethylsilyl Groups	M. Fuji, H. Iwata, T. Takei T. Watanabe and M. Chikazawa	649 – 659

Title	Author(s)	Page
• Synthesis of Y-Fe-O Ultrafine Particles Using RF Thermal Plasma	M. Sugasawa, N. Kikukawa and N. Ishikawa	660 – 667
• Computer Simulation of the Initial Stage Sintering of Particles	A. Shimosaka, T. Sawai and J. Hidaka	668 – 674
• The Effect of a Carrier Solution on Particle Size Measurement by Sedimentation Field-Flow Fractionation	Y. Mori, M. Harada, K. Miyamoto S. Inoue, M. Suzuki and M. Tanigaki	675 – 680
• The Conceptual Design of a New Type of Powder Mixer with Fluctuating Air: The Effects of Shearing and Diffusive Mixing	K. Shinohara and S. Suwa	706 – 712
• Collection Efficiency of Granular Bed Filters Resulting from Inertial Impaction and Interception	H. Mori and N. Kimura	713 – 721
• Effect of Particle Shape on Particle Size Analysis Using the Electrical Sensing Zone Method and Laser Diffraction Method	K. Inaba and K. Matsumoto	722 – 730
• The Relationship Between the Pharmaceutical Properties and Dispensing of a Fine Granule – The Examination of the Evaluation Method for Dispensing of a Fine Granule –	K. Kawano, M. Ohkuma, K. Nakazawa, S. Takamatsu, K. Kawada, S. Nakajima, K. Ohtsuki, Y. Ohtani and T. Ishikawa	731 – 737
• Dust load Distributions in Fibrous Mat and Granular Bed Filters with Particle Reentrainment	H. Mori, N. Kimura and S. Ishii	788 – 795
• The Effect of the Refractive Index Input Value on Particle Size Distribution Measured by the Laser Diffraction & Scattering Method	O. Hayakawa, Y. Yasuda, M. Naito and J. Tubaki	796 – 803
• The Effects of a Volatile Additive on the Dry Grinding of Talc	K. Hamada, S. Yamamoto and M. Senna	804 – 811
• The Performance of Needle Punched Felt Filters	H. Mori, N. Kimura, M. Kakizoe and S. Uesaka	856 – 865
• The Quantitative Measurement of Forces Acting on a Powder Bed During a Specific Mechanical Process for Preparation of Composite Particles	H. Yoshino, Y. Taya, H. Kaga and K. Mukaida	866 – 873
• A Study of a Generation Process of Oxide Ultra Fine Particles with Arc Energy	Y. Endo, T. Araya, M. Kanamura, Y. Ibaraki, T. Yamada and S. Hioki	874 – 880

#### Kagaku Kogaku Ronbunshu Vol. 21 (1995)

Title	Author(s)	Page
• Production of Needle – like $\alpha$ -Fe <sub>3</sub> O <sub>4</sub> Fine Particles by an Intermittent and Rapid Oxidation Method	N. Hashimoto, N. Fukuda, K. Ohshima and M. Matsunaga	8 – 14
• Development of a Fluidized-Bed Limestone Calciner	K. Tsutsumi, I. Hashimoto, S. Kanamori, M. Murao, N. Ichinoya, K. Yoshida and J. Tatebayashi	15 – 21
• Classification Characteristics of a Centrifugal Powder Classifier	M. Ito, H. Ninomiya and S. Fujii	56 – 65
• Simultaneous Reduction Techniques of Nitrous and Nitrogen Oxides from Fluidized – Bed Coal Combustor	H. Hosoda, T. Hiramata and H. Aoki	74 – 82
• Effect of Grinding Condition on Hydrophobic Surface Treatment of Quartz Sand Using Planetary Mill	M. Suzuki, H. Iguchi, A. Ohtani M. Hirota and T. Oshima	111 – 117

Title	Author(s)	Page
• Effect of Stepwise and Continuous Reduction in Impeller Speed on Particle Size Distributions in Suspension Polymerization of Styrene	M. Tanaka, H. Tanaka, I. Kimura, N. Saito and K. Hosoguchi	118 – 125
• Preparation of Al/Zr Composite Powder by Solid Propellant Combustion	S. Deguchi, A. Takahashi, H. Matsuda, M. Hasatani, K. Kato and G. Nakashita	126 – 131
• Bubble Characteristics of Circulating Three-Phase Fluidized Bed	M. Yarime, A. Tsutsumi, A. Sasaki, T. Charinpanikul, Y. Matsumura and K. Yoshida	132 – 136
• Mixing Times of Liquid in Gas – Liquid Contactors with Mechanical Agitation	K. Satoh, T. Menju, M. Mochizuki and A. Shono	137 – 142
• Dynamic Shape Factors of Regular Shaped Agglomerates	T. Niida and S. Ohtsuka	173 – 180
• Flow Characteristics of Solid Particle Suspensions	K. Ogawa, C. Kuroda, S. Yoshikawa and A. Umemoto	189 – 195
• Calcination of Diatomaceous Earth in Fluidized Bed and Entrained Bed	T. Kojima, T. Kimura, M. Kurimoto, T. Nakagawa, J. Nishioka, S. Uemiya and H. Sumi	241 – 247
• Regeneration of Ceramic Filter Applied to Coal Char Separation	S. Ito, S. Kawamura and S. Komura	265 – 271
• On-Line Temperature Control of Fluidized Bed Incinerator Using Fuzzy Algorithm	S. Okayasu, T. Kuratani and H. Imai	272 – 278
• Liquid Mixing and Gas-Liquid Mass Transfer of Bubble Column with Packed Double Perforated Draft Tube	Y. Bando, M. Nishimura, H. Hayakawa, N. Kawase and A. Idota	279 – 285
• Computer-Aided Synthesis of Metal Separation Processes by Precipitation	E. Kunugita, Y. Inoue, J. H. Kim and I. Tsuboi	294 – 299
• Characterization of CaCO <sub>3</sub> ground by a Multi-Ring Media Mill	K. Hamada and M. Senna	334 – 340
• Control of Dispersion of Agglomerated Particles in Water by Electrostatic Repulsion Force	Y. Kousaka, Y. Endo, T. Horiuchi and Y. Sasaki	372 – 377
• Effect of Additives on Oxygen Removal for AlN Fine Particles Synthesised by Surface Corona Discharge-CVD	K. Kondo, K. Harima, K. Shinohara, Y. Ohyama and S. Chiba	424 – 429
• Nucleation and Growth Phenomena in Producing Monodispersed Lead Sulfate Particles by Reactive Crystallization	I. Hirasawa, K. Muraoka, D. Katou and K. Toyokura	495 – 501
• Motion of Grinding Media in Axial Direction and Its Effect on Comminution in an Agitation Beads Mill	Y. Hashi and M. Senna	502 – 507
• Maximum Stable Drop Size in Turbulent Agitated Vessel	M. Kuriyama, M. Ono, E. Harada and H. Konno	508 – 513
• Catalytic Pyrolysis of Plant-Biomass in a Powder-Particle Fluidized Bed	C. Wang, H. Machida, N. Nakagawa, T. Takarada and K. Kato	531 – 539
• Effect of Catalyst, Fluidized Gases and Operating Conditions upon Light Aromatic Hydrocarbon Yield for Catalytic Pyrolysis of Woody – chip by Powder Particle Fluidized Bed	C. Wang, N. Nakagawa and K. Kato	540 – 546
• Pressure Distribution of Funnel Flow Silos with Consideration of Flow Channel	M. Suzuki	554 – 564

Title	Author(s)	Page
• On-Line Simultaneous Measurement of Powder Flow Rate and Electric Charge of Particles in Gas – Solids Pipe Flow – Effect of air velocity on accuracy of measurement –	H. Masuda, S. Matsusaka and H. Fujimoto	573 – 580
• Flow Rate and Fluctuation of Wall Pressure During Discharge of Granular Materials from Bin-Hopper System	J. Hidaka, J. Kano and A. Shimosaka	581 – 587
• Gas Holdup in a Bubble Column with a Single Hole Orifice	H. Kawasaki and H. Tanaka	588 – 593
• Effect of Blow – Down on Fluid Flow and Particle Movement in Cyclone Classifier	H. Yoshida, T. Fujioka, K. Hashimoto and K. Nagahashi	594 – 602
• Analysis of Flame Gas Velocity and Temperature Distribution from Double – Pipe Nozzle Jet in a Production Unit for Spherical Particles by Flame Spray Metohd	T. Go, M. Honda and K. Kato	641 – 647
• Analysis of Fusing and Sphering Phenomena of Solid Particles in Flame Spray Unit	T. Go, M. Honda and K. Kato	648 – 656
• Comminution Kinetics of Cement in Tobu Milling	M. Ito	657 – 665
• Effect of Comminution Kinetics Parameters and Classification Efficiencies on Capacity in the Closed – Circuit Grinding of Cement	M. Ito	666 – 673
• Mechanism of Air Jet Removal of Particles	K. Gotoh, M. Tagaya and H. Masuda	723 – 731
• Numerical Analysis of Pressure Drop in Separator Type Filter and Estimation of Its Optimum Separator Height	S-J. Cho, Y. Otani and H. Emi	776 – 784
• Dispersion Mechanism of Coagulated Particles (Doublets) in Shear Field in Water	T. Horiuchi, Y Kousaka and Y Endo	785 – 792
• Combustion Characteristics of a Circulating Fluidized Bed Gas Combustor for Low Calorific Fuel	A. Kataoka, T. Ihara, H. Matsuda, M. Hasatani, W. Nowak and A. Oda	793 – 799
• Application of On-Line Near – Infrared Analyser to Process Control in Fermentation Plant	S. Okayasu, M. Katayama, and S. Miyashiro	847 – 852
• Preparation of Monodisperse Composite Particles by Hydrolysis of Metal Alkoxides with Seed Particle	M. Hasegawa, M. Kimata, S. Ishibashi and Y. Kanda	879 – 885
• New Estimation Method of Particle Size Distribution by Anisokinetic Sampling	H. Makino, H. Tsuji, M. Kimoto, H. Yoshida and K. Iinoya	896 – 903
• Formation of Colloidal Gold with Acetone – Dicarboxylic Acid in Aqueous Phase	Y. Miyake, T. Muta, K. Ishizuka, T. Shiraishi, M. Iwasaki and Y. Mori	929 – 935
• Distributions of Size and Composition in Carbon – Supported Pt-Ru Composite Metal Fine – Particle Catalysts	Y. Saito, H. Ogino and T. Fukushima	984 – 989
• CVD Synthesis of Supported Molybdenum Carbide Catalyst and its Catalytic Activity for CO <sub>2</sub> Hydrogenation	T. Miyao, M. Matsuoka, I. Shishikura and M. Nagai	1015 – 1023
• Isomerization of 1-Methy “1” naphthalene over HY Zeolite	T. Nobusawa, Y. Takagi and T. Suzuki	1090 – 1095
• Prevention and Estimation of Catalytic Deactivation in Isomerization of 1-Methyl “1” Naphthalene	Y. Takagi, T. Nobusawa and T. Suzuki	1096 – 1103
• A Study on Degradation Phenomena of Reforming Catalyst in DIR-MCFC	Y. Miyake, N. Nakanishi, T. Nakajima, Y. Itoh, T. Saitoh, A. Saiai and Y. Yanaru	1104 – 1109
• Molecular Simulation of Thermal Destruction Processes in Aluminophosphates [F]	H. Yamano, Y. Oumi, M. Kubo, R. Vetrivel and A. Miyamoto	1139 – 1146

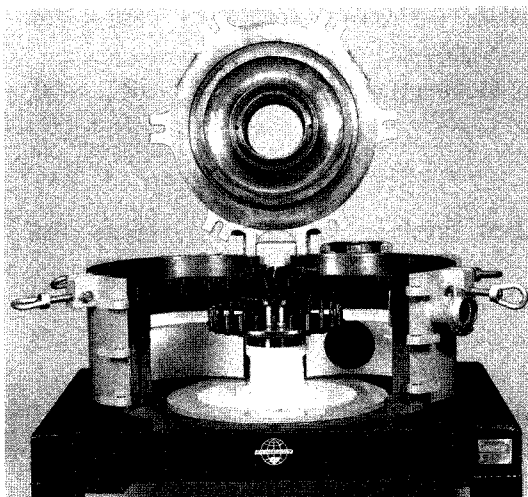
---

## New Product News

---

### Mikro ACM SB Air Classifier Mill

We introduce the new air classifier mill model 'ACM SB' which designed for fast access/fast cleaning/fast turnaround/maximum availability. A continuous policy of research and development over the years has resulted in MikroPul introducing new technologies into the powder coatings industry.



#### Features

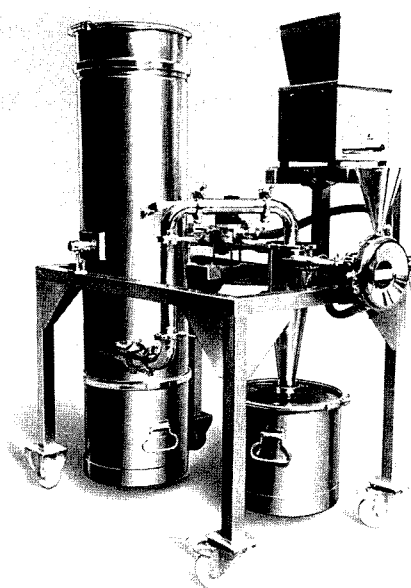
- The mill cover opens to allow both body sections to swing open giving total unhindered access to all internals.
- Special construction offers an operating noise level not exceeding 85dBA a 1 meter.
- High efficiency classifier design with air purging enables the ACM SB to produce ultra fine materials with  $D_{92} = 10$  microns on most products.
- The ACM SB is designed for explosion pressure shock resistant to 11 bar (PSR11).
- The machine is constructed for easy disassembling and cleaning.

#### HOSOKAWA MIKRON LIMITED.

Rivington Road, Whitehouse Industrial Estate, Runcorn, Cheshire WA7 3DS  
Tel: (01928) 710101 Fax: (01928) 714325

---

### Pharmaceutical Lab Mill System with Alpine Spiral jet Mill 100AS — system design to conform with GMP standards —



#### Application Areas/Features

- The 100AS jet mill systems pulverize and classify powders to particle finenesses ranging from 0.5 to approx. 50 microns.
- Operate with compressed air or inert gas.
- All stainless steel construction. Internal and external surfaces finished to pharmaceutical standards.
- Cover and housing in monoblock design.
- Complete accessibility for cleaning. No tools required for dismantling.
- The 100AS jet mill systems are delivered ready for operation, completely mounted on a mobile installation table.

#### HOSOKAWA ALPINE Aktiengesellschaft

P.O. Box 101109, D-86001 Augsburg, Germany  
Tel: +821/5906-0 Fax: +821/57 35 58

---

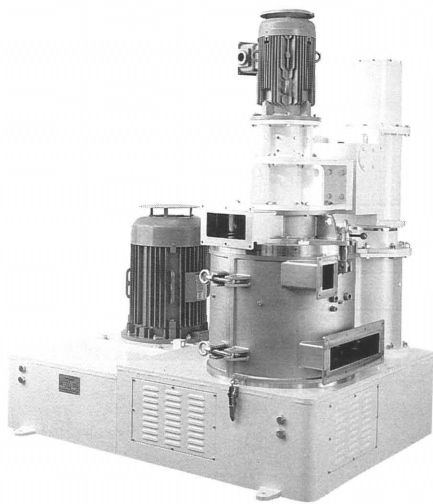
## New Product News

---

### Hosokawa Micron

#### Inomizer INM – Innovation in the mechanical ultra fine grinding

The Inomizer is a high speed impact type mechanical pulverizer which has been designed to pursue the ultimate grinding efficiency in the dry ultra fine powder production. The latest design challenges and surpasses the bounds of an impact type mill.



#### Features

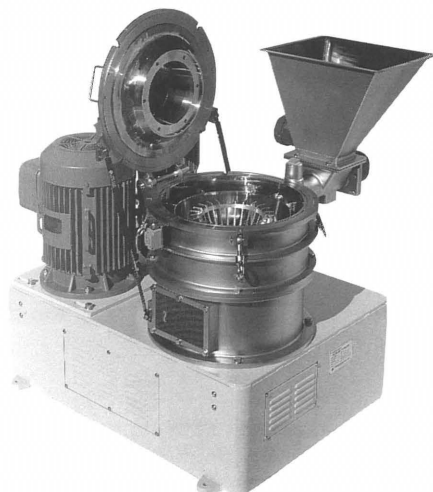
- Supreme grinding performance  
Ultra fine powder can be produced in the average product size of several microns effectively by this new concept mechanical pulverizer. It is possible to achieve maximum 2 to 3 time higher grinding capacity in the specific power (kilogram/kW) than that of a conventional jet mill system. Beside 30 – 50% energy can be saved compared with a conventional jet milling system in the toner powder production.
- Top product quality adds more value  
Particle shape control and production of new composite material can be accomplished.
- Sharp particle size distribution and precise top size control  
A built-in variable high speed type classifier enables flexible and precise particle size control desired.
- Fast access for easy maintenance and cleaning  
The mill housing (INM30 & 60) is designed with double-leafed hinged door to allow full access to all internals easily.
- Comprehensive range of system design and options  
The mill can be designed with a water cooling jacket housing, cryogenic grinding, closed circuit system, etc. for wide range of specific needs.

---

### HOSOKAWA/Mikro

#### ACM Pulverizer A Type – High Speed Impact type Air Classifying Mill

A new generation of Air Classifying Mill ACM-A has been released succeeding to the abundant application and installation more than 2000 units of ACM worldwide.



#### Feature

- Increase of grinding performance  
Newly designed vertical grooved hammer generates powerful grinding capability performing the average 1.3 to 1.5 times higher capacity than that of former ACM.
- Easy and precise product fineness control  
A built-in variable speed classifier achieves flexible and precise particle size control. High speed type classifying rotor is also available as option.
- Comprehensive range of optional grinding elements  
Wide range of optional hammers, liners and classifying rotors are available in several different material construction and combination for extensive requirement.
- Easy maintenance and cleaning work  
The design of ACM has been devised to simplify maintenance and cleaning work, and all driving parts are protected by totally enclosed common base for safety.

# HOSOKAWA MICRON

## Global Capability of Hosokawa Micron Group

Hosokawa is the nucleus of a global powder technology structure, thinking of what can help to create as a worldwide mountain range, formed from the peaks of powder processing technology.



HOSOKAWA MICRON THROUGHOUT THE WORLD



## HOSOKAWA MICRON

### Asia/Australian Block

#### **HOSOKAWA MICRON CORPORATION**

5-14, 2-chome, Kawaramachi, Chuo-ku,  
Osaka 541, Japan

Tel: 81-6-233-3968

Fax: 81-6-229-9267

### Americas Block

#### **HOSOKAWA MICRON INTERNATIONAL INC.**

780 Third Avenue, New York,  
NY 10017, U.S.A

Tel: 1-212-826-3830

Fax: 1-212-826-6612

### European Block

#### **HOSOKAWA MICRON INTERNATIONAL B.V.**

World Trade Center, Strawinskylaan  
249, 1077XX Amsterdam, Holland

Tel: 31-20-673-5571

Fax: 31-20-676-2061